Polyoxometalates Confined within Nanotubes

Jack William Jordan

Thesis submitted to the University of Nottingham for the degree of Doctor of Philosophy

2021

Abstract

The work presented in this thesis investigates polyoxometalates (POMs) confined within nanotubes and their structure, host-guest interactions and electrochemical properties. Utilising a suite of spectroscopic and microscopic techniques, the encapsulation of POMs within single walled carbon nanotubes (SWNTs) was revealed to be redox driven, in which spontaneous charge transfer from the SWNTs to POMs in solution gave rise to coulombic attraction between the two species, driving encapsulation of the POMs within the SWNTs. The level of SWNT oxidation was dictated by the energy levels of the corresponding encapsulant POM. In cases where spontaneous electron transfer between the two could not occur, the levels of encapsulation were seemingly lowered. Utilising a range of imaging conditions, transmission electron microscopy (TEM) revealed that the encapsulated POMs were extremely beam sensitive, leading to a rapid decomposition of the native {POM}@SWNT structure. The high level of encapsulation meant that the reactivity of ~100 molecules could be studied at once, as well as using AC-TEM methods to study the atomic nature of the reaction. Electrochemical analysis of the {POM}@SWNT materials revealed the electron transfer between the encapsulated POMs and the electrode was rapid during electrochemical charge-discharge, mediated by the intimate electronic contact between the POMs and SWNTs. The SWNTs also served to stabilise the encapsulated POMs, allowing the material to be cycled over 1000 times with minimal changes to the current response, as well as allowing a cyclic voltammogram of the encapsulated POMs to be obtained in an electrolyte with an extremely high pH. When moving from protic electrolytes, the CV responses of the {POM}@SWNT materials drastically altered due to the inhibited mass transport of larger cations during POM reduction, allowing the POM@SWNT materials to be used as a model system to better understand the mass transport of ions in these nanodomains during electrochemical cycling. By encapsulating POMs within boron nitride nanotubes (BNNTs) the nature of host-guest interactions in these systems could be better understood by probing the vibrational spectra of the guest POMs. Photoluminescence (PL) measurements and low temperature Raman measurements demonstrated that the interaction between the two allowed electronic communication, manifested as quenching of PL emissions and the emergence of new ones at low temperatures.

Publications

<u>Jordan, J. W.</u>, Lowe, G. A., McSweeney, R. L., Stoppiello, C. T., Lodge, R. W., Skowron, S. T., Biskupek, J., Rance, G. A., Kaiser, U., Walsh, D. A., Newton, G. N., Khlobystov, A. N., Host–Guest Hybrid Redox Materials Self-Assembled from Polyoxometalates and Single-Walled Carbon Nanotubes. *Adv. Mater.* **2019**, 31, 1904182.

Acknowledgements

I've been very lucky to be surrounded by a group of very talented and supportive colleagues and friends during my PhD, without whom I would not have continued to learn or enjoy my experience. My supervisors, Prof. Andrei Khlobystov and Dr. Graham Newton, have provided a stimulating scientific environment and have both pushed me to be the best that I could be. I'd particularly like to thank Andrei for our branching philosophical discussions, and Graham for always leaving me feeling energised and refreshed.

I would also like to acknowledge Dr. Darren Walsh and would like to thank him for all his electrochemical knowledge and advice. I'd also like to acknowledge the hard work of Dr. Grace Lowe, for helping with the early electrochemical studies whilst in Darren's group, as well as Beth Mortiboy for continuing some of this work. Working with both was a pleasure.

Understanding how these species behaved under electron beam irradiation would not have been possible without Dr. Kayleigh Fung and her complete control of an electron microscope. Dr. Stephen Skowron also played a large part in this area of work (as well as theoretical studies in other areas of this thesis). Whilst more than "just a computer", Steve has always been on hand to discuss science or read my work and has become a good friend. I would also like to thank Dr. Robert McSweeney for his help at the start of my PhD and beginning of the overall project.

Dr. Graham Rance acquired the room temperature Raman in this thesis as well as providing important insight into the data and answering any questions that I had. His input into the work on boron nitride nanotubes and discussions were always extremely helpful and useful. I would like to thank Nanoscale and Microscale Research Centre (nmRC) for access to the instruments that provided pivotal data for this thesis. In particular, I would like to thank Dr. Michael Fay for TEM training and Dr. Emily Smith and Dr. Craig Stoppiello for acquiring XPS data. I would like to thank Dr. Jesum Alves Fernandes and Dr. Emily Smith for discussing XPS data with me.

I would also like to thank Prof. Ute Kaiser and Dr. Johannes Biskupek from the University of Ulm for acquiring the AC-TEM data in this thesis, and Dr. Alexander Chernov for acquiring the low temperature Raman data, and his detailed analysis, whilst at the University of Cologne. I would also like to acknowledge the work of Dr.

Chris Allen at the electron Physical Science Imaging Centre (ePSIC) at Diamond Light Source for the low flux AC-TEM imaging. I am also very grateful to Dr. Ellen Matson and her group at the University of Rochester who graciously synthesized the vanadate cluster used for encapsulation in this thesis. I would also like to thank Dr. James Kerfoot for acquiring some confocal photoluminescence measurements.

I would like to thank the EPSRC CDT in Sustainable Chemistry for funding my PhD and providing extra training, as well as the management team and directors for running the programme smoothly and providing support and advice. Being a part of my CDT cohort was also a pleasure.

Both research groups that I was a part of made me feel welcome and provided the right environment to better myself, with too many people to mention becoming good friends in the process. In particular, I would like to thank Dr. Jamie Cameron and Dr. Alexander Kibler for helpful discussions on POM chemistry and reading some of my work. Dr. Maxwell Astle, Dr. Craig Stoppiello, William Townsend and Luke Norman were also extremely helpful in the lab/with instruments and for discussing my science with.

I'm extremely fortunate to have made many friends during my PhD and would like to particularly thank Neelam, Sarah and Sharad for their friendship. A special acknowledgement should be paid to Max and Craig for their version of "support" and general antics, which were always sure to lift a low mood.

Finally, I would like to thank my friends and family for their continued support during these 4 years. My girlfriend Laura has also provided me with unwavering support throughout the personal ups and downs during my PhD and took good care of me whilst I locked myself away to write.

List of Abbreviations

... @ ...	... encapsulated within ...
AC-TEM	Aberration corrected transmission electron microscopy
AQ	9,10-anthrquinone
BN	Boron nitride
BNNT	Boron nitride nanotube
CNT	Carbon nanotube
CV	Cyclic voltammogram
CVD	Chemical vapour deposition
DEA	Dissociative electron attachment
DEC	Diethyl carbonate
DFT	Density functional theory
DKO	Direct knock-on
DMC	Dimethyl carbonate
DMF	Dimethylformamide
DoS	Density of states
DWNT	Double walled carbon nanotube
EC	Ethylene carbonate
EDX	Energy dispersive x-ray spectroscopy
EMC	Ethylmethyl carbonate
ESI	Electrospray ionisation
Fc	Ferrocene
FWHM	Full width half max
GCE	Glassy carbon electrode
GNF	Graphitised nanofibre
GO	Graphene oxide
h-BN	Hexagonal boron nitride
HER	Hydrogen evolution reaction
HOMO	Highest occupied molecular orbital
HRTEM	High resolution transmission electron microscopy
IR	Infrared
IVCT	Intervalence charge transfer
LbL	Layer-by-layer
LMCT	Ligand to metal charge transfer
LSV	Linear sweep voltammetry
LUMO	Lowest unoccupied molecular orbital
MALDI-TOF	Matrix assisted laser desorption/ionisation Time of flight
MWNT	Multiwalled carbon nanotube
NMR	Nuclear magnetic resonance spectroscopy
O-SWNT	Oxidised single walled carbon nanotube
PCC	Perchlorocoronene
PCET	Proton coupled electron transfer
PDDA	Poly(diallyldimethylammonium chloride)
PhQ	9,10-phenanthrenequinone
PL	Photoluminescence
POM	Polyoxometalate
PTFE	Poly(tetrafluoroethylene)
RBM	Radial breathing mode

RFB	Redox flow battery
SCE	Saturated calomel electrode
SEI	Surface electrolyte interface
SOMO	Singly occupied molecular orbital
SPM	Scanning probe microscopy
STEM	Scanning transmission electron microscopy
STEM-EELS	Scanning transmission electron microscopy electron energy loss spectroscopy
SWNT	Single walled carbon nanotube
TBA	Tetrabutyl ammonium
TEA	Triethylamine
TEGDME	Tetraethylene glycol dimethyl ether
TEM	Transmission electron microscopy
TGA	Thermogravimetric analysis
TOF	Turn over frequency
TON	Turn over number
UV-vis	Ultraviolet-visible adsorption spectroscopy
$[V_6]$	$V_6O_7(OMe)_{12}$
Vis-NIR	Visible near infrared adsorption spectroscopy
XPS	X-Ray photoelectron spectroscopy

Table of Contents

Chapter 1: Nanoconfined Electrochemistry within Carbon Nanotubes

1.1 Energy Storage

As the planet's population continues to grow at an ever-increasing rate,[1] the worldwide energy requirement is also increasing.[2] Fossil fuels, which led to the industrial revolution and rapid human and technological developments from the 19th century onwards, are still utilised as the primary source of energy today. The formation of oil, coal and natural gas takes millennia, rendering these precious resources finite.

Whilst overall the gains made from utilising these fuels has had a positive impact on society today, upon combustion these fuels generate water, methane and carbon dioxide, so-called greenhouse gasses. The level at which these fuels have been, and continue to be, used has led to the release of large quantities of these gasses, leading to stark changes in the molecular composition of the earth's atmosphere.[3, 4] Such large changes in atmospheric composition has already led to increases in global temperatures[5] and is expected to further raise the earth's average surface temperature, altering climates through rising sea levels,[6] intensification of single weather events[7] and devastation of flora and fauna.[8]

In order to move away from current levels of fossil fuel use, nations must adopt more sustainable technologies. Largely, this appears to be happening at a global scale and the use of wind, solar and hydroelectric power appears to be increasing year on year.[9] However, one of the key practical benefits of combustible fuel sources is that they can be used as and when they are needed, such as combusting more fuel at a power station, or increasing the amount of fuel supplied to an engine in a car. For more sustainable energy sources, the electrical energy must be used as and when it is generated.

Particular sustainable chemical solutions to this energy storage problem have focused on either conversion of electrical energy *via* hydrolysis to hydrogen gas which can then be combusted or used in a hydrogen fuel cell,[10] or through electrochemical energy storage. Secondary batteries, where the battery can be repeatedly charged and discharged to repeatedly provide energy, are the most widely used batteries today, powering portable devices such as computers, mobile phones and, more recently, electric vehicles.[11] However, as this demand for renewable energy increases, so too does the demand for charge storage devices; future electrical grid storage, electrification of transport and chargeable devices will all require next generation charge storage devices that will need to be tailored to their specific role.[11-13] Some devices will require extremely high specific power (W kg^{-1}) but for short periods of time, whereas others will have lower power requirements but will require a high specific energy (Wh kg^{-1}) (**Fig. 1.1**). This has led to increased interest in the development of advanced charge storage materials.

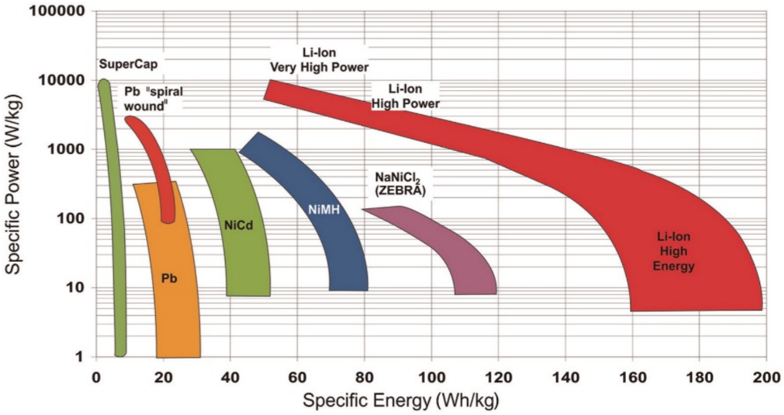

Figure 1.1. Ragone plot of various charge storage technologies. Reproduced from reference 13 with permission from SAGE publications.

The development of robust, solid-state redox active materials will likely have the largest impact in this area of research due to their wide applicability. Such materials will require highly conductive matrices to connect redox active materials to electrodes and current collectors. Carbon nanotubes (CNTs) are a class of highly stable carbon nanomaterials with high surface areas and conductivities, which can be widely functionalised, making them an attractive target for solid-state charge storage materials.

1.2 Carbon Nanotubes

Whilst the first report of carbon nanotubes (CNTs) is a much debated topic,[14] and is often attributed to Russian scientists at the start of the Cold War, there is no doubt that the paper written by Iijima in 1991 led to the wider research interest in CNTs.[15] The timing of the publication (following Kroto's isolation of buckminsterfullerene[16]) perfectly matched the scientific community's appetite and ability to study these fascinating structures. CNTs are cylindrical and hollow tubular structures, composed of graphitic sheets of sp^2 hybridised carbon atoms. Many different classes of CNTs exist; the predominantly identifying feature is usually the number of graphitic sheets that the CNT is composed of. In CNTs, these graphitic sheets are often referred to as

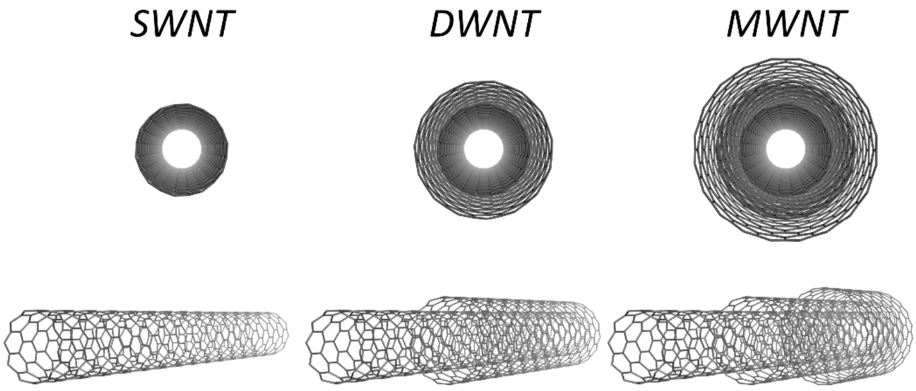

Figure 1.2. Cross-sectional and side projections of model SWNT, DWNT and MWNTs (labelled above).

walls and can range from single walled carbon nanotubes (SWNTs) and double walled carbon nanotubes (DWNTs) to multi walled carbon nanotubes (MWNTs) (**Fig. 1.2**).

Although the isolation and characterisation of SWNTs[17, 18] (definitively proven by Iijima and Bethune and their co-authors simultaneously in 1993) pre-dates that of graphene,[19] SWNTs can be considered rolled up sheets of a single layer of graphene, resulting in an atomically thick CNT sidewall. The type of SWNT, referred to as the chirality, can be described by arbitrary vectors along the two-dimensional graphene lattice that determines the structure of the SWNT. These vectors are described by chiral indices (*m, n*) which express units of the repeating graphene lattice vectors. Where *m* = *n* an armchair nanotube is formed, when *n* = 0 a zigzag nanotube is formed (named after the shape of the terminating carbon lattice at the SWNT ends) (**Fig. 1.3**). All other possibilities of *m* and *n* are referred to as chiral nanotubes. These chiral indices dictate the diameter, helicity and electronic properties of the individual nanotube. The diameter of SWNT is described by:

$$d_{NT} = \frac{a}{\pi}\sqrt{m^2 + n^2 + nm}$$

Where a = repeating graphene lattice vector (2.46 Å) and *m* and *n* are the chiral indices described previously.

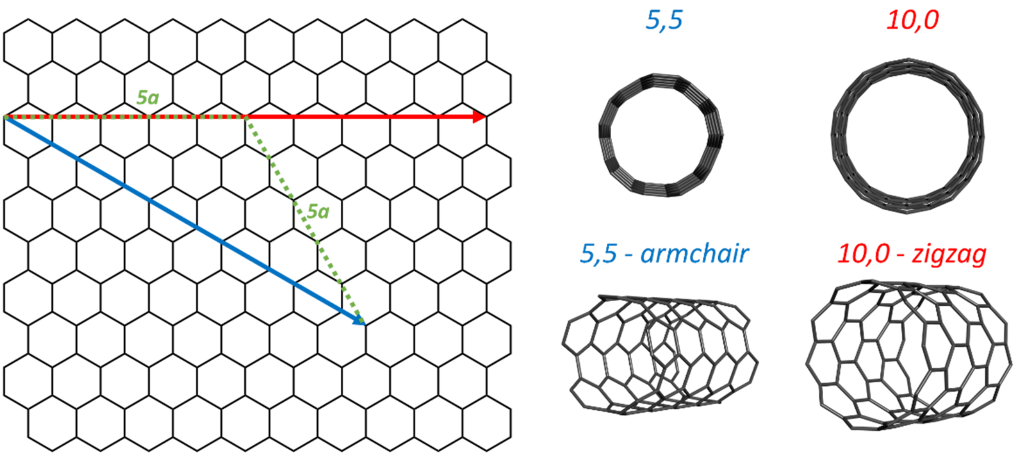

Figure 1.3. Graphene sheet showing roll up vectors and their resultant SWNTs. The chiral indices for the 5,5 SWNT are shown in green for clarity.

Similar to the derivation of their structure, the electronic properties of SWNTs can be explained by deriving the electronic properties of graphene. Graphene is considered a semi-metal with a symmetrical density of states (DoS) and a valence band that coincides with the bottom of the conduction band with zero DoS where they meet. The DoS of the material coupled with the confinement of mobile electrons to a 2D plane (electrons begin to behave like massless particles), low atomic mass of carbon (reducing spin-orbit coupling) and low amount of nuclear magnetic spins (graphene is mostly composed of ^{12}C) mean that the conductivity, low resistivity, electron mobility and spin transport properties of graphene are astounding.[20] This has led to significant interest in graphene's use as components in electronic and spintronic devices.[21] Whilst the beneficial features discussed above are largely retained within SWNTs, the DoS of a given chirality of SWNT can significantly vary; SWNTs can be either metallic or semiconducting in terms of their electronic nature.[22] This can be described by:

$$\textit{If } m - n = 3k \textit{ (metallic)}$$

$$\textit{If } m - n \neq 3k \textit{ (semiconducting)}$$

Where k can be any integer including zero. The exact DoS of a nanotube is highly variable depending on their chirality, but include variable band gaps in semiconducting SWNTs and Van Hove singularities[22, 23] (**Fig. 1.4**).

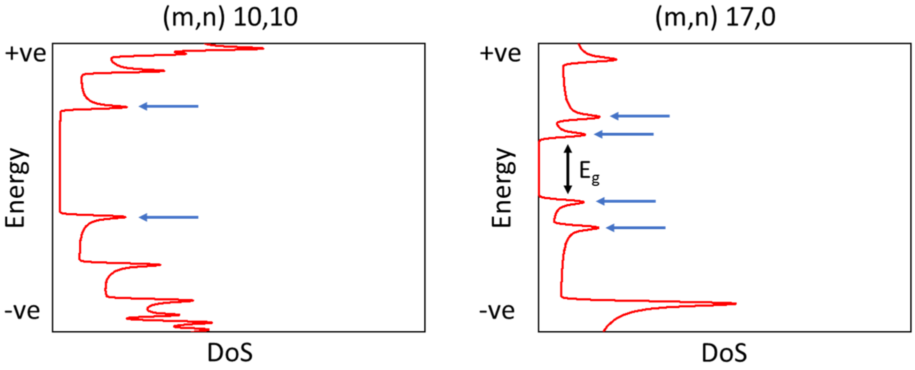

Figure 1.4. Calculated density of states for a metallic (10,10) and semiconducting (17,0) SWNT. Van Hove singularities are shown with the blue arrows.

There are many different synthetic methodologies that are used today to produce CNTs. Iijima's 1991 paper described their preparation from the arc-discharge of graphite, where two graphite rods are separated by approximately 1 mm in an inert atmosphere and a direct current is applied, vaporising the graphite and leading to the formation of fullerenes or carbon nanotubes.[24] The graphite in this case can be doped with a variety of metallic catalysts that influence the formation of either SWNTs (reported to be Fe or Co simultaneously in 1993) or MWNTs. Graphite is also utilised as the carbon source in the laser ablation technique, where laser pulses vaporise a graphite sample which is heated to high temperatures. A flow of inert gas carries the carbon vapours to a cooler site, where these carbon vapours condense on metallic catalysts.[25]

The only synthetic method that does not use graphite as the carbon source is chemical vapour deposition (CVD) in which methane, ethene or other small carbon containing molecules are introduced to a heated furnace with metallic catalysts. The thermally decomposed molecules produce vapours of carbon which condense on the metallic catalysts.[26] All methods have pros and cons based on their scalability, level of CNT defects and the amount of post-synthetic refinement required. Metallic catalysts are often utilised, particularly for SWNT synthesis, often leaving metallic contaminants in the CNT products, however these can be removed through wet chemical methods.[27] Although these methods have been developed to the point at which the distribution of nanotube diameters is very narrow, the production of a chirally pure product has yet to be established. Statistically any given sample of SWNTs will contain around 30% metallic and 70% semiconducting nanotubes, of varying chirality, differing slightly between different batches.[28]

In addition to the properties discussed above, SWNTs also have low densities,[29] high tensile strength,[30] high heat conductivity[31] and high chemical and thermal stability.[32] Under the right conditions SWNTs are also chemically modifiable.[33] Due to this exhaustive list of fascinating physicochemical properties CNTs have received wide-spread interest as components in catalytic systems,[34] drug design[35] and strengthening additives.[36] The exceptional conductivity and high aspect ratio of CNTs has naturally led to interest into their use in electronic devices[37] as well as significant research into their inclusion in solid state energy storage and flash storage materials.[38] Unlike fullerenes, which may reversibly accept multiple electrons over a large potential range,[39] CNTs cannot undergo formal redox processes themselves. This is due to the near continuous DoS that they possess, lacking discrete molecular orbitals that can readily accept electrons. Instead SWNTs may store charge through capacitance, the overall charging of the electric double layer at applied potentials, similar to many conductive carbons.

However, the regular ordering of the CNT structure offers increased wettability and high surface areas, leading to better ion permeation into the conductive film.[40] Examples of supercapacitors either composed of CNTs[41] or utilising their high conductivity and high surface area as a component are prevalent in the literature.[42] Although lacking faradaic redox process that would allow charge storage through the deposition of electrons through formal redox processes, the high surface areas and high conductivities make CNTs ideal additives to energy storage materials, allowing the adsorption of large amounts of redox active species onto their surface to come into electrical contact with current collectors in an electrochemical cell. The host of beneficial electronic properties and regimented structure at the nanoscale means that future energy storage materials will likely rely on such wonder materials as graphene and CNTs, in conjunction with redox active materials.

1.3 Nanoconfined Electrochemistry within SWNTs and DWNTs

As discussed above, their conductivities, low densities and high surface areas mean that CNTs have often been used as additives to connect otherwise insulating materials to electrodes or current collectors, thus mediating electron transfer between redox active species and the rest of the electrochemical cell. This is normally by loading the active species onto the exterior surface of CNT. However, CNTs also possess an interior dimension to which guest species can be incorporated[43] (this is discussed further in chapter 2). Confinement of molecular species and materials to nanoscale dimensions, either within a cavity, pore, pocket, channel or between sheets of a layered material can alter their chemical and physical properties[44] as well as leading to novel morphologies of the guest species.[45, 46] However, the effect of confinement on electrochemical processes is only now beginning to be fully explored,[47, 48] likely due to the extreme complexity of the many competing effects influencing reactivity in these exotic environments.

Confinement of molecular species within CNTs can increase catalytic rates, increase the cyclability of catalysts and sterically confine a reaction to alter selectivity.[49] Confinement can also enhance the electronic properties of both the CNT and guest species through guest-guest and host-guest charge transfer effects.[50] Whilst examples of confined electrochemistry within SWNTs is relatively rare in the literature, a number of species have been encapsulated within narrow SWNTs and DWNTs (diameter of 5 nm and below) that have been studied with electrochemical methods.

1.3.1 Fullerenes

Early studies into the specific electronic properties of redox active materials with discrete faradaic processes confined within CNTs were based on C_{60}@CNT. Being one of the first molecules to be encapsulated within SWNTs[51] (**Fig. 1.5**) the material was

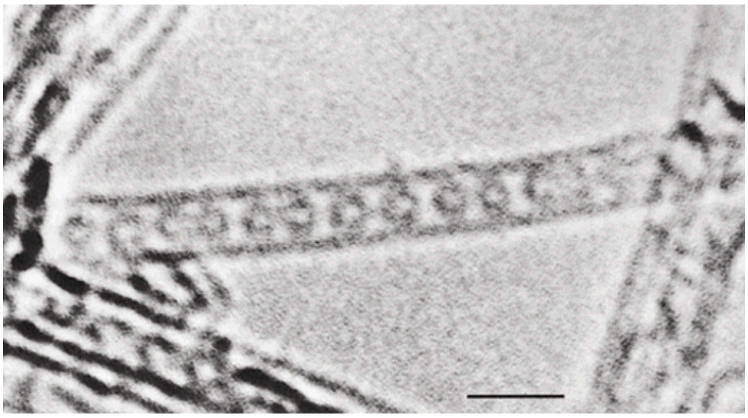

Figure 1.5. TEM image of C_{60} molecules encapsulated within a single walled carbon nanotube. Reproduced from reference 51 with permission from Springer Nature.

widely explored during the end of the 1990s and 2000s. The rich redox chemistry of fullerenes meant that the doping effects through chemical and heterogenous charge transfer methods were widely studied. Much of the early literature on the electrochemistry of encapsulated fullerenes demonstrated that electrolyte composition and pre-treatment of the CNT was vital, with both factors crucial to minimise the hinderance on the transport of cations to the fullerenes upon their reduction.

Work on accessing the discrete, reversible reductions of encapsulated C_{60} molecules was first explored in 2002. The paper, authored by Kavan *et al.,* described studies into reducing encapsulated C_{60} molecules within SWNTs.[52] Encapsulated C_{60} had previously been reported to be reduced with potassium vapours to polymeric chains of $[K^+]_n(C_{60}^{6-})_n$ which had displayed similar conductivity to metallic materials;[53] the authors were attempting to reproduce these results with an applied potential bias. Cyclic voltammograms (CVs) of the "peapod" (common terminology for C_{60}@SWNT materials) material in acetonitrile with a 0.2M $LiClO_4$ supporting electrolyte appeared completely analogous to that of pristine SWNTs, with none of the reversible redox processes of the C_{60} apparently conserved upon encapsulation.

The lack of C_{60} faradaic processes was attributed to poor penetration of Li^+ ions to the C_{60} sites upon reduction, required to compensate the negative charge deposited onto the fullerenes. The "through-wall" charge compensation, where the Li^+ could balance the now negatively charged C_{60} molecules through the SWNT wall, must have also been insufficient to charge balance due to the negative charging of the SWNT surface required to allow the approach of hydrated Li^+ ions. Nevertheless, the authors observed, *via* Vis-NIR spectroscopy and Raman vibrational spectroscopy, electrochemical bleaching (removing the SWNTs from resonance conditions) of the electronic transitions between Van Hove singularities with applied potentials (both anodic and cathodic) through the population and depopulation of the SWNT DoS. The authors reported an increase in the intensity of the Raman C_{60} bands upon anodic charging of the system, due to the bleaching of the SWNTs, which could not be reproduced for the cathodic charging of the system. The authors later reported similar results in C_{70}@SWNT, however the same increase in intensity of the fullerene bands was not observed upon anodic charging.[54, 55]

A later study published in 2005 by Sun *et al.* reported the first observation of faradaic processes from encapsulated C_{60} and C_{70} in SWNTs.[56] Overall the authors were able to probe three reversible processes in the peapod materials in acetonitrile with a 0.1M Bu_4NClO_4 supporting electrolyte, which corresponded to C_{60}/C_{60}^{-}, C_{60}^{-}/C_{60}^{2-} and C_{60}^{2-}/C_{60}^{3-} respectively (**Fig. 1.6**). Accessing the third process at the widest potential ranges destabilised the electrode to the point where lower currents were observed on the subsequent scan, which continued to decrease in intensity with repeated cycling. When keeping the probed potential window limited to the first two processes both appeared more stable and exhibited solid-sate behaviour based on the relationship between peak current and scan rate (**Fig. 1.6**). The full width half max (FWHM) values

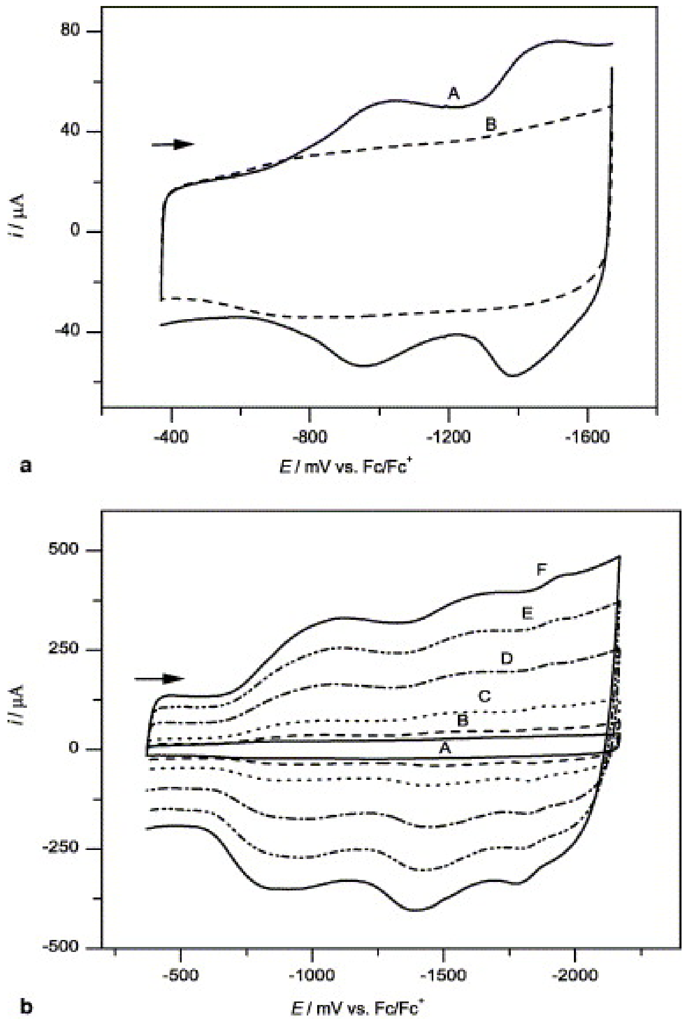

Figure 1.6. (a) Cyclic voltammograms of C_{60}@SWNT (A) and SWNTs (B) recorded in acetonitrile with a 0.1M Bu_4NClO_4 supporting electrolyte at a scan rate of 0.1 V s^{-1}. (b) Cyclic voltammograms of C_{60}@SWNT recorded under the same conditions at increasing scan rates (0.05 V s^{-1} – 0.5 V s^{-1}. Reproduced from reference 56 with permission from Elsevier.

of the processes were wider than what would be expected for a single electron solid state process (90.6 mV at 25 ^{O}C) likely due to favourable interactions between the guest and host, altering the electron transfer kinetics of the reaction.[57] Cycling the material repeatedly over the stable potential window eventually led to a loss of all faradaic processes in the material. Utilising transmission electron microscopy (TEM), the group identified that the degradation of the C_{60} molecules was not to blame for the faradaic loss, which could have been due to an increase in the resistivity of the deposited material.

Additionally, the authors investigated the lack of faradaic processes in the work published previously by Kavan *et al.* by altering the supporting electrolyte in the cell. There was a loss of faradaic processes when utilising $LiClO_4$, in good agreement with the work of Kavan *et al.*, indicating that solvated Li^+ ions could not sufficiently penetrate the SWNT to the reduced C_{60} species, as previously discussed, yet n-Bu_4N^+ (TBA^+) cations could. Altering the anion of the TBA^+ electrolyte between ClO_4^- and PF_6^- still yielded faradaic processes from the encapsulated C_{60} molecules, indicating that the role of the cation was key. The authors claimed that upon reduction TBA^+ could readily enter the SWNT and associate with the reduced fullerene molecules, forming $[TBA^+][C_{60}^-]$for both the C_{60}/C_{70} species. X-ray photoelectron spectroscopy (XPS) of the materials after repeated cycling showed the presence of two nitrogen environments, rather than the single environment observed if a peapod electrode was dipped into the electrolyte solution, indicating that the TBA^+ cations had become intercalated during cycling. Experiments conducted with aqueous electrolytes were also devoid of fullerene faradaic processes, suggesting that solvent cage, solvent-nanotube interactions or thermodynamic driving forces for desolvation were also important. The penetration of Bu_4N^+ cations over Li^+ seems counter intuitive however, considering the relative sizes of the cations.

Perhaps a critical piece of the puzzle concerning early work on the observed faradaic activity in peapods is the pre-treatment of SWNTs before fullerene encapsulation. Sun *et al.* described a vigorous acid treatment of the SWNTs before fullerene encapsulation,[56] with the purpose of introducing defects in the SWNT sidewall to allow better access to fullerene molecules from the vapour phase during encapsulation. The authors themselves noted that Bu_4N^+ access to the fullerene molecules could be achieved this way. Such vigorous pre-treatment was not reported in either work by Kavan and co-workers. Still, this cannot explain the absence of faradaic processes when altering the electrolyte between TBA$^+$ and Li$^+$, further supporting the hypothesis that an intimate interplay between solvent sphere, polarity of the supporting electrolyte and the thermodynamic driving forces for desolvation could also influence the interactions between the solid-state peapods and ionic species.

The same group later published work on C_{60}@DWNT in 2012 that further investigated the cation effect on the encapsulated C_{60} electrochemistry.[58] Altering the cation between Li$^+$, Me_4N^+, Pe_4N^+ and the Bu_4N^+ cation used in their previous work the authors demonstrated yet again that the redox behaviour of the encapsulated fullerenes was highly dependent on the choice of supporting electrolyte. Only when using a Bu_4N^+ and Pe_4N^+ supporting electrolyte were redox processes from the encapsulated fullerenes observed, however the results with Pe_4N^+ showed extremely large peak to peak separations in the material, indicative of poor electron transfer rates. Performing a similar XPS experiment to that of their previous work, the authors showed that Me_4N^+ was not readily intercalated between the C_{60} molecules encapsulated within the DWNTs, whereas Bu_4N^+ readily was, based on the multiple N environments observed after electrochemical cycling (**Fig. 1.7**). This provided some evidence of Bu_4N^+ penetration within the DWNT. However, this is counter intuitive, as Bu_4N^+ and Pe_4N^+ are much larger cations, and the mass transport of these ions would

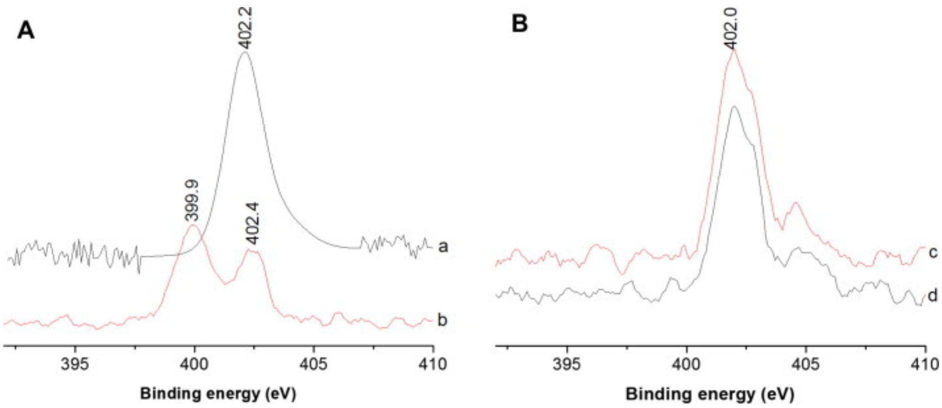

Figure 1.7. XPS spectra of C_{60}@DWNT modified electrodes simply exposed to electrolyte (a and d) and after 5 linear sweeps in the supporting electrolyte (b and c) for 0.1M Bu_4NClO_4 (A) and 0.1M Me_4NCl (B). Reproduced from reference 58 with permission from Elsevier.

likely be more inhibited relative to Me_4N^+. Transport through sidewall defects, as mentioned in previous studies, would also be sterically blocked in the double walled system. The width of the DWNTs used in the study from analysis of the images provided in the paper appear to be ~2.5 nm, which when partially blocked with C_{60}, as shown in the images, would lead to large energetic barriers to the mass transport of the large quaternary ammonium cations to the site of the reduced fullerene. Similarly, when the channels of SWNTs are blocked with C_{60} an approximate gap of 0.3 nm[51] is generally observed. This would prevent the transport of the Bu_4N^+ along the nanotube axis to the site of the reduced fullerenes in the group's earlier studies, suggesting that the interaction may have been through-wall.

Studies carried out by the Kawasaki group on the lithium-ion storage capacity[59] and sodium-ion storage[60] capacity of C_{60}@SWNT provide accounts on the ability of ions to penetrate the interior of the peapod structure, with both papers reporting higher reversible capacities for peapod materials versus that of unfunctionalised SWNTs for both Li^+ and Na^+ ion storage. Referring to the formation of $nK^+(C_{60}{}^{6-})_n$, as previously mentioned, the authors seemed confident with the insertion of Li^+ and Na^+ ions during electrochemical charging when utilising a Li/$NaClO_4$ supporting electrolyte dissolved in an ethylene carbonate:diethyl carbonate (EC:DEC) mixture (1:1), in a contradiction to the work discussed above. The mechanism that led to the increase in sodium ion storage in the latter example was not entirely clear, suggesting that there wasn't definitive evidence to support intercalation during charging. In both cases the authors discussed the possible presence of a surface electrolyte interface (SEI) layer close to the SWNT open ends where the ions could be desolvated, thus lowering the steric barrier of cation transport along the SWNT interior. Notably the insertion of Li^+ ions was only observed at slow charging rates, suggesting that the process was kinetically inhibited, as would be expected. Likening the interior SWNT sidewall to that of the basal plane of graphite the authors argued that an unfunctionalised SWNT interior presented an unfavourable surface for Li^+/Na^+ adsorption, despite previous reports on Li^+ intercalation within SWNTs,[61] whereas the peapod structure contained many sites for cation adsorption, leading to the observed increase in capacity in the peapods.

Increases in the lithium ion storage capacity of SWNTs was similarly increased by the incorporation of the C_{60} and ferrocene ($FeCp_2$, Cp = cyclopentadiene, herein referred to as Fc) in a later publication by Li *et al.* in 2010.[62] Largely in agreement with the earlier results from the Kawasaki group, CVs of the SWNT, C_{60}@SWNT and Fc materials in a $LiPF_6$ supporting electrolyte dissolved in an ethylene carbonate (EC), dimethyl carbonate (DMC) and ethylmethyl carbonate (EMC) mixture showed a single reduction on the first CV cycle which was not reversible in the SWNT or C_{60}@SWNT materials and was lost on subsequent scans. There were no differences in the CV response of the SWNT and C_{60}@SWNT materials, yet changes were observed in the return oxidation scan for Fc@SWNT, as well as a reversible reduction that was observed over multiple CV cycles instead of being lost after the first cycle. The authors suggested that this was due to extra reactions directly with Fc after lithium diffusion into the SWNT interior space, proving that Li^+ transport was more favourable in Fc@SWNT than in the C_{60}@SWNT and SWNT.

1.3.2 Metallocenes

Ferrocene undergoes rapid heterogenous charge transfer in solution (Fe^{2+}/Fe^{3+}), with an extremely well defined reversible oxidation potential. Its well-defined oxidation potential means that it is routinely used as in internal reference in cyclic voltammetry experiments, and the rapid nature of the heterogenous charge transfer mean that it is often utilised as a charge mediator in electrochemical systems. Coupled with its geometric size being close to that of the interior of SWNTs, groups began to investigate the encapsulation and redox chemistry of Fc in the mid-2000s. Whilst some work focussed on the effect of ion mass transport in the nano-confined system, there has also been work on sensing (due to the charge mediation of Fc) and the nature of host-guest interactions and its effect on redox chemistry.

The first report of encapsulated ferrocene within SWNTs (Fc@SWNT) and observations of confined electrochemistry were reported by Guan *et al.* in 2005.[63] The group achieved encapsulation *via* a vapour encapsulation process, similar to that used to produce C_{60}@SWNT. The single reversible oxidation process of ferrocene observed in solution was observed upon encapsulation, (**Fig. 1.8**) similar to the encapsulation of C_{60}, proving that encapsulated ferrocene could be electrochemically addressed. The group utilised a 0.1M Bu_4NClO_4 electrolyte dissolved in acetonitrile and reported a linear increase of the peak currents with increasing scan rate similar to that of encapsulated C_{60}@SWNT. Infra-red (IR) spectroscopy measurements of the material showed a red shift of the C–H stretching mode of the cyclopentadiene groups from the ferrocene molecule upon encapsulation and a blue shift of the C–C bonds in the SWNT, suggesting a charge interaction between the guest and host. This hypothesis was further evidenced by the wide FWHM values of the ferrocene redox process,

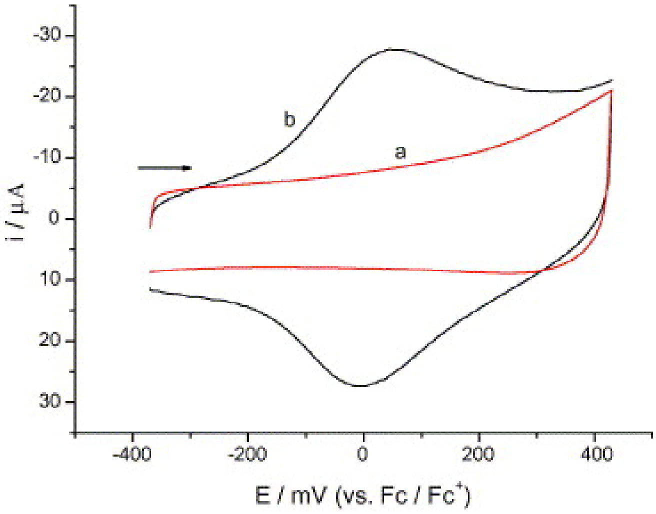

Figure 1.8. Cyclic voltammograms of SWNTs (a, red) and Fc@SWNT (b, black) in acetonitrile with a 0.1M Bu_4NClO_4 supporting electrolyte at a scan rate of 0.05 V s^{-1}. Reproduced from reference 63 with permission from Elsevier.

indicating favourable interactions between the two. Later studies by the group showed that the encapsulation of ferrocene within DWNTs led to narrower FWHM values, due to less favourable interactions between the ferrocene molecules and the much wider DWNTs.[64]

The group later utilised the material in a second piece of work published by Sun *et al.* a year later.[65] In this paper the authors applied the Fc@SWNT material as a H_2O_2 sensor, using the encapsulated ferrocene molecules as charge mediators in the reduction and oxidation of hydrogen peroxide. The group reported the effect of the electrolyte on the CV profile of the material, screening $LiClO_4$, LiCl, KCl, KH_2PO_4, Na_2HPO_4 and Bu_4NBr supporting electrolytes as 0.1M aqueous solutions, with the best current response achieved with a $LiClO_4$ supporting electrolyte. The encapsulation of Fc improved the stability during cycling *versus* Fc on the SWNT surface, likely due to lower levels of leaching, however 80% of the faradaic current was lost after 4000 cycles. The observation of redox activity when using a $LiClO_4$ electrolyte contrasts with that described by the groups working on C_{60}@SWNT, which required Bu_4N^+ cations in the supporting electrolyte to extract faradaic current from their materials. Additionally, the authors noted the influence of the electrolyte anion on the observed redox chemistry, demonstrated by poorer stability and current response when using LiCl as a supporting electrolyte. This suggests that the SWNT interior (approximately 1.2-1.4 nm from TEM) was penetrated by both the hydrated Li^+ and Cl^- ions.

Questions surrounding the mass transport of small reactive species were further explored in the paper when the material was applied to H_2O_2 sensing. The addition of H_2O_2 to the electrolyte solution during cyclic voltammetry experiments led to an increase in both the anodic and cathodic peak currents, which increased with increasing H_2O_2 concentration. This was due to the ferrocene mediated reduction and

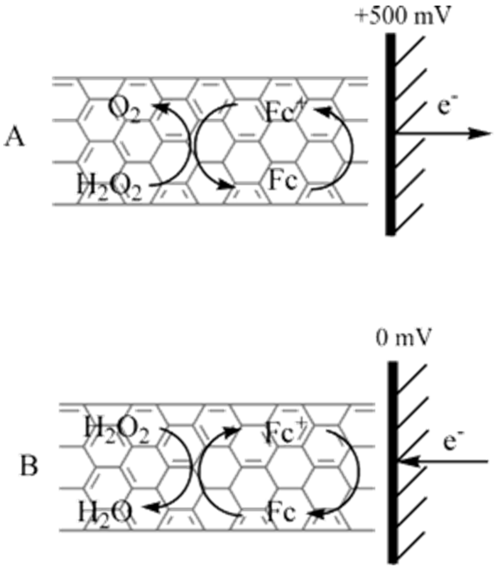

Figure 1.9. Reaction schemes depicting the oxidation of H_2O_2 to O_2 (A) and reduction of H_2O_2 to H_2O (B) within the SWNT, mediated by encapsulated ferrocene molecules. Reproduced from reference 65 with permission from The American Chemical Society.

oxidation of H_2O_2 within the SWNT, (**Fig. 1.9**) indicating that the peroxide could readily access the encapsulated ferrocene redox centres. The group further commemorated their observations of C–H red-shifting in Cp rings of ferrocene observed in their previous study by investigating the SWNT vibrational properties with Raman spectroscopy, noting a shift in the G-band of the material, indicative of charge transfer from the guest to host. The larger than expected FWHM values, evidence of favourable interactions between the SWNT and encapsulated ferrocene molecules, further demonstrated this host-guest interaction.

The group later applied ferrocene encapsulated within DWNTs to dopamine sensing.[66] The work reported by Cheng *et al.* demonstrated that $LiClO_4$ was still an optimal electrolyte due to the ability of Li^+ to intercalate with the DWNTs, and the poor coordination of the ClO_4^- anion to the positively charged Fc^+ molecules. There were large peak-to-peak separations even at slow scan rates of 5 mV s^{-1}, which the authors attributed to resistance and underlying capacitance from the SWNTs, however it is also likely that the inhibited diffusion of ions to the encapsulated ferrocene molecules was also a culprit. Peak current increased linearly with increasing scan rate as expected, and larger than expected FWHM values were reported too, again attributed to favourable interactions between the Cp group and interior DWNT sidewall. Upon the addition of dopamine to the electrolyte solution the authors observed increased anodic currents (oxidation of Fc to Fc^+) and reduced cathodic currents (Fc^+ reduced to Fc) in the ferrocene redox couple, with effects becoming more pronounced with increasing dopamine concentration. The native redox processes of dopamine were seemingly suppressed by the Fc@DWNT electrode, possibly due to the localised pH within the DWNT. The scheme for the reaction occurring within the Fc@DWNT material (**Fig. 1.10**) demonstrated that Fc^+ from the heterogenous charge transfer could oxidise dopamine molecules, hence decreasing the return cathodic current. The group later applied Fc@SWNT to the same reaction, reporting similar results.[67]

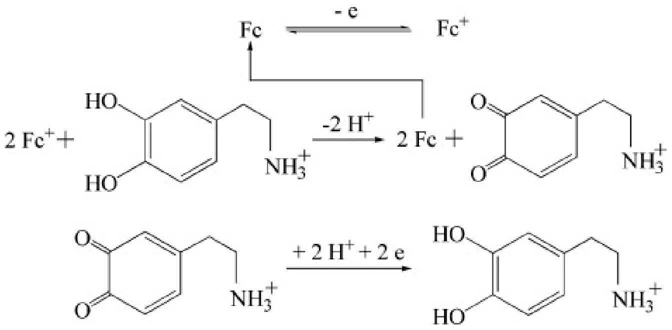

Figure 1.10. Reaction scheme for the electron mediated oxidation of dopamine via ferrocene molecules encapsulated within DWNTs. Reproduced from reference 66 with permission from Elsevier.

Work carried out in the Khlobystov group, reported in 2016 by McSweeney *et al.,* later employed metallocenes encapsulated within SWNTs to probe the host-guest charge interactions between metallocenes and SWNTs *via* cyclic voltammetry and chronoamperometric methods.[68] Encapsulation of both cobaltocene and methylated ferrocene ($Fe(Cp^{xMe})_2$, x = 0, 1, 4 and 5) led to them being electrochemically addressable within the SWNT with a 0.1M Bu_4NBF_4 supporting electrolyte dissolved in acetonitrile. Both the single electron reduction and oxidation processes of the cobaltocene (Co^{2+}/Co^+ and Co^{2+}/Co^{3+} respectively) could be accessed upon encapsulation as well as the single oxidation of the ferrocene analogues. Large positive

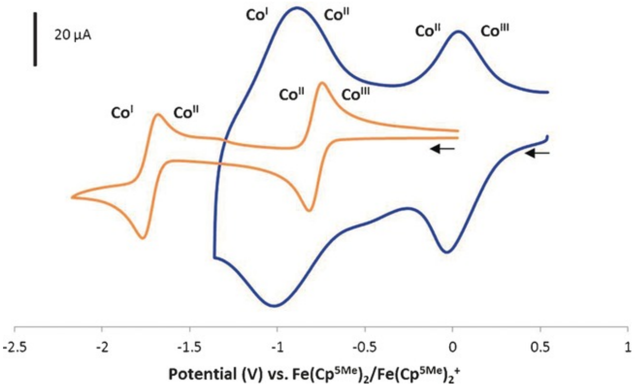

Figure 1.11. Cyclic voltammograms of $CoCp_2$ (orange) and $\{CoCp_2\}$@SWNT (blue) recorded in acetonitrile with a 0.1M Bu_4NBF_4 supporting electrolyte at a scan rate of 0.1 V s^{-1}. Reproduced from reference 68 with permission from John Wiley & Sons.

shifts (~770 mV) in potentials of the redox processes in the cobaltocene were observed, (**Fig. 1.11**) indicative of electron transfer from the guest to host, leading to an overall n-doping effect of the SWNT hosts. For ferrocene the shift in the oxidation processes were far more subtle, ranging between 0 mV for $Fe(Cp)_2$ (as previously reported) and +200 mV for $Fe(Cp^{5Me})_2$ with increasing levels of methylation of the cyclopentadiene ligands. The shifts in the processes of both the cobaltocene and ferrocene were studied with linear sweep voltammetry (LSV) of unfunctionalised SWNTs (providing an experimental profile of the DoS[69]) and chronoamperometry of the metallocene@SWNT materials. Utilising LSV, the DoS of the SWNTs used in the study could be visualised allowing the energies of the Fermi level, akin to the highest occupied molecular orbital (HOMO), and bottom of the conduction band, akin to the lowest unoccupied molecular orbital (LUMO), to be accurately determined. Cyclic voltammetry of the metallocenes acquired in identical conditions was carried out to locate the energy levels of the singly occupied molecular orbital (SOMO) of $Co(Cp)_2$ and the highest occupied molecular orbital (HOMO) of $Fe(Cp^{xMe})_2$. From these experiments the direct comparison of energies could be carried out, showing that charge transfer would be expected from cobaltocene to the empty DoS in the conduction band of the SWNT and from ferrocene to depleted (due to oxygen containing surface groups on the SWNT) energy levels in the valence band.

Chronoamperometry measurements of the metallocene@SWNT materials confirmed this charge transfer, which was indicated by shifts in the fermi levels of the SWNTs upon encapsulation of the varying metallocene species. This study was the first to utilise shifts in redox processes of encapsulated molecules and amperometric methods to accurately determine charge transfer direction and magnitude in host SWNT materials, which was in good agreement with previous results.[70]

McSweeney *et al.* also published a paper on the encapsulation of a "piano-stool" manganese complex, $Cp^{Me}Mn^{I}(CO)_3$, where the authors were able to stabilise the complex whilst undergoing a redox reaction by altering the reactive pathway.[71] Normally, the $Cp^{Me}Mn^{I}(CO)_3$ molecule can undergo a heterogenous one-electron

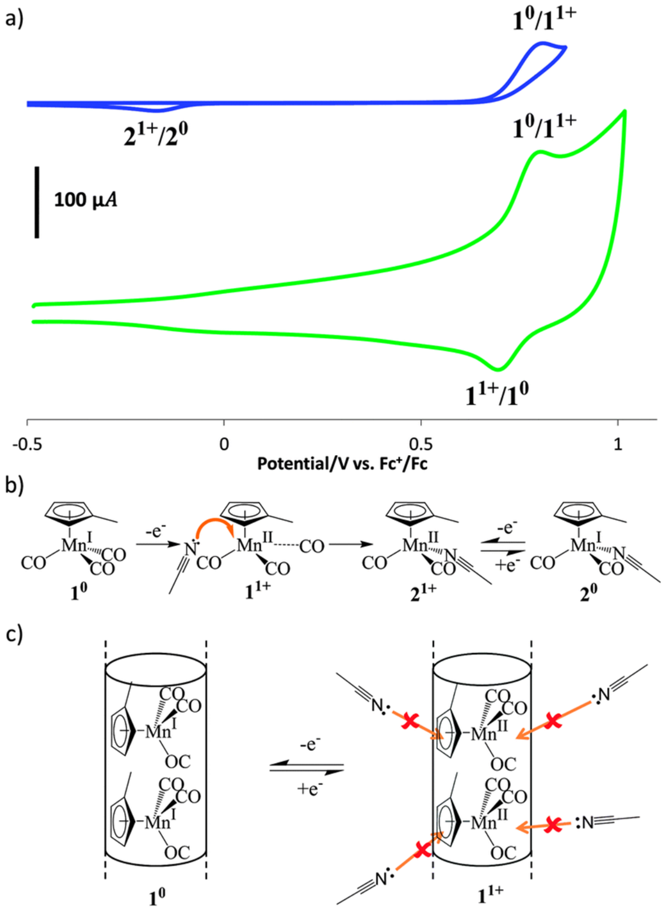

Figure 1.12. (a) Cyclic voltammograms of $Cp^{Me}Mn^{I}(CO)_3$ in solution (blue) and encapsulated within SWNTs (green) recorded in acetonitrile with a 0.1 Bu_4NBF_4 supporting electrolyte. (b) The normal reaction pathway which is observed via the blue CV above. (c) Proposed new reaction pathway upon confinement of the complex within SWNTs. Reproduced from reference 71 with permission from The Royal Society of Chemistry (RSC).

oxidation in solution, at approximately 0.8 V *vs.* Fc^+/Fc, which forms the highly reactive $[Cp^{Me}Mn^{II}(CO)_3]^+$ species. This normally then undergoes a nucleophilic substitution reaction (normally with acetonitrile, the solvent) which is accompanied by the loss of a CO ligand, forming $[Cp^{Me}Mn^{II}(CO)_2(NCCH_3)]^+$ (**Fig.1.12, b**). This is then only reduced to $Cp^{Me}Mn^{I}(CO)_2(NCCH_3)$ at a much more negative potential, -0.18 V. By encapsulating the piano-stool complex within SWNTs, the authors were able to alter the observed CV (**Fig. 1.12, c**) which was acquired with a supporting 0.1M Bu_4NBF_4 supporting electrolyte dissolved in acetonitrile. The change in the reduction potential was likely due to the steric hinderance of the SWNT wall, essentially protecting the complex during reduction from nucleophilic attack of the solvent and allowing rapid reduction of the species at a similar potential to the initial oxidation. This is in stark contrast to many of the publications discussed on the redox activity of species encapsulated within SWNTs, which expect diffusion of solvent and electrolyte to readily occur along the SWNT channels. This study served as an interesting example of SWNTs protecting encapsulated species during a redox cycle.

1.3.3 Organic Molecules

Most of the work on the encapsulation of moderately sized organic molecules for lithium ion storage has been carried out by the Kawasaki group. In 2009 Kawasaki *et al.* published their work on the encapsulation and lithium charge storage capacity of three organic molecules, 9,10-dichloroanthracene, β-carotene, and coronene, encapsulated within SWNTs.[72] The authors reported that the encapsulation of all three organic molecules increased the overall capacitance *versus* unfunctionalised SWNTs, when utilising an ethylene carbonate : diethyl carbonate (DEC) (1:1) solvent with a 1M $LiClO_4$ supporting electrolyte, attributing this to the increased number of sites for Li^+ intercalation compared to an empty SWNT with a basal plane, similar to their work on C_{60}@SWNT discussed above. The counter intuitive nature of higher lithium transport within a material that exhibits higher spatial constraint on the diffusing species was briefly discussed and addressed; the capacities of the separate materials were compared at varying current densities (C rates) and the capacity retention of SWNTs with encapsulated organic molecules all appeared superior to unfunctionalised SWNTs at higher current densities. The reversible capacity of the materials appeared to reduce little over 5 charge-discharge cycles. The encapsulation of coronene led to the biggest increase in reversible capacity, which was attributed to the large size of the molecule. The steric hinderance of the larger encapsulated molecules leading to inhibited transport of hydrated lithium ions, likely led to their effective desolvation at the coronene capped SWNT ends, thus lowering energetic barriers to ion diffusion. This was further investigated with surface area adsorption measurements, which showed the largest decrease in the surface area of the coronene@SWNT sample, supporting this hypothesis.

Kawasaki and his group later turned their attention to encapsulated quinones as a charge storage medium. A first paper, published in 2016 by Ishii *et al.,* demonstrated the ability of two quinone molecules, 9,10-anthraquinone (AQ) and 9,10-phenanthrenequinone (PhQ), to encapsulate within SWNTs and intercalate lithium ions.[73] Using the same electrolyte mixture (EC:DEC 1:1) as described above, charge-discharge curves of the quinones loaded onto activated carbon, the SWNT external surface and encapsulated within SWNTs showed distinct plateaus for lithium adsorption and desorption upon reduction of the quinones, and capacities of the materials (when based on the mass of active material) approached the theoretical maximum when encapsulated within the SWNT interior, suggesting that the majority of molecules were partaking in electrochemical processes upon encapsulation (**Fig. 1.13**). Additionally, the plateaus appeared to be more elongated when the molecules were encapsulated within the SWNTs *versus* loaded onto their external surfaces. The

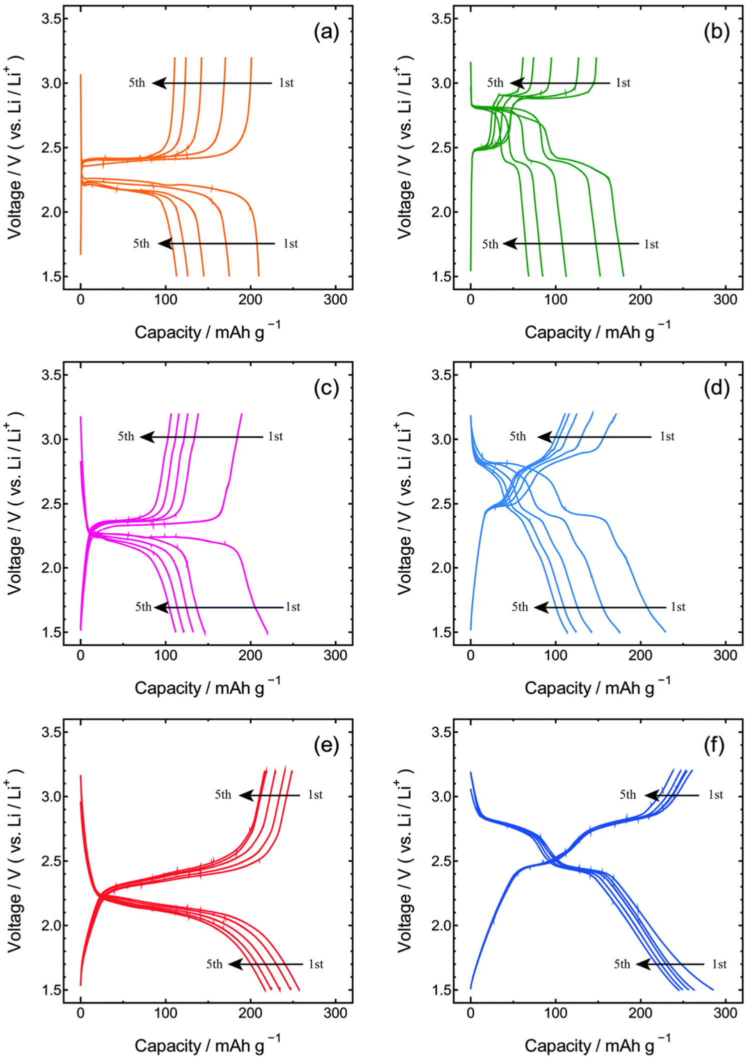

Figure 1.13. Charge-discharge curves of (a) AQ-activated carbon, (b) PhQ-activated carbon, (c) AQ-SWNTs, (d) PhQ-SWNTs, (e) AQ@SWNT and (f) PhQ@SWNT. All measurements were performed with specific currents of 100 mA g^{-1} and capacities based on the weight of the active material only. Reproduced from reference 73 with permission from The Royal Society of Chemistry (RSC).

difference in overpotentials for the charging and discharging process was negligible in the 9,10-phenanthrenequinone material but was around 50 mV in the 9,10-anthraquinone material. When comparing IR spectra of the two there was no shift of the carbonyl group of 9,10-phenanthrenequinone yet in 9,10-anthraquinone the carbonyl stretch was blueshifted, suggesting that this molecule-nanotube interaction led to the differences in overpotentials during charge-discharge. In addition to the reduced overpotentials and the high level of active material, the encapsulated quinones had increased capacity retention over multiple cycles.

In 2017 the Kawasaki group further probed the effects of ion transport within quinone@SWNT materials. The study by Li *et al.* investigated the application of the encapsulated 9,10-phenanthrenequinone material for lithium ion and also sodium ion storage.[74] In this study the authors encapsulated the quinone in two different samples of SWNTs, with average diameters of 1.5 and 2.5 nm respectively. Encapsulation of the quinone within the smaller diameter nanotube gave a capacity that was close to the theoretical maximum for the molecule, when utilising the EC:DEC 1M $LiClO_4$ electrolyte, yet encapsulation within the larger diameter SWNTs led to a decrease in the capacity of the material to around 50% of this theoretical value, as a result of less favourable interactions between the larger SWNT and guest, hindering electronic communication between the two. However, plateaus in the galvanostatic charge-discharge curves, indicative of lithium adsorption/desorption, had greater gradients

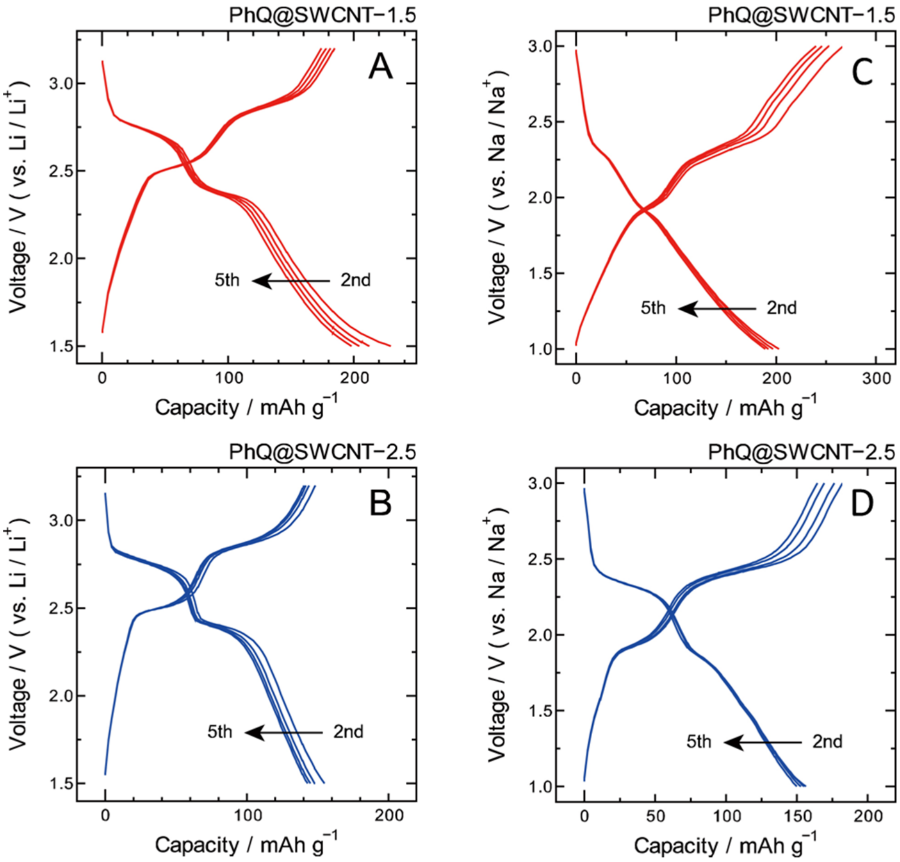

Figure 1.14. Lithium storage charge-discharge curves for PhQ@SWNT in (A) narrow SWNTs and (B) wider SWNTs. Sodium storage charge discharge curves for PhQ@SWNT in (C) narrow SWNTs and (D) wider SWNTS. Acquired with specific currents of 100 mA g^{-1}, capacity based on the mass of active material. Adapted from reference 74 with permission from IOP publishing.

when the quinone was encapsulated within the narrow SWNTs, indicative of a lower levels of intercalation (**Fig. 1.14**). When comparing the sodium storage ability of the materials there was a small decrease in the overall capacities compared to their lithium storage capacities, but plateaus were observed at similar potentials, although it appeared that the gradient of the plateaus had increased. When carrying out charge-discharge measurements at 0 °C there was further increases to the plateau gradients for both Li^+ and Na^+ storage, indicating less reversible ion intercalation, and there were small decreases in the overall capacity of the materials. Recently work published by Tsuzuki *et al.* applied density functional theory (DFT) to investigate the mass transport of Li^+ ions in quinone@SWNT materials.[75] The authors found that Li^+ could travel along the interior SWNT side walls, as well as "hop" between the encapsulated quinone molecules, which was accompanied by considerable changes in the cross-sectional geometry of the SWNT in their model.

The group later went on to utilise I@SWNT with their previously reported quinone@SWNT materials in a paper by Li *et al.* where the I@SWNT formed the cathode.[76] CVs of encapsulated 9,10-phenanthrenequinone with a 1M LiI aqueous electrolyte showed only one reversible redox process, and the galvanostatic charge-discharge curves showed only one plateau, which was in contrast to their previous work which showed two distinct plateaus (attributed to the lithiation of each C=O bond). The loss of one redox process, and reduction of capacity to approximately 50% of the theoretical max, was likely due to only one C=O bond becoming lithiated during cycling. The authors attributed this change in redox behaviour and decrease in capacity to the polar water solvent molecules not readily entering the highly hydrophobic environment, reducing the amount of lithiation that could occur. When utilising NaI, there were no observed redox processes in the CV or charge-discharge curves and the overall capacity was lower, suggesting that the larger size of the Na^+ ion hindered mass transport.

The change in lithiation of quinones in aqueous electrolytes is similar to work carried out on encapsulated fullerenes discussed above, suggesting that differences in solvent cages can alter the observed redox chemistry. This could be due to several reasons, such as size of the solvated complex, nanotube-solvent interactions and the enthalpic and entropic changes associated with ion intercalation into guest@CNT systems. Such anecdotes serve to further highlight the complexity of confined redox chemistry.

1.3.4 Halogens

Similar to organic encapsulants, much of the work on the electrochemistry of confined halides within SWNTs was carried out by Kawasaki and co-workers. Their first paper by Song *et al.* reported that I^- species encapsulated within SWNTs could be electrochemically oxidised to I_2 molecules, leading to large charge interactions with the SWNT host, observed *via* Raman spectroscopy and increasing the dispersibility of the SWNTs in aqueous solvents.[77] The group further used this material to study charge transfer between the SWNT host and iodide guest.[78] Taniguchi *et al*. then utilised this material to increase the capacitance of SWNTs by intercalating iodine within the SWNT interior dimension[79] as well applying bromine in a similar manner.[80]

The group then reported a work investigating the mechanism for lithium insertion into I@SWNT, by Kato *et al.*, in 2019.[81] Utilising an organic electrolyte with a lithium source, the authors were able to reversibly insert Li^+ into the I@SWNT material. CVs of the material at a scan rate of 1 mV s^{-1} showed multiple processes, which were attributed to the formation of LiI_3 and LiI atomic chains upon lithium insertion. These processes were lost at higher scan rates of 5 mV s^{-1} (**Fig. 1.15**) suggesting that the insertion process was particularly slow, in good agreement with the groups previous examples

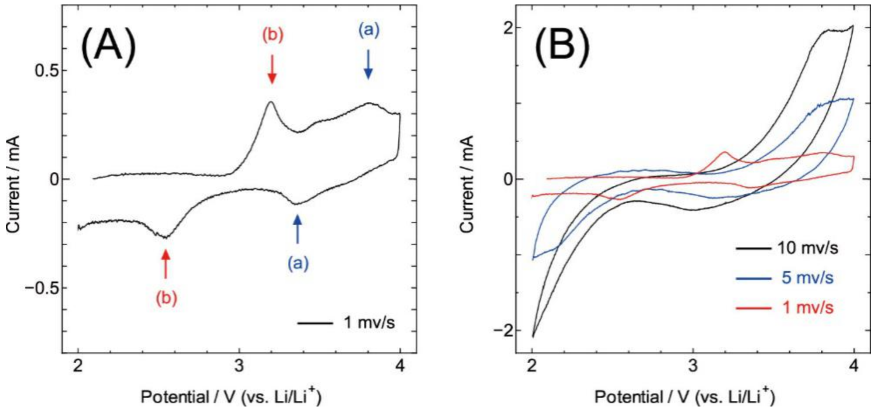

Figure 1.15. Cyclic voltammograms of I@SWNT at 1 mV s^{-1} (A) and at 1-10 mV s^{-1} recorded in 1,3-dioxolane/dimethyl ether with a 1M lithium bis(trifluoromethanesulfonyl) supporting electrolyte. Reproduced from reference 81 with permission from The American Chemical Society.

of Li^+ insertion into functionalised SWNTs when utilising organic electrolytes, discussed above. The scan rate dependence suggested Li^+ diffusion along the length of the SWNT axis, and not through the sidewall or defects inherently present in the sidewall, which was substantiated with electrochemical impedance measurements. The capacity of the material was around 75% of the theoretical maximum based on the weight of iodine, suggesting that one-in-four iodine atoms was not partaking in the electrochemical processes. Two plateaus were observed in the charge-discharge experiments, in accordance with the observed CVs, and the capacity retention was high over the first few cycles. This was likely due to the iodine being held within the SWNT and not becoming solvated by exposure to solvent in the cell. Utilising Raman spectroscopy and diagnostic SWNT vibrational modes, the authors reported that the that the products of the reaction could be followed, proving that the LiI_x species and I_2 species were formed within the SWNT dimension upon lithium insertion. Preparing a sample of CsI@SWNT, the authors utilised Raman to further prove that they could extract an alkali metal from its iodide salt from within the SWNT electrochemically. The authors also applied their material to a solid-state electrolyte, demonstrating that the material could intercalate Li^+ from the solid state. This work was a good example of altering LiI from what is typically considered a primary cell (one use) to a secondary cell (rechargeable), due to the encapsulated environment protecting the iodine from solvation during cycling.

1.3.5 Sulfur

First reported in the 1960s, lithium-sulfur batteries have been investigated due to their extremely high specific energies (2600 Wh kg^{-1}) and the high abundance of sulfur within the earth's crust, making them ideal future battery materials. Although the lithium ion battery has become the gold standard in recent years, sulfur presents an opportunity to greatly increase the electrification of transport and the miniaturisation of batteries.[82] However, issues such as low conductivity, large volume changes during cycling and high solubility mean that more optimisation of the Li-S system are needed to realise widespread implementation.

The isolation of linear chains of sulfur, reported by Fujimori *et al.* in 2013, through the encapsulation of sulfur within SWNTs[45] naturally generated a surge of interest in the applicability of sulfur redox chemistry confined within SWNTs for energy storage. In 2015 Yang *et al.* published the first paper on the lithiation of these linear 1D chains of sulfur confined within SWNTs.[83] The authors showed that the capacity of the material (mass of carbon removed) approached 2000 mAh g^{-1}, and with the mass of the carbon included approached 1500 mAh g^{-1}, suggesting that the one dimensional chains of sulfur were highly electroactive (**Fig. 1.16**). CVs of the material at a scan rate of 0.1 mV

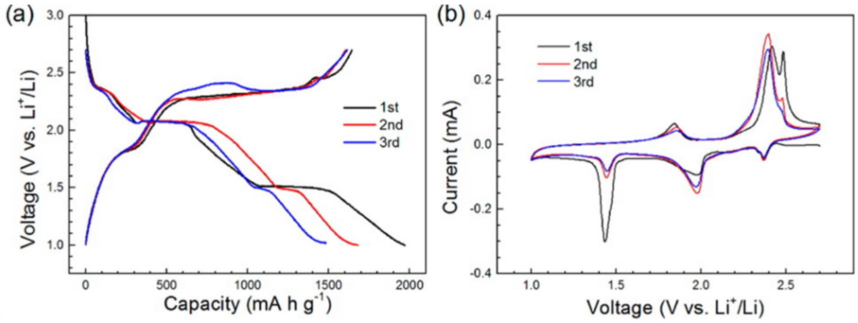

Figure 1.16. (a) Charge-discharge curves of S@SWNT charged at 0.1C (both C and capacitance based on the weight of S only) (b) CVs of S@SWNT showing the 3 initial cycles at a scan rate of 0.1 mV s^{-1}. Reproduced from reference 83 with permission from The American Chemical Society.

s^{-1} showed multiple redox processes, which were seen in the charge-discharge curves as distinct plateaus. A particularly large reduction process was observed at 1.45 V which the authors stated was only observed in the linear sulfur chains confined within SWNTs, which decreased in intensity after the first CV cycle, and appeared to correspond with the increase in a different reduction process at 2 V. However large initial reductions have previously been observed during the lithiation of unfunctionalised SWNTs,[61] which could be attributed to the formation of an SEI layer, suggesting that a similar process was occurring in S@SWNT. The presence of the plateaus in the charge-discharge curves and the presence of reductions and oxidation in the CV of the material were evidence of reversible sulfur lithiation. After an initial drop in capacity, the material appeared to have a reversible capacity of around 800 mAh g^{-1} over 20 cycles (mass of carbon included). The authors noted the kinetic limitations of the system, due to the lithium diffusion along the high aspect ratio SWNTs, meaning that lower current densities and scan rates were required for the electrochemical analysis. Utilising *ex situ* XPS measurements of the material during discharge the authors were able to observe the reduction of the sulfur chains, initially forming Li_2S_4, then Li_2S_2 and Li_2S. Although the final reduction product Li_2S was observed, there also appeared to be Li_2S_x ($x \geq 4$) at the same potential, likely due to the sulfur chains close to the centre of the SWNT axis, where lithiation would be more inhibited due to poor mass transport of Li^+. Utilising x-ray diffraction methods, they were able to follow the products of the confined lithiation, demonstrating that the long linear sulfur chains were gradually shortened during repeated cycles, enhancing lithium transport in subsequent cycles (**Fig. 1.17**). Raman spectroscopy showed that

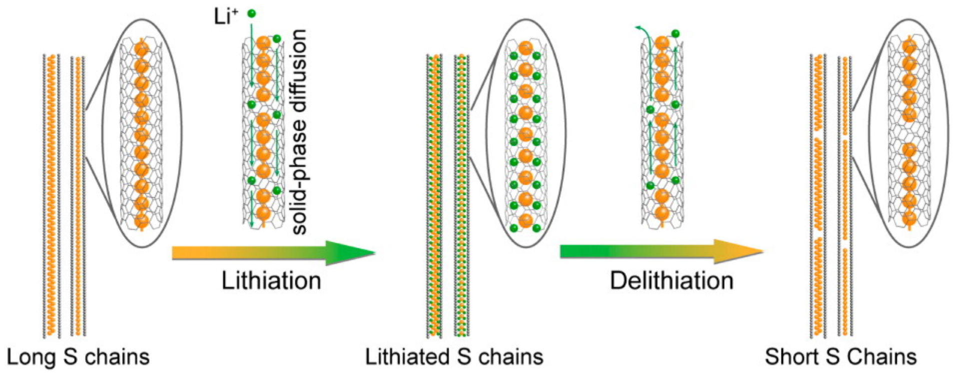

Figure 1.17. Scheme demonstrating the electrochemical lithiation/delithiation of sulfur chains confined within SWNTs. Reproduced from reference 83 with permission from The American Chemical Society.

upon lithiation the products interacted strongly with the SWNT sidewalls. In 2017, Milroy *et al.* published the fabrication of a thin film "microbattery" based on S@SWNT using an inkjet method.[84] The authors could control the morphology of the active material on SiO_2 or aluminium foil, reporting reversible capacities of around 700 mAh g^{-1} over 100 cycles, opening up the applicability of sulfur in the miniaturisation of battery technology.

In 2018, Urita *et al.* attempted to directly prove that Li_2S_x chains were formed within SWNTs and DWNTs.[85] Utilising TEM analysis of the materials, the authors showed that nature of the sulfur chains was highly dependent on the diameter of the CNT used for encapsulation, with double atomic S chains, single atomic S chains and even smaller S_3 chains observed in varying diameter CNTs. Charge-discharge curves of the different samples gave varied responses with different numbers of plateaus observed depending on the SWNT used for encapsulation. This was also observable in the different CV responses, suggesting that the diameter of the CNT used for encapsulation intrinsically altered the observed redox chemistry for Li insertion.

The authors concluded from the lack of plateaus in the charge-discharge measurements that lithium insertion would be severely inhibited for CNTs with a diameter below 1.4 nm. Utilising *ex situ* scanning transmission electron microscopy electron energy loss spectroscopy (STEM-EELS), the authors mapped the location of lithium after cycling of the S@CNT materials and found that for the narrower CNTs, lithium did not appear within the interior space, consistent with the poorer electrochemical response (**Fig. 1.18**). For the larger CNTs, lithium was observed within the interior space of the SWNT, suggesting that the increased diameter reduced the steric hinderance of lithium transport in the CNT, allowing lithiation to take place. This was also in good agreement with their galvanostatic charge-discharge curves. Probing the lithium K- and sulfur $L_{2,3}$- edges allowed the authors to probe the local bonding environments of the redox species, with the authors concluding that the Li was bound to the sulfur in their elemental maps.

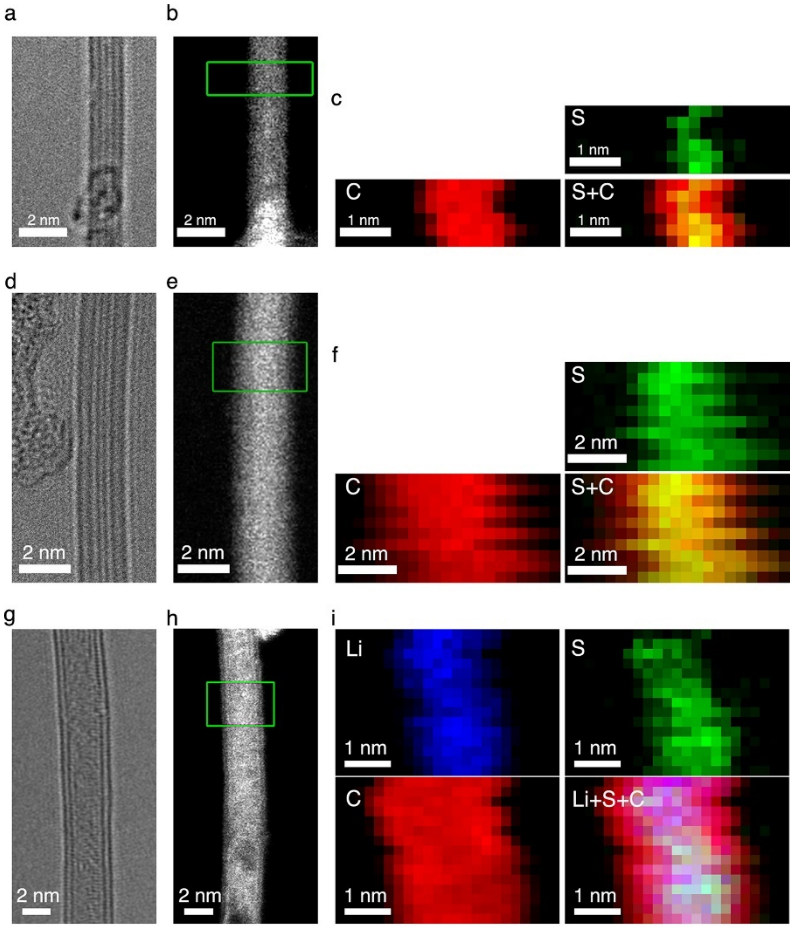

Figure 1.18. TEM, annular dark field (ADF) and STEM-EELS images of single S chains in DWNTs (a-c) double S chains in DWNTs (d-f) and small S chains in wider DWNTs (g-i) after electrochemically cycling. Reproduced from reference 85 with permission from The American Chemical Society.

Alternatively, Fu *et al.* published work (later in 2018) on S@SWNT in which they discussed sulfur interacting with solvated Li^+ ions through the SWNT side wall.[86] In the paper, the authors reported encapsulated sulfur within SWNTs with an average diameter of 1.55 nm and 1 nm, as well as carrying out charging experiments in tetraethylene glycol dimethyl ether (TEGDME) and the equivalent crown ether (15-crown-5) with a 1M lithium bis(trifluoromethane sulfonyl)imide supporting electrolyte. TEM analysis of their S@SWNT materials showed short chains of sulfur, which they described as being closer to the optimal S_8 ring geometry, different to the previous work on the encapsulation of sulfur within SWNTs mentioned above.

Utilising mass spectrometry and DFT the authors were able to describe the solvent shell of Li^+ ions, demonstrating the true size of the solvated cation, aiding in understanding the mass transport of Li^+ in each solvent system. CVs of each S@SWNT material in both solvents gave varied responses (**Fig. 1.19**). In the wider SWNT system,

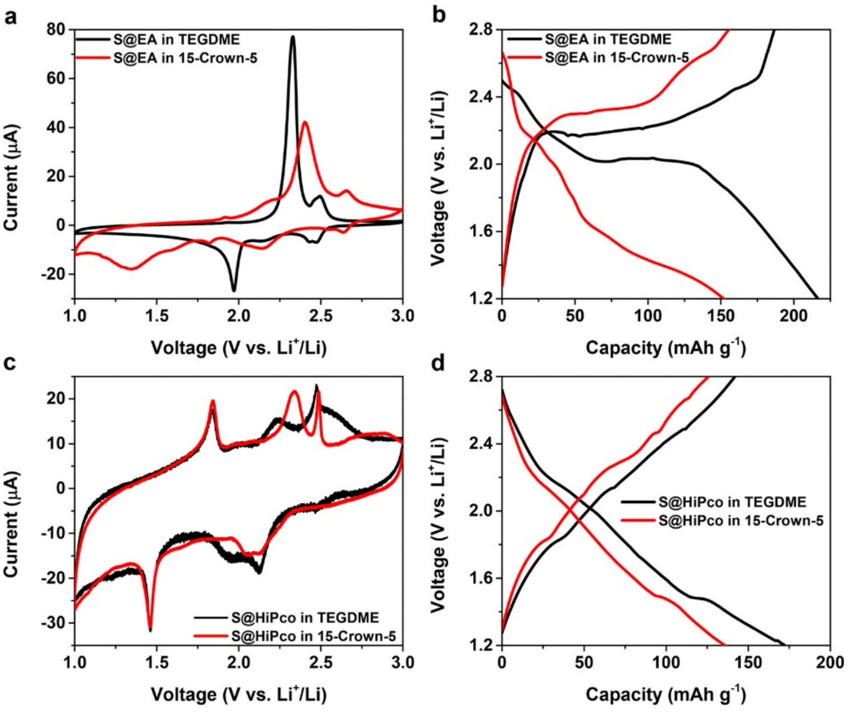

Figure 1.19. CV (a) and charge-discharge curve (b) of S@SWNT (EA has diameter of 1.5 nm) in TEGDME and 15-crown-5. CV (c) and charge-discharge curve (b) of S@HiPco (HiPco has diameter of 1 nm) in TEGDME and 15-crown-5. CVs acquired at a scan rate of 0.05 mV s^{-1} and the charge-discharge curves acquired with a current density of 4 mA g^{-1}. Current density and capacity are with respect to the total mass (S and carbon) of the electrode material. Reproduced from reference 86 with permission from The American Chemical Society.

the change in CV that accompanied the change in solvent could be explained by the differences in solvent viscosity, which could hinder the lithium transport to the encapsulated sulfur. However, considering the entropic driving force for Li^+ desolvation in both the TEGDME solvent and the crown ether, which would be much more favourable in the TEGDME solvent, suggests that this could also play a role in the observed redox chemistry of the material in different solvents. The charge-discharge curves of the wider SWNTs nevertheless showed a distinct plateau in both solvent systems, attributed to the lithiation of sulfur within the SWNT, which could occur due to the wider diameter being able to incorporate solvated Li^+ ions in both systems. In contrast, the narrower SWNTs showed CVs with smaller processes at different potentials. The change in solvent appeared to lead to smaller changes in the CV response of the material, expected as neither solvated Li^+ ion should have been able to penetrate the SWNT interior, however there were still small shifts in two of the anodic processes. The charge-discharge curves of the material did not appear to show distinct plateaus as in the wider SWNT sample, indicating that lithiation was inhibited, in agreement with the study above. The overall capacities also appeared to be much lower. Instead, the authors proposed that sulfur confined within the SWNT was reduced through the SWNT sidewall *via* an out-of-plane π-electron interaction, with the lithium cation located outside the SWNT but interacting the π orbitals of the sp2 carbon making up the SWNT sidewall, despite the likely negatively charged SWNT surface. The authors further utilised *operando* Raman spectroscopy to further clarify the sulfur products during charge-discharge, which also suggested that lithium did not directly react with the encapsulated sulfur chains in the narrower SWNTs during cycling. XPS showed lower amounts of Li_2S in the narrower SWNTs *versus* the wider SWNTs, suggesting that lithium could not penetrate the interior space.

1.3.6 Landscape

Although the literature seems relatively sparse with examples of nanoconfined electrochemistry within SWNTs and DWNTs, likely due to the perceived issues of mass transport within the nanoscale channels, the few examples demonstrate the complexity of the topic. For example, the agreement of poor lithiation of sulfur in narrower SWNTs and contrast of lithiation mechanism between the two 2018 papers on S@SWNT[85, 86] is a perfect microcosm of the wider literature on the redox chemistry of species confined within CNTs (specifically SWNTs and DWNTs). Generally, there is no largely agreed upon mechanism for mass transport within these highly confined nano domains, and there are also conflicting reports on if electrolyte ions may even penetrate at all. Particularly the work surrounding the lithiation of encapsulated C_{60} molecules, seemingly disproven by Kavan and co-workers, yet hypothesised by Kawasaki's group, and the work described above on the lithiation of sulfur chains encapsulated within SWNTs highlight this. This is further complicated by the observed redox chemistry of fullerenes when utilising large quaternary ammonium salts as supporting electrolytes by a number of different groups, which one would expect to exhibit a larger steric hindrance on mass transport, as well the solvents effects on the observed electrochemistry of encapsulated fullerenes, organic molecules and sulfur.

The solvent shell of electrolyte ions also appears to have significant effects on the observed electrochemical response of encapsulated materials, either through steric effects as shown when alternating between bulky solvated ions, or through nanotube-solvent interactions as shown with inhibited lithiation of encapsulated quinones when utilising an aqueous electrolyte. SEI's are often mentioned in the literature, supposedly leading to the desolvation of ions, allowing them to more freely move between the "entrance" of the CNTs and the redox active species found deep within the main axis, however these are never addressed in detail. This also suggests the enthalpic and entropic driving forces for desolvation may also play a crucial role. Overall this leads to a landscape where there are no standard requirements for accessing the redox chemistry of guest species within CNTs, and that many different factors, such as solvent cage, ion-ion interactions, solvent polarity and steric barriers, are at play when electrochemically addressing these confined species.

Whilst the consensus surrounding the mechanistic effects of encapsulation within SWNTs on electrochemical processes is largely disputed, overall the literature appears to be of the opinion that confinement can have many beneficial effects too, such as improved cyclability due to lower levels of leaching[87] and protection from degradation, and the ability to connect redox active materials to the electrode or current collector, allowing large amounts of active material to partake in electrochemical processes collectively. Beneficial host-guest interactions lead to lower levels of degradation, whilst also altering the kinetics of the electrochemical reactions.

Whilst several different redox active species have been confined within SWNTs/DWNTs and electrochemically investigated, none of these examples have demonstrated highly stable redox chemistry which is also well defined and reversible. Polyoxometalates (POMs) are molecular metal oxides which reversibly undergo multiple redox events and range in size from sub-nm to 5 nm. Their rich redox chemistry and well-suited dimensions make them an ideal candidate for encapsulating within SWNTs for next generation charge storage materials.

1.4 Polyoxometalates

POMs are discrete metal oxide anions. They are usually composed of at least three transition metal oxyanions bound together to form well defined, three dimensional structures and exhibit a wide range of different structural analogues (**Fig. 1.20**). Composed of early transition metals (V, Nb, Ta, Mo and W) each metal is usually fully oxidised as a d^0 centre (however d^1 configurations are also common). Bridging oxygen atoms connect the metal centres, and the molecules are terminated by oxo ligands that are shorter in length, and close to that of a metal-oxo double bond. POMs are formed *via* the condensation of multiple oxometallate precursors (normally MO_4^{2-} units, M = Mo, W) in acidic solutions, (**Fig. 1.21**) driven by the increase in Lewis acidity of the oxometallate precursors upon protonation. These structures are terminated due to the short terminal metal-oxo bonds present within the MO_6 octahedra, which exhibit a strong trans effect by weakening the bond to the bridging oxygen atom at the opposite vertex of the octahedron. This leads to the displacement of the metal atom from the centre of the octahedron towards the terminal oxygen atom, decreasing the basicity of the external oxide bonds and in turn their ability protonate and condense to larger structures.[88] The addition of hetero anions (XO_x^{n-}, X = P, Si, As) leads to their incorporation within the core of the POM molecule and as such are often referred to as templating anions. POMs featuring heteroatoms are referred to as

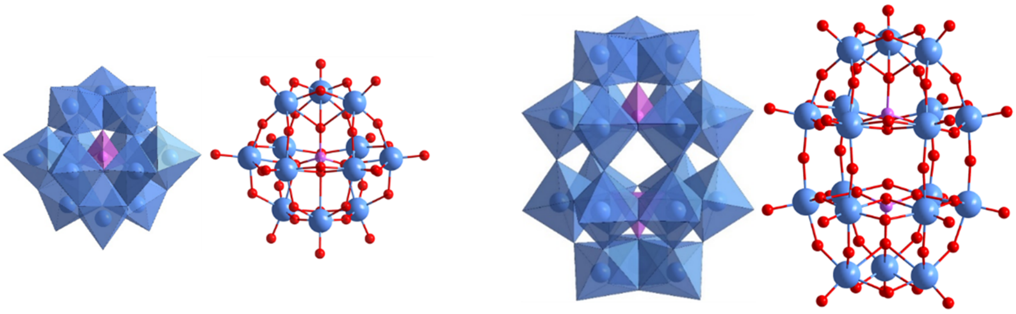

Keggin
$[XM_{12}O_{40}]^{3-}$

Wells-Dawson
$[X_2M_{18}O_{62}]^{3-}$

Figure 1.20. Keggin and Wells-Dawson POMs. Oxygen atoms positioned at the vertex of every polyhedral, ball and stick models added for clarity. Metal centres shown in blue, oxygen in red and hetero atoms in pink.

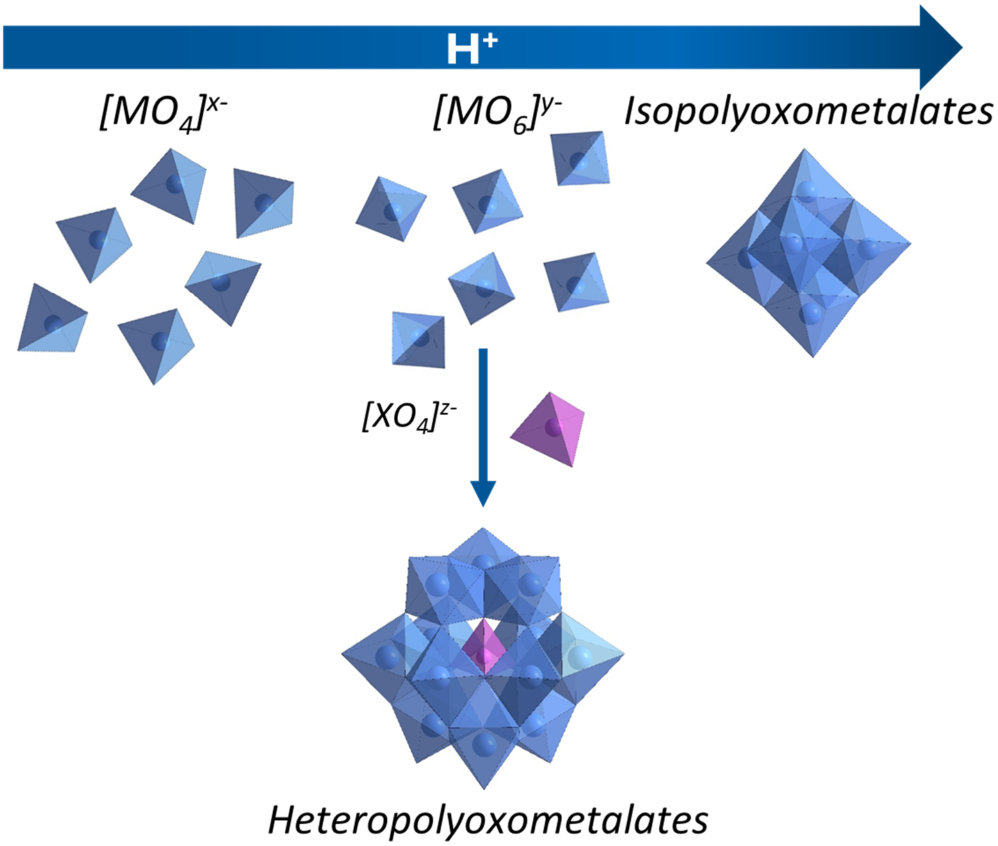

Figure 1.21. Schematic demonstrating POM formation from oxometallate precursors in acidic conditions.

heteropolyoxometalates, with POMs composed of purely oxometallate sub-units referred to as isopolyoxometalates. The myriad of POM structures range in size from species at the sub-nm level, to macromolecular species over 5 nm.[89] This range in sizes means that POMs bridge between the molecular scale and the nanoscale.

The high oxidation states and multiple metal centres that POMs are composed of lead to interesting physical properties that are manifested as extremely rich and reversible redox chemistry and photoactivity, which is highly dependent on their structure and elemental composition.[90-93] Reducing POMs often leads to the addition of an electron to a non-bonding orbital, leading to minimal structural changes.[90, 91] The high number of metal centres mean that POMs can be reversibly reduced many times through single and multiple reduction events. One such example demonstrated the ability of a keggin anion, $[PMo_{12}O_{40}]^{3-}$, to reversibly accept 24 electrons, reducing every Mo centre to

Mo^{4+}.[94] Upon their reduction, POMs exhibit an intense blue colour, first observed in reduced molybdenum oxides,[95] due to the intervalence charge transfer (IVCT) between the fully oxidised metal centres of the POM.[96] This transfer occurs rapidly and leads to the absorptions of low energy photons in the visible region. The well-defined absorption profiles of the IVCT bands mean that they can be utilised as diagnostic tools for studying POM reduction in solution.[97, 98]

The anionic nature of these well-defined structures (each O ligand is formally O^{2-}) means that they are accompanied by cations, which can equally contribute to the functional properties of the POM.[99] Formed *via* electrostatic interactions between the POM anion and desired cation, class I hybrids are POM systems where the POM and organic component are associated *via* non-covalent interactions. They are synthetically some of the more easily accessible POM hybrids, realised through ion exchange reactions. Such exchanges also allow the tuning of the POMs physical properties, such as altering the melting point, stability or solubility of the POM hybrid as well as altering the redox profiles or photoactivity of the POMs.[99]

The extremely rich redox and photochemistry of POMs and their high stability, both thermally and chemically, has led to much interest into their applications in catalysis, optoelectronics, charge storage media, magnetic devices, sensing and redox active nodes in flash storage devices.[91, 100] Although the high chemical stability of POMs is often cited as a beneficial property, at high pH the structures are rapidly hydrolysed. The controlled hydrolysis of POMs can be taken advantage of, particularly with the more stable tungsten based POMs, allowing the removal of a select number of metal centres, exposing reactive lacunary sites that hetero transition metals may bind to (inorganic hybrids) or that organic ligands may covalently bond to (class II organic-inorganic hybrids), with the hybrid structures often presenting altered physical properties such as variable band gaps, adsorption profiles and redox chemistry.[101, 102] The synthesis of these hybrids demonstrates the further tuneability of POMs, beyond that of their elemental composition and base structure, which can lead to their successful application in photocatalysis[98] and macromolecular systems.[103]

The rich and reversible redox chemistry coupled with the highly tuneable nature of POMs makes them attractive targets for future electrochemical storage devices. Whilst they possess rich redox chemistry themselves, due to their wide band gaps and discrete molecular structure they are effectively electrical insulators. Therefore, in order to utilise the full potential of their beneficial redox properties, the discrete molecular species have to either be solvated within a conductive electrolyte solution or dispersed onto a solid-state electrically conductive matrix. Dissolution of the POMs within a conductive electrolyte is problematic, due to the diffusional limitations of solution electrochemistry, and the large size of the POMs. Effectively, this means that not all POMs in solution can be accessed for charge storage (only those within the diffusional layer of the electrode can be reduced) or that upon their reduction transport between electrodes could be inhibited. Whilst elegant solutions such as the redox flow battery (RFB),[104] in which two electrolyte solutions are pumped through a cell and exchange electrons, have utilised POMs to address these issues, the use of pumping systems and the specific energies of these solutions mean that they are not widely applicable in practice. Therefore, the immobilisation of POMs onto high surface area, conductive matrices, such as conductive carbons, is likely to have the biggest impact on the use of POMs as charge storage nodes.[105]

1.5 POM-CNT Hybrid Materials

The interesting electronic properties exhibited by both CNTs and POMs, described above, has led to both species being separately investigated for a myriad of applications. However, each species suffers from their own pitfalls; the redox rich POMs suffer from electrical insulation and CNTs are mostly devoid of inherent catalytic and faradic charge storing activity. Nevertheless, the specific tuneability and functionalisation of POMs, coupled with the extremely high conductivity and high surface area of CNTs has naturally led to investigations into the combination of both species and their specific redox properties for catalytic, energy storage and sensing applications.[106, 107]

There are multiple different methodologies that can be utilised in synthesising POM-CNT hybrid materials, based mostly on the ability to chemically modify either the CNT, POM or both species to form strong interactions or bonds between the two species to allow electronic communication, enhanced stability and molecular dispersions. The final point, molecular dispersion, is critical for functional solid-state materials. This allows every active molecular species, in this case POMs, to partake in catalytic and redox events, maximising the functional activity. For POMs and CNTs there many synthetic strategies to hybrid materials, due to the broad chemical modification that

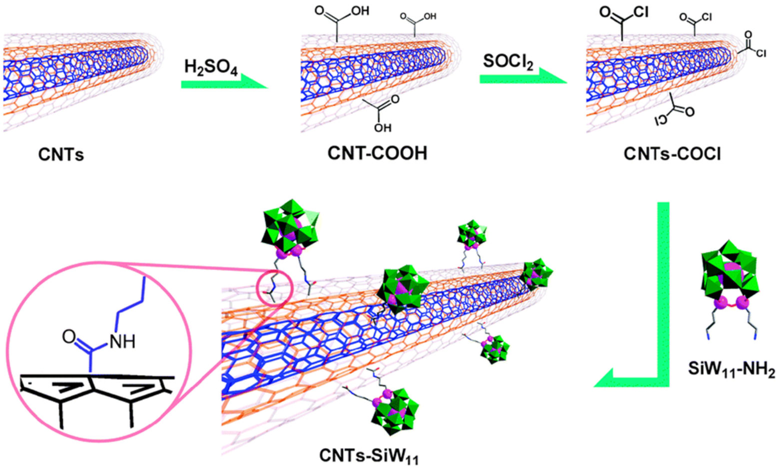

Figure 1.22. Figure describing the covalent functionalisation of CNTs with POM-hybrids. Reproduced from reference 108 with permission from The Royal Society of Chemistry (RSC).

can be applied to both species. Overall, these can be broken down into two fundamentally different methodologies: covalent attachment and non-covalent attachment of POM molecules to CNT surfaces. Covalent functionalisation is achieved by first modifying the POM through the covalent attachment of ligands to a lacunary POM. Separately, covalent functionalisation must also be carried out to introduce CNT surface groups. Both covalent functionalisation must include reactive functional groups, which are then reacted together to form strong covalent bonds between the POM and CNT[108] (**Fig. 1.22**). The wide variety of possible POM hybrids and CNT surface groups mean that there is plenty of scope for this route, and the covalent tether can be further tailored to bolster the functional properties of the material.

Non-covalent functionalisation is achieved by manipulating the intermolecular interactions between both species and can be equally creative. Due to the inherent negative charge of POMs, electrostatic interactions can easily lead to CNT functionalisation with POMs. Due to oxygen containing groups present on CNT surfaces they often are negatively charged, and covalent functionalisation of these groups is normally required to encourage POM deposition onto the CNT surface.[109] Such electrostatic interactions can also be utilised in layered assemblies of POM-CNT composites on electrode surfaces.[110] Other intermolecular interactions such as van der Waals can be utilised to encourage loading of the POMs onto the CNT surface, presenting yet another route to the formation of these hybrid materials.[111]

The continuous graphitic lattice of the CNT sidewalls also means that the aromaticity of CNTs can also be utilised. Hybrid POMs with extended aromatic functional groups may also be grafted to the external CNT surface through π-π stacking interactions[112] as well as grafting cationic groups to the CNT surface through π-π stacking interactions.[113] The reduction of noble metal salts with pre-reduced POMs is also a route to loading optically active nanoparticles decorated with POMs onto CNT surfaces, which allows good electronic communication between all three species.[114] Generally, all of the examples discussed above require an element of direct chemical modification of either/or both species leading to greater degrees of chemical complexity within the functional system, leading to more routes to chemical decomposition and lower stabilities.

These fascinating hybrid materials often have enhanced properties that are manifested as solid-state electrochemical behaviour, increased charge separation for photocatalysis and enhanced cyclability. POM-CNT hybrids have now been applied to variety of different catalytic reactions, such as methanol oxidation,[115, 116] water oxidation[109, 113] and oxygen reduction[117, 118] as well as both cathode[111] and anode[112] materials in lithium ion batteries, supercapacitors[119, 120] and sensors.[121] (Relevant examples are discussed in further detail in Chapter 4, 4.1)

1.6 Scope for Further Investigation

The ability to encapsulate redox active molecular species within SWNTs coupled with the extremely robust and rich redox chemistry of POMs means that there is ample room for further investigation. As discussed above, POM-CNT hybrids in the literature mainly consist of POMs being externally bound to the CNT surface, requiring modifications that lead to greater levels of chemical complexity which are open to a multitude of chemical degradation pathways, as well as potentially suffering from chemical leaching due to readily being exposed to solvent. However, encapsulation has been shown to increase the stability of encapsulated species during electrochemical cycling, as well as reduce the loss of active material to the electrolyte.

The rich and well-defined redox chemistry of POMs make them well suited for studying the effects of nanoconfinement on the electrochemical properties of species confined within narrow CNTs. Although some examples of encapsulated POMs within CNTs exist (discussed in Chapter 2, section 2.1) there have yet to be any in depth analyses on {POM}@CNT (POMs encapsulated with CNT) interactions, structure or physical properties reported in the literature. Such analysis may pave the way for the use of POM@CNT materials, or indeed encapsulated redox species, as viable materials for energy storage.

1.7 References

1. A. E. Raftery, N. Li, H. Ševčíková, P. Gerland and G. K. Heilig, *Proc. Natl. Acad. Sci.*, 2012, **109**, 13915-13921.
2. R. B. Jackson, C. Le Quéré, R. M. Andrew, J. G. Canadell, J. I. Korsbakken, Z. Liu, G. P. Peters and B. Zheng, *Environ. Res. Lett.*, 2018, **13**, 120401.
3. G. P. Peters, R. M. Andrew, J. G. Canadell, P. Friedlingstein, R. B. Jackson, J. I. Korsbakken, C. Le Quéré and A. Peregon, *Nat. Clim. Change*, 2020, **10**, 3-6.
4. P. Friedlingstein, M. W. Jones, M. O'Sullivan, R. M. Andrew, J. Hauck, G. P. Peters, W. Peters, J. Pongratz, S. Sitch, C. Le Quéré*, et al.*, *Earth Syst. Sci. Data*, 2019, **11**, 1783-1838.
5. R. Neukom, L. A. Barboza, M. P. Erb, F. Shi, J. Emile-Geay, M. N. Evans, J. Franke, D. S. Kaufman, L. Lücke, K. Rehfeld*, et al.*, *Nat. Geosci.*, 2019, **12**, 643-649.
6. R. S. Nerem and J. Fasullo, *Bull. Am. Meteorol. Soc.*, 2019, **100**, S15-S18.
7. S. C. Herring, N. Christidis, A. Hoell, M. P. Hoerling and P. A. Stott, *Bull. Am. Meteorol. Soc.*, 2019, **100**, S1-S117.
8. M. New, D. Liverman, H. Schroder and K. Anderson, *Philos. Trans. R. Soc. A*, 2011, **369**, 6-19.
9. D. Gielen, F. Boshell, D. Saygin, M. D. Bazilian, N. Wagner and R. Gorini, *Energy Strategy Rev.*, 2019, **24**, 38-50.
10. G. Chisholm and L. Cronin, in *Storing Energy*, ed. T. M. Letcher, Elsevier, Oxford, 2016, DOI: 10.1016/B978-0-12-803440-8.00016-6, pp. 315-343.
11. H. Budde-Meiwes, J. Drillkens, B. Lunz, J. Muennix, S. Rothgang, J. Kowal and D. U. Sauer, *Proc. Inst. Mech. Eng. D*, 2013, **227**, 761-776.
12. B. Dunn, H. Kamath and J.-M. Tarascon, *Science*, 2011, **334**, 928-935.
13. B. D. McCloskey, *J. Phys. Chem. Lett.*, 2015, **6**, 3592-3593.

14. M. Monthioux and V. L. Kuznetsov, *Carbon*, 2006, **44**, 1621-1623.
15. S. Iijima, *Nature*, 1991, **354**, 56-58.
16. H. W. Kroto, J. R. Heath, S. C. O'Brien, R. F. Curl and R. E. Smalley, *Nature*, 1985, **318**, 162-163.
17. S. Iijima and T. Ichihashi, *Nature*, 1993, **363**, 603-605.
18. D. S. Bethune, C. H. Kiang, M. S. de Vries, G. Gorman, R. Savoy, J. Vazquez and R. Beyers, *Nature*, 1993, **363**, 605-607.
19. K. S. Novoselov, A. K. Geim, S. V. Morozov, D. Jiang, Y. Zhang, S. V. Dubonos, I. V. Grigorieva and A. A. Firsov, *Science*, 2004, **306**, 666-669.
20. P. Avouris, *Nano Lett.*, 2010, **10**, 4285-4294.
21. A. K. Geim and K. S. Novoselov, *Nat. Mater.*, 2007, **6**, 183-191.
22. E. Joselevich, *ChemPhysChem*, 2004, **5**, 619-624.
23. S. Niyogi, M. A. Hamon, H. Hu, B. Zhao, P. Bhowmik, R. Sen, M. E. Itkis and R. C. Haddon, *Accounts Chem. Res.*, 2002, **35**, 1105-1113.
24. T. W. Ebbesen and P. M. Ajayan, *Nature*, 1992, **358**, 220-222.
25. T. Guo, P. Nikolaev, A. Thess, D. T. Colbert and R. E. Smalley, *Chem. Phys. Lett.*, 1995, **243**, 49-54.
26. R. Andrews, D. Jacques, D. Qian and T. Rantell, *Accounts Chem. Res.*, 2002, **35**, 1008-1017.
27. P.-X. Hou, C. Liu and H.-M. Cheng, *Carbon*, 2008, **46**, 2003-2025.
28. S. Cambré, W. Wenseleers, E. Goovaerts and D. E. Resasco, *ACS Nano*, 2010, **4**, 6717-6724.
29. C. Laurent, E. Flahaut and A. Peigney, *Carbon*, 2010, **48**, 2994-2996.
30. M.-F. Yu, O. Lourie, M. J. Dyer, K. Moloni, T. F. Kelly and R. S. Ruoff, *Science*, 2000, **287**, 637-640.
31. E. Pop, D. Mann, Q. Wang, K. Goodson and H. Dai, *Nano Lett.*, 2006, **6**, 96-100.
32. G. E. Begtrup, K. G. Ray, B. M. Kessler, T. D. Yuzvinsky, H. Garcia and A. Zettl, *physica status solidi (b)*, 2007, **244**, 3960-3963.
33. S. Banerjee, T. Hemraj-Benny and S. S. Wong, *Adv. Mater.*, 2005, **17**, 17-29.
34. I. C. Gerber and P. Serp, *Chem. Rev.*, 2020, **120**, 1250-1349.
35. Y. Mo, H. Wang, J. Liu, Y. Lan, R. Guo, Y. Zhang, W. Xue and Y. Zhang, *J. Mater. Chem. B*, 2015, **3**, 1846-1855.

36. Q. Liu, L. Ke, F. Liu, C. Huang and L. Xing, *Materials & Design*, 2013, **45**, 343-348.
37. M. M. Shulaker, G. Hills, N. Patil, H. Wei, H.-Y. Chen, H. S. P. Wong and S. Mitra, *Nature*, 2013, **501**, 526-530.
38. E. Bichoutskaia, A. M. Popov and Y. E. Lozovik, *Materials Today*, 2008, **11**, 38-43.
39. Q. Xie, E. Perez-Cordero and L. Echegoyen, *J. Am. Chem. Soc.*, 1992, **114**, 3978-3980.
40. H. Liu, J. Zhai and L. Jiang, *Soft Matter*, 2006, **2**, 811-821.
41. X. Li, J. Rong and B. Wei, *ACS Nano*, 2010, **4**, 6039-6049.
42. L. Sun, X. Wang, Y. Wang and Q. Zhang, *Carbon*, 2017, **122**, 462-474.
43. M. Monthioux, *Carbon*, 2002, **40**, 1809-1823.
44. A. B. Grommet, M. Feller and R. Klajn, *Nat. Nanotechnol.*, 2020, **15**, 256-271.
45. T. Fujimori, A. Morelos-Gómez, Z. Zhu, H. Muramatsu, R. Futamura, K. Urita, M. Terrones, T. Hayashi, M. Endo, S. Young Hong*, et al.*, *Nat. Commun.*, 2013, **4**, 2162.
46. A. Botos, J. Biskupek, T. W. Chamberlain, G. A. Rance, C. T. Stoppiello, J. Sloan, Z. Liu, K. Suenaga, U. Kaiser and A. N. Khlobystov, *J. Am. Chem. Soc.*, 2016, **138**, 8175-8183.
47. S. Fleischmann, M. A. Spencer and V. Augustyn, *Chem. Mater.*, 2020, **32**, 3325-3334.
48. V. Augustyn and Y. Gogotsi, *Joule*, 2017, **1**, 443-452.
49. S. A. Miners, G. A. Rance and A. N. Khlobystov, *Chem. Soc. Rev.*, 2016, **45**, 4727-4746.
50. M. V. Kharlamova, *Prog. Mater. Sci.*, 2016, **77**, 125-211.
51. B. W. Smith, M. Monthioux and D. E. Luzzi, *Nature*, 1998, **396**, 323-324.
52. L. Kavan, L. Dunsch and H. Kataura, *Chem. Phys. Lett.*, 2002, **361**, 79-85.
53. T. Pichler, H. Kuzmany, H. Kataura and Y. Achiba, *Phys. Rev. Lett.*, 2001, **87**, 267401.
54. L. Kavan, L. Dunsch, H. Kataura, A. Oshiyama, M. Otani and S. Okada, *J. Phys. Chem. B*, 2003, **107**, 7666-7675.
55. L. Kavan, L. Dunsch and H. Kataura, *Carbon*, 2004, **42**, 1011-1019.
56. N. Sun, L. Guan, Z. Shi, Z. Zhu, N. Li, M. Li and Z. Gu, *Electrochem. Commun.*, 2005, **7**, 1148-1152.

57. A. J. Bard and L. R. Faulkner, *Electrochemical Methods Fundamentals and Applications* John Wiley & Sons, Second Edn., 2001.

58. K. Wu, H. Qiu, J. Hu, N. Sun, Z. Zhu, M. Li and Z. Shi, *Carbon*, 2012, **50**, 4401-4408.

59. S. Kawasaki, Y. Iwai and M. Hirose, *Mater. Res. Bull.*, 2009, **44**, 415-417.

60. T. Matsushita, Y. Ishii and S. Kawasaki, *Mater. Express*, 2013, **3**, 30-36.

61. A. s. S. Claye, J. E. Fischer, C. B. Huffman, A. G. Rinzler and R. E. Smalley, *J. Electrochem. Soc.*, 2000, **147**, 2845.

62. J.-X. Li, Y. Zhao and L.-H. Guan, *Electrochem. Commun.*, 2010, **12**, 592-595.

63. L. Guan, Z. Shi, M. Li and Z. Gu, *Carbon*, 2005, **43**, 2780-2785.

64. H. Qiu, N. Sun, M. Li, Z. Shi, J. Qiu, Z. Gu and J. Yang, *J. Nanosci. Nanotechnol.*, 2011, **11**, 4034-4038.

65. N. Sun, L. Guan, Z. Shi, N. Li, Z. Gu, Z. Zhu, M. Li and Y. Shao, *Anal. Chem.*, 2006, **78**, 6050-6057.

66. H. Cheng, H. Qiu, Z. Zhu, M. Li and Z. Shi, *Electrochimica Acta*, 2012, **63**, 83-88.

67. H. Cheng, L. Guan, Z. Shi, Z. Zhu, Z. Gu and M. Li, *Electroanalysis*, 2013, **25**, 2041-2044.

68. R. L. McSweeney, T. W. Chamberlain, M. Baldoni, M. A. Lebedeva, E. S. Davies, E. Besley and A. N. Khlobystov, *Chem. - Eur. J.*, 2016, **22**, 13540-13549.

69. A. Al-zubaidi, T. Inoue, T. Matsushita, Y. Ishii, T. Hashimoto and S. Kawasaki, *J. Phys. Chem. C*, 2012, **116**, 7681-7686.

70. Y. Iizumi, H. Suzuki, M. Tange and T. Okazaki, *Nanoscale*, 2014, **6**, 13910-13914.

71. R. L. McSweeney, T. W. Chamberlain, E. S. Davies and A. N. Khlobystov, *Chem. Commun.*, 2014, **50**, 14338-14340.

72. S. Kawasaki, Y. Iwai and M. Hirose, *Carbon*, 2009, **47**, 1081-1086.

73. Y. Ishii, K. Tashiro, K. Hosoe, A. Al-zubaidi and S. Kawasaki, *Phys. Chem. Chem. Phys.*, 2016, **18**, 10411-10418.

74. C. Li, Y. Ishii, S. Inayama and S. Kawasaki, *Nanotechnology*, 2017, **28**, 355401.

75. T. Tsuzuki, S. Ogata and M. Uranagase, *Comput. Mater. Sci.*, 2020, **171**, 109281.

76. C. Li, Y. Ishii and S. Kawasaki, *Jpn. J. Appl. Phys.*, 2018, **58**, SAAE02.

77. H. Song, Y. Ishii, A. Al-zubaidi, T. Sakai and S. Kawasaki, *Phys. Chem. Chem. Phys.*, 2013, **15**, 5767-5770.
78. Y. Yoshida, Y. Ishii, N. Kato, C. Li and S. Kawasaki, *J. Phys. Chem. C*, 2016, **120**, 20454-20461.
79. Y. Taniguchi, Y. Ishii, A. Al-Zubaidi and S. Kawasaki, *J. Nanosci. Nanotechnol.*, 2017, **17**, 1901-1907.
80. C. Li, Y. Yoshida, R. Date, K. Matsushita, Y. Ishii and S. Kawasaki, *Mater. Express*, 2018, **8**, 555-561.
81. N. Kato, Y. Ishii, Y. Yoshida, Y. Sakamoto, K. Matsushita, M. Takahashi, R. Date and S. Kawasaki, *ACS Omega*, 2019, **4**, 2547-2553.
82. M. Zhao, B.-Q. Li, X.-Q. Zhang, J.-Q. Huang and Q. Zhang, *ACS Cent. Sci.*, 2020, **6**, 1095-1104.
83. C.-P. Yang, Y.-X. Yin, Y.-G. Guo and L.-J. Wan, *J. Am. Chem. Soc.*, 2015, **137**, 2215-2218.
84. C. A. Milroy, S. Jang, T. Fujimori, A. Dodabalapur and A. Manthiram, *Small*, 2017, **13**, 1603786.
85. K. Urita, T. Fujimori, H. Notohara and I. Moriguchi, *ACS Applied Energy Materials*, 2018, **1**, 807-813.
86. C. Fu, M. B. Oviedo, Y. Zhu, A. von Wald Cresce, K. Xu, G. Li, M. E. Itkis, R. C. Haddon, M. Chi, Y. Han, *et al.*, *ACS Nano*, 2018, **12**, 9775-9784.
87. H. Tabassum, A. Mahmood, B. Zhu, Z. Liang, R. Zhong, S. Guo and R. Zou, *Energy Environ. Sci.*, 2019, **12**, 2924-2956.
88. L. C. W. Baker and D. C. Glick, *Chem. Rev.*, 1998, **98**, 3-50.
89. A. Müller, E. Beckmann, H. Bögge, M. Schmidtmann and A. Dress, *Angew. Chem., Int. Ed.*, 2002, **41**, 1162-1167.
90. M. Sadakane and E. Steckhan, *Chem. Rev.*, 1998, **98**, 219-238.
91. N. I. Gumerova and A. Rompel, *Nat. Rev. Chem*, 2018, **2**, 0112.
92. J. M. Cameron, D. J. Wales and G. N. Newton, *Dalton Trans.*, 2018, **47**, 5120-5136.
93. S. Garai, A. Merca, S. Bhowmik, H. El Moll, H. Li, F. Haso, H. Nogueira, T. Liu, L. Wu, P. Gouzerh, *et al.*, *Soft Matter*, 2015, **11**, 2372-2378.
94. H. Wang, S. Hamanaka, Y. Nishimoto, S. Irle, T. Yokoyama, H. Yoshikawa and K. Awaga, *J. Am. Chem. Soc.*, 2012, **134**, 4918-4924.
95. P. Gouzerh and M. Che, *L'actualite chimique*, 2006, 9-22.

96. T. Yamase, *Chem. Rev.*, 1998, **98**, 307-326.
97. K. Kastner, A. J. Kibler, E. Karjalainen, J. A. Fernandes, V. Sans and G. N. Newton, *J. Mater. Chem. A*, 2017, **5**, 11577-11581.
98. B. Matt, J. Fize, J. Moussa, H. Amouri, A. Pereira, V. Artero, G. Izzet and A. Proust, *Energy Environ. Sci.*, 2013, **6**, 1504-1508.
99. A. Misra, K. Kozma, C. Streb and M. Nyman, *Angew. Chem., Int. Ed.*, 2020, **59**, 596-612.
100. C. Streb, *Dalton Trans.*, 2012, **41**, 1651-1659.
101. J. M. Cameron, S. Fujimoto, K. Kastner, R.-J. Wei, D. Robinson, V. Sans, G. N. Newton and H. H. Oshio, *Chem. - Eur. J.*, 2017, **23**, 47-50.
102. A. Dolbecq, E. Dumas, C. R. Mayer and P. Mialane, *Chem. Rev.*, 2010, **110**, 6009-6048.
103. S. Amin, J. M. Cameron, J. A. Watts, D. A. Walsh, V. Sans and G. N. Newton, *Mol. Syst. Des. Eng.*, 2019, **4**, 995-999.
104. J.-J. Chen, M. D. Symes and L. Cronin, *Nat. Chem.*, 2018, **10**, 1042-1047.
105. M. Genovese and K. Lian, *J. Mater. Chem. A*, 2017, **5**, 3939-3947.
106. Y. Ji, L. Huang, J. Hu, C. Streb and Y.-F. Song, *Energy Environ. Sci.*, 2015, **8**, 776-789.
107. C. G. Lin, J. Hu and Y. F. Song, in *Adv. Inorg. Chem.*, eds. R. van Eldik and L. Cronin, Academic Press, 2017, vol. 69, pp. 181-212.
108. W. Chen, L. Huang, J. Hu, T. Li, F. Jia and Y.-F. Song, *Phys. Chem. Chem. Phys.*, 2014, **16**, 19668-19673.
109. F. M. Toma, A. Sartorel, M. Iurlo, M. Carraro, P. Parisse, C. Maccato, S. Rapino, B. R. Gonzalez, H. Amenitsch, T. Da Ros, *et al.*, *Nat. Chem.*, 2010, **2**, 826-831.
110. T. Akter, K. Hu and K. Lian, *Electrochimica Acta*, 2011, **56**, 4966-4971.
111. N. Kawasaki, H. Wang, R. Nakanishi, S. Hamanaka, R. Kitaura, H. Shinohara, T. Yokoyama, H. Yoshikawa and K. Awaga, *Angew. Chem., Int. Ed.*, 2011, **50**, 3471-3474.
112. D. Ma, L. Liang, W. Chen, H. Liu and Y.-F. Song, *Adv. Funct. Mater.*, 2013, **23**, 6100-6105.
113. F. M. Toma, A. Sartorel, M. Iurlo, M. Carraro, S. Rapino, L. Hoober-Burkhardt, T. Da Ros, M. Marcaccio, G. Scorrano, F. Paolucci, *et al.*, *ChemSusChem*, 2011, **4**, 1447-1451.

114. S. Li, X. Yu, G. Zhang, Y. Ma, J. Yao, B. Keita, N. Louis and H. Zhao, *J. Mater. Chem.*, 2011, **21**, 2282-2287.

115. D. Pan, J. Chen, W. Tao, L. Nie and S. Yao, *Langmuir*, 2006, **22**, 5872-5876.

116. S. Li, X. Yu, G. Zhang, Y. Ma, J. Yao and P. de Oliveira, *Carbon*, 2011, **49**, 1906-1911.

117. D. Wang, S. Lu and S. P. Jiang, *Chem. Commun.*, 2010, **46**, 2058-2060.

118. R. Liu, S. Li, X. Yu, G. Zhang, Y. Ma and J. Yao, *J. Mater. Chem.*, 2011, **21**, 14917-14924.

119. A. K. Cuentas-Gallegos, R. Martínez-Rosales, M. Baibarac, P. Gómez-Romero and M. E. Rincón, *Electrochem. Commun.*, 2007, **9**, 2088-2092.

120. M. Sosnowska, M. Goral-Kurbiel, M. Skunik-Nuckowska, R. Jurczakowski and P. J. Kulesza, *J. Solid State Electrochem.*, 2013, **17**, 1631-1640.

121. A. Salimi, A. Korani, R. Hallaj, R. Khoshnavazi and H. Hadadzadeh, *Analytica Chimica Acta*, 2009, **635**, 63-70.

Chapter 2: Redox Mediated Encapsulation of Polyoxometalates within Single Walled Carbon Nanotubes

2.1 Background

As discussed in chapter 1, carbon nanotubes (CNTs) have been of significant interest due to their extraordinary physicochemical properties. As well as this, CNTs also possess an interior dimension which can incorporate guest species within.[1, 2] The recoverability and chemical stability of CNTs has led to investigations into their guest@CNT materials' use as catalytic reactors[3] and as structures to alter the properties of their guests.[4] Their high conductivity and variable electronic structures has led to interest in their use in electronic applications[5] and energy storage.[6]

Different methodologies for encapsulating guest species within CNTs have been reported,[1, 2, 7] with the nature of the guest species generally dictating the methodology that is required. For single walled carbon nanotubes (SWNTs), guest species preferentially encapsulate rather than surface adsorb due to greater favourable van

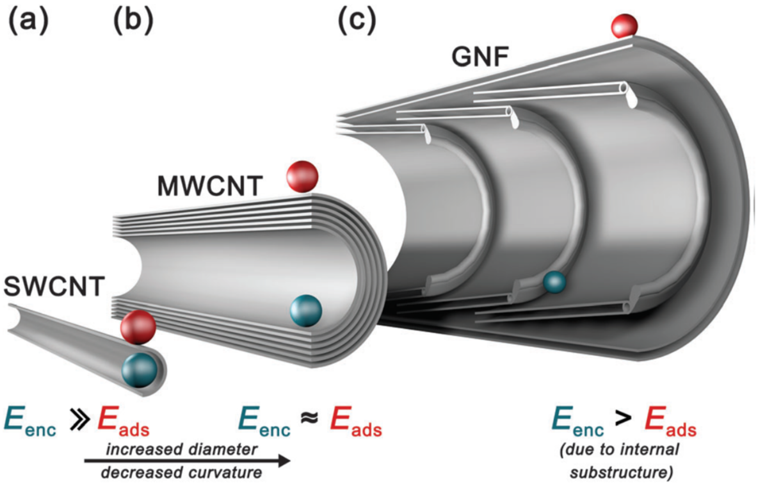

Figure 2.1. Cross section of three types of CNT class (not to scale) showing encapsulated (blue) and adsorbed (red) species. Each grey surface represents a CNT graphitic wall. The energies for encapsulation (E_{enc}) and external adsorption (E_{ads}) exhibit a general trend depending on wall curvature and thus CNT diameter. Reproduced from reference 3 with permission from The Royal Society of Chemistry (RSC).

der Waals interactions between the host and guest upon encapsulation (**Fig. 2.1, a**). However, this is entirely dependent on the size of the species being encapsulated as the geometric constraints of the SWNTs dictate the maximum critical dimensions of the guest. CNTs with larger diameters may more readily adsorb species to their exteriors than SWNTs (**Fig 2.1, b**), due to larger surface areas for van der Waals contact, however there is still a large driving force for species to encapsulate within the interior dimension due to intermolecular interactions.[3] Larger CNTs such as graphitised nanofibers (GNFs) possess corrugated interiors, providing van der Waals surfaces which favourably drive deposition onto these edge-like sites[8] (**Fig. 2.1, c**). For this reason, it is vital that the correct CNT host and methodology for encapsulation is chosen.

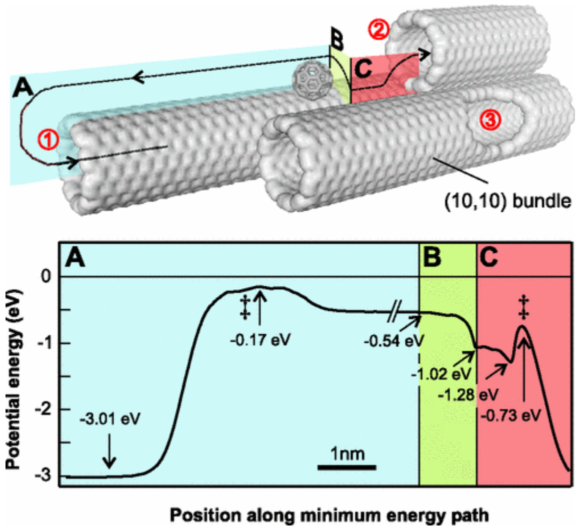

Figure 2.2. Potential energy diagram for C_{60} interaction with a SWNT bundle. Reproduced from reference 12 with permission from the American Chemical Society.

Early examples of encapsulation were an unintended product of CNT synthesis, such as the first observation of the encapsulation of fullerenes within SWNTs synthesised by the laser vaporisation of graphite.[9] This was also later achieved using both vapour deposition[10] and synthesis in supercritical fluids.[11] The encapsulation of C_{60} within SWNTs is extremely favourable if the SWNT width closely matches that of the critical dimensions of the C_{60} molecule, maximising van der Waals interactions. As such, the encapsulation of C_{60} can be nearly 3 eV more stable than surface adsorption onto the SWNT[12] (**Fig. 2.2**). The encapsulation of C_{60} was later achieved using solution methods.[13] Firstly, by dispersion C_{60} in ethanol and adding SWNTs to the dispersion, named "nano-extraction". The solubility of C_{60} in ethanol is extremely poor, (0.001 mg/mL) therefore encapsulation of the C_{60} within the SWNTs was much more favourable, providing an enthalpic driving force for encapsulation. Secondly, by saturating toluene with C_{60} and adding a microlitre of the solution to open SWNTs the uptake of C_{60} was driven by the evaporation of the solvent, named "nano-condensation" in which the C_{60} molecules were driven into the SWNT as the amount of solvent reduced with evaporation (**Fig. 2.3**).

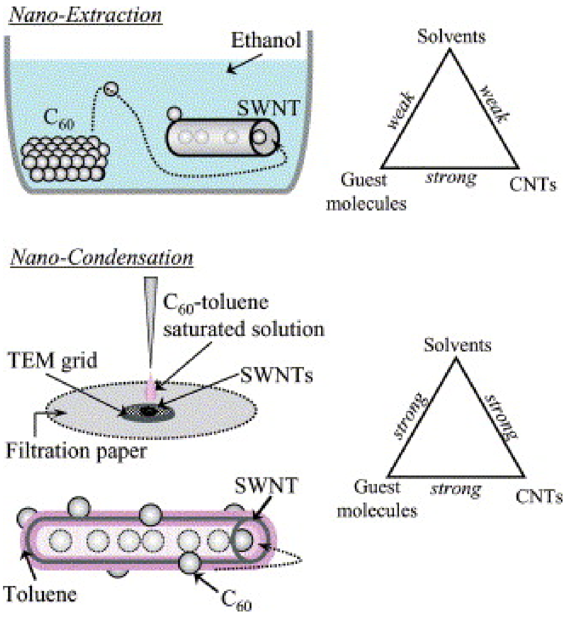

Figure 2.3. Schematics for nano-extraction and nano-condensation. On the right are diagrams describing the relationship between guest, host and solvent. Reproduced from reference 13 with permission from Elsevier.

Early methodologies to encapsulate metals and their salts generally involved melting the guest species and dispersing CNTs into the molten liquid.[1, 14] The hollow CNT interior allows filling by capillary action, leading to extremely high levels of encapsulation. More recently, encapsulation has been achieved through the sublimation of small molecules in the presence of CNTs, leading to the diffusion of the species within the CNT cavity, with favourable intermolecular interactions leading to preferential encapsulation. This has been achieved for metal carbonyls,[15] metal acetylacetonates[16] and other small molecules.[17-19] The technique generally gives high encapsulation rates, is solvent-less and is not restricted by surface tension requirements of a solvent. Limitations to this methodology are naturally the ability of the guest species to sublime at reasonable pressures and temperature, or before they reach their decomposition temperatures.

Due to the perceived hydrophobicity of CNTs,[20, 21] much of the work on the encapsulation of guests within their interior dimension has focussed on charge-neutral materials, however polyoxometalates have previously been encapsulated within SWNTs, using solvent methods. Fei *et al.* reported the formation of “ionic peapods” by mixing opened DWNTs with an aqueous solution of $H_3[PW_{12}O_{40}]$.[22] The authors reported a high level of encapsulation within the interior of the DWNTs, as well as a change in the Raman spectrum of the DWNTs and POM, which indicated that there was a strong interaction between the terminal W=O bonds and the interior DWNT sidewall.

Sloan *et al.* reported the encapsulation of the lindqvist $[W_6O_{19}]^{2-}$ anion within DWNTs.[23] To encapsulate the lindqvist ions the nano-extraction technique was employed, where ethanol was saturated with $[nBu_4N]_2[W_6O_{19}]$, and opened DWNTs

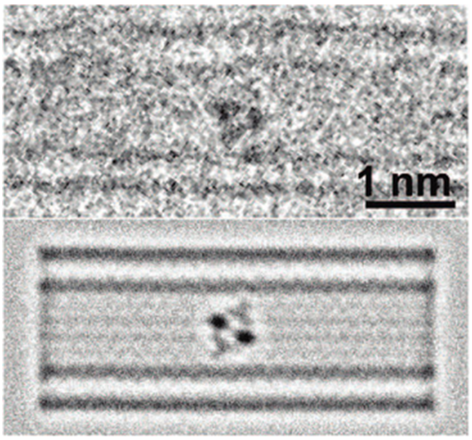

Figure 2.4. Lindqvist anion encapsulated within a DWNT (top) and image simulation (bottom). Reproduced from reference 23 with permission from The American Chemical Society.

were added the ethanol solution. The authors reported a low level of encapsulation within the DWNTs, however they demonstrated a close match between the experimental images of the anion and simulated images (**Fig. 2.4**). The $[W_6O_{19}]^{2-}$ anion was observed to rapidly translate along the interior of the DWNTs and take part in reactions with confined molecular neighbours. Whilst the anion appeared to rapidly translate along the DWNT interior, the rotation of the molecule was inhibited due to the close geometric fit between the lindqvist anion and the internal diameter of the DWNT.[24]

Wang *et al.* encapsulated $H_3[PMo_{12}O_{40}]$ as a precursor for the formation of encapsulated molybdenum sulfide nanoribbons.[25] The authors added opened DWNTs to an aqueous solution of $H_3[PMo_{12}O_{40}]$, and refluxed the mixture. The authors did not report any characterisation or properties of the encapsulated POM material, however the encapsulation rate of the MoS_2 ribbons formed by heating the material at 800 ^{o}C in an atmosphere of H_2S/H_2 was high. The authors reported MoS_2 nanoribbon widths of 1-4 nm, and 1-3 layers, dependent on the DWNT diameter.

The authors later encapsulated $H_3[PW_{12}O_{40}]$ as a precursor for the formation of encapsulated tungsten sulfide nanoribbons.[26] The authors utilised the same method for encapsulation as they reported previously. Again, the properties of the intermediate material were not reported. The authors found that using the DWNTs as a template led to the formation of ultra-narrow WS_2 ribbons, with widths of 1-3 nm and layers between 1-3, again dependent on the nanotube diameter, allowing them to drastically alter the magnetic properties of the synthesised WS_2.

Many examples of materials encapsulated within CNTs portray the CNT as an inert nanoscale vessel, with the main purpose of the CNT to act purely as way to restrict the dimensions of the encapsulated material. The complex electronic character of CNTs means that guests confined within their interior dimension, or indeed adsorbed to their external surfaces, may experience electronic transitions between host and guest.

Investigations utilising Raman spectroscopy have focussed on the effect of encapsulated guests on the electronic structure of the host nanotube. Eliseev *et al.* demonstrated that upon encapsulation of silver halides (AgX, X = Cl, Br, I) within SWNTs, changes in the G-band of the material (**Fig. 2.5**) were due to electron donation from the SWNTs to the encapsulated silver salt.[27] Blue shifts in the G-band were reported for all AgX species in the study and the magnitude of this shift was found to be dependent on the silver salt, the chirality of the SWNT and the excitation energy used for spectroscopy. The shape of the G-band was also altered upon encapsulation of the AgX, with the profile becoming much more similar to that of purely semi-conducting SWNTs. These changes were attributed to the loss of resonant excitation for metallic SWNTs upon the encapsulation of AgX, due to direct modification of the CNT band structure.

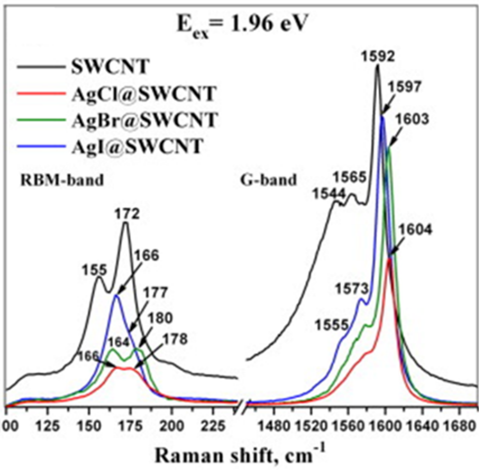

Figure 2.5. Radial breathing mode (RBM) and G-band regions of the Raman spectra of SWNTs and silver halide encapsulated within SWNTs. Reproduced from reference 27 with permission from Elsevier.

As discussed in chapter 1, many host-guest interactions were observed for electrochemically active species confined within SWNTs, in particular the work of McSweeney *et al.* demonstrated that the redox activity of metallocenes was altered upon encapsulation within SWNT hosts.[28] This appeared to manifest as charge donation from encapsulated ferrocene, $Fe(Cp^{XMe})_2$ (X = 0, 1, 4, 5), or cobaltocene, $Co(Cp)_2$, to the SWNT support. Previous reports on the encapsulation of ferrocene were also in good agreement with this.[29-33] A report by Li *et al.* also demonstrated that encapsulation of $Co(Cp)_2$ led to a charge transfer from the cobaltocene to the SWNT.[34] In the paper the authors describe the diameter selective encapsulation of cobaltocene molecules, which were probed with UV-vis spectrometry. The spectrum of the $Co(Cp)_2$@SWNT material showed a redshift of the adsorption associated with ligand to metal charge transfer (LMCT) and indicated that $[Co(Cp)_2]^+$ had formed upon encapsulation. Looking at adsorption bands associated with the SWNT, intensity enhancements indicated that the SWNTs had been n-doped, in good agreement with spectrum of the encapsulated $Co(Cp)_2$.

Similarly, Kharlamova *et al*. reported that the encapsulation of $Ni(Cp)_2$ lead to charge donation from the metallocene to the SWNT, which was confirmed with X-ray photoelectron spectroscopy (XPS), ultraviolet photoelectron spectroscopy and Raman spectroscopy.[35] Upon heating the sample to form metallic nickel, the amount of charge donation to the SWNT initially increased, however with further heating and the

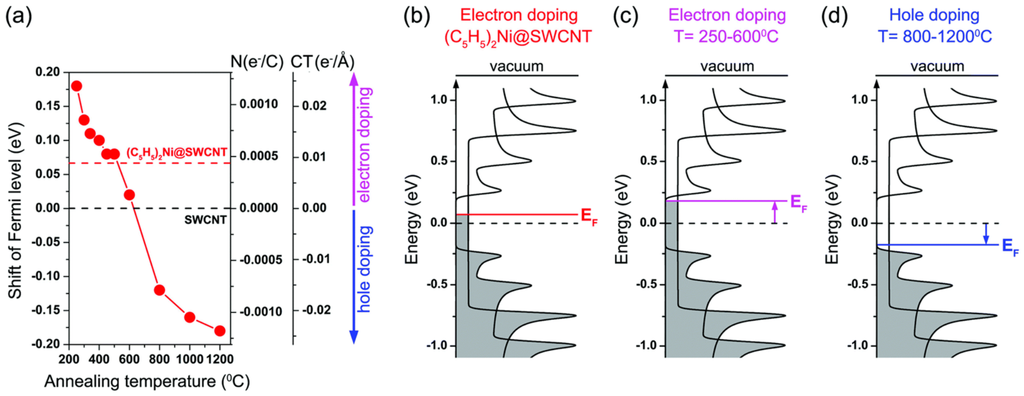

Figure 2.6. (a) Fermi level shifts for the $NiCp_2$@SWNT material heated at varying temperatures. Right axis details the number of electrons per carbon atom this corresponds to and charge density per SWNT length. (b – d) show schematics for electron and hole doping of the SWNTs with DoS shown. Reproduced from reference 35 with permission from The Royal Society of Chemistry (RSC).

formation of a secondary encapsulated CNT, this appeared to reverse, leading to electron donation from the SWNT (**Fig. 2.6**).

The encapsulation of early transition metal iodide species has also demonstrated the ability of SWNTs to act as electron donator, similar to the work by Eliseev *et al.* described above. The work, reported by Botos *et al.* described the encapsulation of $M(CO)_6$ (M = Mo, W) and I_2 within SWNTs *via* vapour deposition, which was subsequently heated to high temperature in an inert atmosphere to yield molecules of $[M_6I_{14}]^{2-}$.[36] The authors were able to characterise the synthesised $[M_6I_{14}]^{2-}$ molecules encapsulated within the SWNT with TEM and energy dispersive X-ray spectroscopy (EDX). The authors further utilised Raman spectroscopy to probe the oxidation state of the SWNT support by using the diagnostic G-band. The encapsulation of the metal carbonyl and iodine produced the largest blue shift in the G-band (approximately 8 and 14 cm^{-1} for Mo & W respectively) which was expected due to the known formation of I_n^- polymeric chains[37, 38] which could accept electrons from the SWNT. Following heating to 500 °C and the formation of $[M_6I_{14}]^{2-}$ a blue shift in the G-band was still present, shifted by the same amount in the case of Mo, and shifted by a lesser amount in the case of W (**Fig 2.7**). This suggested there was still electron donation from the SWNTs to the metal iodides encapsulated within the SWNTs, suggesting that $[M_6I_{14}]^{2-}$@SWNT^{2+} had formed, with the SWNT acting at the

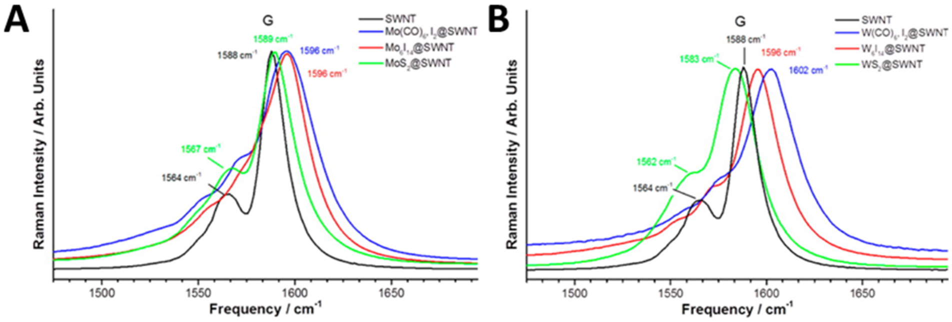

Figure 2.7. G-band of the raman spectra of (A) Mo species encapsulated within SWNTs and (B) W species encapsulated within SWNTs. Adapted from reference 36 with permission from The American Chemical Society.

cation of the cluster. The authors reacted these clusters under an atmosphere of H_2S to produce MS_2 (M = Mo, W) nanoribbons similar to the work by Wang *et al.* described above.

The observations of host-guest electronic transitions in SWNT nanotube systems means that the encapsulation of POMs could likely lead to varied levels of SWNT electronic tuning. The rich redox properties of POMs allow them to work as both oxidising agents in their native, fully oxidised states and reducing agents in their reduced states.[39] Additionally, they can be utilised as building blocks in supramolecular hierarchical assemblies.[40-42] As mentioned previously in Chapter 1, hybrid POM-CNT materials[43] have shown the ability to enhance charge separation in photocatalytic systems[44] and perform well as electrocatalysis[45] and charge storage media.[46]

The current literature suggests that CNTs may donate (as with AgX salts, iodine, metal iodides) or accept (as with metallocenes) electrons from species encapsulated within their interior dimensions. The ability of POMs to act as redox agents which can reversibly accept multiple electrons means that that these species are ideal for studying charge transfer interactions between SWNT-host and guest. Examples of POMs encapsulated with SWNTs in the literature mentioned above have so far not addressed the expected charge interactions between the two species, which based on the literature, and redox properties of POMs, would be expected. Although the high charge POMs possess may be perceived to render the encapsulation incompatible, the ability of both species to transfer electrons may mean that they are readily compatible. Additionally, the formation of such hybrid materials, where POMs are confined within the SWNT interior, may lead to a new class of hybrid materials with enhanced electroactive properties (as discussed in chapter 1) that could be applicable to charge storage.

2.2 Aims and Objectives

The aim of this study is to synthesise POM@SWNT materials and understand the interactions between the two species that lead to POM encapsulation, aiding in the understanding of the driving forces behind POM encapsulation and contributing to the overall knowledge of host-guest chemistry in carbon nanotubes.

This will be achieved through the following objectives:

1. Synthesise a variety of POMs with varied redox properties.
2. Encapsulate these POMs within SWNTs.
3. Utilise a complementary suite of methods to:
    i) Study the interactions between the two species during the encapsulation process;
    ii) Determine the local structure and study the interactions between the species once the POMs are confined within the SWNTs, and the electronic effects they impart on one another.

2.3 Results and Discussion

2.3.1 Synthesis and Characterisation of Keggin and Wells-Dawson Anions

The Keggin and Wells-Dawson anions were chosen for their stability, size, rich redox chemistry and ease of synthesis, to yield a chemically simple and well understood system. Both the Mo and W analogues of the Keggin and Wells-Dawson anion, $[PM_{12}O_{40}]^{3-}$ and $[P_2M_{18}O_{62}]^{6-}$ respectively (collectively referred to as Mo-POMs or W-POMs from herein), are well studied and are known to undergo multiple reversible reductions,[47] rendering them promising candidates in catalytic and energy storage applications. Both the Keggin and Wells-Dawson anions were synthesised using known literature methods.[48-51] Typically, a metal oxide precursor, Na_2MO_4 (M=Mo or W) or MoO_3, was dissolved in water and acidified in the presence of PO_4^{3-} anions. The low pH of the solution leads to the condensation of multiple oxometallate precursor anions, which in the presence of the templating PO_4^{3-} anion leads to the Keggin and Wells-Dawson heteropolyanions (**Fig. 2.8**). Both the Wells-Dawson anions, $[P_2M_{18}O_{62}]^{6-}$ (M = Mo, W), were obtained as the potassium salt, $K_6[P_2M_{18}O_{62}]$ whilst the Keggin anions were obtained as acids, $H_3[PM_{12}O_{40}]$ (M = Mo, W). Both ^{31}P NMR of the

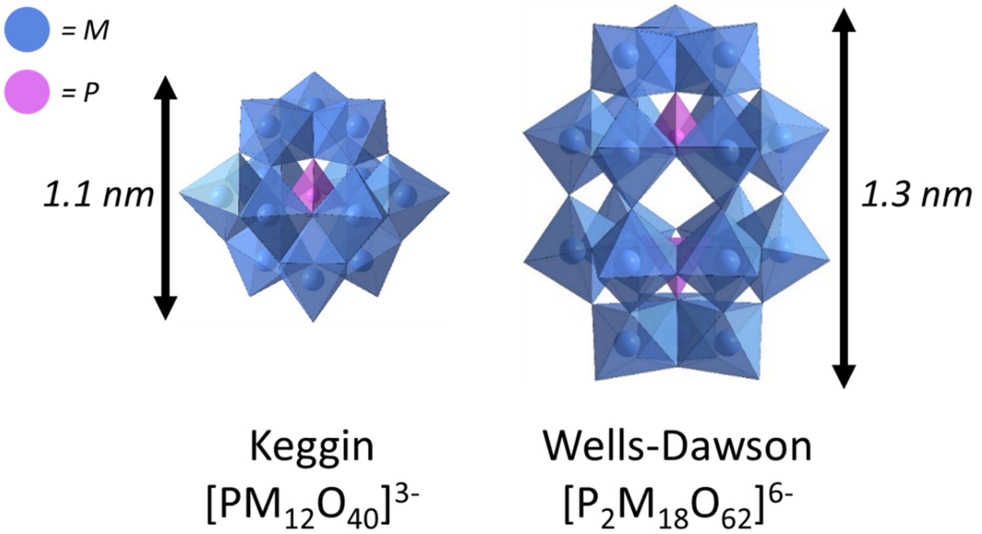

Figure 2.8. Structures of the Keggin and Wells-Dawson anions used in this study. Each of the polyhedra contain a metal centre, with an oxygen atom at every vertex. Templating anions are shown as pink polyhedra in the centres of the POMs.

compounds and mass spectrometry were used to identify the products (see experimental section).

Due to their rich redox chemistry, cyclic voltammetry is a useful electrochemical technique to study POMs. Cyclic voltammograms (CVs) of the synthesised POMs in 1M H_2SO_4 solutions (**Fig. 2.9**) demonstrated the ability of the anions to accept multiple electrons reversibly. The number of these reductions and the number of electrons the clusters were reduced by are summarised in **table 2.1**. These results were also used as a characterisation method, with the potentials for the processes in agreement with the literature.[47] All reductions proceeded with minimal changes to the overall cluster, with only processes exhibiting proton coupled electron transfer (PCET) resulting in protonation of the cluster. (This is discussed in more detail in chapter 4) The reduction potentials of the Mo-POMs were generally more electropositive than those of the W-

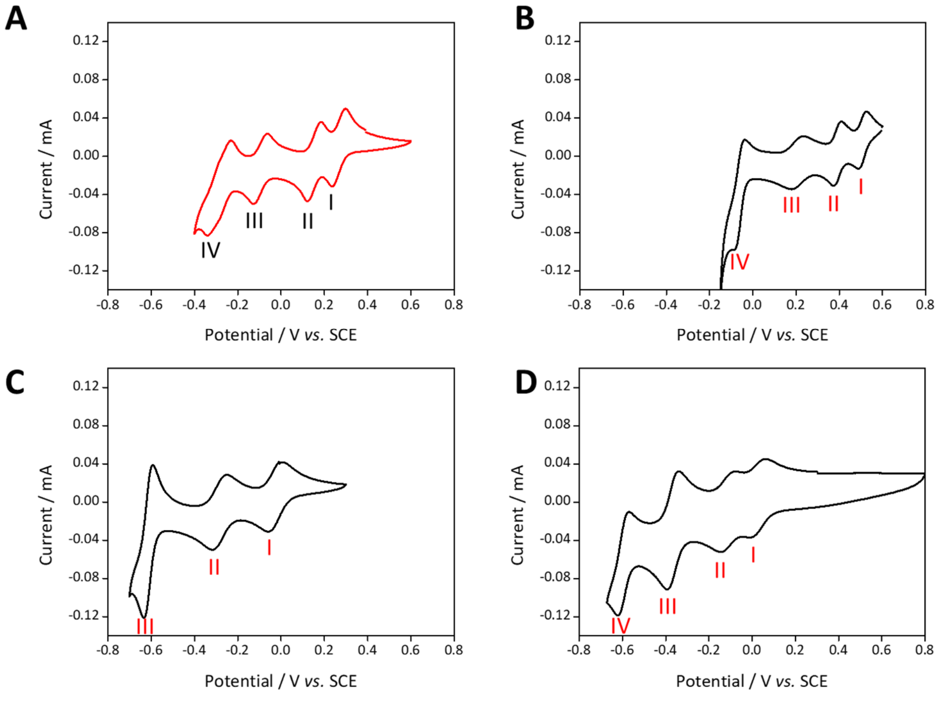

Figure 2.9. Cyclic voltammograms (CVs) of the Keggin and Wells-Dawson anions used in this study. (A) $H_3[PMo_{12}O_{40}]$ recorded in 0.1 M H_2SO_4 with 80% v/v MeCN. (B) $K_6[P_2Mo_{18}O_{62}]$ (C) $H_3[PW_{12}O_{40}]$ (D) $K_6[P_2W_{18}O_{62}]$ recorded in 1M H_2SO_4. All CVs recorded with a glassy carbon working electrode (GCE), saturated calomel reference electrode (SCE) and platinum counter electrode at a scan rate of 0.1 V s^{-1} with an analyte concentration of 10 mM. All reductions labelled I, II, III, IV.

POMs and they also exhibited more multi electron processes with PCET. Both Mo-POMs could reversibly accept ten electrons per anion, whereas the $[PW_{12}O_{40}]^{3-}$ and $[P_2W_{18}O_{62}]^{6-}$ anions could accept four and six electrons reversibly in acidic conditions respectively.[47]

Without the addition of an organic solvent it is difficult to obtain a clear CV of $[PMo_{12}O_{40}]^{3-}$ due to its hydrolysis in aqueous solutions upon reduction.[47, 52] For the $[PMo_{12}O_{40}]^{3-}$ anion, a large amount of acetonitrile (MeCN 80% v/v) was added to 0.1M H_2SO_4 to prevent the hydrolysis of the anion upon reduction, allowing a clear CV to be

Table 2.1. Table summarising the formal potentials of the POM reductions, taken from figure 2.9.

<table>
<tr><th colspan="3">$[PMo_{12}O_{40}]^{3-}$ *</th></tr>
<tr><td>Process</td><td>Potential / V</td><td>No. of e^{-} ^{a}</td></tr>
<tr><td>1^{b}</td><td>0.271</td><td>2</td></tr>
<tr><td>2^{b}</td><td>0.151</td><td>2</td></tr>
<tr><td>3^{b}</td><td>-0.094</td><td>2</td></tr>
<tr><td>4^{b}</td><td>-0.282</td><td>4</td></tr>
<tr><th colspan="3">$[P_2Mo_{18}O_{62}]^{6-}$</th></tr>
<tr><td>Process</td><td>Potential / V</td><td>No. of e^{-} ^{a}</td></tr>
<tr><td>1^{b}</td><td>0.430</td><td>2</td></tr>
<tr><td>2^{b}</td><td>0.330</td><td>2</td></tr>
<tr><td>3^{b}</td><td>0.130</td><td>2</td></tr>
<tr><td>4^{b}</td><td>-0.125</td><td>4</td></tr>
<tr><th colspan="3">$[PW_{12}O_{40}]^{3-}$</th></tr>
<tr><td>Process</td><td>Potential / V</td><td>No. of e^{-} ^{a}</td></tr>
<tr><td>1</td><td>-0.020</td><td>1</td></tr>
<tr><td>2</td><td>-0.275</td><td>1</td></tr>
<tr><td>3^{b}</td><td>-0.590</td><td>2</td></tr>
<tr><th colspan="3">$[P_2W_{18}O_{62}]^{6-}$</th></tr>
<tr><td>Process</td><td>Potential / V</td><td>No. of e^{-} ^{a}</td></tr>
<tr><td>1</td><td>-0.005</td><td>1</td></tr>
<tr><td>2</td><td>-0.135</td><td>1</td></tr>
<tr><td>3^{b}</td><td>-0.380</td><td>2</td></tr>
<tr><td>4^{b}</td><td>-0.610</td><td>2</td></tr>
</table>

*All potentials acquired with a 1M H_2SO_4 supporting electrolyte versus a saturated calomel electrode (SCE). *$[PMo_{12}O_{40}]^{-}$ potentials acquired in 0.1 M H_2SO_4 with 80% v/v MeCN. The first processes are approximate energies of the POM LUMOs. [a)] no. of electrons taken from reference 47. [b)] Process is proton coupled.*

obtained. The CVs could be used to estimate the energy of the lowest unoccupied molecular orbital (LUMO) for each anion, which corresponded to the first reduction in solution. Generally, reductions are much more energetically favourable in acidic solutions; the large concentrations of H^+ can stabilise negative charge accepted by redox species in solution. This, coupled with PCET processes exhibited by the POMs (chapter 4), meant that the potentials of the POM reductions were heavily pH dependent.[47] Additionally, the difference in dielectric constants of the solvents will have altered the reduction potentials further.[53] Therefore, due to the addition of large amounts of MeCN to an already diluted solution of H_2SO_4 (0.1 M), the pH of the electrolyte was significantly reduced, as well as having a lower dielectric constant. This likely artificially raised the potential of the first $[PMo_{12}O_{40}]^{3-}$ reduction,[53] meaning that the actual LUMO value of 0.271 V was not directly comparable to the other anions.

2.3.2 Polyoxovanadate-alkoxide

The high molecular weight of the Mo/W-POMs means that any {Mo/W-POM}@SWNT materials should exhibit relatively low specific energies (Wh Kg^{-1}). Future energy storage devices for the electrification of transport require much higher specific energies to reduce weight. Research in the area of battery materials therefore

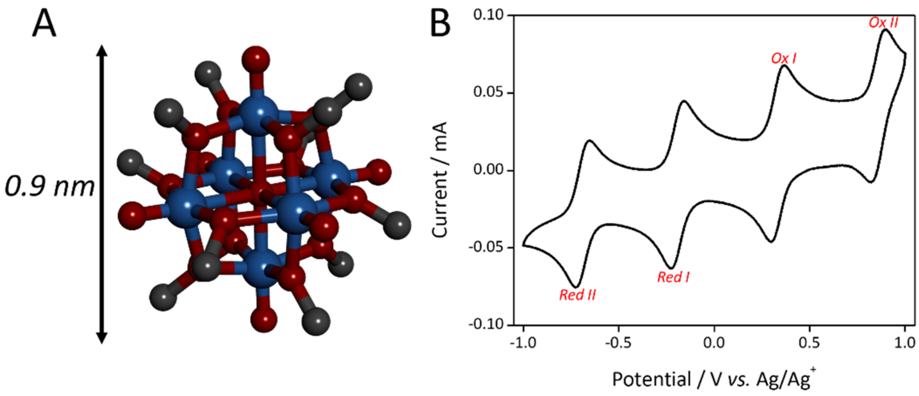

Figure 2.10. (A) Structure of $V_6O_7(OMe)_{12}$. Vanadium atoms in blue, oxygen atoms in red and carbon atoms in grey. Hydrogen omitted for clarity. (B) CV of $V_6O_7(OMe)_{12}$ with reductions and oxidations labelled. The formal potentials are summarised in table 2.2. CV recorded in MeCN with 0.1M $TBAPF_6$ supporting electrolyte, GCE working electrode, non-aqueous Ag/Ag^+ reference electrode and platinum counter electrode at a scan rate 0.1 V s^{-1}.

focusses on utilisation of the lighter chemical elements such as first row transition metals and sulfur,[54] making a vanadate POM with multi electron processes a more ideal candidate for energy storage.

$V_6O_7(OMe)_{12}$ herein referred to as $[V_6]$, a charge neutral vanadate POM, (**Fig. 2.10, A**) was selected for this study due to its close geometric match to the SWNTs, rich redox activity and charge neutrality (to encourage encapsulation within the hydrophobic SWNT channel). The cluster consists of six vanadate centres, four V(IV) centres and two V(V) centres, arranged as lindqvist core structure, with bridging oxygens also bonded to surface alkoxide ligands. $V_6O_7(OMe)_{12}$ is synthesised by heating $VO(OBu)_3$ in methanol for 24 hours in an autoclave followed by oxidation with I_2.[55] (sample synthesised by Dr. Ellen Matson's group, University of Rochester) Cyclic voltammetry of $[V_6]$ in MeCN (**Fig. 10, B**) showed four redox processes, two oxidations and two reductions, summarised in **table 2.2**, in good agreement with the literature.[56, 57] All four processes proceeded *via* the one electron oxidation or reduction resulting in a change in the charge of the overall molecule, with no structural changes.

Table 2.2. Summary of $[V_6]$ processes from figure 2.10. Red I is the LUMO of $[V_6]$. All processes are versus Ag/Ag^+.

$V_6O_7(OMe)_{12}$ Processes		
Process	Equation	Potential / V
Ox II	$[V^{IV}_3V^{V}_3O_7(OMe)_{12}]^{+} \rightleftharpoons [V^{IV}_2V^{V}_4O_7(OMe)_{12}]^{2+} + e^{-}$	0.864
Ox I	$[V^{IV}_4V^{V}_2O_7(OMe)_{12}]^{0} \rightleftharpoons [V^{IV}_3V^{V}_3O_7(OMe)_{12}]^{+} + e^{-}$	0.328
Red I	$[V^{IV}_4V^{V}_2O_7(OMe)_{12}]^{0} + e^{-} \rightleftharpoons [V^{IV}_5V^{V}O_7(OMe)_{12}]^{-}$	-0.193
Red II	$[V^{IV}_5V^{V}O_7(OMe)_{12}]^{-} + e^{-} \rightleftharpoons [V^{IV}_6O_7(OMe)_{12}]^{2-}$	-0.690

Red I is the LUMO of $[V_6]$. All processes are versus Ag/Ag^+. Equations taken from reference 56.

2.3.3 Keggin and Wells-Dawson Encapsulation

Arc-discharge SWNTs with an average internal diameter of 1.4 nm were used for the encapsulation due to the close match between the internal diameter and the van der Waals size of the POMs, thus maximising surface interactions between the host and guest. SWNTs received from the manufacturer had closed ends, meaning that guest molecules could not access the internal cavity of the SWNT as received. To remove these tips, the SWNTs were heated to their oxidation temperature in air, determined by thermal gravimetric analysis (TGA) of the sample. Upon heating, the carbon reacts with atmospheric oxygen and forms carbon dioxide. The strain on the C-C bonds at the tips means that these are the first to react during the annealing process, allowing the selective removal of the SWNT tips first.[58] The oxidation temperature was determined from TGA of the sample to be 600 °C (**Fig. 2.11**) and the SWNTs were heated for 30 minutes, typically giving a 50% mass loss. After heating, the mass of the SWNTs was recorded and the sample was promptly added to an aqueous solution of POM, during which the solution turned blue in colour, which was sonicated briefly and stirred for

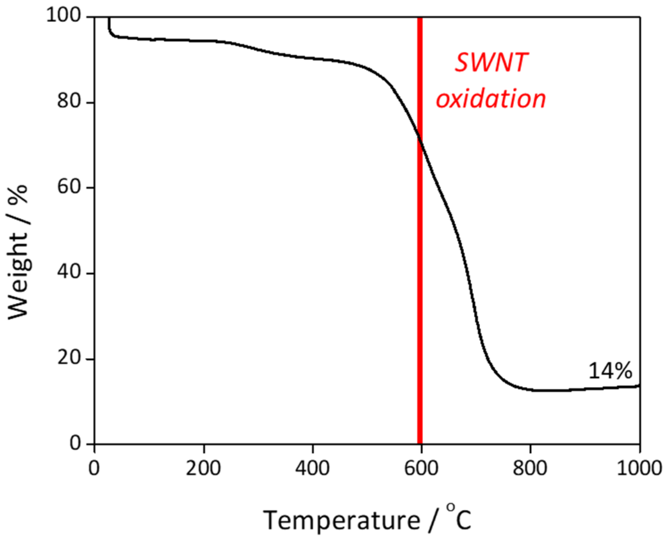

Figure 2.11. TGA of SWNTs as received from the manufacturer. Sample heated in air at a ramp rate of 10 °C per minute.

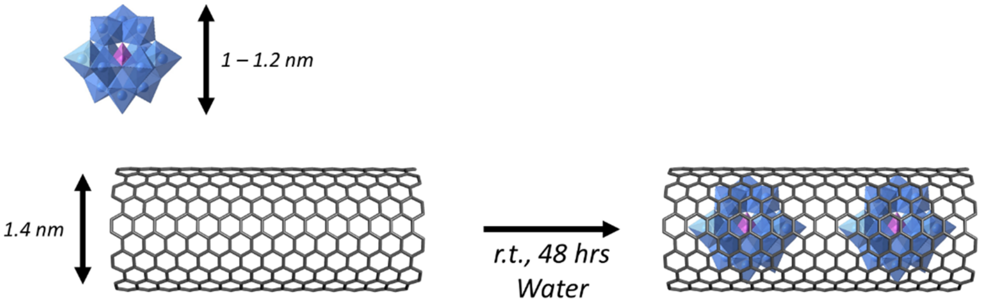

Figure 2.12. POM encapsulation scheme, with the $[PM_{12}O_{40}]^{3-}$ anion shown for clarity.

48 hours (**Fig. 2.12**). The black dispersion was then filtered and washed with a small amount of water on the filter membrane, yielding a black solid of {POM}@SWNT.

Transmission electron microscopy (TEM) is a highly informative technique for imaging and analysis of nanomaterials. As the e-beam can easily penetrate SWNTs, the size, location and morphology of molecules within the SWNTs can clearly be visualised. TEM of SWNTs showed two parallel contrasting lines, a two-dimensional projection of the sidewalls, with areas of low contrast between them (**Fig. 2.13, B**). TEM of the {POM}@SWNT materials indicated the presence of molecules within the interior walls of SWNTs for all {POM}@SWNT samples, visible as high contrast features within the walls of the SWNTs (**Fig. 2.13, C-F**). Virtually all SWNTs contained encapsulated material for all {POM}@SWNT materials suggesting a high degree of encapsulation. In the {Mo-POM}@SWNT materials, molecules ranged in size between 1-1.6 nm and 1-1.7 nm, for $\{PMo_{12}O_{40}\}$@SWNT and $\{P_2Mo_{18}O_{62}\}$@SWNT respectively, slightly larger than the molecular sizes of 1 nm and 1.2 nm reported.[59] The $\{P_2Mo_{18}O_{62}\}$@SWNT contained many micrometre-sized crystals on the surface of SWNT bundles, (**Fig. 2.13, A**) suggesting that during the encapsulation process the $K_6[P_2Mo_{18}O_{62}]$ compound easily crystallised, similar to previous work by Hu *et al.* describing the deposition of POM nanocrystals onto SWNT surfaces by sonication.[60] This was not present in any of

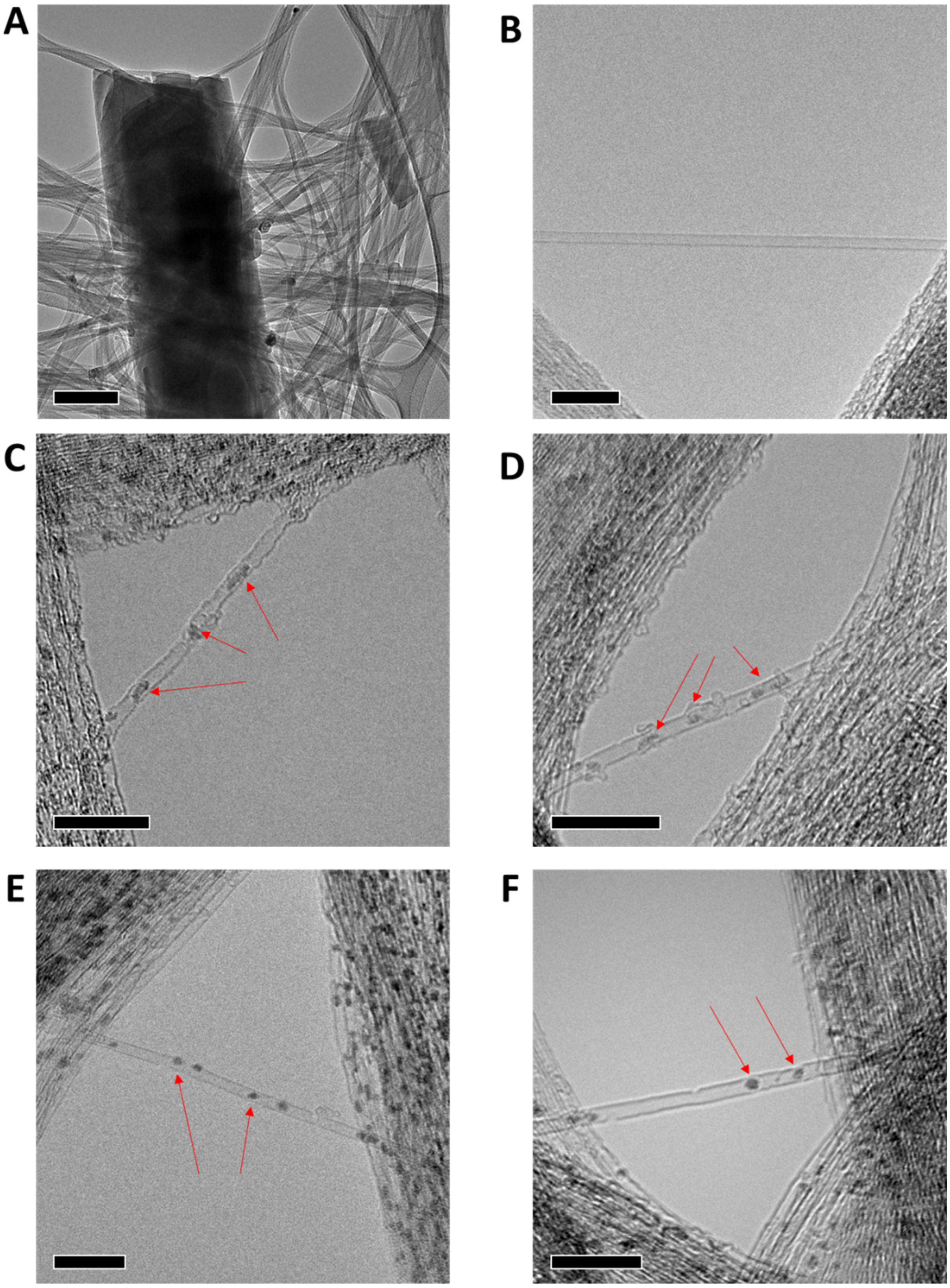

Figure 2.13. TEM images showing (A) the micrometre-sized crystals in the {$P_2Mo_{18}O_{62}$}@SWNT material, acquired with an accelerating voltage of 100 kV, scale bar 100 nm. (B) Image of an unfunctionalised SWNT, image acquired with an accelerating voltage of 80 kV, scale bar 10 nm. (C) {$PMo_{12}O_{40}$}@SWNT, acquired with an accelerating voltage of 200 kV, scale bar 10 nm. (D) {$P_2Mo_{18}O_{62}$}@SWNT, acquired with an accelerating voltage of 100 kV, scale bar 10 nm. (E) {$PW_{12}O_{40}$}@SWNT, acquired with an accelerating voltage of 80 kV, scale bar 10 nm. (F) {$P_2W_{18}O_{62}$}@SWNT, acquired with an accelerating voltage of 100 kV, scale bar 10 nm.

the other {POM}@SWNT materials, with all of these exhibiting high purity of POM molecules confined within the interior of SWNTs. In the {W-POM}@SWNT materials, molecules ranged in size between 1-1.8 nm and 1-2 nm, for {$PW_{12}O_{40}$}@SWNT and

$\{P_2W_{18}O_{62}\}$@SWNT respectively, slightly larger their reported sizes of 1 nm and 1.2 nm.[59] Aberration corrected TEM (AC-TEM) of the materials (**Fig. 2.14**) gave Mo – Mo interatomic distances between 0.2-0.3 nm and W – W interatomic distances between 0.2-0.3 nm, slightly shorter than the reported metal – metal interatomic spacings found in the POM molecules (approximately 0.3–0.6 nm).[61] The range in sizes of the POM molecules (which were also generally larger) in the {POM}@SWNT materials and slightly shorter metal interatomic distances suggested that the POM molecules were beam sensitive, undergoing chemical reactions caused by incident electrons from the electron beam. This is discussed in detail in chapter 3.

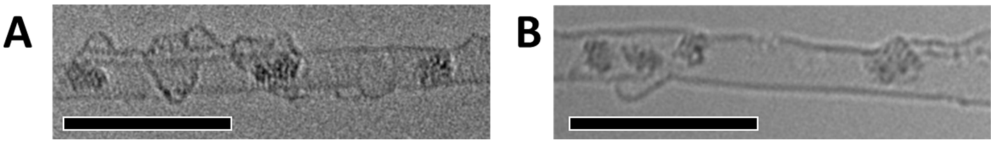

Figure 2.14. AC-TEM images of (A) $\{PMo_{12}O_{40}\}$@SWNT and (B) $\{P_2W_{18}O_{62}\}$@SWNT. Images were acquired with accelerating voltages of 60 and 80 kV respectively. Scale bars 5 nm.

Energy dispersive X-ray spectroscopy (EDX) utilises the beam of electrons in TEM to excite core electrons, which in turn leads to the emission of X-rays distinctive to each chemical element. EDX analysis of the {Mo-POM}@SWNT materials gave elemental ratios of P, Mo and O for the $\{PMo_{12}O_{40}\}$@SWNT material in good agreement with the expected values for the $[PMo_{12}O_{40}]^{3-}$ anion. For $\{P_2Mo_{18}O_{62}\}$@SWNT, the ratio of K : P : Mo : O was in good agreement with the expected ratio (**Fig. 2.15, A & B**). EDX elemental analysis of the {W-POM}@SWNT materials gave elemental ratios of P, W and O (**Fig. 2.15, C & D**) in good agreement with the expected ratios for the $[PW_{12}O_{40}]^{3-}$ and $[P_2W_{18}O_{62}]^{6-}$ anions respectively. These ratios are summarised in **table 2.3**. Higher oxygen content was likely due to oxygen containing functional groups inherently present within the SWNT structure. Interestingly, the potassium signal was absent in the $\{P_2W_{18}O_{62}\}$@SWNT material. A potassium signal was observed in the

{$P_2Mo_{18}O_{62}$}@SWNT sample. The H^+ cation for both the Keggin anions could not be observed, due to the lack of core electrons.

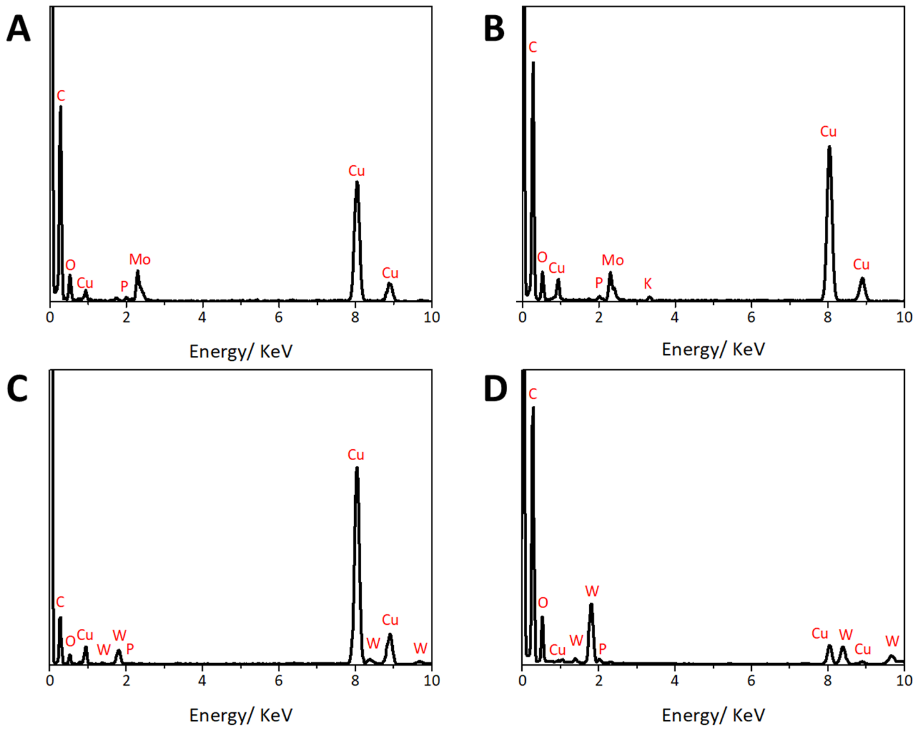

Figure 2.15. EDX spectra of the {POM}@SWNT materials. (A) {$PMo_{12}O_{40}$}@SWNT (B) {$P_2Mo_{18}O_{62}$}@SWNT (C) {$PW_{12}O_{40}$}@SWNT and (D) {$P_2W_{18}O_{62}$}@SWNT.

Table 2.3. Elemental ratios of the {POM}@SWNT materials from EDX.

Mo-POM		
Sample	Experimental Ratio K : P : Mo : O	Expected Ratio K : P : Mo : O
{$PMo_{12}O_{40}$}@SWNT	- : 0.02 : 0.22 : 0.74	0.02 : 0.23 : 0.75
{$P_2Mo_{18}O_{62}$}@SWNT	0.08 : 0.02 : 0.18 : 0.72	0.07 : 0.02 : 0.20 : 0.70
W-POM		
Sample	Experimental Ratio P : W : O	Expected Ratio P : W : O
{$PW_{12}O_{40}$}@SWNT	0.02 : 0.18 : 0.79	0.02 : 0.23 : 0.75
{$P_2W_{18}O_{62}$}@SWNT	0.02 : 0.19 : 0.80	0.02 : 0.22 : 0.76

Thermal gravimetric analysis (TGA) of the {POM}@SWNT samples was used to quantify the loading of encapsulated POM. For the W-POM, the lack of mass loss up to 1000 °C meant that wt % loading could easily be obtained.[62] For the {W-POM}@SWNT materials this was found to be around 16% and 11% for {$PW_{12}O_{40}$}@SWNT and {$P_2W_{18}O_{62}$}@SWNT respectively, (**Fig. 2.16, B**) indicating a high level of encapsulation within the SWNTs.[17, 63] Small shifts in the oxidation temperature of the SWNTs were also observed, suggesting host-guest interactions. For the {Mo-POM}@SWNT materials quantifying the loading of the POM proved more difficult, due to mass loss associated with the Mo-POM at high temperature from sublimation, a common motif in molybdenum metal oxides.[64] Due to the mass loss of the POM, TGA was not a reliable way to quantify the POM loading for the {Mo-POM}@SWNT materials. TGA of the {Mo-POM}@SWNT materials showed a large shift in the oxidation temperature of the carbon, approximately 200 °C (**Fig. 2.16, A**), consistent with previous observations of MoO_x nanoparticles confined within GNFs.[63] This large shift was indicative of a strong interaction between the encapsulated POM-guest and SWNT-host, and consistent with their more electropositive reduction potentials, rendering them more powerful oxidising agents.

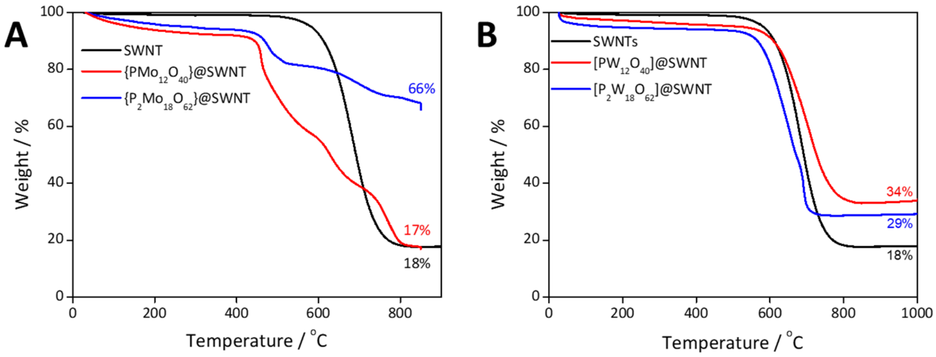

Figure 2.16. (A) TGA data for {Mo-POM}@SWNT materials (B) TGA data for {W-POM}@SWNT materials. Samples heated in air at a ramp rate of 10 °C per minute.

The high purity of the {POM}@SWNT materials, where most POMs were confined within SWNTs rather than deposited on their surfaces, apart from {$P_2Mo_{18}O_{62}$}@SWNT, was due to the close geometric match between the internal diameter of the SWNTs and the size of the POMs, maximising surface interactions between the two species. This is similar to results with fullerene encapsulation within SWNTs discussed above. The relatively small surface for interaction with the SWNT exterior leads to energetically favourable uptake of the species within the SWNTs. However, to further purify the materials, they were redispersed in deionised water with brief sonication, stirred for 2 hours and filtered.

It is known that encapsulation of a guest-molecular species within host-SWNTs can stabilise the guest in harsh conditions.[65] As mentioned previously, POMs form in acidic solutions but when exposed to basic solutions, the reverse process occurs, which is often utilised to remove MO units for POM functionalisation.[66] To further the attempts at purification, the {$P_2W_{18}O_{62}$}@SWNT material was redispersed in 1M NaOH, sonicated for approximately 10 minutes and filtered. $[P_2W_{18}O_{62}]^{6-}$ molecules encapsulated within the SWNTs persisted (**Fig. 2.17**) and AC-TEM analysis showed W – W interatomic spacings, 0.2 – 0.3 nm, consistent with the sample before redispersion

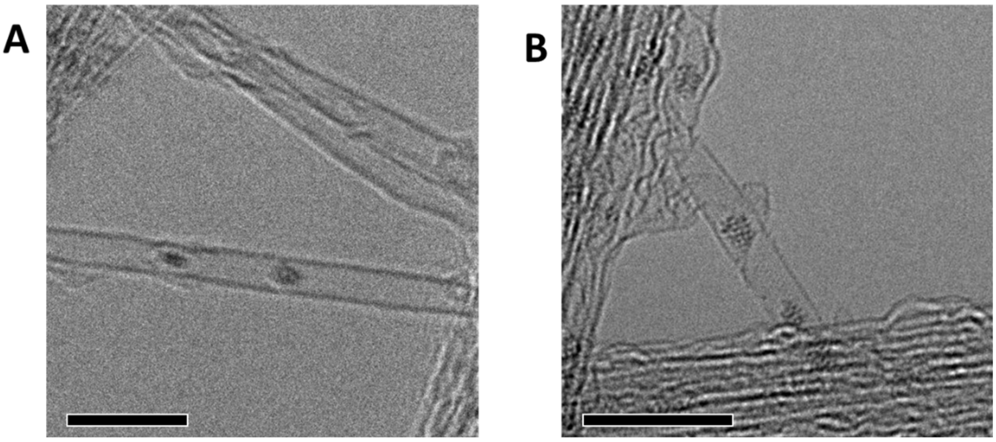

Figure 2.17. (A) TEM and (B) AC-TEM images of {$P_2W_{18}O_{62}$}@SWNT material after washing with 1M NaOH. (A) acquired with an accelerating voltage of 100 kV and (B) acquired with an accelerating voltage of 80 kV. Scale bars 5 nm.

in NaOH. Further to this, the CVs of the material provided further evidence for the successful protection of the encapsulated POM molecules in 1M NaOH. (Chapter 4)

For the $\{P_2Mo_{18}O_{62}\}$@SWNT material, dispersion within NaOH was not a successful purification strategy. The large crystals persisted within the sample after sonication of the sample and filtration (**Fig. 2.18**). Centrifugation of the material in basic solution also yielded poor results. This is likely due to the large size of the crystals within the sample, ensuring that the crystals remained in contact with the bundles of SWNT, rather than dissolving in solution.

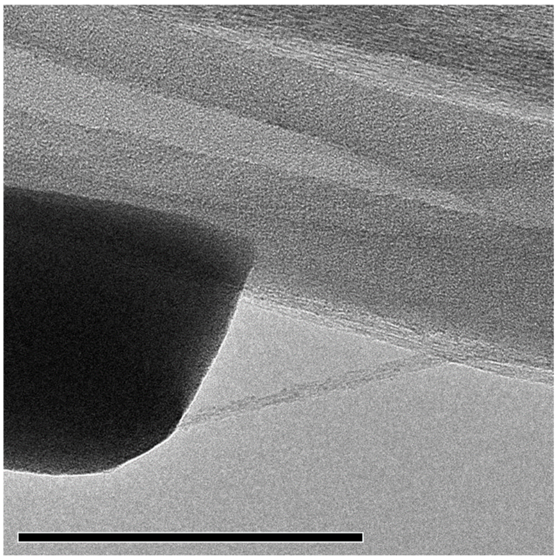

Figure 2.18. TEM image of $\{P_2Mo_{18}O_{62}\}$@SWNT after washing with 1M NaOH. Image acquired with an accelerating voltage of 80 kV. Scale bar 100 nm.

2.3.4 Polyoxovanadate Encapsulation

The SWNTs used in this study were the same as the ones used in the Mo/W-POM study, with an average diameter of 1.4 nm. To encapsulate the POM a similar methodology was employed to the one used in the encapsulation of the Mo/W-POM. Freshly annealed SWNTs were added to a solution of $[V_6]$ dissolved in MeCN. The resultant solution was sonicated and then stirred for 48 hours before being filtered through a PTFE membrane and washed with small amounts of MeCN on the filter membrane, to give a black solid of $\{V_6\}$@SWNT and a green filtrate.

TEM confirmed that the $[V_6]$ had become encapsulated within the SWNTs, with multiple SWNTs showing contrasting features within sidewalls (**Fig. 2.19, A**). The low atomic number of vanadium (Z = 23) led to lower contrast of the $[V_6]$ POM within the SWNTs compared to the Mo/W-POMs, meaning that the overall contrast of the $[V_6]$ molecules was less defined. The encapsulated material appeared to be non-uniform and many of the particles appeared to be more continuous in nature, with average lengths of 2 nm, suggesting the sample was highly beam sensitive. Overall however, there did not appear to be as many SWNTs with encapsulated $[V_6]$ molecules. As well as the presence of material within the SWNT sidewalls, the sample also contained large surface particles, similar to those in the $\{P_2Mo_{18}O_{62}\}$@SWNT material (**Fig. 2.19, B**). The high contrast and EDX analysis (**Fig. 2.20**) indicated that these large nanoparticles were composed of vanadium oxide, suggesting that during the 48 hours of stirring with SWNTs there was a degree of decomposition of the $[V_6]$.

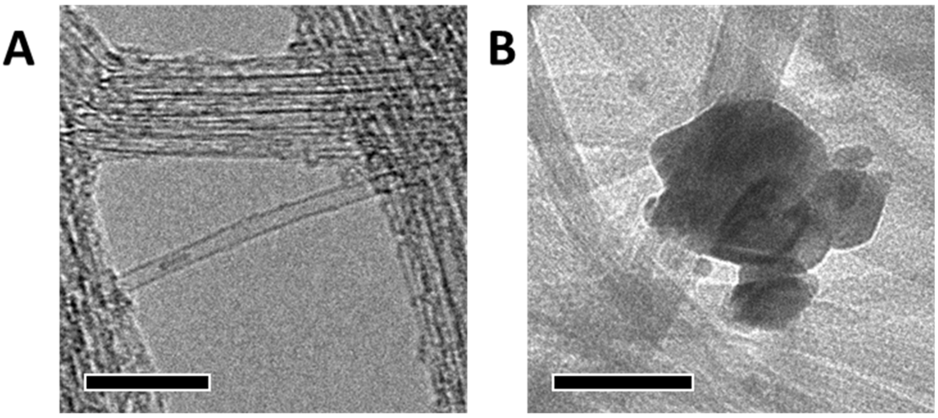

Figure 1.19. (A) TEM image of $\{V_6\}$@SWNT showing encapsulated $[V_6]$, scale bar 5 nm. (B) TEM image of a large VO_x nanoparticle in the $\{V_6\}$@SWNT material, scale bar 50 nm. Images acquired at 80 kV.

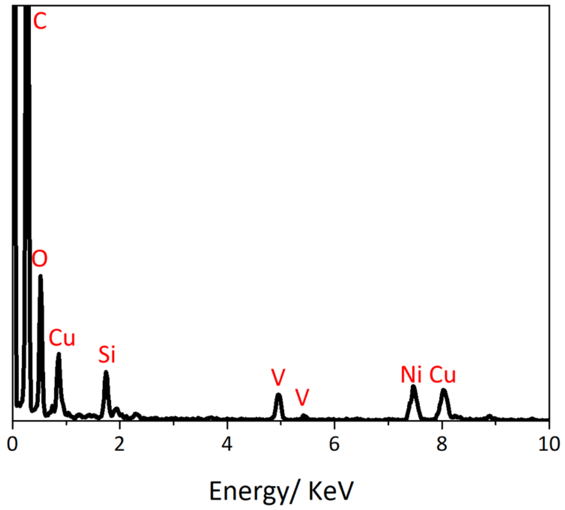

Figure 2.20. EDX spectra of the {V₆}@SWNT material. Ni is from the residual metallic catalyst used in SWNT synthesis.

TGA of the [V_6] molecule gave a single weight loss below 300 °C, (**Fig. 2.21**) likely corresponding to the decomposition of the organic methoxide capping ligands, with a residual weight of approximately 47% after ramping to 1000 °C. TGA of the {V_6}@SWNT material also presented multiple weight losses, with a large shift in the oxidation temperature of the SWNTs also observed. The weight loading was found to be 8%. Such a high loading was consistent with the large amount of amorphous surface features present within the material.

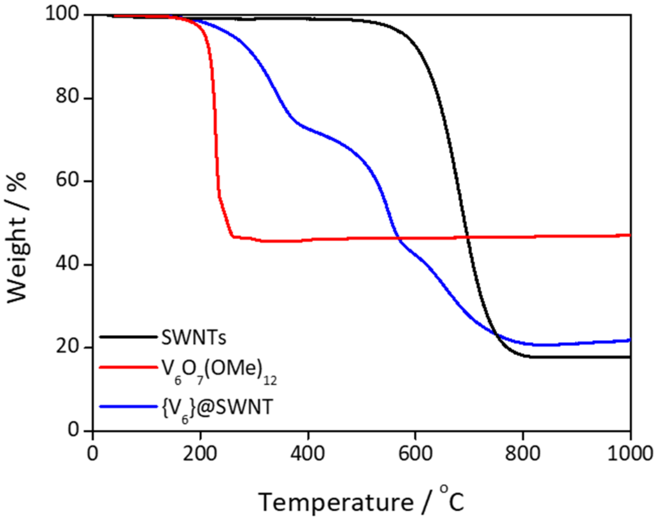

Figure 2.21. TGA of [V_6], {V_6}@SWNT and SWNTs. Samples heated in air to 1000 °C at a ramp rate of 10 °C per minute.

2.3.5 Electronic Analysis of {Mo/W-POM}@SWNT Materials

The encapsulation of such highly charged and hydrophilic species within the relatively hydrophobic channels of the SWNTs cannot be explained by only the close geometric fit between the SWNTs and POM molecules. As mentioned previously, POMs have rich redox properties, rendering them both oxidising and reducing agents.[39] Upon the addition of the recently opened SWNTs to the POM solution, the solution instantly changed colour (**Fig. 2.22**). In the case of W-POMs, the solutions changed from colourless to blue at the solid-liquid interface and in the case of the Mo-POMs the solution changed from dark yellow to green, indicative of the formation of a blue species within a dark yellow solution. These colour changes were due to the intervalence charge transfer (IVCT) that occurs upon POM reduction. The nature of the blue colour formed during the encapsulation of $[P_2W_{18}O_{62}]^{6-}$ was probed using UV-vis spectroscopy, (**Fig. 2.23**) which found that the IVCT band that developed upon addition of the SWNTs was centred around 820 nm, in good agreement with the literature.[67]

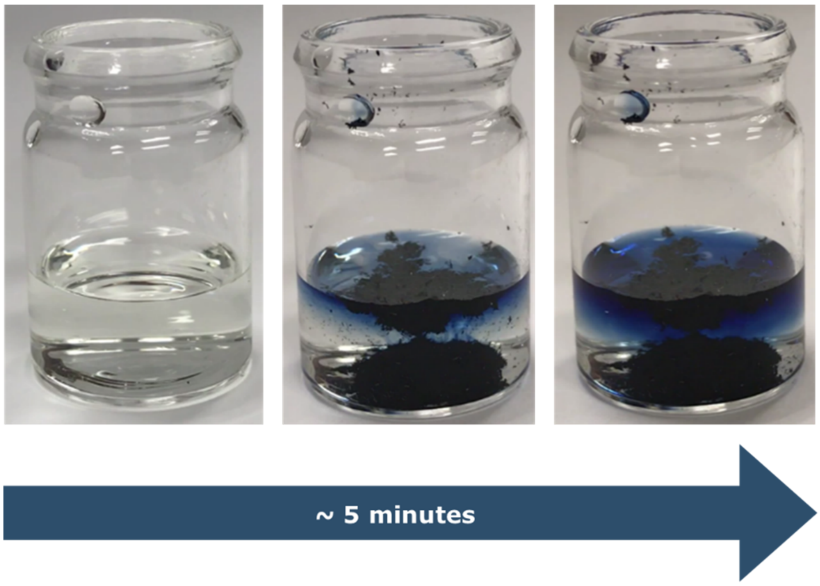

Figure 2.22. Images showing the colour change observed when recently opened SWNTs were added to an aqueous solution of $K_6[P_2W_{18}O_{62}]$.

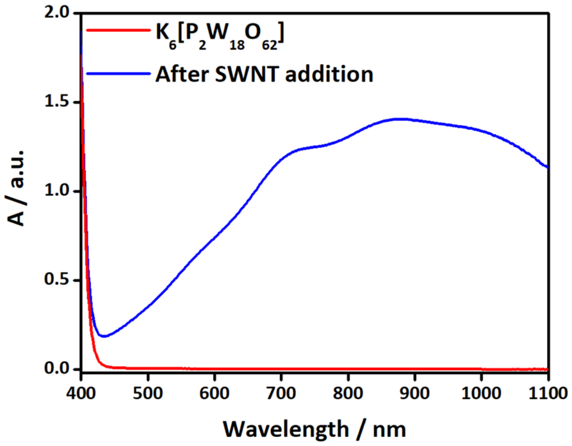

Figure 2.23. UV-vis spectra of the aqueous solution of $K_6[P_2W_{18}O_{62}]$ before (red) and after SWNT addition (blue).

The IVCT band also contained a slight shoulder, centred at around 710 nm, indicating the presence of a two electron reduced species in solution as well.[67, 68]

The reduction of the POMs in solution likely proceeded with the oxidation of the SWNTs, leading to positively charged SWNTs in a solution of negatively charged POMs. This transfer in electron density between the host and guest gave rise to strong electrostatic attraction between the two, driving encapsulation through enthalpic gain. The close match between the van der Waals dimension of the POMs and the internal diameter of the SWNT also likely aided the enthalpic gain through beneficial dispersion interactions. The geometric match also likely led to POM desolvation upon encapsulation, further entropically driving the encapsulation *via* the liberation of solvent molecules.

To ensure the spontaneous electron transfer between the SWNT and POM molecules was energetically viable, CVs of the POMs and SWNTs were used to obtain the position of the LUMO of the POMs and the Fermi level (akin to the HOMO) of the SWNTs. The CV of empty SWNTs showed that low currents flowed at voltages corresponding to the energy of the SWNT band gap, and higher currents flowed at voltages corresponding to the density of states (DoS) of the SWNTs[69] (**Fig. 2.24, A**). These can correspond to oxidation (occupied states) or reduction (unoccupied states), with small peaks observed at Van Hove singularities. These CVs were used to identify the Fermi potential of the SWNTs, the highest energy level of the valence band, which was found to be approximately –0.2 V vs. SCE in 1M H_2SO_4. The first reduction of the POMs in solution were used to estimate the LUMO energy. Since the CVs were recorded under the same conditions (apart from $[PMo_{12}O_{40}]^{3-}$) the energies given were directly comparable. It was found that the Fermi level of the SWNTs was higher than the LUMO of all four POMs, meaning that spontaneous electron transfer from the SWNT to the

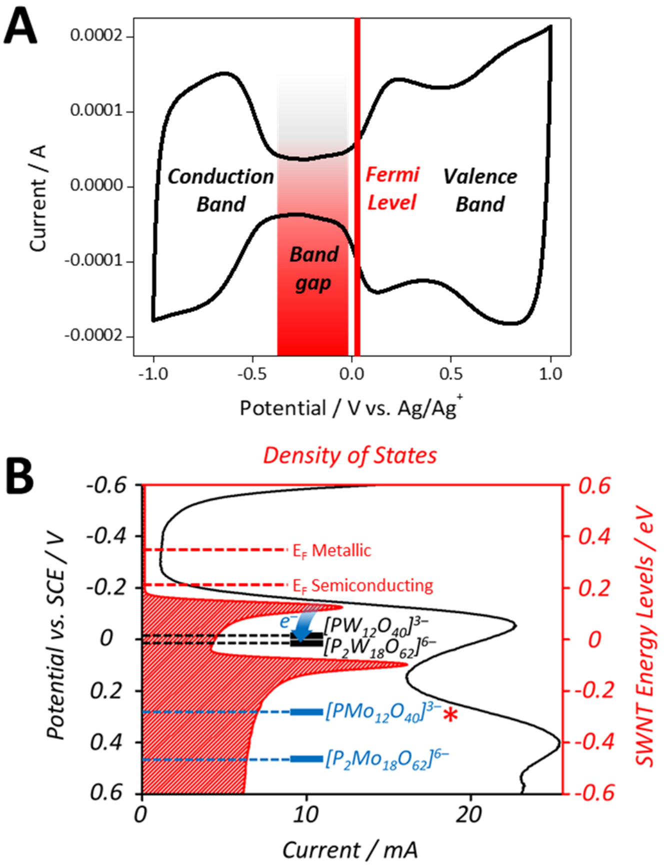

Figure 2.24. (A) An example of a CV of SWNTs, recorded with SWNTs deposited from a dimethylformamide (DMF) ink onto a glassy carbon electrode (GCE), in MeCN with a 0.1 M $TBAPF_6$ supporting electrolyte, Ag/Ag$^+$ reference electrode and platinum counter electrode at a scan rate of 0.1 V s^{-1}. The valence band, conduction band, band gap and Fermi level of the SWNTs are labelled. (B) Calculated electronic states of a (17, 0) carbon nanotube (red plot), a linear sweep voltammogram (LSV) of open, empty SWNTs recorded in 1M H_2SO_4 with a SCE reference electrode (black line) and LUMOs of Mo-POMs and W-POMs (labelled) estimated from the CVs of the POMs obtained under the same conditions. $[PMo_{12}O_{40}]^{3-}$ data acquired under different experimental conditions.

POMs was energetically favourable[28] (**Fig. 2.24, B**). When comparing the UV-vis of the $K_6[P_2W_{18}O_{62}]$ solution after the addition of the SWNTs, it was apparent that there was the presence of $2e^-$ reduced species present in the solution, indicating that the second reduction of the $[P_2W_{18}O_{62}]^{6-}$ anion was also possible upon SWNT addition. This reduction could also proceed spontaneously due to the second reduction also being below the Fermi level of the SWNTs. This suggests that the overall oxidation of the SWNTs may have also been influenced by the number of accessible reductions for each POM, as well as the position of the LUMO of the anion relative to the SWNT Fermi level.

To probe the electronic state of the SWNTs following the encapsulation of the POMs, Raman spectroscopy was utilised.[70] The Raman spectrum of SWNTs has multiple bands that can be used as diagnostic tools to investigate the nature of host-guest interactions. Particularly useful bands for probing SWNT host-guest materials are the radial breathing mode (RBM) and the G-band (graphitic band). The RBM can be thought of as a collective expansion and contraction of the SWNT sidewalls, (**Fig. 2.25, A**) which can shift due to encapsulated species mechanically inhibiting the contraction of the SWNT side walls.[71] The G-band can be thought of as the in-plane scissoring vibration of the graphitic lattice that makes up the SWNT sidewalls (**Fig. 2.25, B**). Oxidation of the SWNT leads to this vibration becoming blue shifted.[27, 35, 70] POM@SWNT samples were irradiated with an excitation wavelength of 660 nm (1.88 eV) which is in resonance with both metallic and semiconducting transitions between Van Hove singularities of SWNTs with an average diameter of 1.4 nm.[72]

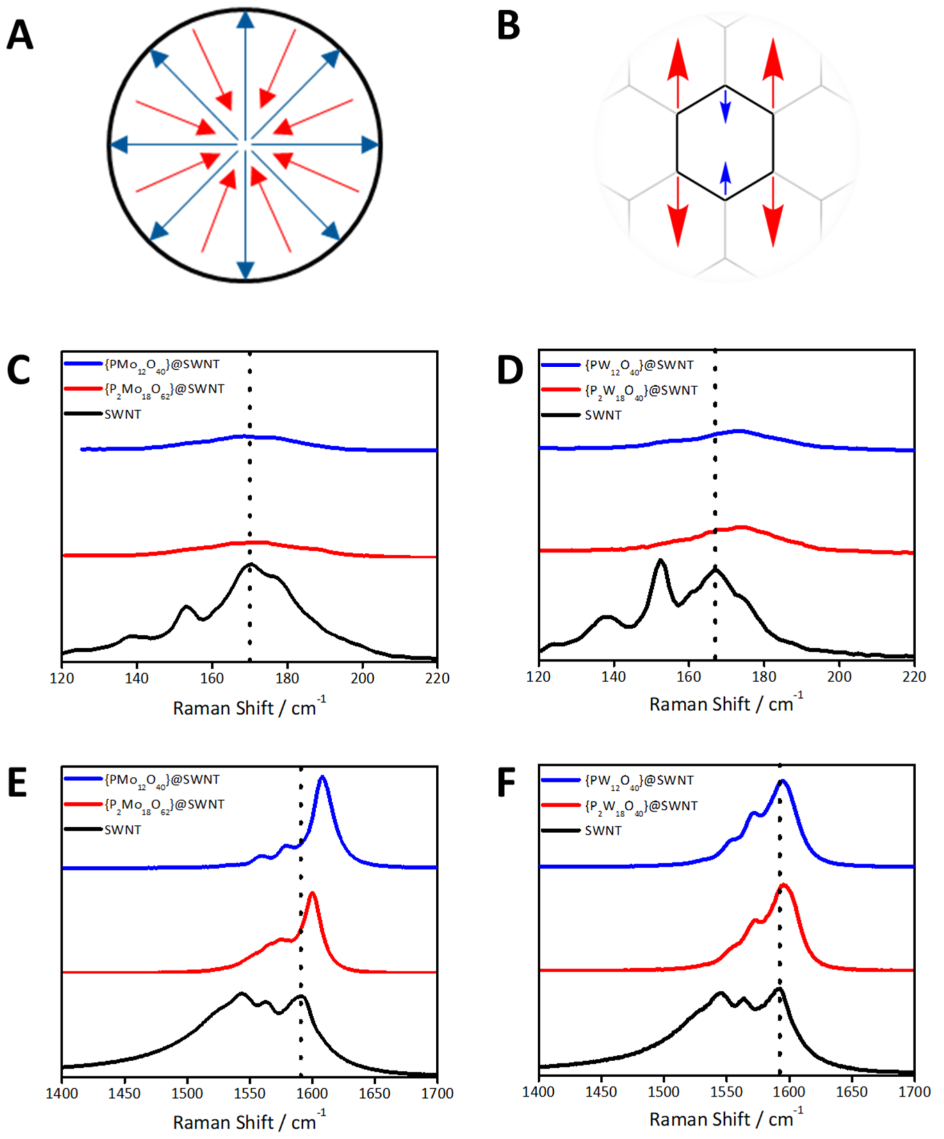

Figure 2.25. (A) Cross section of a SWNT showing the radial breathing mode (RBM). (B) Section of a graphitic lattice showing the G-band mode. (C) RBM bands of the Mo-POM samples, showing a clear suppression of the band as well as slight blue shifts. (D) RBM bands for W-POM samples, showing a clear suppression of the band as well as clear blue shifts. (E) G-band modes of the Mo-POM samples showing large blue shifts of the mode, as well as a change in the shape of the G-band. (F) G-band modes of the W-POM samples showing blue shifts, as well a change in shape of the mode. All spectra acquired with a 660 nm laser and normalised to the height of the G-band.

The RBM of the POM@SWNT materials was largely shifted relative to opened, unfunctionalised SWNTs indicating that POM molecules were encapsulated within the interior of the SWNTs (**Fig. 2.25, C & D**). For the W based POMs, $\{PW_{12}O_{40}\}$@SWNT and $\{P_2W_{18}O_{62}\}$@SWNT, the RBM appeared to blue shift by 4 cm^{-1} and 5.5 cm^{-1} (spectral resolution was 1.2 cm^{-1}) respectively, indicating that the larger size of the of the $[P_2W_{18}O_{62}]^{6-}$ anion provided a stronger interaction between the POM guests and SWNT host due to a closer geometric match. For the Mo based POMs, {$PMo_{12}O_{40}$}@SWNT and {$P_2Mo_{18}O_{62}$}@SWNT, only the RBM of the {$P_2Mo_{18}O_{62}$}@SWNT sample was blue shifted by 2.5 cm^{-1} relative to unfunctionalised SWNTs. This suggests that upon encapsulation the Mo-POMs did not interact as strongly with the interior of the SWNT.

All POM@SWNT samples showed a clear blue shift in the G-band (**Fig. 2.25, E & F**) relative to opened, unfunctionalised SWNTs treated with the same heating process. The blue shift confirmed SWNT oxidation, providing further evidence for electron transfer from the SWNTs to the POMs during encapsulation. G-band shifts were much larger for the Mo-POMs, indicating greater oxidation of the SWNTs (**table 2.4**). This was in good agreement with the Mo-POM LUMOs being lower in energy relative to the SWNT Fermi level than that of the W-POMs, rendering them stronger oxidising agents. The shift in the G-band of the POM@SWNT materials was correlated with the number of holes per carbon atom based on electrochemistry measurements which reported a value of 320 cm^{-1} per unit of charge per carbon atom as a quantitative measure of charge transfer.[73] Naturally, a greater number of holes/C-atom were present in the materials with a greater G-band shift, indicating a greater degree of SWNT oxidation. These results are summarised in **table 2.5**. Overall, the oxidation of the SWNTs can be corroborated with the LUMO of the encapsulated POM, for both

Table 2.4. Table summarising the positions and Raman shifts of the RBM and G-band modes for the {POM}@SWNT samples.

Mo-POM				
Sample	RBM / cm^{-1}	Rel. Shift / cm^{-1}	G-band / cm^{-1}	Rel. Shift / cm^{-1}
SWNT	170	–	1590	–
{$PMo_{12}O_{40}$}@SWNT	170	0	1608	18
{$P_2Mo_{18}O_{62}$}@SWNT	172.5	2.5	1600	10
W-POM				
Sample	RBM / cm^{-1}	Rel. Shift / cm^{-1}	G-band / cm^{-1}	Rel. Shift / cm^{-1}
SWNT	168	–	1590	–
{$PW_{12}O_{40}$}@SWNT	174	6	1595.5	5.5
{$P_2W_{18}O_{62}$}@SWNT	175.5	7.5	1596.5	6.5

Table 2.5. Table summarising the holes per carbon atom in the {POM}@SWNT samples.

Mo-POM		W-POM	
Sample	Holes / C-atom	Sample	Holes / C-atom
$\{PMo_{12}O_{40}\}$@SWNT	0.056	$\{PW_{12}O_{40}\}$@SWNT	0.017
$\{P_2Mo_{18}O_{62}\}$@SWNT	0.031	$\{P_2W_{18}O_{62}\}$@SWNT	0.020

W-POMs and Mo-POMs, where the lower the LUMO energy, the greater the oxidation of the SWNTs (**Fig. 2.26**). However, the number of holes per carbon atom of $\{PMo_{12}O_{40}\}$@SWNT is much greater than expected, likely due to the different conditions required to obtain a CV of the $[PMo_{12}O_{40}]^{3-}$ anion, leading to an estimated LUMO energy higher than the true relative energy.

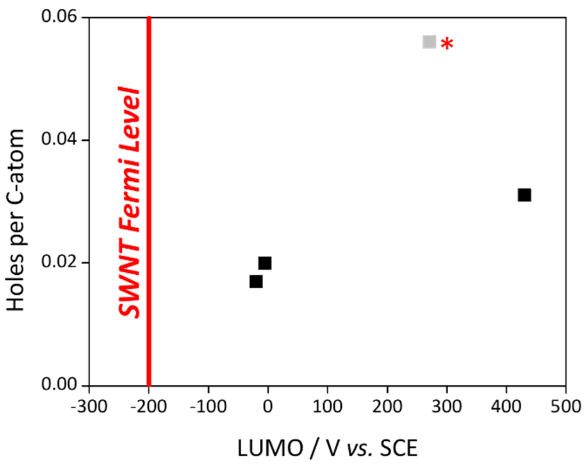

Figure 2.26. A plot of POM LUMOs versus the level of oxidation in their corresponding {POM}@SWNT material. The plot for $[PMo_{12}O_{40}]^{3-}$ is starred due to the collection of this data in different experimental conditions. The plot shows a clear relationship between the LUMO of the encapsulated POM and the oxidation level of the SWNT.

As mentioned previously, based on UV-vis analysis, it was likely that multiple reductions of the $[P_2W_{18}O_{62}]^{6-}$ were accessed upon the charge transfer during encapsulation. This suggests that the number of reductions and amount of charge passed per reduction may have influenced the overall level of SWNT oxidation as well. The number of accessible reductions to the SWNTs and total equivalents of charge that each POM could be reduced by is summarised in **table 2.6**, based on the position of the Fermi level in the semiconducting subset of SWNTs, visualised by CV as

Table 2.6. Table summarising the total number of accessible reductions to SWNTs for each POM, as well as the total equivalents of electrons passed for these reductions.

Mo-POM			W-POM		
POM	No. of accessible reductions	Total no. of e^{-}	POM	No. of accessible reductions	Total no. of e^{-}
$[PMo_{12}O_{40}]^{3-}$*	3	6	$[PW_{12}O_{40}]^{3-}$	1	1
$[P_2Mo_{18}O_{62}]^{6-}$	4	10	$[P_2W_{18}O_{62}]^{6-}$	2	2

**[PMo*$_{12}$*O*$_{40}$*]*$^{3-}$ *acquired under different experimental conditions.*

described above. Generally, the reductions of the Mo-POMs were more electropositive, leading to a greater number of accessible reduction processes. For the W-POMs only the first and first two processes were accessible for $[PW_{12}O_{40}]^{3-}$ and $[P_2W_{18}O_{40}]^{6-}$ respectively, suggesting the very small increase in the LUMO energy of $[PW_{12}O_{40}]^{3-}$ was not the only contributing factor in the lower level of SWNT oxidation.

As well as a blue shift in the G-band of the {POM}@SWNT materials, the shape of the G-band mode changed relative to unfunctionalised SWNTs (**Fig. 2.25, E & F**). The G-band profile of the {POM}@SWNT materials closely resembled the G-band profile of pure semi-conducting SWNTs. This was likely caused by charge donation from the occupied DoS of the metallic subset of SWNTs to the POMs during the encapsulation process, altering the resonance conditions of the sample and taking them out of resonance with the 660 nm laser.[27] This is in good agreement with the position of the Fermi level of the metallic SWNTs shown previously.

The SWNTs used in this study as-received from the manufacturer contained Ni/Y alloy nanoparticles, impurities left over from the arc-discharge process that was used to produce them. The amount of these impurities can be quantified using TGA, using the residual weight after reaching 1000 °C in air. This was found to be approximately 14 wt% for the SWNTs used in this study. Whilst these nanoparticles are generally encased in carbon shells from the arc-discharge process, rendering them chemically

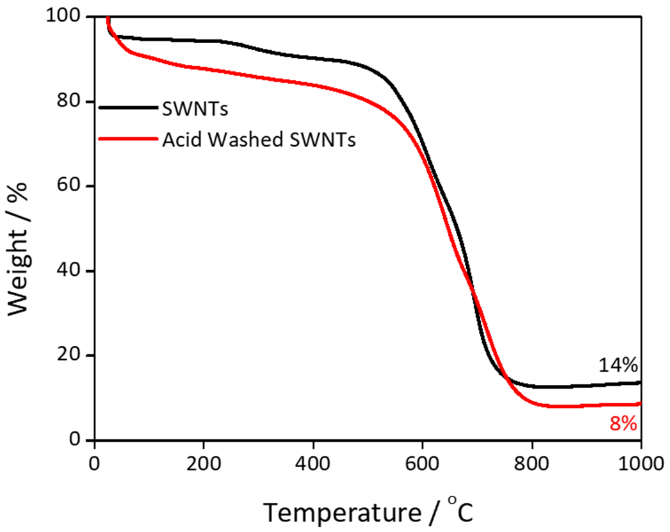

Figure 2.27. TGA of unopened SWNTs and acid washed SWNTs. Samples heated in air at a ramp rate of 10 °C per minute.

inaccessible, such a large loading of metallic nanoparticles could have also feasibly led to the observed POM reduction upon SWNT addition to the solution.

To test this hypothesis, SWNTs were refluxed in 3M HNO_3 to dissolve all chemically accessible Ni/Y nanoparticles.[74] After treatment the residual weight after heating to 1000 °C in air was reduced to 8 wt% (**Fig. 2.27**). Any Ni or Y not removed by the HNO_3 was likely not chemically accessible, protected by a stable carbon shell. A by-product of the acid washing step was the formation of oxygen containing groups on the external SWNT surface. Such surface groups are known to lower the Fermi level of SWNTs[75] potentially rendering them inactive in the POM-SWNT redox reaction. Acid washed SWNTs (O-SWNTs) were heated under the same conditions as the pristine SWNTs, yielding an approximate 50% weight loss. When promptly added to a solution of POM, the same colour change was observed as when SWNTs had been added to the POM solution previously, suggesting that metallic nanoparticles present in the sample were not responsible for the observed POM reduction upon SWNT addition to the solution.

As well as probing the chemical composition of the SWNT sample added, the time between SWNT annealing and addition was probed. When SWNTs were heated to give a 50% weight loss, allowed to cool, left under ambient conditions for a week and then added to a POM solution, there was no observable formation of the blue colour at the solid-liquid interface. This was hypothesised to be due to the Fermi level of the SWNTs decreasing in energy due to chemisorbed atmospheric molecules, such as O_2, which are removed from the sample during the annealing process.[76]

To test this hypothesis, a computational study was carried out. Density functional theory (DFT) calculations (performed by Dr. Stephen Skowron) on a small model section of a SWNT showed that O_2 chemisorbs to the external SWNT wall in a peroxide-like configuration, in agreement with previous theoretical results[77, 78] (**Fig. 2.28, A**). This binding mode decreases the energy of the highest occupied molecular orbital (HOMO) of the model SWNT relative to the model SWNT with no chemisorbed O_2. Increasing the density of oxygen uptake by the SWNT linearly depressed the energy of the HOMO; with the model of SWNT used, the HOMO decreased in energy by approximately 50 meV per weight percentage of O_2 bound to the SWNT model (**Fig. 2.28, B**).

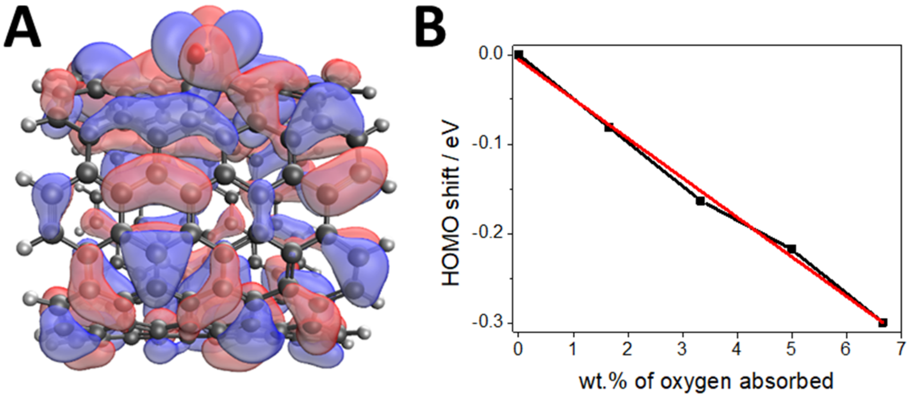

Figure 2.28. (A) Illustrates the HOMO-8 orbital of the simulated system, showing the oxygen molecule at the top, centre of the model, binding in the peroxide-like configuration. (B) shows the linear relationship between an increasing weight percent of chemisorbed O_2 and a lowering of the HOMO energy in the model nanotube, equivalent to the Fermi level in SWNTs. (Figure produced by Dr. Stephen Skowron).

The lowering of the SWNT HOMO can be related to the lowering of the Fermi level of SWNTs as the sample was left under ambient conditions, to a point where the Fermi level was lowered so much that electron transfer between the SWNT and POM could not spontaneously occur, leading to the absence of the formation of blue colour at the solid-liquid interface.

Confirmation of the oxidation of the SWNT-host and electron transfer to the POM-guest in solution prior to encapsulation meant that the oxidation state of the POMs encapsulated within the SWNT could have been altered. To test this hypothesis, X-ray photoelectron spectroscopy (XPS) was employed to probe the oxidation state of the encapsulated POMs. XPS of SWNTs showed the presence of Ni and Y from residual nanoparticles. XPS of the free POMs (**Fig. 2.29**) gave atomic percentages in good agreement with the calculated values and are summarised in **table 2.7**. Measurements carried out under the same conditions of the {POM}@SWNT materials showed similar

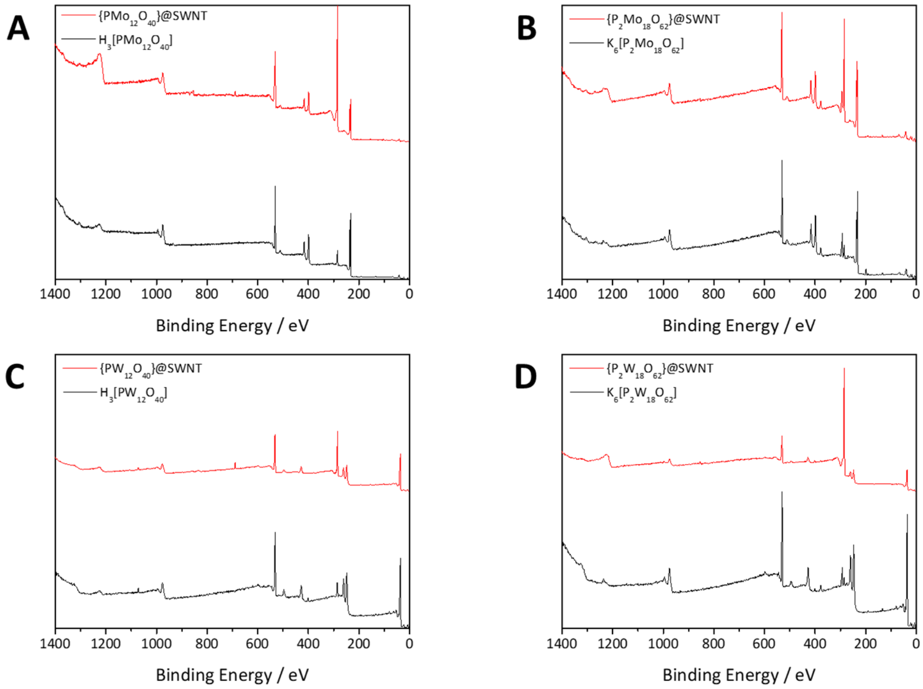

Figure 2.29. (A) Wide scans of $H_3[PMo_{12}O_{40}]$ and $\{PMo_{12}O_{40}\}$@SWNT (B) wide scans of $K_6[P_2Mo_{18}O_{62}]$ and $\{P_2Mo_{18}O_{62}\}$@SWNT (C) $H_3[PW_{12}O_{40}]$ and $\{PW_{12}O_{40}\}$@SWNT (D) $K_6[P_2W_{18}O_{62}]$ and $\{P_2W_{18}O_{62}\}$@SWNT. Data charge corrected to the C 1s peak at 284.5 eV.

Table 2.7. Summary of atomic percentages of elements present in POM and {POM}@SWNT samples taken from wide scans. Missing atomic % made up of contaminants Cl, Na, F, Si.

<table>
<tr><th colspan="8">SWNT</th></tr>
<tr><td>Sample</td><td>C %</td><td>O %</td><td>Ni %</td><td>Y %</td><td></td><td></td><td></td></tr>
<tr><td>SWNT</td><td>93.5</td><td>4.8</td><td>1</td><td>0.5</td><td></td><td></td><td></td></tr>
<tr><th colspan="8">Mo-POM</th></tr>
<tr><td>Sample</td><td>C %</td><td>O %</td><td>Mo %</td><td>P %</td><td>K %</td><td>Ni %</td><td>Y %</td></tr>
<tr><td>$H_3[PMo_{12}O_{40}]$</td><td>41.8</td><td>41.5</td><td>15.6</td><td>1.2</td><td>-</td><td>-</td><td>-</td></tr>
<tr><td>$K_6[P_2Mo_{18}O_{62}]$</td><td>14.5</td><td>53</td><td>18.94</td><td>2.3</td><td>6.84</td><td>-</td><td>-</td></tr>
<tr><th colspan="8">W-POM</th></tr>
<tr><td>Sample</td><td>C %</td><td>O %</td><td>W %</td><td>P %</td><td>K %</td><td>Ni %</td><td>Y %</td></tr>
<tr><td>$H_3[PW_{12}O_{40}]$</td><td>36</td><td>42.1</td><td>14.8</td><td>2.3</td><td>-</td><td>-</td><td>-</td></tr>
<tr><td>$K_6[P_2W_{18}O_{62}]$</td><td>16.5</td><td>54.8</td><td>19.8</td><td>2.2</td><td>6.7</td><td>-</td><td>-</td></tr>
<tr><th colspan="8">{Mo-POM}@SWNT</th></tr>
<tr><td>Sample</td><td>C %</td><td>O %</td><td>Mo %</td><td>P %</td><td>K %</td><td>Ni %</td><td>Y %</td></tr>
<tr><td>$\{PMo_{12}O_{40}\}$@SWNT</td><td>85</td><td>12.3</td><td>2.6</td><td>0.2</td><td>-</td><td>-</td><td>-</td></tr>
<tr><td>$\{P_2Mo_{18}O_{62}\}$@SWNT</td><td>66.7</td><td>15.7</td><td>4.4</td><td>0.6</td><td>12.7</td><td>-</td><td>-</td></tr>
<tr><th colspan="8">{W-POM}@SWNT</th></tr>
<tr><td>Sample</td><td>C %</td><td>O %</td><td>W %</td><td>P %</td><td>K %</td><td>Ni %</td><td>Y %</td></tr>
<tr><td>$\{PW_{12}O_{40}\}$@SWNT</td><td>68</td><td>22.2</td><td>5.3</td><td>0.5</td><td>-</td><td>0.3</td><td>-</td></tr>
<tr><td>$\{P_2W_{18}O_{62}\}$@SWNT</td><td>89.9</td><td>7.5</td><td>1.2</td><td>-</td><td>-</td><td>1.4</td><td>-</td></tr>
</table>

elemental ratios to that of the free POM, with higher oxygen content due to oxygen containing groups naturally present on the SWNT surface, confirming that the POM molecules were chemically unchanged during encapsulation (summarised in **table 2.7**). Notably, in the $\{P_2W_{18}O_{62}\}$@SWNT sample a potassium signal was absent, consistent with EDX, suggesting that charge balancing was fulfilled by the cationic SWNTs. For $\{P_2Mo_{18}O_{62}\}$@SWNT, the K signal was present, however this can be explained by the presence of large crystals on the SWNT surface, consistent with observations from TEM. Like EDX, the H^+ cation of the Keggin anion could not be observed with XPS. The position of the carbon 1s peak was used as reference peak for all samples, however the full width at half maximum (FWHM) of the C 1s peak (**Fig.**

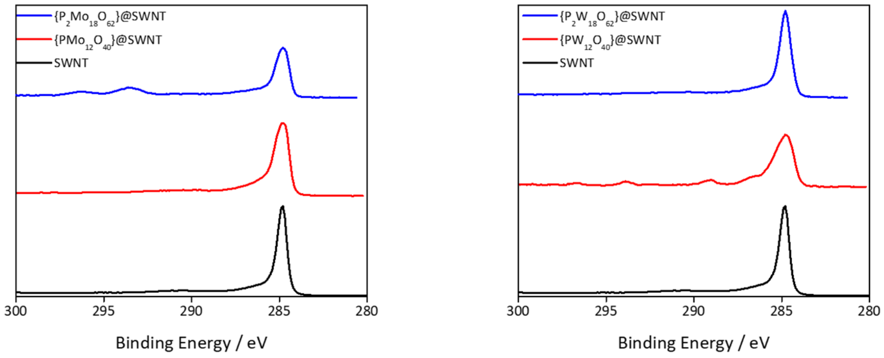

Figure 2.30. C 1s peaks for the {POM}@SWNT materials (charge corrected to 284.5 eV).

2.30) increased from 0.66 in the SWNT sample (**table 2.8**) suggesting that oxidation of SWNTs had taken place, in good agreement with Raman spectra of the materials.

High resolution elemental scans of the free Mo-POMs showed Mo 3d peaks at 233.1, 236.3 eV and 232.7, 235.8 eV for $[PMo_{12}O_{40}]^{3-}$ and $[P_2Mo_{18}O_{62}]^{6-}$ respectively, corresponding to fully oxidised Mo centres[79] (**Fig. 2.31, A & B**). For the encapsulated POMs Mo 3d peaks slightly increased in binding energy to 233.2, 236.3 eV for the $\{PMo_{12}O_{40}\}$@SWNT sample. For the $\{P_2Mo_{18}O_{62}\}$@SWNT sample, the peaks were shifted to 233.5, 236.7 eV (**Fig. 2.31, A & B**). This larger shift was likely due to the presence of the large crystals on the surface leading to a greater number of Mo chemical environments present in the material. Narrow scans of the free W-POMs showed W 4f peaks at 36.1, 38.2 eV and 35.7, 37.8 eV for the $[PW_{12}O_{40}]^{3-}$ and $[P_2W_{18}O_{62}]^{6-}$ species respectively, corresponding to fully oxidised W centres[80] (**Fig. 2.31, C &**

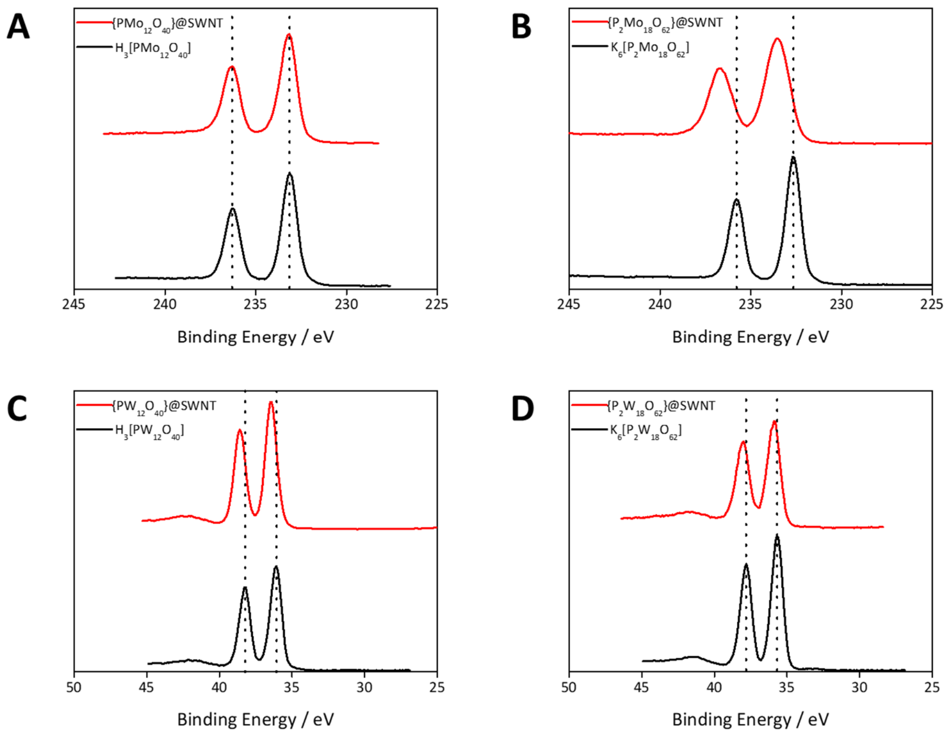

Figure 2.31. (A) Mo 3d peaks for $H_3[PMo_{12}O_{40}]$ and $\{PMo_{12}O_{40}\}$@SWNT (B) Mo 3d peaks for $K_6[P_2Mo_{18}O_{62}]$ and $\{P_2Mo_{18}O_{62}\}$@SWNT (C) W 4f peaks for $H_3[PW_{12}O_{40}]$ and $\{PW_{12}O_{40}\}$@SWNT (D) W 4f peaks for $K_6[P_2W_{18}O_{62}]$ and $\{P_2W_{18}O_{62}\}$@SWNT. Data charge corrected to the C 1s peak at 284.5 eV.

D). For the {W-POM}@SWNT materials the peaks were shifted positively to 36.4, 38.6 eV, and 35.9, 38 eV for {$PW_{12}O_{40}$}@SWNT and {$P_2W_{18}O_{62}$}@SWNT respectively.

Additionally, the FWHM of the Mo and W peaks largely remained unaltered between the native POMs and encapsulated POMs (**table 2.9**). There was a large change in the FWHM of Mo 3d peaks in the {$P_2Mo_{18}O_{62}$}@SWNT material, again likely due to the large crystals present on the exterior of the material leading to multiple chemical environments. The small shifts in the Mo 3d and W 4f peaks, along with no large change in the peak shape, suggested that encapsulated POMs were chemically unaltered, and in their native, fully oxidised state.

Table 2.9. Mo 3d and W 4f FWHM values for the POM and {POM}@SWNT materials.

Mo 3d FWHM	
Sample	FWHM
$H_3[PMo_{12}O_{40}]$	0.99
{$PMo_{12}O_{40}$}@SWNT	1.08
$K_6[P_2Mo_{18}O_{62}]$	0.98
{$P_2Mo_{18}O_{62}$}@SWNT	1.57
W 4f FWHM	
Sample	FWHM
$H_3[PW_{12}O_{40}]$	0.92
{$PW_{12}O_{40}$}@SWNT	0.93
$K_6[P_2W_{18}O_{62}]$	0.92
{$P_2W_{18}O_{62}$}@SWNT	1.04

This can be explained by considering the relative concentrations of reduced and unreduced, but still negatively charged, POMs in the solution surrounding the SWNTs. Upon reduction, the now positively charged SWNTs are surrounded by a solution comprising of mostly unreduced POMs, making it more likely that this unreduced species is taken up by the cationic SWNTs. This process can be summarised by the following reaction:

$$x[POM]^{y-} + C_n \rightarrow \{POM\}^{y-}@C_n^{y+} + (x\text{-}1)[POM]^{(y+\delta)-}$$

where:

$$x = \frac{y}{\delta} + 1$$

and δ is equal to the equivalents of electrons that can be transferred from the valence band of the SWNT to the POM, estimated from a comparison of the LUMOs to the semiconducting Fermi level of the SWNT (pg. 83). For $[P_2W_{18}O_{62}]^{6-}$:

$$x = \frac{6}{2} + 1$$

$$x = 4$$

This means that in the case of $[P_2W_{18}O_{62}]^{6-}$, four equivalents of the POM are required for the encapsulation of a native POM. Once the oxidation has formed the C_n^{y+} species, native POMs are preferentially encapsulated, due to their much higher local concentration (**Fig. 2.32**). This negates the need for the counterions associated with the POM when added to the solution, and explains the absence of potassium in the EDX and XPS data of the $\{P_2W_{18}O_{62}\}$@SWNT sample.

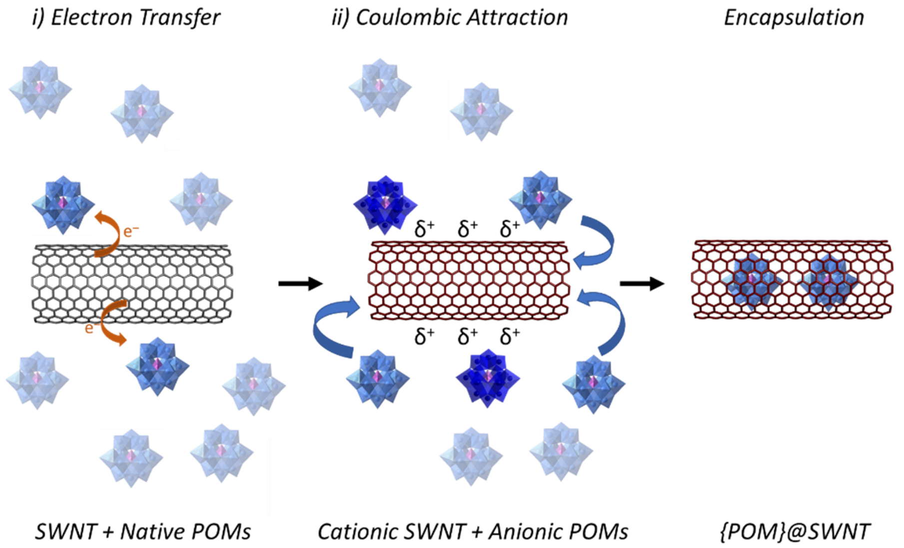

Figure 2.32. Proposed mechanism for encapsulation of the Mo/W-POM species, with the Keggin anion shown. Reduced POMs are shown in dark blue.

2.3.6 Tailoring the POM LUMO

As shown above, the level of SWNT oxidation could be tuned by the LUMO of the POM used for encapsulation, dictated by the elemental composition and structure of the POM. Additionally, pH, the nature of the cation[81] and dielectric constant of the solvent[53] can alter the redox activity of POMs. Such strategies can be utilised to tune the redox properties of POMs to tailor them for a specific application.[81]

To further investigate the ability of POMs to tune the electronic properties of SWNTs, the $[P_2W_{18}O_{62}]^{6-}$ anion was chosen, due to the LUMO being close to the Fermi level of the SWNTs in acidic solutions. The solubility of $K_6[P_2W_{18}O_{62}]$ was found to be low in MeCN, therefore the cation was exchanged for tetrabutylammonium (TBA) *via* the addition of excess TBA bromide to an aqueous solution of $K_6[P_2W_{18}O_{62}]$, giving $TBA_6[P_2W_{18}O_{62}]$. Cyclic voltammetry of $TBA_6[P_2W_{18}O_{62}]$ showed multiple reductions, and the LUMO (first reduction) was found to be -0.397 V *vs.* Ag/Ag$^+$ in acetonitrile with 0.1 M $TBAPF_6$ supporting electrolyte (**Fig. 2.33**). When recently annealed SWNTs were added to a solution of $TBA_6[P_2W_{18}O_{62}]$ dissolved in acetonitrile, using the same methodology as above, no colour change was observed. The mixture was then briefly sonicated, stirred for 48 hours and filtered to give a black solid. TEM of the material

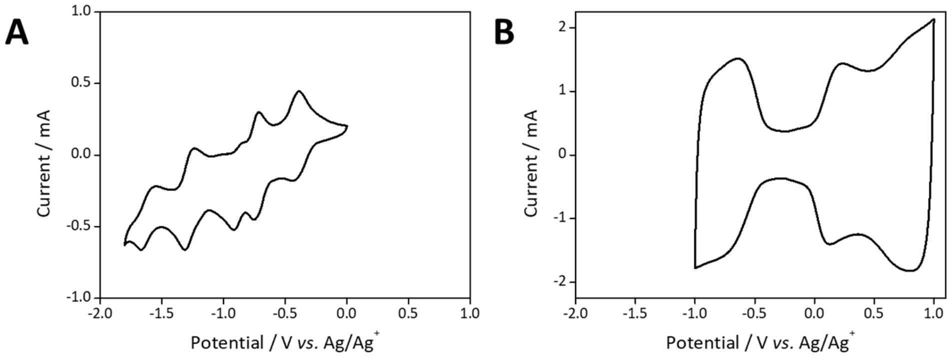

Figure 2.33. (A) CV of $TBA_6[P_2W_{18}O_{62}]$ and (B) CV of SWNTs. Both CVs recorded in MeCN with 0.1M $TBAPF_6$ supporting electrolyte, GCE working electrode, non-aqueous Ag/Ag$^+$ reference electrode and platinum counter electrode at a scan rate of 0.1 V s^{-1}. SWNTs deposited onto GCE from DMF ink.

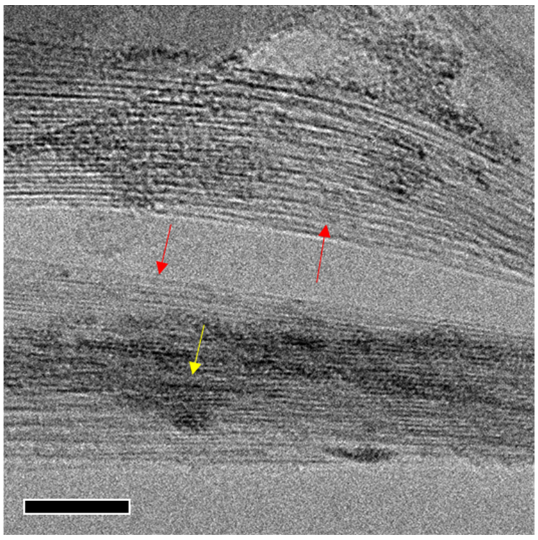

Figure 2.34. TEM image of TBA{$P_2W_{18}O_{62}$}@SWMT material. Image acquired with an accelerating voltage of 80 kV, scale bar 10 nm. Red arrows indicate SWNTs without any encapsulated material. Yellow arrows indicate the presence of material on the exterior of the SWNTs.

showed a low amount of encapsulation, (**Fig. 2.34**) with large amounts of POM adsorbed to the exterior of the SWNTs.

The absence of the blue colour upon SWNT addition could be explained by using the CV of $TBA_6[P_2W_{18}O_{62}]$ and SWNTs, to again estimate the LUMO of the POM and the Fermi level of the SWNT. Recording a CV of SWNTs deposited on a GCE under the same conditions found the Fermi level of the SWNTs to be approximately 0 V *vs* Ag/Ag$^+$ (**Fig. 2.35**). The LUMO of the POM was found to be ~0.4 V above the SWNT Fermi level, therefore spontaneous electron transfer from the SWNT to the POM in solution could not occur, (**Fig. 2.35**) consistent with the hypothesis of spontaneous electron transfer from the SWNT to POM molecules in solution if the LUMO of the POM was lower in energy than the Fermi level of the SWNT. The low level of encapsulation observed in TEM analysis suggests that the proposed redox mediated encapsulation mechanism for the POMs and SWNTs was vital to achieve high levels of POM encapsulation.

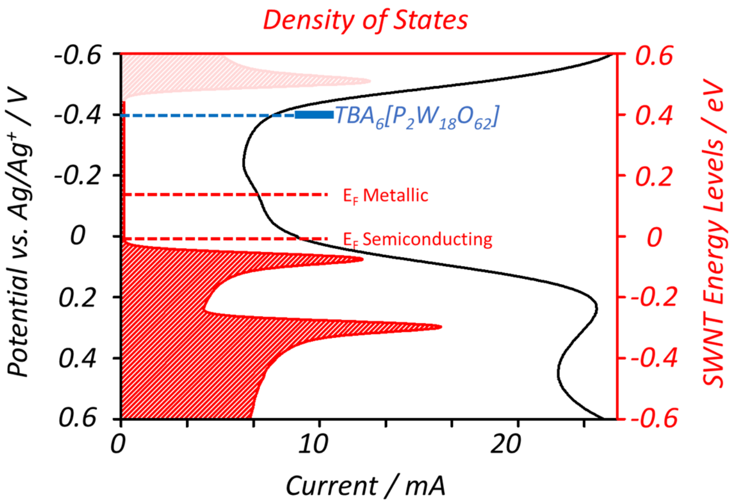

Figure 2.35. DoS of 17, 0 SWNT (red) LSV of SWNTs (black) and position of TBA$_6$[P$_2$W$_{18}$O$_{62}$] LUMO (blue). LSV and LUMO acquired in MeCN with 0.1M TBAPF$_6$ supporting electrolyte with a Ag/Ag$^+$ reference electrode and a platinum counter electrode. SWNTs deposited onto GCE from DMF ink.

Raman analysis of the {TBA-P$_2$W$_{18}$O$_{62}$}@SWNT material provided further evidence that charge transfer between the POM in solution and the SWNT had not taken place (**Fig. 2.36**). There appeared to be no shift in the G band of the [TBA]{P$_2$W$_{18}$O$_{62}$}@SWNT material relative to unfunctionalised SWNTs, indicating that no oxidation of the SWNT had taken place, in good agreement with the lack of blue colour during the encapsulation experiment and the prediction from the POM LUMO relative to the SWNT Fermi level.

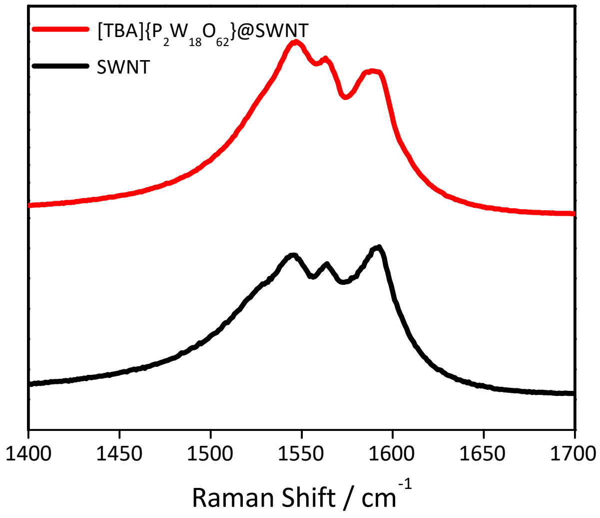

Figure 2.36. G-band in the Raman spectrum of the {TBA-P$_2$W$_{18}$O$_{62}$}@SWNT material acquired with an excitation wavelength of 660 nm.

The low level of encapsulation from TEM analysis and the lack of charge transfer during the encapsulation experiment indicated that the redox reaction between the POM and SWNT was crucial to achieve high levels of POM encapsulation within SWNTs.

2.3.7 Electronic analysis of $\{V_6\}$@SWNT

There was no colour change upon the addition of the opened SWNTs to the $[V_6]$ solution. The LUMO of the $[V_6]$ cluster corresponds to the first reduction in solution, which was estimated to be -0.193 V from the CV of the $[V_6]$ in MeCN. This was found to be above the Fermi level of the SWNTs from a CV of SWNTs under similar conditions, (**Fig. 2.37**) making any spontaneous electron transfer from the SWNTs to the $[V_6]$ in solution energetically unfavourable. Furthermore, any oxidation of the SWNT would not lead to any coulombic interactions between the host SWNT and the neutrally charged $[V_6]$ guest.

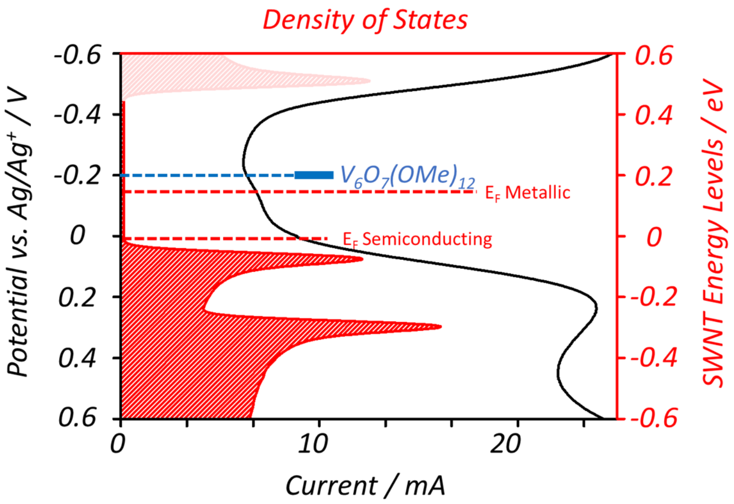

Figure 2.37. DoS of 17,0 SWNTs (red) LSV of SWNTs (black) and LUMO of $[V_6]$ molecule (blue). LSV and LUMO recorded in MeCN with 0.1 M $TBAPF_6$ supporting electrolyte, GCE working electrode, Ag/Ag^+ non-aqueous reference electrode and platinum counter electrode. SWNTs deposited onto GCE from DMF ink.

Raman analysis of the $\{V_6\}$@SWNT material (**Fig. 2.38**) showed a small blue shift in the RBM of approximately 1.5 cm^{-1} relatively to unfunctionalised SWNTs, indicating the presence of encapsulated species within the SWNTs. There was no shift in the G-band, indicating that no oxidation of the SWNTs had taken place, consistent with the

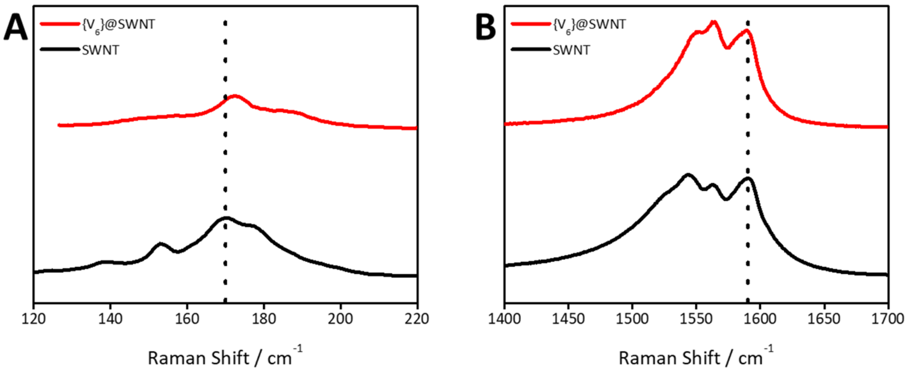

Figure 2.38. (A) RBM region in the Raman spectra of SWNTs and {V_6}@SWNT materials. (B) G-band of SWNTs and {V_6}@SWNT materials. Data acquired with an excitation wavelength of 660 nm.

hypothesis that the LUMO of the [V_6] molecule was too high in energy for spontaneous electron transfer to take place.

This result is consistent with the hypothesis of spontaneous electron transfer from the SWNT to dissolved molecular species, provided that the LUMO of the reductant is sufficiently below the Fermi level of the SWNT. Similar to the example of $TBA_6[P_2W_{18}O_{62}]$ above, energetically this was not favourable for [V_6] and SWNTs. A lower level of encapsulation was observed for the {V_6}@SWNT material, as well as the presence of a large amount of surface species, also suggesting that the redox mediated encapsulation mechanism was vital to the overall level of encapsulation of POM within the SWNT.

2.4 Conclusion

A successful methodology for the encapsulation of POMs within SWNTs was established, using a simple solution filling method. The observation of the colour change that occurred upon SWNT addition to the aqueous POM solution suggested that charge transfer between the SWNTs and POMs took place, which was found to be energetically favourable based on the LUMOs of the POMs and the Fermi level of the SWNTs experimentally observed with voltammetric methods.

The oxidation of the carbon was assessed using Raman spectroscopy and it was observed that all of the Keggin and Wells-Dawson anions oxidised the SWNTs, with the level of oxidation found to be highly dependent on the LUMO of the POM. Such analysis suggests that the POMs allow the tuning of the overall electronic structure of SWNTs to be tailored. XPS analysis showed that the encapsulated POMs were in their native oxidation states, suggesting that native POMs in higher concentrations in solution were preferentially encapsulated. By manipulating the POM cation and solvent used in the encapsulation reaction, the LUMO of the POM could be raised sufficiently so that the charge transfer from SWNT to POM could be inhibited, preventing the oxidation of the SWNTs and lowering the overall encapsulation of the POM, suggesting that the redox reaction between the POM and SWNT was crucial to achieve high rates of encapsulation.

Using a neutrally charged POM that was also redox innocent to the SWNTs, filling was also achieved, likely driven by favourable van der Waals interactions between the cluster and the SWNT interior. The lack of charge transfer between the SWNTs and the vanadate was confirmed with Raman spectroscopy, suggesting that the encapsulation of the species was entirely driven by van der Waals interactions. Again, a lower level of encapsulation was observed, suggesting that the redox mediated self-assembly process is extremely important in the uptake of charged species.

The encapsulation of POMs within SWNTs has shown to be redox-driven, with the guest able to directly tune the electronic structure of the SWNTs. The surprising incorporation of such a hydrophilic species within a hydrophobic cavity could lead to the incorporation of other charged species within the SWNTs, mediated by either the redox chemistry of POMs, or by other redox active species.

2.5 Experimental

2.5.1 General

All common reagents and solvents were used as received from Sigma-Aldrich, Acros Organics or Thermo Fisher. Single walled carbon nanotubes (P2) were purchased from Carbon Solutions Inc. $V_6O_7(OMe)_{12}$ was acquired from Dr. Ellen Matson's group (University of Rochester).

NMR data was acquired using a Bruker DPX300 300 MHz spectrometer and Bruker AVIII400 400 MHz spectrometer using the University of Nottingham's open access analytical services.

Thermogravimetric analysis was obtained using a TA Q500 analyser, on platinum pans. In all cases the ramp rate was 10 °C per minute to 1000 °C followed by an isothermal hold for 10 minutes, all in an air flow of 90 mL/min.

UV-vis spectroscopy was performed on a Perkin-Elmer Lambda 25 UV/Vis spectrometer in quartz cuvettes. The sample was dissolved in water.

MALDI-ToFMS analyses were performed on a Bruker ultraFlexIII instrument. Samples were mixed in solution with (DCTB), here used as a matrix, and deposited on a stainless-steel target plate (type MTP384). A pulsed solid-state UV laser (355nm) was used to ionise the sample and matrix. The instrument was operated in REFLECTRON mode. A Broker TOF spectrometer using electrospray ionisation (ESI) in negative ion mode was used to acquire the mass spectrum of $H_3[PMo_{12}O_{40}]$ using the University of Nottingham's open access analytical service.

Electrochemistry experiments were performed on an Autolab PGSTAT302N. Aqueous electrochemistry was performed using a three-electrode set up with a reference saturated calomel electrode, a glassy carbon working electrode and platinum counter electrode. MeCN electrochemistry used a three-electrode set up with a Ag/Ag^+ non-aqueous reference electrode, glassy carbon working electrode and platinum counter electrode. The analytes were dissolved in the supporting electrolyte to a concentration of 10 mM. SWNTs were first sonicated for 15 minutes in a 10 mg/mL DMF suspension. After sonication 10 µL of the suspension was deposited onto the glassy carbon working electrode and left till completely dry. Electrodes were purchased from IJ Cambria.

Micro-Raman spectroscopy was performed using a Horiba-Jobin-Yvon LabRAM HR spectrometer. Single-point spectra were recorded using a 100x objective, a 300-µm confocal pinhole, and a 660 nm (1.88 eV) laser at < 0.3 mW. The spectral resolution was 1.2 cm^{-1}. Instrument calibration was performed using the zero-order line and a standard Si(100) reference band at 520.7 cm^{-1}. Samples were prepared by depositing a small quantity of sample from a methanolic suspension onto Si(100) wafers. A typical spectrum was recorded by averaging 4-8 acquisitions, each of 5-30 s duration.

HRTEM images were acquired on a JEOL 2100+ LaB_6 emission microscope and a JEOL 2100F field emission gun microscope with an accelerating voltage of 80-200 kV. Samples were prepared by first dispersing them in isopropyl alcohol which were then dropped onto a copper grid mounted with a “lacey” carbon film.

AC-TEM images were acquired at the University of Ulm on a C_s corrected FEI Titan 80-300 TEM (images were acquired using a Gatan Ultrascan 1000XP with exposure times of 0.25 to 1.00 s) and a C_s/C_c corrected SALVE microscope (images were acquired using a gatan Ultrascan 1000XP with exposure times of 0.25 to 1.00 s). Samples were prepared by first dispersing them in isopropyl alcohol and then dropped onto a copper grid mounted with a “lacey” carbon film.

All TEM images were processed using Gatan Digital Micrograph, and quoted distances were measured by drawing a line profile and measuring the electron density histogram.

EDX spectra were acquired during TEM imaging, using Oxford Instruments INCA X-Ray microanalysis systems.

XPS data was acquired with a Kratos AXIS ULTRA with a mono-chromated Al kα X-ray source (1486.6eV) operated at 10 mA emission current and 12 kV anode potential (120 W). Spectra were acquired with the Kratos VISION II software. A charge neutralizer filament was used to prevent surface charging. Hybrid –slot mode was used measuring a sample area of approximately 300 x 700 µm. The analysis chamber pressure was better than 5 x 10^{-9} mbar. Three areas per sample were analysed. A wide scan was performed at low resolution (Binding energy range 1400 eV to -5 eV,with pass energy 80 eV, step 0.5 eV, sweep time 20 minutes). High resolution spectra at pass energy 20 eV, step of 0.1 eV, and sweep times of 10 minutes each were also acquired for photoelectron peaks from the detected elements and these were used to model the chemical composition. The spectra were charge corrected to the C 1s peak set to 284.5 eV.

The model SWNT HOMO energy was calculated for each of the ground state species of zero to four di-oxygen molecules chemisorbed to a 1.3 nm long model (8,8) SWNT structure, with hydrogen atoms terminating unsaturated edge carbon atoms. Geometry optimizations were performed using the Q-Chem 5.0 quantum chemistry software package at the B3LYP/6-31G* level of theory, with structures and energies confirmed using ωB97X-D/6-311G**.

2.5.2 Synthesis of $H_3[PMo_{12}O_{40}]$[51]

MoO_3 (14 g, 0.097 moles) was dissolved in water (150 mL). H_3PO_4 (14.8 M, 570 µL) was added to the resultant green suspension. The mixture was refluxed for 3 hours at 110 °C, giving a bright yellow suspension. The suspension was filtered whilst still hot, giving a clear yellow solution. The solvent was reduced with heat and allowed to stand overnight yielding a yellow precipitate. This was filtered and washed with cold ethanol (5 mL) and cold water (5 mL) giving a yellow solid (5.37 g, 37%) ^{31}P NMR (D_2O) (δ, ppm) -3.88 (s). TOF-ESI (negative ion) m/z 1825.38 (M^-, $H_3[PMo_{12}O_{40}]$). Data in good agreement with the literature.[47, 51]

2.5.3 Synthesis of $K_6[P_2Mo_{18}O_{62}]$[50]

$Na_2MoO_4.2H_2O$ (20 g, 0.083 moles) was dissolved in water (30 mL). HCl (12.1 M, 16.5 mL) was added to the solution upon which a white precipitate formed, which was dissolved with stirring, giving a yellow solution. H_3PO_4 (14.8 M, 3 mL) was then added to the solution. The resultant yellow solution was refluxed overnight at 110 °C, resulting in a deep orange solution. Once the reaction had cooled to room temperature KCl (27 g, 0.36 moles) was added, producing a yellow precipitate. This precipitate was filtered and washed with cold ethanol (5 mL) and cold water (5 mL) giving a yellow solid (3.50 g, 25%). ^{31}P NMR (D_2O) (δ, ppm) -3.14 (s). MALDI-TOF (negative ion) (DCTB) m/z 2976.1 (M^-, $HK_5[P_2Mo_{18}O_{62}]$). Data in good agreement with the literature.[47, 50]

2.5.4 Synthesis of $H_3[PW_{12}O_{40}]$[49]

$Na_2WO_4.2H_2O$ (100 g, 0.3 moles) and Na_2HPO_4 (50 g, 0.35 moles) were dissolved in water (100 mL) and refluxed for 45 minutes. HCl (12.1 M, 100 mL) was added, and the resulting mixture was refluxed for 24 hours at 110 °C, resulting in a yellow solution with a white precipitate. The precipitate was filtered whilst hot, dried overnight under ambient conditions, and then recrystalised from the minimum amount of boiling water, giving a precipitate which was filtered and washed with cold water (2 x 10 mL) giving a white crystalline solid (57.5 g, 77%). ^{31}P NMR (D_2O) (δ, ppm) –15.30 (s). TOF-ESI (negative ion) m/z 2880.05 (M^{2-}, $ClH_3[PW_{12}O_{40}]$). Data in good agreement with the literature.[47, 49]

2.5.5 Synthesis of $K_6[P_2W_{18}O_{62}]$[48]

$Na_2WO_4.2H_2O$ (100 g, 0.3 moles) was dissolved in water (120 mL). HCl (4 M, 83 mL) was added dropwise. A white precipitate formed, which was dissolved upon the completion of the addition. H_3PO_4 (4 M, 83 mL) was then added dropwise. The resultant yellow solution was refluxed for 24 hours at 110 °C. Once the reaction was complete the clear yellow solution was allowed to cool to room temperature. KCl (50 g, 0.67 moles) was added to the solution, forming a yellow precipitate. This was filtered to give a pale-yellow solid which was allowed to air dry overnight. The yellow solid was dissolved in water (220 mL), heated to remove excess solvent and left to cool overnight giving a yellow precipitate which was washed with cold water (2 x 10 mL) giving a yellow crystalline solid (43.3 g, 53%). ^{31}P NMR (D_2O) (δ, ppm) –13.01 (s). MALDI-TOF (negative ion) (DCTB) m/z 4560.5 (M^{-}, $HK_5[P_2W_{18}O_{62}]$). Data in good agreement with the literature.[47, 48]

2.5.6 Synthesis of {Mo/W-POM}@SWNT

POM was dissolved in water (3 mL) to give a solution with a 10 mM concentration. SWNTs (20 mg) were heated to 600 ^{o}C in air for 30 minutes yielding a black solid (10 mg), which was subsequently added to the POM solution. Upon the addition the formation of a blue (W) or green (Mo) solution was observed at the solid interface. The suspension was then sonicated for approximately 5 minutes and stirred at room temperature for 48 hours. The suspension was then filter through a PTFE membrane (pore size 0.2 µm) to yield a black solid (11-15 mg).

2.5.7 Acid Treatment of SWNTs

SWNTs (50 mg) were added to HNO_3 (3 M, 50 mL) and sonicated for 5 minutes. The resulting dispersion was then refluxed for 3 hours, then filtered through a PTFE membrane (pore size 0.2 µm) and washed with deionised water (200 mL). The solid was subsequently dried under vacuum overnight yielding a black solid (45 mg).

2.5.8 Synthesis of $[Bu_4N]_6[P_2W_{18}O_{62}]$

$K_6[P_2W_{18}O_{62}]$ (2 g, 0.4 mmol) was dissolved in water (30 mL). Tetrabutylammonium bromide (0.8 g, 2.5 mmol) was added to this solution, giving a pale yellow precipitate. This mixture was subsequently stirred for 30 minutes, then centrifuged (8000 xg, 15 minutes). Following this most of the solvent was decanted, and the solid was dispersed in fresh water (20 mL). This was then sonicated for 2 minutes and filtered yielding a pale (almost white) solid (1.54 g, 82 %) ^{31}P NMR (CD_3CN) (δ, ppm) –13.29 (s).

2.5.9 Synthesis of {TBA-$P_2W_{18}O_{62}$}@SWNT

$[Bu_4N]_6[P_2W_{18}O_{62}]$ (208 mg, 0.04 mmol) was dissolved in MeCN (3 mL). SWNTs (20 mg) were heated to 600 ^{o}C for 30 minutes yielding a black solid (10 mg), which was subsequently added to the POM solution. No colour change was observed. The mixture was sonicated for 5 minutes the stirred at room temperature for 48 hours.

The suspension was filtered through a PTFE membrane (pore size 0.2 µm) to yield a black solid (10 mg).

2.5.10 Synthesis of $\{V_6\}$@SWNT

$V_6O_7(OMe)_{12}$ (50 mg, 0.06 mmol) was dissolved in MeCN (3 mL). SWNTs (20 mg) were heated to 600 °C for 30 minutes yielding a black solid (10 mg), which was subsequently added to the POM solution. The suspension was sonicated for 5 minutes and stirred at room temperature for 48 hours and was then filtered through a PTFE membrane (pore size 0.2 µm) to yield a black solid (10 mg).

2.6 References

1. J. Sloan, J. Hammer, M. Zwiefka-Sibley, M. L. H. Green and J. Sloan, *Chem. Commun.*, 1998, 347-348.
2. M. Monthioux, *Carbon*, 2002, **40**, 1809-1823.
3. S. A. Miners, G. A. Rance and A. N. Khlobystov, *Chem. Soc. Rev.*, 2016, **45**, 4727-4746.
4. T. Fujimori, A. Morelos-Gómez, Z. Zhu, H. Muramatsu, R. Futamura, K. Urita, M. Terrones, T. Hayashi, M. Endo, S. Young Hong*, et al.*, *Nat. Commun.*, 2013, **4**, 2162.
5. M. M. Shulaker, G. Hills, N. Patil, H. Wei, H.-Y. Chen, H. S. P. Wong and S. Mitra, *Nature*, 2013, **501**, 526-530.
6. L. Sun, X. Wang, Y. Wang and Q. Zhang, *Carbon*, 2017, **122**, 462-474.
7. M. Monthioux, *Carbon Meta-Nanotubes: Synthesis,Properties and Applications*, 2012.
8. M. A. Lebedeva, T. W. Chamberlain, M. Schröder and A. N. Khlobystov, *Chem. Mater.*, 2014, **26**, 6461-6466.
9. B. W. Smith, M. Monthioux and D. E. Luzzi, *Nature*, 1998, **396**, 323-324.
10. H. Kataura, Y. Maniwa, T. Kodama, K. Kikuchi, K. Hirahara, K. Suenaga, S. Iijima, S. Suzuki, Y. Achiba and W. Krätschmer, *Synth. Met.*, 2001, **121**, 1195-1196.
11. A. N. Khlobystov, D. A. Britz, J. Wang, S. A. O'Neil, M. Poliakoff and G. A. D. Briggs, *J. Mater. Chem.*, 2004, **14**, 2852-2857.

12. H. Ulbricht, G. Moos and T. Hertel, *Phys. Rev. Lett.*, 2003, **90**, 095501.
13. M. Yudasaka, K. Ajima, K. Suenaga, T. Ichihashi, A. Hashimoto and S. Iijima, *Chem. Phys. Lett.*, 2003, **380**, 42-46.
14. R. R. Meyer, J. Sloan, R. E. Dunin-Borkowski, A. I. Kirkland, M. C. Novotny, S. R. Bailey, J. L. Hutchison and M. L. H. Green, *Science*, 2000, **289**, 1324-1326.
15. T. W. Chamberlain, T. Zoberbier, J. Biskupek, A. Botos, U. Kaiser and A. N. Khlobystov, *Chem. Sci.*, 2012, **3**, 1919-1924.
16. C. T. Stoppiello, J. Biskupek, Z. Y. Li, G. A. Rance, A. Botos, R. M. Fogarty, R. A. Bourne, J. Yuan, K. R. J. Lovelock, P. Thompson, *et al.*, *Nanoscale*, 2017, **9**, 14385-14394.
17. N. Agasti, M. A. Astle, G. A. Rance, J. Alves Fernandes, J. Dupont and A. N. Khlobystov, *Nano Lett.*, 2020, **20**, 1161-1171.
18. T. W. Chamberlain, J. Biskupek, S. T. Skowron, A. V. Markevich, S. Kurasch, O. Reimer, K. E. Walker, G. A. Rance, X. Feng, K. Müllen, *et al.*, *ACS Nano*, 2017, **11**, 2509-2520.
19. Y. Ishii, K. Tashiro, K. Hosoe, A. Al-zubaidi and S. Kawasaki, *Phys. Chem. Chem. Phys.*, 2016, **18**, 10411-10418.
20. P. V. C. Medeiros, S. Marks, J. M. Wynn, A. Vasylenko, Q. M. Ramasse, D. Quigley, J. Sloan and A. J. Morris, *ACS Nano*, 2017, **11**, 6178-6185.
21. J. M. Wynn, P. V. C. Medeiros, A. Vasylenko, J. Sloan, D. Quigley and A. J. Morris, *Phys. Rev. Mater.*, 2017, **1**, 073001.
22. B. Fei, H. Lu, W. Chen and J. H. Xin, *Carbon*, 2006, **44**, 2261-2264.
23. J. Sloan, G. Matthewman, C. Dyer-Smith, A. Y. Sung, Z. Liu, K. Suenaga, A. I. Kirkland and E. Flahaut, *ACS Nano*, 2008, **2**, 966-976.
24. E. Bichoutskaia, Z. Liu, N. Kuganathan, E. Faulques, K. Suenaga, I. J. Shannon and J. Sloan, *Nanoscale*, 2012, **4**, 1190-1199.
25. Z. Wang, H. Li, Z. Liu, Z. Shi, J. Lu, K. Suenaga, S.-K. Joung, T. Okazaki, Z. Gu, J. Zhou, *et al.*, *J. Am. Chem. Soc.*, 2010, **132**, 13840-13847.
26. Z. Wang, K. Zhao, H. Li, Z. Liu, Z. Shi, J. Lu, K. Suenaga, S.-K. Joung, T. Okazaki, Z. Jin, *et al.*, *J. Mater. Chem.*, 2011, **21**, 171-180.
27. A. A. Eliseev, L. V. Yashina, M. M. Brzhezinskaya, M. V. Chernysheva, M. V. Kharlamova, N. I. Verbitsky, A. V. Lukashin, N. A. Kiselev, A. S. Kumskov, R. M. Zakalyuhin, *et al.*, *Carbon*, 2010, **48**, 2708-2721.

28. R. L. McSweeney, T. W. Chamberlain, M. Baldoni, M. A. Lebedeva, E. S. Davies, E. Besley and A. N. Khlobystov, *Chem. - Eur. J.*, 2016, **22**, 13540-13549.
29. L. Guan, Z. Shi, M. Li and Z. Gu, *Carbon*, 2005, **43**, 2780-2785.
30. N. Sun, L. Guan, Z. Shi, N. Li, Z. Gu, Z. Zhu, M. Li and Y. Shao, *Anal. Chem.*, 2006, **78**, 6050-6057.
31. H. Qiu, N. Sun, M. Li, Z. Shi, J. Qiu, Z. Gu and J. Yang, *J. Nanosci. Nanotechnol.*, 2011, **11**, 4034-4038.
32. H. Cheng, H. Qiu, Z. Zhu, M. Li and Z. Shi, *Electrochimica Acta*, 2012, **63**, 83-88.
33. Y. Iizumi, H. Suzuki, M. Tange and T. Okazaki, *Nanoscale*, 2014, **6**, 13910-13914.
34. L.-J. Li, A. N. Khlobystov, J. G. Wiltshire, G. A. D. Briggs and R. J. Nicholas, *Nat. Mater.*, 2005, **4**, 481-485.
35. M. V. Kharlamova, M. Sauer, T. Saito, Y. Sato, K. Suenaga, T. Pichler and H. Shiozawa, *Nanoscale*, 2015, **7**, 1383-1391.
36. A. Botos, J. Biskupek, T. W. Chamberlain, G. A. Rance, C. T. Stoppiello, J. Sloan, Z. Liu, K. Suenaga, U. Kaiser and A. N. Khlobystov, *J. Am. Chem. Soc.*, 2016, **138**, 8175-8183.
37. H. Song, Y. Ishii, A. Al-zubaidi, T. Sakai and S. Kawasaki, *Phys. Chem. Chem. Phys.*, 2013, **15**, 5767-5770.
38. L. Grigorian, K. A. Williams, S. Fang, G. U. Sumanasekera, A. L. Loper, E. C. Dickey, S. J. Pennycook and P. C. Eklund, *Phys. Rev. Lett.*, 1998, **80**, 5560-5563.
39. C. Streb, *Dalton Trans.*, 2012, **41**, 1651-1659.
40. M. Bonchio, Z. Syrgiannis, M. Burian, N. Marino, E. Pizzolato, K. Dirian, F. Rigodanza, G. A. Volpato, G. La Ganga, N. Demitri, *et al.*, *Nat. Chem.*, 2019, **11**, 146-153.
41. S. Amin, J. M. Cameron, J. A. Watts, D. A. Walsh, V. Sans and G. N. Newton, *Mol. Syst. Des. Eng.*, 2019, **4**, 995-999.
42. D.-L. Long, R. Tsunashima and L. Cronin, *Angew. Chem., Int. Ed.*, 2010, **49**, 1736-1758.
43. Y. Ji, L. Huang, J. Hu, C. Streb and Y.-F. Song, *Energy Environ. Sci.*, 2015, **8**, 776-789.

44. S. Li, X. Yu, G. Zhang, Y. Ma, J. Yao, B. Keita, N. Louis and H. Zhao, *J. Mater. Chem.*, 2011, **21**, 2282-2287.
45. F. M. Toma, A. Sartorel, M. Iurlo, M. Carraro, P. Parisse, C. Maccato, S. Rapino, B. R. Gonzalez, H. Amenitsch, T. Da Ros*, et al.*, *Nat. Chem.*, 2010, **2**, 826-831.
46. D. Ma, L. Liang, W. Chen, H. Liu and Y.-F. Song, *Adv. Funct. Mater.*, 2013, **23**, 6100-6105.
47. M. Sadakane and E. Steckhan, *Chem. Rev.*, 1998, **98**, 219-238.
48. C. R. Graham and R. G. Finke, *Inorg. Chem.*, 2008, **47**, 3679-3686.
49. M. Makoto, M. Noritaka, K. Koichi, K. Atsushi, K. Yasuo, S. Kanji, O. Toshio and Y. Yukio, *Bull. Chem. Soc. Jpn.*, 1982, **55**, 400-406.
50. L. E. Briand, G. M. Valle and H. J. Thomas, *J. Mater. Chem.*, 2002, **12**, 299-304.
51. A. Linz, *Ind. Eng. Chem. Anal. Ed.*, 1943, **15**, 459-459.
52. H. Sadayuki, O. Toshiyuki and S. Atsuyoshi, *Bull. Chem. Soc. Jpn.*, 1989, **62**, 1335-1337.
53. A. J. Bard and L. R. Faulkner, *Electrochemical Methods Fundamentals and Applications* John Wiley & Sons, Second Edn., 2001.
54. M. Zhao, B.-Q. Li, X.-Q. Zhang, J.-Q. Huang and Q. Zhang, *ACS Cent. Sci.*, 2020, **6**, 1095-1104.
55. C. Daniel and H. Hartl, *J. Am. Chem. Soc.*, 2005, **127**, 13978-13987.
56. L. E. VanGelder, A. M. Kosswattaarachchi, P. L. Forrestel, T. R. Cook and E. M. Matson, *Chem. Sci.*, 2018, **9**, 1692-1699.
57. A. M. Kosswattaarachchi, L. E. VanGelder, O. Nachtigall, J. P. Hazelnis, W. W. Brennessel, E. M. Matson and T. R. Cook, *J. Electrochem. Soc.*, 2019, **166**, A464-A472.
58. S. Niyogi, M. A. Hamon, H. Hu, B. Zhao, P. Bhowmik, R. Sen, M. E. Itkis and R. C. Haddon, *Accounts Chem. Res.*, 2002, **35**, 1105-1113.
59. Y. Wang and I. A. Weinstock, *Dalton Trans.*, 2010, **39**, 6143-6152.
60. J. Hu, Y. Ji, W. Chen, C. Streb and Y.-F. Song, *Energy Environ. Sci.*, 2016, **9**, 1095-1101.
61. B. Dawson, *Acta Crystallographica*, 1953, **6**, 113-126.
62. L. E. Briand, H. J. Thomas and G. T. Baronetti, *Appl. Catal., A*, 2000, **201**, 191-202.

63. M. A. Astle, G. A. Rance, H. J. Loughlin, T. D. Peters and A. N. Khlobystov, *Adv. Funct. Mater.*, 2019, **29**, 1808092.

64. E. G. Ivanov, *Protection of Metals*, 2008, **44**, 386-389.

65. R. L. McSweeney, T. W. Chamberlain, E. S. Davies and A. N. Khlobystov, *Chem. Commun.*, 2014, **50**, 14338-14340.

66. A. Dolbecq, E. Dumas, C. R. Mayer and P. Mialane, *Chem. Rev.*, 2010, **110**, 6009-6048.

67. K. Kastner, A. J. Kibler, E. Karjalainen, J. A. Fernandes, V. Sans and G. N. Newton, *J. Mater. Chem. A*, 2017, **5**, 11577-11581.

68. B. Matt, J. Fize, J. Moussa, H. Amouri, A. Pereira, V. Artero, G. Izzet and A. Proust, *Energy Environ. Sci.*, 2013, **6**, 1504-1508.

69. A. Al-zubaidi, T. Inoue, T. Matsushita, Y. Ishii, T. Hashimoto and S. Kawasaki, *J. Phys. Chem. C*, 2012, **116**, 7681-7686.

70. M. V. Kharlamova, *Prog. Mater. Sci.*, 2016, **77**, 125-211.

71. S. Bandow, M. Takizawa, H. Kato, T. Okazaki, H. Shinohara and S. Iijima, *Chem. Phys. Lett.*, 2001, **347**, 23-28.

72. L. Alvarez, A. Righi, T. Guillard, S. Rols, E. Anglaret, D. Laplaze and J.-L. Sauvajol, *Chem. Phys. Lett.*, 2000, **316**, 186-190.

73. G. U. Sumanasekera, J. L. Allen, S. L. Fang, A. L. Loper, A. M. Rao and P. C. Eklund, *J. Phys. Chem. B*, 1999, **103**, 4292-4297.

74. H. Hu, B. Zhao, M. E. Itkis and R. C. Haddon, *J. Phys. Chem. B*, 2003, **107**, 13838-13842.

75. J. Vavro, M. C. Llaguno, J. E. Fischer, S. Ramesh, R. K. Saini, L. M. Ericson, V. A. Davis, R. H. Hauge, M. Pasquali and R. E. Smalley, *Phys. Rev. Lett.*, 2003, **90**, 065503.

76. P. G. Collins, K. Bradley, M. Ishigami and A. Zettl, *Science*, 2000, **287**, 1801-1804.

77. G. U. Sumanasekera, C. K. W. Adu, S. Fang and P. C. Eklund, *Phys. Rev. Lett.*, 2000, **85**, 1096-1099.

78. D. C. Sorescu, K. D. Jordan and P. Avouris, *J. Phys. Chem. B*, 2001, **105**, 11227-11232.

79. A. Siokou, G. Leftheriotis, S. Papaefthimiou and P. Yianoulis, *Surf. Sci.*, 2001, **482-485**, 294-299.

80. C. Bosch-Navarro, B. Matt, G. Izzet, C. Romero-Nieto, K. Dirian, A. Raya, S. I. Molina, A. Proust, D. M. Guldi, C. Marti-Gastaldo*, et al.*, *Chem. Sci.*, 2014, **5**, 4346-4354.

81. A. Misra, K. Kozma, C. Streb and M. Nyman, *Angew. Chem., Int. Ed.*, 2020, **59**, 596-612.

Chapter 3: Electron Beam Induced Reactions of Polyoxometalates Confined within Single Walled Carbon Nanotubes

3.1 Background

Understanding the structure of any chemical system is critical to understanding its manifested properties. Electron microscopy, where electrons are accelerated to extremely high energies to form a beam which is used to illuminate the sample rather than a beam of photons, can in principle resolve sub-angstrom features.[1] Although practically these resolutions are starting to be realised[2] they are yet to be widely utilised by the general scientific community. However, the high resolution of electron microscopy means that many electron microscopy techniques are routinely used to study chemical,[3] biological[4] and material[5] samples with complex structures at the sub-microscale.

Transmission electron microscopy (TEM) requires a relatively thin sample (~100 nm or less) to ensure that electrons can pass through the material, interact with the sample

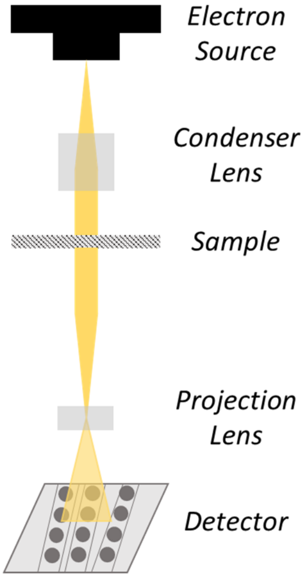

Figure 3.1. Basic principle of transmission electron microscopy.

and generate a projection[1] (**Fig. 3.1**). Modern aberration-corrected TEM (AC-TEM) can achieve spatial resolutions sufficient enough to image individual atoms,[5, 6] rendering it a powerful tool for the characterisation single molecules.[7] For SWNTs their extremely low dimensions mean that TEM is an ideal local probe technique for understanding their structure as well as the structure of their hybrid materials.[8] Alternatively, their low dimensionality, ability to incorporate guest-species within their interior dimensions and rigid structures mean that SWNTs have been used as a substrate for imaging confined molecules,[9] nanowires[10] and metal salts[6] akin to a nanoscale microscope slide.

Examples of single molecule imaging utilising TEM and nanocarbon supports originally were focussed on fullerenes encapsulated within SWNTs.[11-14] Due to their highly symmetrical nature and elemental composition (high atomic numbers), polyoxometalates (POMs) are ideal molecules for single molecule imaging with TEM. As mentioned previously, Sloan *et al.* initially encapsulated Lindqvist anions, $[W_6O_{19}]^{2-}$ within double walled carbon nanotubes and were able to image single molecules.[15] The rate of encapsulation appeared to be low, however. Sloan *et al.* later imaged a lacunary Keggin species, $[SiW_{10}O_{36}]^{8-}$, on a graphene oxide (GO) support.[16] The authors reported that the anions remained stationary long enough to image a variety of different projections of the molecule, revealing the molecular structure. Continued electron beam exposure led to rotation and translation, leading to different

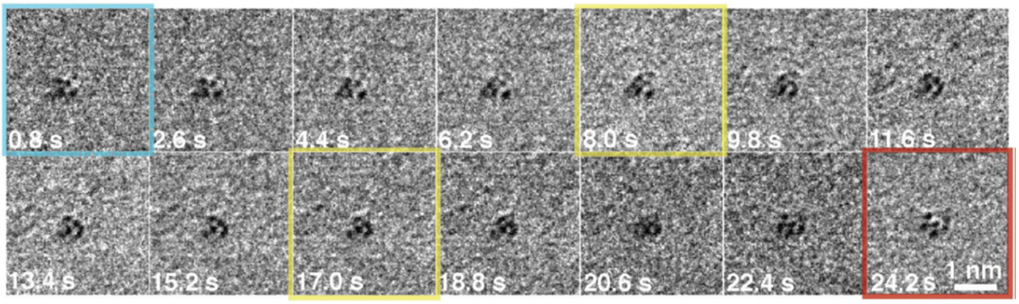

Figure 3.2. AC-TEM images of a rotating $[SiW_{10}O_{36}]^{8-}$ anion deposited on GO surface. Reproduced from reference 16 with permission from The American Chemical Society.

orientations of the same molecule (**Fig. 3.2**). The authors suggested that the inhibited motion of the POM was due to intermolecular interactions between the anion and the GO support, indicating that GO was not an inert imaging substrate.

Sloan *et al.* also imaged a substituted mono-lacunary Keggin anion, $[CoSiW_{11}O_{39}]^{6-}$, on a GO support.[17] The authors were able to selectively tune the accelerating voltage to better resolve either the GO support or individual tungsten atoms. The authors found that using an accelerating voltage of 80 kV gave better resolution of the GO support and monosubstituted cobalt atom as well as stabilising the GO support, whereas at 200 kV individual tungsten atoms were much better resolved but the GO support rapidly degraded. Vats *et al.* also imaged the Keggin anion, $[PW_{12}O_{40}]^{3-}$, on a graphene monolayer.[18] The sample was prepared by depositing the POM anions onto the graphene support *via* electrospray ion beam deposition. The authors found that the energy of the ion beam controlled whether the POM anion remained intact upon

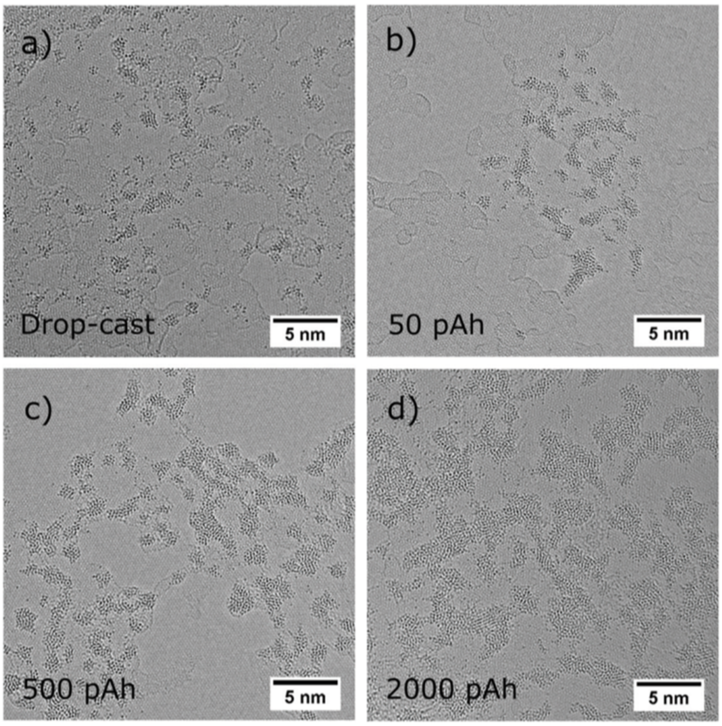

Figure 3.3. Images of $[PW_{12}O_{40}]^{3-}$ *anions deposited onto graphene via (A) drop cast and (B, C & D) molecular electrospray ion beam deposition. Charges in the bottom left of the images refer to the total charge of the ion beam deposited. Scale bars inset. Reproduced from reference 18 with permission from The Royal Society of Chemistry (RSC).*

impact, varying the voltage of the ion-beam between 15 – 300 eV, with intact anions visible as dense aggregates at energies between 15 and 150 eV. At voltages over 300 eV, the anions appeared to fragment, however the graphene appeared to retain its structure. The authors were also able to control the surface coverage of the POM by monitoring the deposited charge (**Fig. 3.3**) and noted how aggregates of the POM were only observed at hydrocarbon impurities on the graphene surface, suggesting that the graphene was not entirely stable under the conditions used. Although most POMs appeared in large aggregates, some individual POMs were also observed.

As well as imaging single molecules, electron microscopy methods can be used to image single molecule reactions.[19-23] In practice, direct observation of a reaction at the single molecule scale can provide definitive information about reaction mechanisms through the direct observation of the processes that drive reactants to products over time *via* metastable intermediates. Usually this requires an external stimulus to induce the desired reaction which is then directly observed with the electron microscope. The use of external stimuli such as heating,[24] applied potentials[25, 26] and relatively high pressures of reactive gasses[27] can sometimes lead to losses in the spatial resolution of images. Alternatively, scanning probe microscopy (SPM) and scanning transmission electron microscopy (STEM) methods, where an atomic tip or focussed beam of electrons is utilised to image the sample, have been developed to the point at which they can routinely probe reaction products[28-30] and intermediates[31] directly, to a high degree of spatial accuracy.

A downside to electron microscopy as an analytical tool is that large amounts of energy can be transferred to the sample that is being imaged from the high energy electron beam. This leads to unwanted reactions through multiple mechanisms which are usually manifested as sample degradation, collectively referred to as beam damage.[1]

There are multiple strategies to mitigate beam damage. Firstly, the imaging conditions can be altered. This can be achieved either through limiting the electron flux[32] and the total electron dose received by the sample or altering the accelerating voltage of the electron beam.[33] Secondly, the sample preparation can be altered through the encapsulation of the sample either between a graphene bilayer or within SWNTs[34] and cryogenically freezing the sample.[3] Generally viewed as an unwanted side effect of TEM imaging, more recently the high energy electron beam has been used as a deliberate stimulus to drive reactions and direct structural modifications.[19-21, 35, 36]

Although STEM and SPM methods are successful, as mentioned above, due to the rastering of the electron beam or atomic tip, scanning techniques can lack the temporal resolution required to observe transient reaction mechanisms (**Fig. 3.4**). On the other hand, the constant flux of electrons and broad-field illumination in TEM can

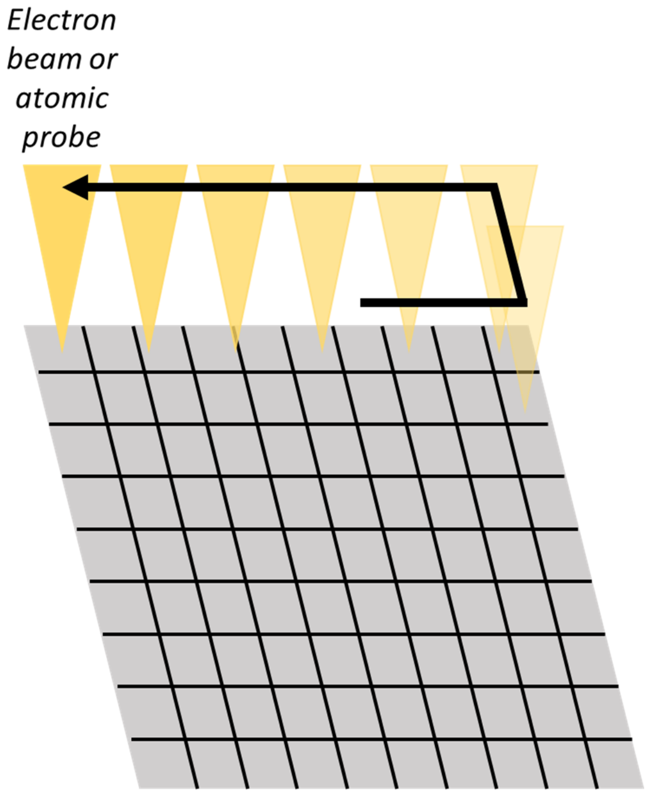

Figure 3.4. Basic principle of STEM/ SPM, where the electron beam or atomic probe is rastered across the sample rapidly in a grid like fashion, acquiring signal at each point to create an image. This can decrease the temporal resolution of the method.

provide a high degree of both spatial and temporal resolution.[37] In utilising the electron beam as both a rapid imaging tool and source of energy to stimulate reactions as mentioned above, an approach termed ChemTEM has been developed.[22] Such dual use of the electron beam enables the simultaneous promotion and observation of chemical reactions, without the need for external stimuli that can reduce the spatial and temporal resolution of the data. Additionally, the electron beam used in TEM can promote different reactions in the same sample or be tuned to control reaction rates. This toolbox allows for the promotion of reactions in a wide range of materials within a similar experimental setup.

The ChemTEM technique has now been utilised and applied to study such chemical systems as metallic nanoparticles,[38] organic molecules[39] and the formation of C_{60}.[40] Chamberlain *et al.* utilised the technique to directly observe reactions of perchlorocoronene (PCC) molecules deposited on graphene and encapsulated within SWNTs.[39] When deposited on graphene, the stimulus of the electron beam was sufficient to induce a reaction between the PCC molecule and the graphene support, evidenced by the translation of the molecule to an edge-on configuration. When the

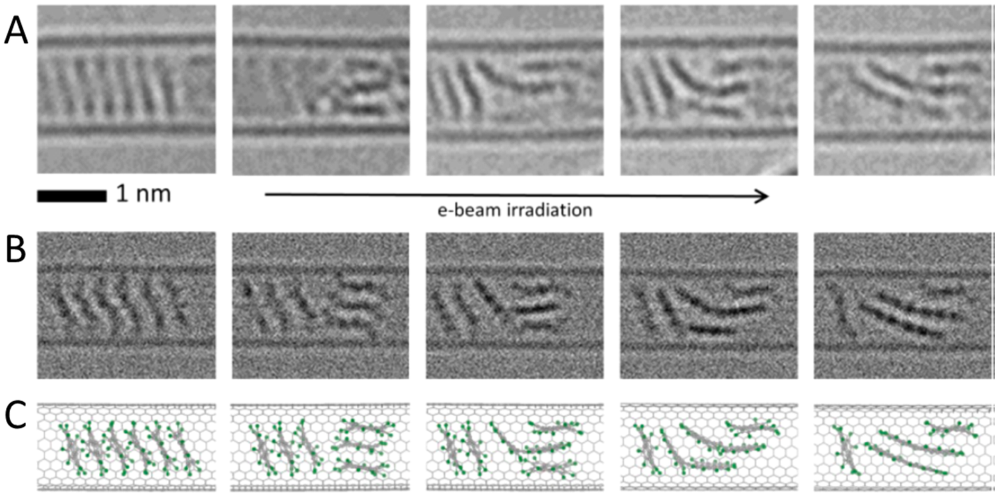

Figure 3.5. (A) Experimental images (B) simulated images and (C) structural models show the transient intermediates observed by TEM of PCC molecules reacting with each other when confined within SWNTs. The reaction was promoted by the electron beam. Reproduced from reference 39 with permission from The American Chemical Society.

PCC molecules were confined within a SWNT, they readily reacted with each other to form chlorine terminated graphene nanoribbons. Both reactions were caused by the removal of terminal Cl atoms, forming highly reactive species. The technique could also be applied to octathiocirculene molecules confined within SWNTs. The ChemTEM approach was able to observe transient intermediates (**Fig. 3.5**) of the reaction demonstrating the temporal resolution of the ChemTEM method. Cao *et al.* also used the ChemTEM methodology to study the reactivity of nanoclusters (~ 20-60 atoms) of 14 different transition metals confined within SWNTs.[38] By observing the interaction of the metallic nanoclusters with the SWNT sidewall, the authors were able to compare the reactivities, manifested as SWNT defect formation rate, against the metal's catalytic activity. The results produced a traditional volcano plot suggesting that reactivity of extremely small nanoclusters behaved more heterogeneously than homogenously, (**Fig 3.6**) an important step forward for the study of small nanocluster catalysis. Both of the above examples demonstrate the ability of ChemTEM to observe transient reactive molecular intermediates, resolve individual atoms and their reactivity and generate important, meaningful data.

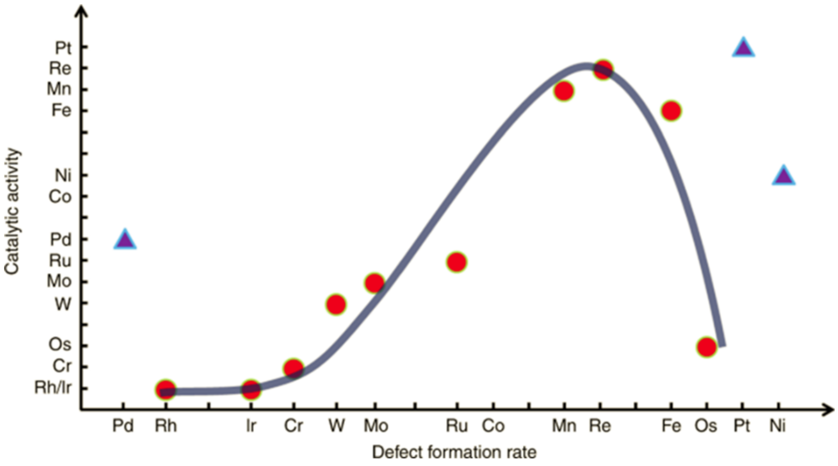

Figure 3.6. Volcano plot based on the reactivity of metallic nanoclusters encapsulated within SWNTs under the electron beam. Reproduced from reference 38 with permission from Springer Nature.

One particular downside to studying reactions using local probe techniques is that each measurement provides observations that are specific to the particular molecule or local environment observed during the measurement. This makes it difficult to link single molecule dynamics with more traditional chemical kinetics. As shown in chapter 2, initial transmission electron microscopy (TEM) of the {POM}@SWNT materials showed high levels of encapsulation, but with the presence of non-uniform species that had M – M interatomic distances close to that of metallic molybdenum and tungsten. However, X-ray photoelectron spectroscopy (XPS), energy dispersive X-ray spectroscopy (EDX) and electrochemical analysis (see chapter 4) of the materials indicated that the encapsulated species were chemically unchanged. This suggested that the POMs were extremely reactive under the influence of the electron beam.

Due to the reactive nature of the POMs and the high levels of encapsulation within the SWNTs, they could be studied using a ChemTEM approach, allowing reactions of individual molecules and groups of 50 – 100 molecules to be studied under similar experimental conditions. Therefore, the in-depth study of the {POM}@SWNT materials could serve two purposes. Firstly, studying the materials at a variety of different voltages, fluxes and total doses could elucidate the true {POM}@SWNT structure, aiding in the understanding of the materials' manifested functional properties. Secondly, the unique structure of the {POM}@SWNT materials could ideally be used to study the effect of the electron beam on imaging POMs at a local probe level (single molecule) and a broader level (multiple molecules) due to the high level of encapsulation, beginning to bridge the gap between molecular reaction dynamics and chemical kinetics in ChemTEM.

3.2 Aims and Objectives

The aim of this study is to better understand the local structure of the {POM}@SWNT materials, what causes the rapid changes in the materials during TEM analysis and utilise the specific material to better understand the kinetics and dynamics of electron beam induced reactions in TEM.

Due to the high levels of encapsulation and apparent high reactivity under the influence of the electron beam, this will be achieved through the following objectives:

1. TEM imaging of the {POM}@SWNT materials at low electron flux, to elucidate the true structure of the {POM}@SWNT materials.
2. Follow the reactions of tens to hundreds of molecules simultaneously by utilising a relatively low magnification technique.
3. Utilise AC-TEM methods to study the POM transformations at the atomic scale.
4. Study the products of the reactions in order to gain better insight into the overall reaction mechanism.

3.3 Results and Discussion

3.3.1 Low Flux HRTEM

The Keggin, $[PM_{12}O_{40}]^{3-}$, and Wells-Dawson, $[P_2M_{18}O_{62}]^{6-}$, anions are ideal species for molecular imaging, owing to their highly symmetrical structures and high contrast elemental composition (**Fig. 3.7**). As previously discussed, this has led to the imaging of the Keggin and its analogues on carbon supports.[15-18, 41] However, observations from the initial HRTEM imaging of the {POM}@SWNT materials shown in chapter 2 revealed that the encapsulated material did not appear uniform. The species were larger than expected for the Keggin and Wells-Dawson anion and the M – M interatomic distances were shorter than expected for that of native POMs. These observations suggested that the POMs were either chemically altered upon encapsulation or reacting rapidly under the influence of the electron beam. XPS data and electrochemical analysis (see chapter 4) provided evidence that the POM molecules were chemically unchanged,

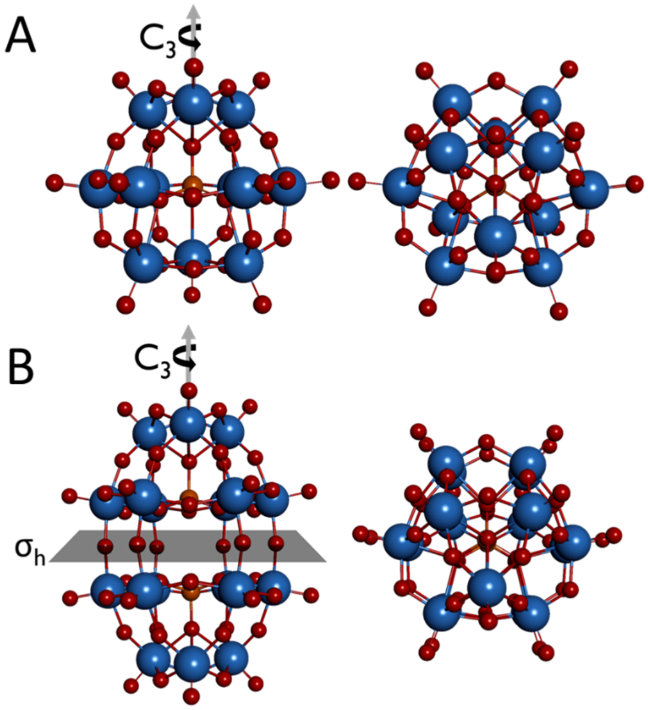

Figure 3.7. Ball and stick models of the $[PM_{12}O_{40}]^{3-}$ *(A) and* $[P_2M_{18}O_{62}]^{6-}$*(B) anions. The* $[PM_{12}O_{40}]^{3-}$ *possesses* T_d *symmetry and the* $[P_2M_{18}O_{62}]^{6-}$ *anion possesses* D_{3h} *symmetry. Metal atoms are blue, oxygen atoms are red and phosphorous atoms are orange.*

suggesting that the latter case was more likely. Initial data was gathered with an electron flux of 1 – 2 x 10^6 e^- nm^{-2} s^{-1} and a range of 80 – 200 keV electron beams, all of which seemed to have little effect on the nature of the observed material.

When acquiring images of the {POM}@SWNT materials (acquired by Dr. Kayleigh Fung) with lower electron fluxes of approximately 6.5 – 9 x 10^4 e^- nm^{-2} s^{-1} (a reduction in flux of a factor of 30) with an electron beam energy of 80 keV the {POM}@SWNT materials showed highly uniform, closely packed discrete molecules within the SWNT, with extremely high levels of encapsulation (**Fig. 3.8**). Each molecule was surrounded by two molecular neighbours, similar to those observed in C_{60}@SWNT.[11] W-POM

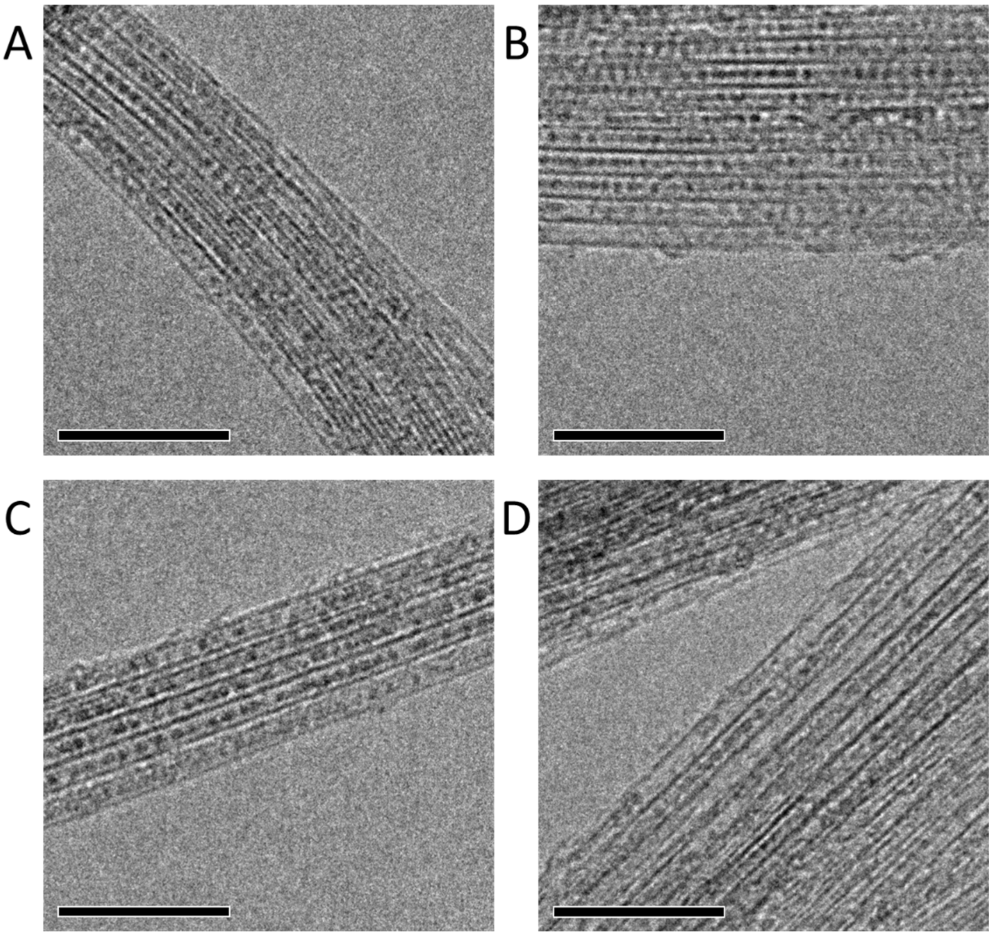

Figure 3.8. TEM images of (A) {$PMo_{12}O_{40}$}@SWNT (B) {$P_2Mo_{18}O_{62}$}@SWNT (C) {$PW_{12}O_{40}$}@SWNT and (D) {$P_2W_{18}O_{62}$}@SWNT. Images acquired with an accelerating voltage of 80 kV and an electron flux between 6.5 – 9 x 10^4 e^- nm^{-2} s^{-1}. Scale bars 10 nm. All {POM}@SWNT materials show the presence of uniform, closely packed discrete POM molecules, with an extremely high level of encapsulation.

molecules had an average size of approximately 0.7 nm and 0.8 nm and ranged between 0.8 – 1.2 nm for $\{PW_{12}O_{40}\}$@SWNT and $\{P_2W_{18}O_{62}\}$@SWNT respectively, with intermolecular (centre to centre) distances between 0.9 – 1.2 nm and 0.9 – 1.4 nm and an average distance between the molecules of 0.45 nm and 0.44 nm (**Fig. 3.9**). TEM images of {Mo-POM}@SWNT materials acquired at a similar electron flux (6.5 – 9 x 10^4 e^- nm^{-2} s^{-1}) also showed a uniform, discrete structure. Mo-POM molecules had an average size of 0.7 nm and 0.9 nm for $[PMo_{12}O_{40}]^{3-}$ and $[P_2Mo_{18}O_{62}]^{6-}$ respectively, ranging between 0.7 – 1.1 nm, with intermolecular distances (centre-to-centre) of between 0.9 – 1.2 nm and 0.9 – 1.4 nm, with average distances between the molecules of 0.4 nm.

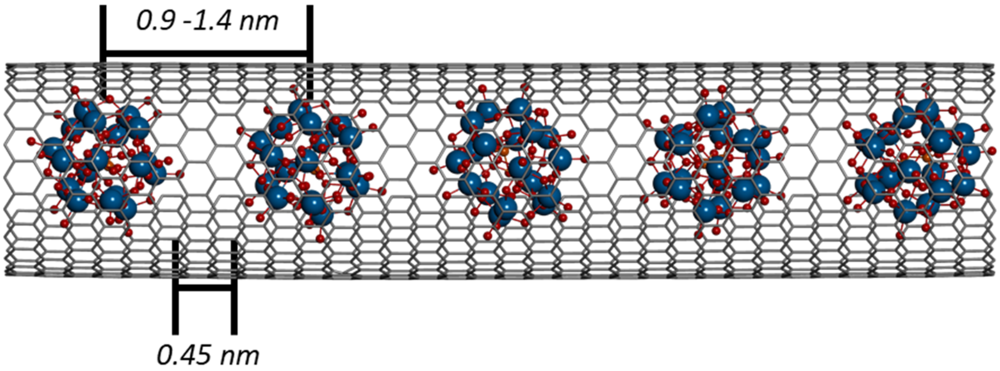

Figure 3.9. Model of the close packed discrete molecules encapsulated within SWNTs from low flux TEM images.

The range in sizes and intermolecular distances of the POM molecules were due to molecular rotations and translations of the POM molecules along the SWNT dimension,[14, 41] observable over the course of imaging. POM molecules could also look elongated, or resemble nanowires, due to these molecular rotations and translations occurring over the course of a single exposure (0.5 s). This effect appeared to be more pronounced for the $\{P_2M_{18}O_{62}\}$@SWNT materials, likely due to anisotropy of the $[P_2M_{18}O_{62}]^{6-}$ anion, leading to more non-equivalent orientations in a single exposure. The material appeared to be stable for several minutes, but after around 10 minutes of exposure with an electron flux of 6.5 – 9 x 10^4 e^- nm^{-2} s^{-1} changes gradually began to accumulate within the {POM}@SWNT materials, with the formation of larger, more contrasting nanoclusters encapsulated within SWNTs, similar to those observed in the initial TEM analysis, as well as visible defects forming on the SWNT sidewalls.

When acquiring images with higher electron fluxes of 3 x 10^5 e^- nm^{-2} s^{-1} and above, these changes accumulated much quicker, (**Fig. 3.10**) leading to images showing larger, non-uniform nanoclusters similar to those discussed in chapter 2. At this electron flux, the encapsulated POMs appeared to be much more reactive than fullerenes[42, 43] or PCC.[39] The volume of the original POM molecules appeared to contract over the course of seconds, leading to condensed structures with higher contrast and large voids within the SWNTs (**Fig. 3.11**). This reaction appeared to be

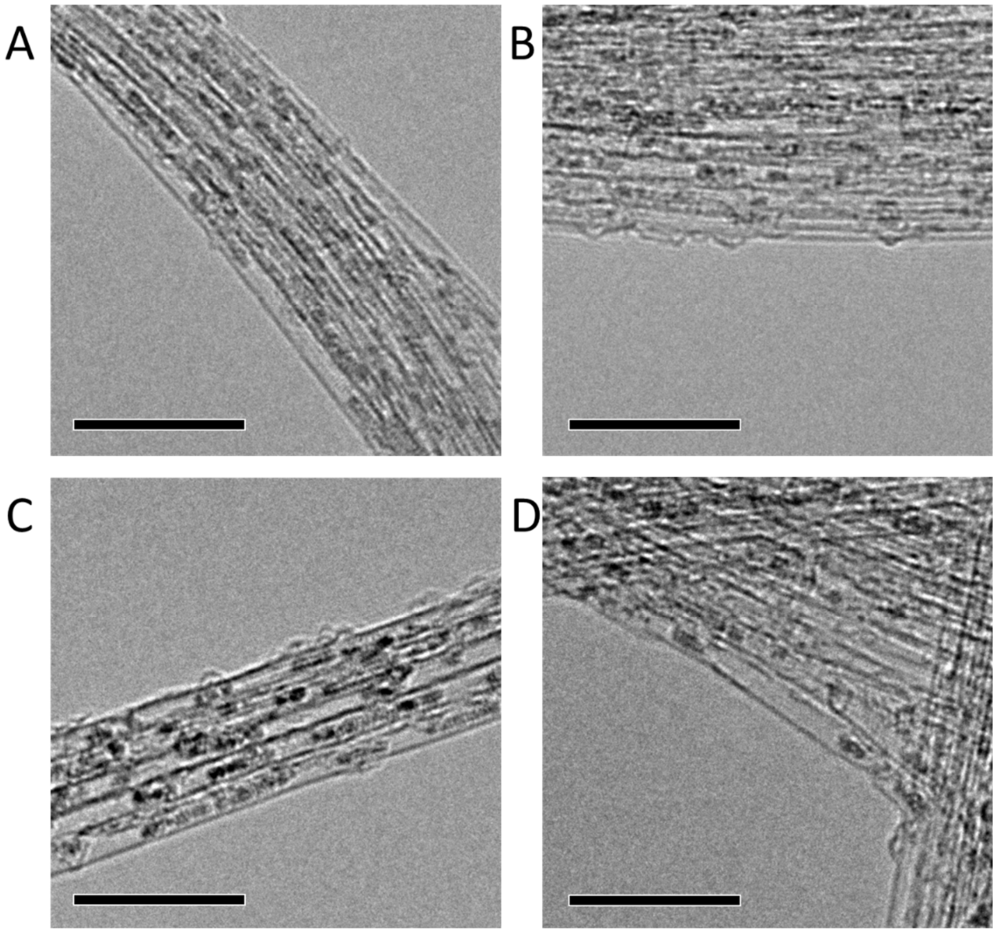

Figure 3.10. High flux TEM images of (A) {$PMo_{12}O_{40}$}@SWNT (B) {$P_2Mo_{18}O_{62}$}@SWNT (C) {$PW_{12}O_{40}$}@SWNT and (D) {$P_2W_{18}O_{62}$}@SWNT. Images acquired with an accelerating voltage of 80 kV and flux rates of between 3 – 6 x 10^5 e^- nm^{-2} s^{-1}. Scale bars 10 nm. All {POM}@SWNT materials show the presence of non-uniform larger contrasting clusters.

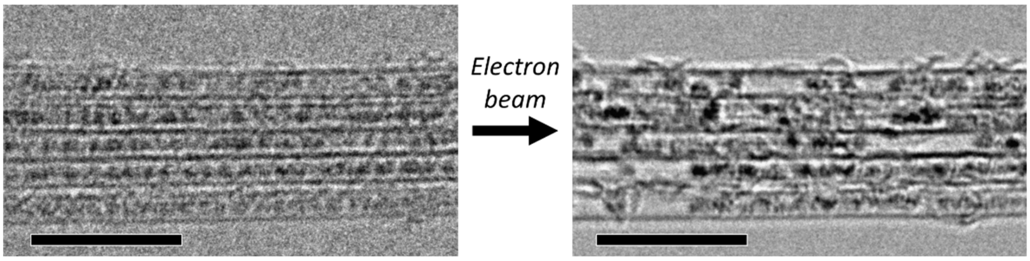

Figure 3.11. TEM images showing the changes in the {$PW_{12}O_{40}$}@SWNT material when imaged with an electron flux of 7.48 x 10^5 e^- nm^{-2} s^{-1} over the course of 20 seconds. Images acquired with an accelerating voltage of 80 kV. Scale bars 10 nm.

irreversible, although accompanied with a degree of molecular motion, which continued through the imaging series until the reaction appeared to become stabilised after several minutes. This suggested that the electron beam induced reaction was flux dependent, rather than dependent only on the total electron dose (e^- nm^{-2}) the sample had received. These observations were made across multiple SWNTs simultaneously, as SWNTs often exist in bundles due to dispersion interactions between individual nanotubes. The existence of SWNT bundles allowed for the reaction to be observed at the same time for a relatively large number of molecules (c.a. 50 – 100) simultaneously.

3.3.2 Low Flux AC-TEM

The lower magnification TEM imaging revealed the actual structure of the POM@SWNT materials, as well as being able to provide sufficient data to track the reaction at the molecular scale and the effect of electron flux on the overall electron beam induced reaction. AC-TEM was employed to probe the nature at the atomic scale of the observed reactions.

Contrast of a given element in HRTEM is dependent on atomic number; the higher the atomic number of an element the greater the contrast in bright field TEM,[44, 45] therefore $\{P_2W_{18}O_{62}\}$@SWNT was chosen for AC-TEM analysis, due to the higher contrast of tungsten atoms (Z = 74) over molybdenum atoms (Z = 42), and the higher number of tungsten atoms (18). A particular downside to AC-TEM in this case was that higher fluxes than were used to image the material at the molecular scale were generally required to observe the atomistic nature of the reaction. To overcome this a Gatan OneView camera, a more sensitive electron detector, was utilised which enabled imaging with an electron beam of 80 keV using a flux of 2.3×10^5 $e^- nm^{-2} s^{-1}$ with an exposure time of 0.1 s. Although the absolute electron flux was akin to the higher flux discussed above, the absolute dose per individual frame (2.3×10^4 $e^- nm^{-2}$ s^{-1}) and quick frame rate limited changes to the sample for any given image. Under these conditions, pristine molecules of $[P_2W_{18}O_{62}]^{6-}$ were observed, (**Fig. 3.12**)

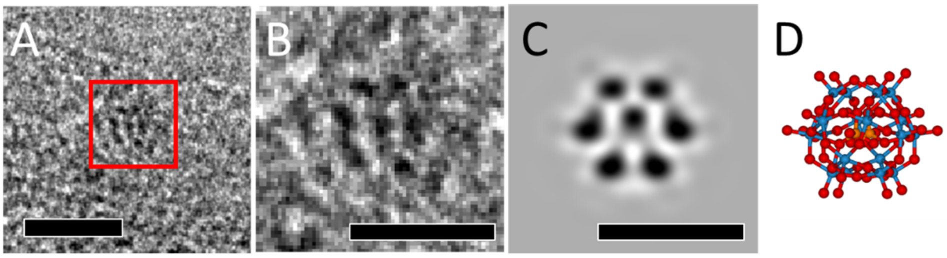

Figure 3.12. AC-TEM image (A, magnified in B) of $[P_2W_{18}O_{62}]^{6-}$ molecule confined within SWNT. Image simulation (C) shows the projection of the $[P_2W_{18}O_{62}]^{6-}$ molecule along the C_3 axis (D). Image acquired with an accelerating voltage of 80 kV, scale bars 1 nm.

showing the position of individual W atoms. W – W interatomic distances were found to be between 0.31 and 0.62 nm, close to those in $[P_2W_{18}O_{62}]^{6-}$ crystals.[46] Comparing experimental data to multislice image simulations of the W-POMs (performed by Dr. Stephen Skowron) (**Fig. 3.13**) showed a good match between the experimental data as well as with the W – W interatomic distances. Additionally, the multislice image simulation suggested that whilst individual atoms of oxygen (Z = 8) and phosphorous (Z = 15) could not be observed, they could contribute to the contrast of the tungsten atoms (Z = 74) if they overlapped in the projection, causing the "elongation" or increased contrast of the tungsten atoms. Similarly, since individual oxygen atoms could not be observed by TEM, the "size" of the molecular projection was dictated by the edge to edge metal distance in the molecule, leading to projections of the molecule that were smaller than its crystallographic dimensions, explaining the smaller sizes of the molecules observed in the lower magnification data described above.

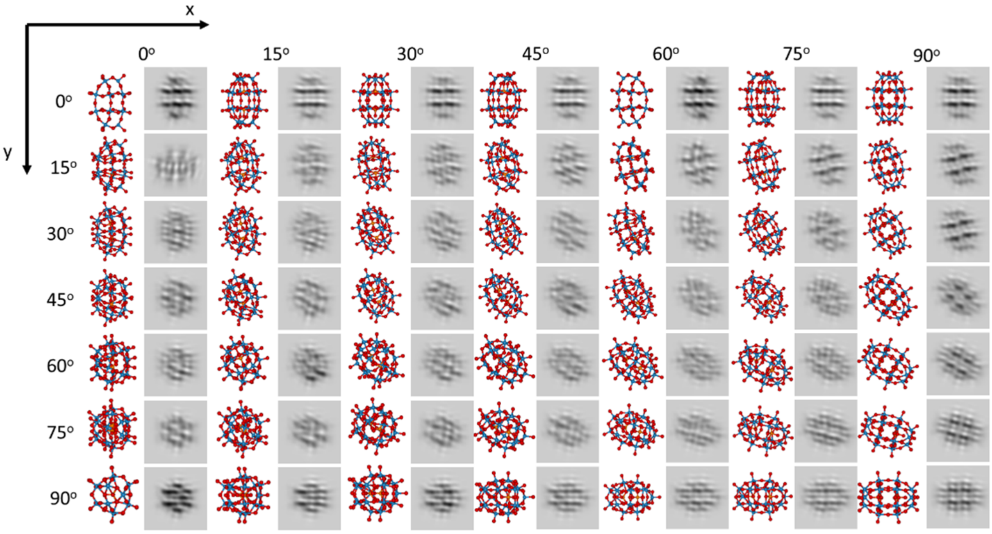

Figure 3.13. Multislice image simulations of the $[P_2W_{18}O_{62}]^{6-}$ anion, through the x and y rotational axis to 90°.

Using the low flux AC-TEM conditions, initial stages of the POM condensation reaction could be observed in the $\{P_2W_{18}O_{62}\}$@SWNT material over the course of 240 seconds

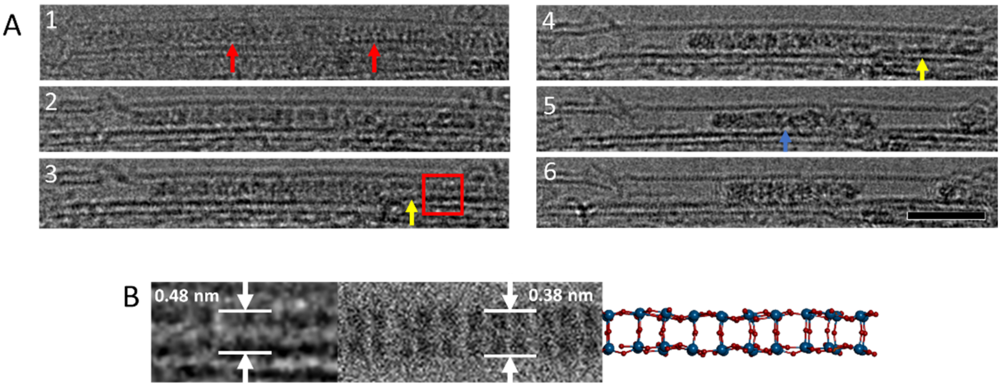

Figure 3.14. (A) AC-TEM image sequence showing a reaction between multiple $[P_2W_{18}O_{62}]^{6-}$ molecules (red arrows) leading to an ordered WO_x nanowire (yellow arrows). This ordered nanowire eventually becomes an amorphous structure of higher contrast (blue arrow), sale bar 5 nm. (B) magnified image of the red inset from (A). The magnified image shows the structure of the intermediate WO_x nanowire, along with an image simulation of the nanowire and the model. Images acquired with an accelerating voltage of 80 kV.

(**Fig. 3.14**). Initial frames showed the presence of multiple POM species along the interior of the SWNT, with M – M distances between 0.3 – 0.6 nm, consistent with pristine POM molecules (**Fig. 3.14, panel 1**). Within approximately 30 seconds, these molecules began to react with one another, forming an ordered nanowire (**Fig. 3.14, panel 3**). The M – M interatomic distance of this nanowire was found to be approximately 0.48 nm. By taking a model of 4 bonded $[P_2W_{18}O_{62}]^{6-}$ molecules and removing the capping region of the POMs, a model of the nanowire was developed (**Fig. 3.15**). When experimental images of this nanowire were compared to image simulations of the modelled nanowire, the image closely resembled that of the imaged nanowire, with a M – M interatomic spacing of 0.38 nm. Comparisons between the structure of the nanowire and orientations of the POM models suggest that as the material began to react the molecules were orientated so that their C_3-axis was perpendicular to the axis of the SWNT, bonding to one another to from a chain of $[P_2W_{18}O_{62}]^{6-}$ molecules. The material continued to condense throughout the time series, leading to a much denser, higher contrast material, similar to observations of the POM condensation observations at lower magnification.

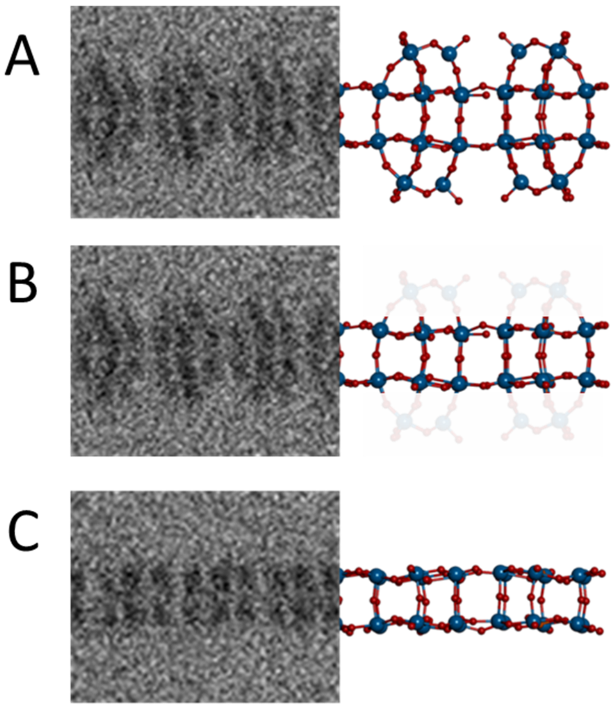

Figure 3.15. (A) Image simulation of four $[P_2W_{18}O_{62}]^{6-}$ *molecules bonded together through bridging M–O–M bonds and the corresponding model. (B) Removal of the top and bottom caps of the POMs. (C) Image simulation of the nanowire seen in figure 3.14, constructed by removing the top and bottom caps of the four bonded* $[P_2W_{18}O_{62}]^{6-}$ *molecules, with no bond relaxation applied.*

3.3.3 Stimulus of the Reaction and Mechanism of M-O Bond Dissociation

The interaction of high energy electrons from the electron beam with TEM samples can induce reactions *via* multiple mechanisms[1, 22, 34] (**Fig. 3.16**). Generally, in thick metal oxide samples damage induced by the electron beam is caused by secondary electrons, radiolysis, heating, charging (ionisation) and surface sputtering. However, due to the molecular nature of the POMs and their encapsulation within SWNTs many

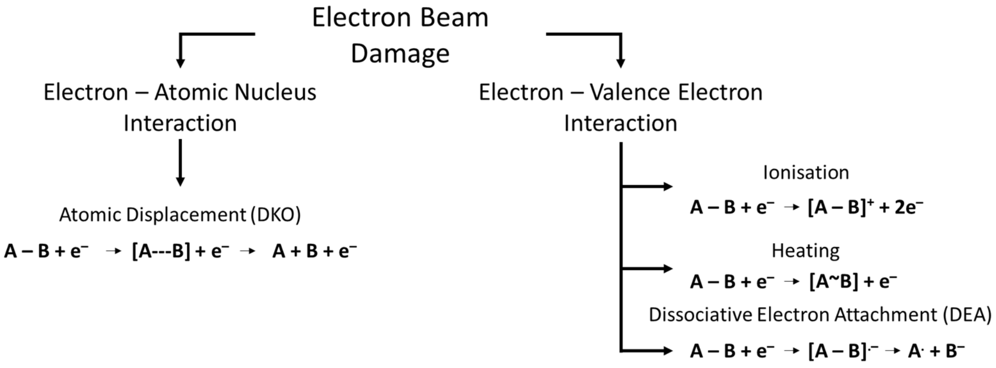

Figure 3. 16. Electron beam damage mechanisms.

of these mechanisms can be ruled out. Firstly, secondary electrons generated through the ionisation of the sample by incident primary electrons may also induce reactions within the sample. The confinement of the POMs to a low dimension means that secondary electrons are mainly emitted from the extremely thin material, limiting their interactions with the sample. Therefore, for encapsulated POMs within SWNTs, secondary electron processes can effectively be ruled out.

Secondly, it is important to consider that the majority of energy transferred from the incident electron beam to the sample, by any mechanism, eventually ends up as thermal energy upon relaxation of the system. In materials that cannot dissipate thermal energy sufficiently, such as insulators, this can lead to the melting or thermal degradation of the sample. However, due to the high conductivity of the SWNT and the close contact with the POMs, any heat is effectively dissipated, eliminating thermal effects.

Thirdly, interactions of the sample with lower energy electrons (primary or secondary) can lead to their interaction with antibonding molecular orbitals in a process known as dissociative electron attachment (DEA). Due to the thinness of the sample, primary electrons that interact with the sample maintain most of their energy, eliminating DEA, leading to ionisation and positive charging of the material. Ionisation and positive charging can also lead to changes in the material, however, due to the exceptional conductive properties of SWNTs and the close contact between the POMs and the SWNTs, charging effects or radiolysis from any ionisation are passivated. Additionally, the high degree of structural stability of POMs across multiple oxidation and excited states means that molecule degradation *via* electronic excitation routes are more unlikely.[47-49]

It is also important to note that encapsulation of molecules within SWNTs is also generally accepted to reduce the damage induced by the electron beam due to molecular isolation of the encapsulated species, limiting the interaction (or reaction) any given molecule undergoes to molecular neighbours in one dimension, however, the extremely high levels of encapsulation in the {POM}@SWNT materials likely led to increased reactivity *versus* encapsulated molecular species which are isolated from any molecular neighbours.[43]

The electron fluxes used for TEM imaging are low enough that electron collision events are at the very least on the order of microseconds apart, limiting all excitations to single electron events. Therefore, with the elimination of secondary electrons, DEA and the SWNT effectively acting as charge and thermal sink, the most significant mechanism to consider under the experimental conditions discussed above is direct knock-on (DKO) damage.

DKO is the interaction of an energetic incident electron with an atomic nucleus in the sample, caused by the electron directly transferring momentum to the atomic nuclei. Upon this momentum transfer, the atom is displaced from the equilibrium position within the bond, causing bond dissociation if the transferred energy, E_T, is greater than atomic displacement threshold energy, E_d[22, 32, 38, 39, 50] (**Fig. 3.17**).

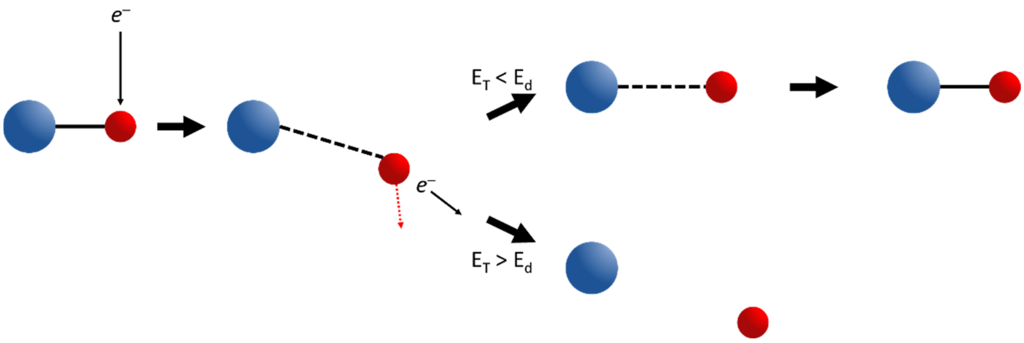

Figure 3.17. DKO diagram, Mo/W shown in blue, oxygen shown in red and is emitted.

The amount of energy that can be transferred to a given atom by an incident electron can be described by:

$$E_T = \frac{2m_n E(E + 2m_e c^2)}{(m_n + m_e)^2 c^2 + 2m_n E} sin^2\left(\frac{\theta}{2}\right) = E_{Tmax} sin^2\left(\frac{\theta}{2}\right)$$

Where m_n = mass of the atom, m_e = mass of electron, E = energy of the electron beam, c = speed of light and θ = the electron scattering angle. The maximum energy that can be transferred from an incident electron to a given atom, E_{Tmax}, is highly dependent on the mass of the atom, with lighter elements receiving larger amounts of energy for any given electron beam. The large difference in atomic masses of oxygen (m_n = 15.99) molybdenum (m_n = 95.95) and tungsten (m_n = 183.84) means that atomic displacement of the former is more likely (**Fig. 3.18**). An electron beam energy of 80 keV, the energy used to acquire the experimental data above, would in turn transfer 11.83, 1.93 and 1.03 eV to oxygen, molybdenum and tungsten respectively, with the former being significantly above the expected threshold energy for the displacement of a surface oxygen atom.[51] Dissociation of the M – O bond caused by DKO would lead to a coordinatively unsaturated metal centre, (**Fig. 3.19**) with highly reactive dangling

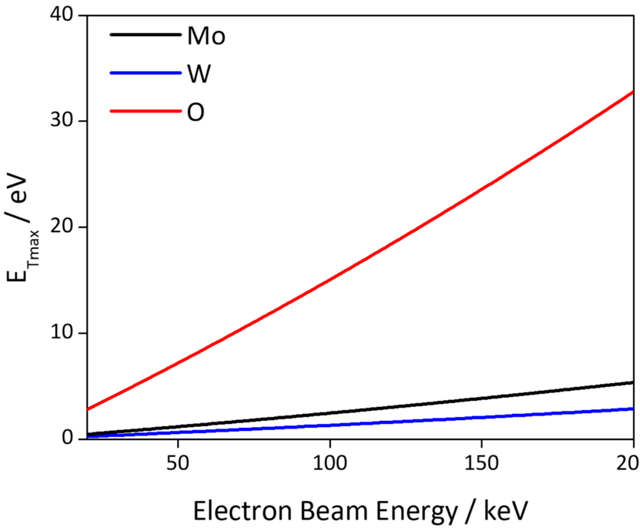

Figure 3.18. E_{Tmax} versus incident electron beam energy for molybdenum, tungsten and oxygen.

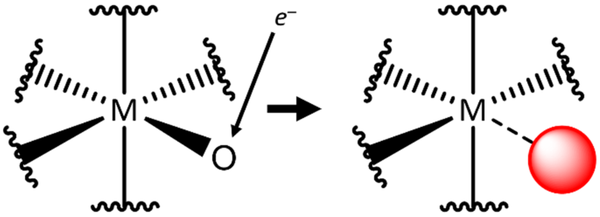

Figure 3.19. Schematic showing the formation of a coordinatively unsaturated metal centre (vacant site shown in red) following oxygen emission from DKO.

bonds, similar to work describing the dissociation of terminal C – H or C – D[52] and C – Cl or C – S bonds.[39] Whilst this DKO induced reaction should lead to minimal observable changes in the structure of the material, the unsaturated M centres likely begin to bond to their nearest neighbour through either M – O – M or M – M bonds, leading to the observation of POM condensation described above. The large number of oxygen atoms within the POM structures mean that many DKO events can occur, leading to the high reactivity described above. Overall, this can be described as an initial electron beam induced reaction subsequently followed by a chemical reaction between two reactive intermediates. As more oxygen becomes emitted, the material encapsulated within the SWNT continues to condense until, after large total doses, the nanoclusters become metallic, similar to observations of the reduction of rhenium oxide to metallic rhenium encapsulated within SWNTs.[53]

2.3.4 Reaction Kinetics

To test the hypothesis of flux dependence rather than total dose dependence, the {W-POM}@SWNT materials were imaged with an 80 keV electron beam at three different electron fluxes (herein referred to as low, medium and high) and the structure of the materials compared at comparable total doses (**Fig. 3.20**). For the {Mo-POM}@SWNT materials the reaction qualitatively appeared to be promoted similarly, however comparable direct analysis of the materials proved more difficult due to the lower contrast of Mo (Z = 42) and as such will not be discussed. Qualitatively, the reaction appeared to progress much quicker as the electron flux was increased, with higher rates of SWNT defect formation observed at higher electron flux. Through the progress of the reaction the material encapsulated within the SWNT also appeared to become higher in contrast, due to the condensation of tungsten atoms, as well as the elimination of oxygen atoms that dilute the contrast of the native POM. At the high electron flux, the POM condensation reaction appeared to occur over the course of 10 seconds, compared to several minutes at low electron flux.

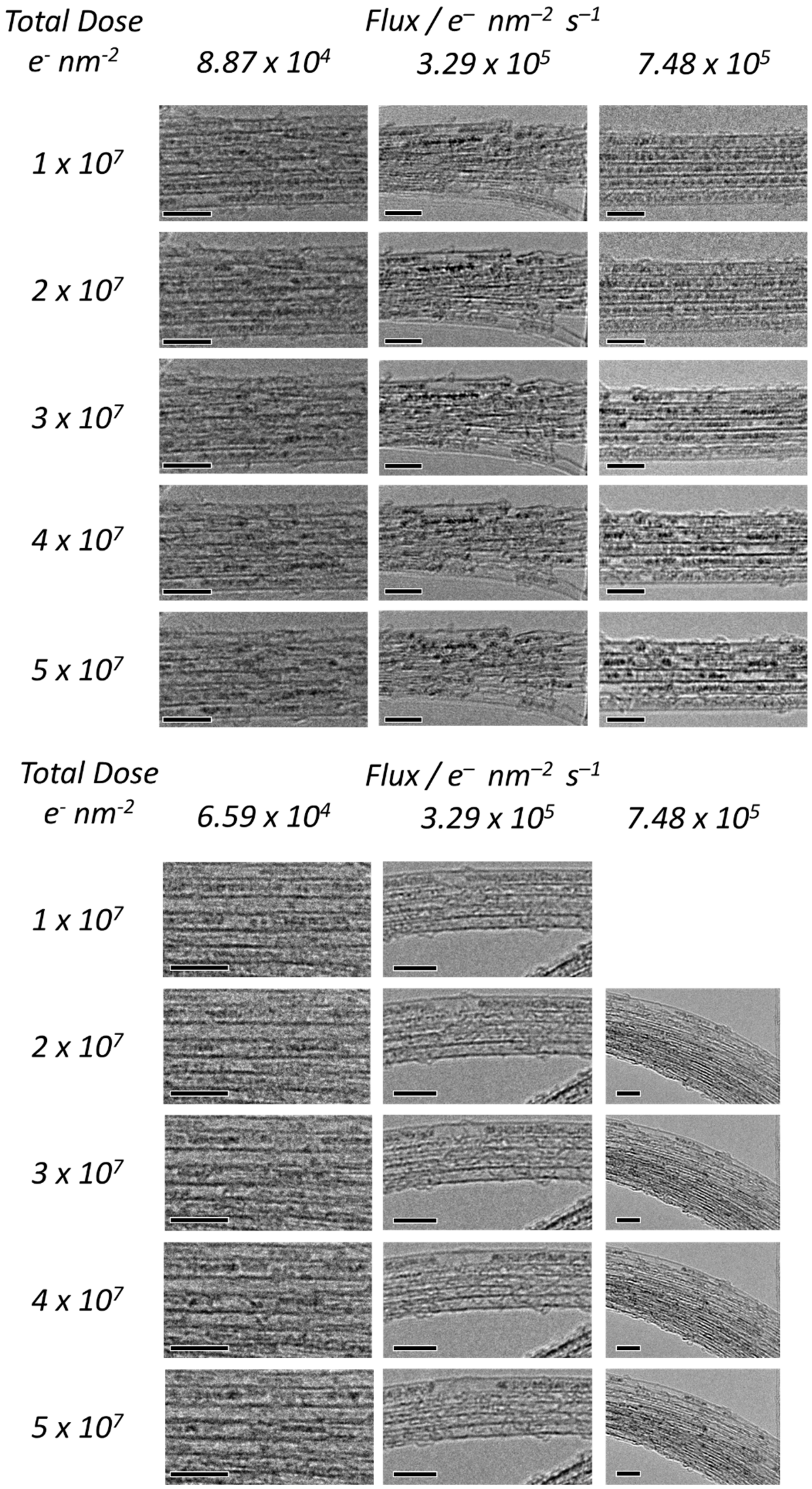

Figure 3.20. TEM time series of {$PW_{12}O_{40}$}@SWNT (top) and {$P_2W_{18}O_{62}$}@SWNT (bottom) acquired at increasing flux rates. Images acquired with an accelerating voltage of 80 kV, scale bars 5 nm.

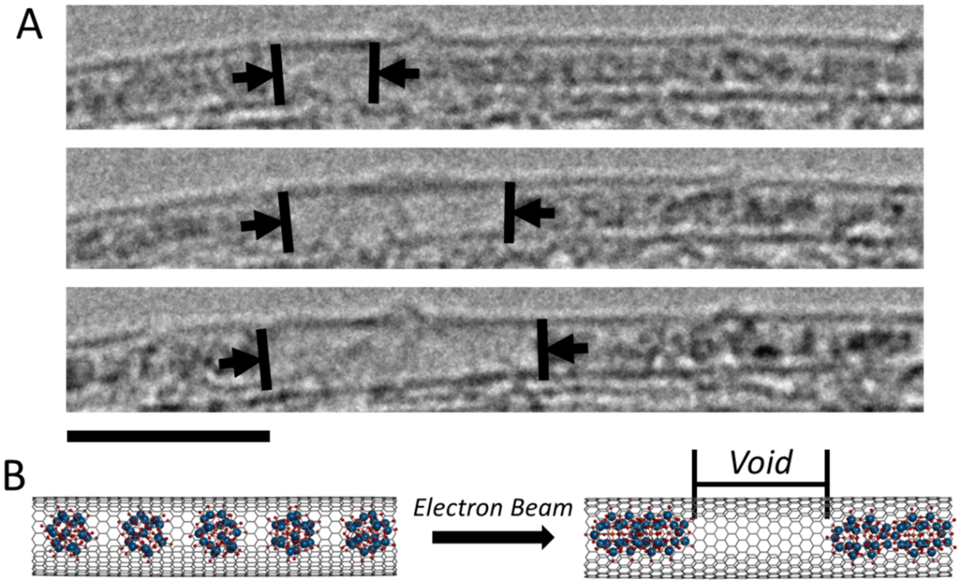

Figure 3.21. (A) Images demonstrating the decrease in volume as the POM condensation reaction proceeded, with arrows indicating void formation. Images acquired with an accelerating voltage of 80 kV, scale bar 5 nm. (B) Model of the void formation.

In order to quantify the reaction progress, the decrease in volume of the POMs and nanoclusters was used as a probe to follow the reaction (**Fig. 3.21**). A conversion factor, where 0% conversion was a SWNT filled with only pristine POM molecules and 100% conversion was representative of the elimination of all oxygen from the POM molecules, was used. To monitor the reaction frame by frame a change in the overall length of encapsulated material was calculated by:

$$\Delta l = \frac{l_0 - l_t}{l_0}$$

Where l_0 = the length of SWNT filled at t_0 and l_t = the length of SWNT filled at t. A maximum contraction in the length of material encapsulated within the SWNT was required in order to fully quantify the reactions' conversion. For example, based on experimental data, a single $[P_2W_{18}O_{62}]^{6-}$ molecule occupied approximately 0.8 nm of the length of a SWNT with a 1.4 nm diameter. A single $[P_2W_{18}O_{62}]^{6-}$ molecule would yield 18 equivalents of metallic tungsten, which based on its density (19.25 g cm^{-3}) would occupy approximately 0.3 nm^3 of a SWNT with a diameter of 1.4 nm, assuming a perfect cylindrical model. Using the same assumptions, the length of SWNT that this could occupy was given by:

$$l = \frac{0.3}{\pi(0.7)^2} = 0.19\ nm$$

Therefore, the maximum observable contraction in the length of a $[P_2W_{18}O_{62}]^{6-}$ molecule if the reaction went to completion was (which could be applied to the overall length of contrasting material):

$$\Delta l_M = \frac{0.8 - 0.19}{0.8} = 77\%$$

Demonstrating that the maximum contraction in the overall length of POMs encapsulated within SWNTs was 77%. This allowed conversion at any given time by:

$$Conversion\ \% = \frac{\Delta l}{0.77}$$

Due to the nearly perfect cylindrical shape of SWNTs and significant volume transformation upon POM condensation, a perfect cylindrical model allowed the reaction to be tracked by simply measuring the change in the length of the filled regions that appeared upon POM condensation.

Tracking the overall conversion of the of the reaction over multiple SWNTs simultaneously allowed significant kinetics data to be compiled (**Fig. 3.22**). Generally the model worked better if POMs encapsulated the entirety of the SWNT, reducing the molecular motion described previously. Overall, the model worked much better for $[P_2W_{18}O_{62}]^{6-}$ than for $[PW_{12}O_{40}]^{3-}$ likely due to the slightly smaller dimensions of the $[PW_{12}O_{40}]^{3-}$ molecule leading to greater molecular translation along the SWNT axis. The effect was particularly pronounced at lower electron flux, even for the $[P_2W_{18}O_{62}]^{6-}$ molecule, demonstrated by the poor R^2 values at low flux (**Fig. 3.22, inset**). At higher fluxes, the conversion from POM to nanocluster was rapid; the

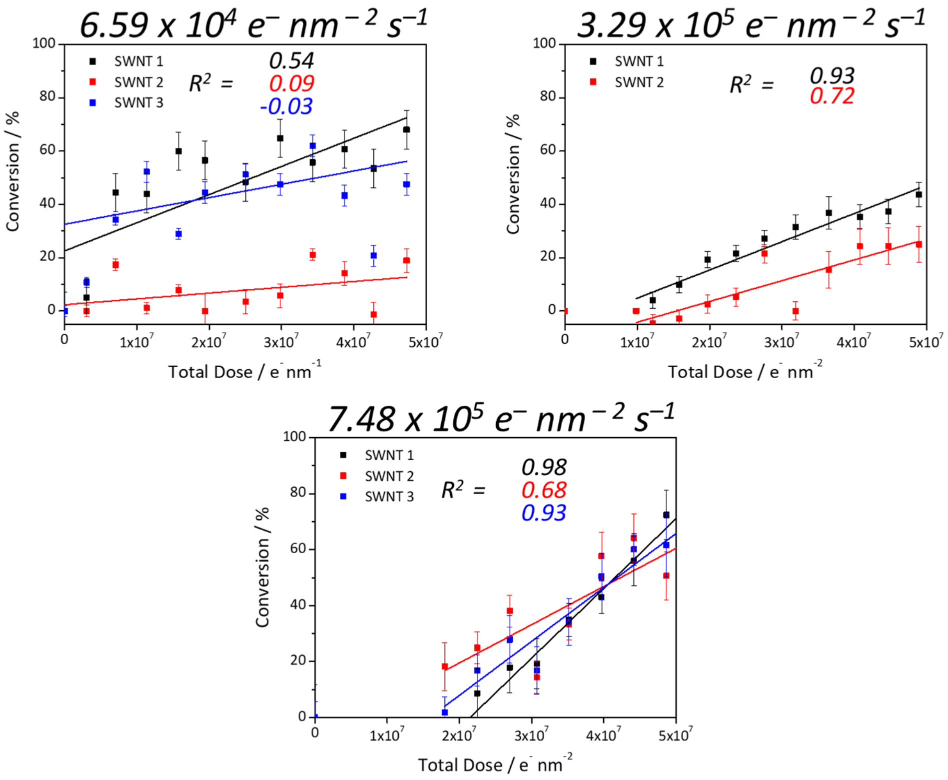

Figure 3.22. Conversion versus total dose of the POM molecules in the $\{P_2W_{18}O_{62}\}$@SWNT material for the three different electron fluxes (labelled) described above. R^2 values shown inset.

formation of large WO_x nanoclusters essentially “locked” them into position along the SWNT axis and prevented further translation. For this reason, conversion appeared higher at low electron flux for the $[PW_{12}O_{40}]^{3-}$ molecule, relative to the $[P_2W_{18}O_{62}]^{6-}$, due to the smaller size of the anion.

Normally reactions caused by the electron beam have a reaction progression that is dependent on the total dose, rather than dependent on the flux, i.e. dependent upon the total number of electrons that have passed through the sample, rather than the time between subsequent electron collisions.[54] For reactions that are total dose dependent, the gradient of the overall reaction progress against total dose can give the cross section of the reaction.[54] For the condensation of POMs, an initial electron beam induced reaction followed by subsequent reactions with molecular neighbours, these gradients give apparent cross-sections as the subsequent reaction steps which lead to the measured changes in the material are not identical to the initial reaction.

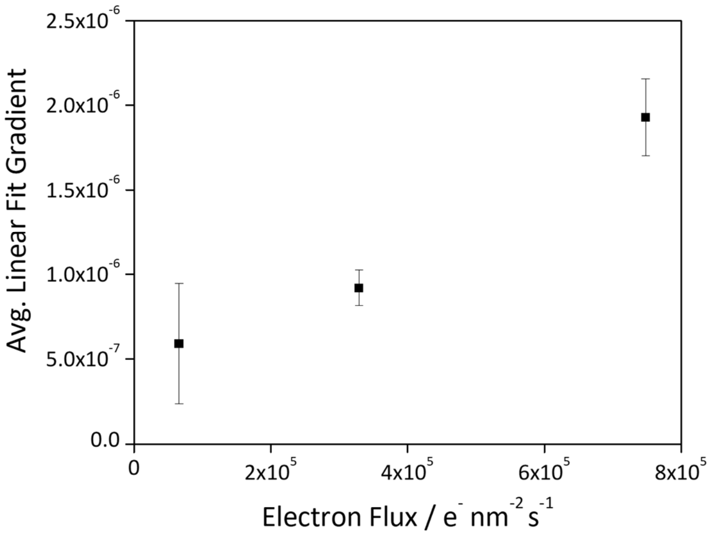

Figure 3.23. Average linear fit gradients of conversion versus total dose for the three different electron fluxes described above.

The apparent cross-sections of the reactions exhibited a dependence on the electron flux, with the gradient of the reaction progress increasing with increasing flux, indicating that at higher flux a lower total dose was required to reach the same point in the reaction (**Fig. 3.23**). This implies that the reaction proceeded *via* a process involving two stages, with reversible steps, as previous reported in graphene[55] and glasses.[56] Similarly, a dependence on electron flux in the damage of bulk metal oxides has also been reported.[51] Whilst dependence on the electron flux suggests a reversibility of the initial electron beam induced reaction, indicating an equilibrium that is controlled by the electron flux that will not progress the reaction,[23] dependence on both the flux and total dose implies both reversibility and multiple steps; an initial pre-equilibrium reaction induced by the electron beam with subsequent irreversible steps.

This suggests that the initial DKO reaction described above can be described by the reversible reaction (with $[P_2W_{18}O_{62}]^{6-}$ used as an example):

$$[P_2W_{18}O_{62}]^{6-} \rightleftharpoons [P_2W_{18}O_{61}]^{(6-n)-} + O^{n-}$$

Leading to coordinatively unsaturated tungsten centres and atomic oxygen. Based on the observation of flux dependence, the reaction can be considered reversible, where the forward DKO reaction rate can be described by:

$$v_1 = k_1[POM] = j\sigma_d[POM]$$

Where j = electron flux, σ_d = cross-section of the reaction and $[POM]$ = the projected areal density of the POM molecules (akin to concentration). The reverse step can be considered the recombination of the emitted oxygen and POM molecule and can be described by:

$$v_{-1} = k_{-1}[POM][O] = Ae^{\frac{-E_a}{RT}}[POM][O]$$

Where A = pre-exponential factor, E_a = activation energy, R = universal gas constant and T = temperature. $[POM]$ and $[O]$ are the projected areal density of the POM molecules and oxygen atoms respectively. The rate of recombination of the W–O bond was likely increased due to confinement within the SWNT due to the "cage effect"[34] which limits the diffusion of reactive species as well as enhancing their recombination rates. Overall, the observed reaction proceeds *via* the irreversible W – O – W and W – W bond formation and further elimination of oxygen, leading to condensation.

The dependence of the observed reaction on electron flux could be demonstrated by imaging the $\{P_2W_{18}O_{62}\}$@SWNT material for an extended period of time with a low electron flux of approximately 6.6 x 10^4 e^- nm^{-2} s^{-1}. Minimal changes in the volume of the encapsulated material were observed for over 600 seconds and discrete POMs were still observable (**Fig. 3.24**). Upon an increase of the electron flux to 6.2 x 10^5 e^- nm^{-2} s^{-1} the overall volume of encapsulated material rapidly decreased (in a matter of seconds) and non-uniform nanoclusters associated with the reaction's products were formed.

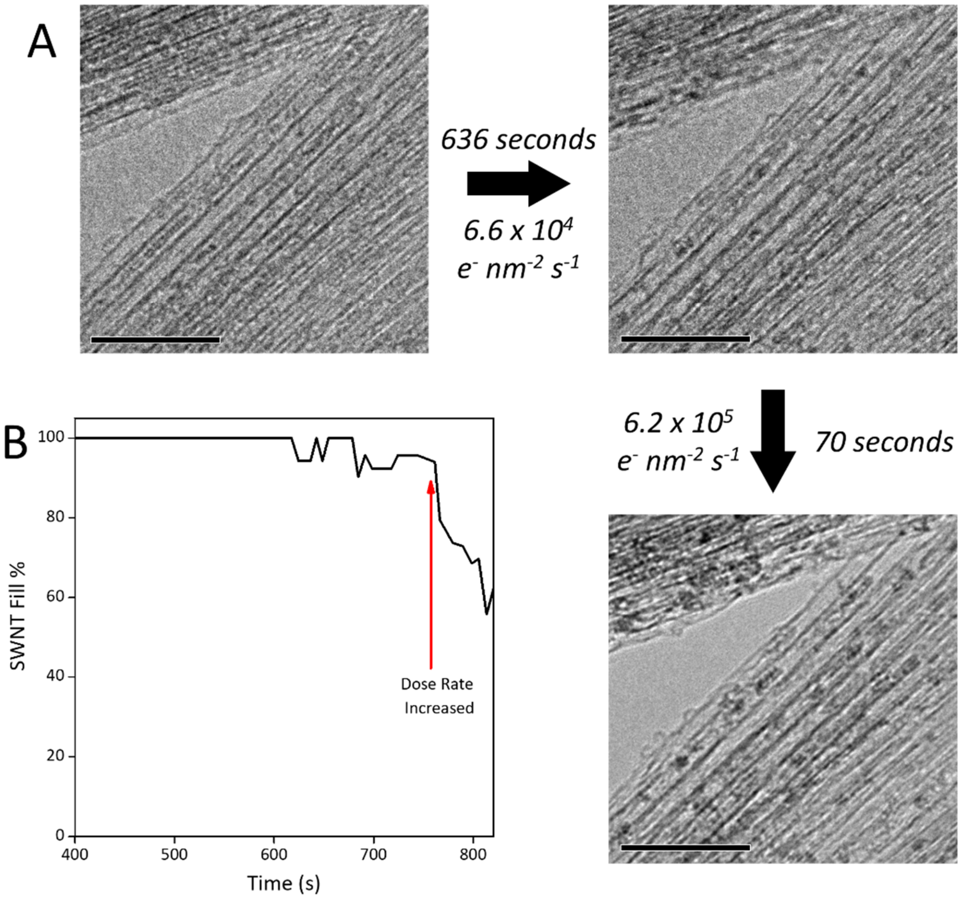

Figure 3.24. (A) TEM image series of {$P_2W_{18}O_{62}$}@SWNT material initially imaged at low electron flux (600 s). Upon increasing the flux rate, the material rapidly changed structure, and the volume of encapsulated material rapidly decreased. Scale bars 10 nm. (B) Plot of SWNT fill % against time. The overall volume of SWNT that was encapsulated with material was stable over 600 seconds. The point of dose rate increase is indicated, after which the volume rapidly decreased.

3.3.5 Studying the Reaction Products

To study the products of the reaction in atomic detail, AC-TEM was again employed. AC-TEM of the {W-POM}@SWNT materials at a flux of 1 – 2 x 10^6 e^- nm^{-2} s^{-1} at 80 keV showed the complete loss of molecular structure of the POMs, and the presence of nanoclusters ranging in size between 1–3 nm for the {POM}@SWNT materials (similar to AC-TEM of the materials described in chapter 2), with M – M spacings of 0.2 – 0.3 nm, much shorter than expected for pristine POMs, and closer to that of metallic

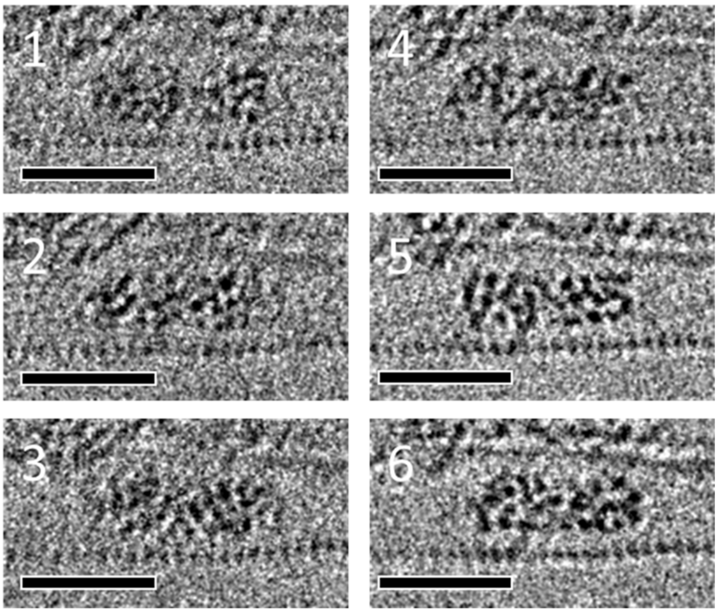

Figure 3.25. TEM image series of {$PW_{12}O_{40}$}@SWNT showing the condensation of two nanoclusters over the course of 10 seconds. Images acquired with an accelerating voltage of 80 kV. Scale bar 1 nm.

tungsten[57] (0.31 nm) due to the emission of oxygen. These nanoclusters appeared to be more stable than the pristine POM molecules, but continued condensation between the nanoclusters was observed (**Fig. 3.25**). Metallic tungsten has previously been reported to be inert to reactions with the interior of SWNTs under similar conditions,[58, 59] however the nanocluster of the {W-POM}@SWNT samples appeared

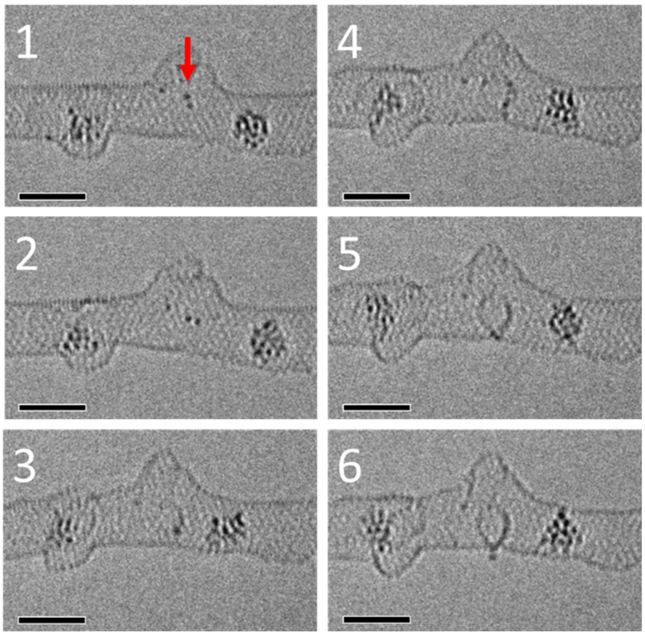

Figure 3.26. TEM image series of {$PW_{12}O_{40}$}@SWNT showing the presence of single atoms (red arrow) interacting with the SWNT side wall over the course of 200 seconds. Images acquired with an accelerating voltage of 80 kV. Scale bar 1 nm.

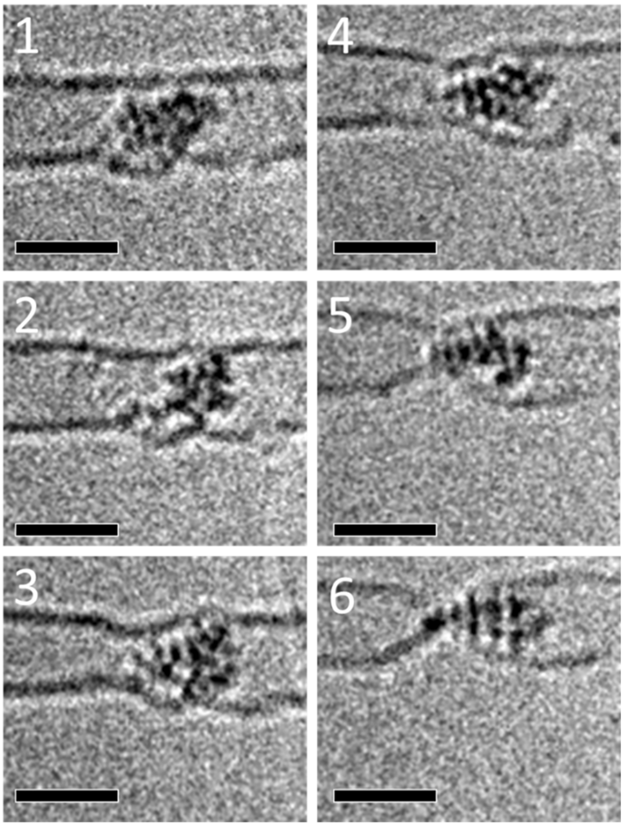

Figure 3.27. TEM image series of {$P_2W_{18}O_{62}$}@SWNT showing a nanocluster severing the SWNT entirely over the course of 150 seconds. Images acquired with an accelerating voltage of 80 kV, scale bar 1 nm.

to readily take part in reactions with the host SWNT walls, promoting the formation of vacancy defects (**Fig. 3.26**) as well as generate species containing single tungsten atoms that actively bound to the SWNT wall or moved between neighbouring nanoclusters. These single atoms could eventually become ejected from the SWNT. Entire nanoclusters were also observed to sever the SWNT entirely (**Fig. 3.27**).

In some timeseries, all three processes were observed at once. **Fig. 3.28** shows images acquired of three nanoclusters in a sample of {$P_2W_{18}O_{62}$}@SWNT acquired at a flux of 1 x 10^6 $e^- nm^{-2} s^{-1}$ with an electron beam energy of 80 keV. These nanoclusters were highly reactive over the course of 170 s. Early in the time series a single atom of tungsten can be observed bridging between two WO_x nanoclusters (**Fig. 3.28, panel 1**) before further condensation occurred between the two species. Further condensation between a third cluster occurred, before the expulsion of multiple single and few atom

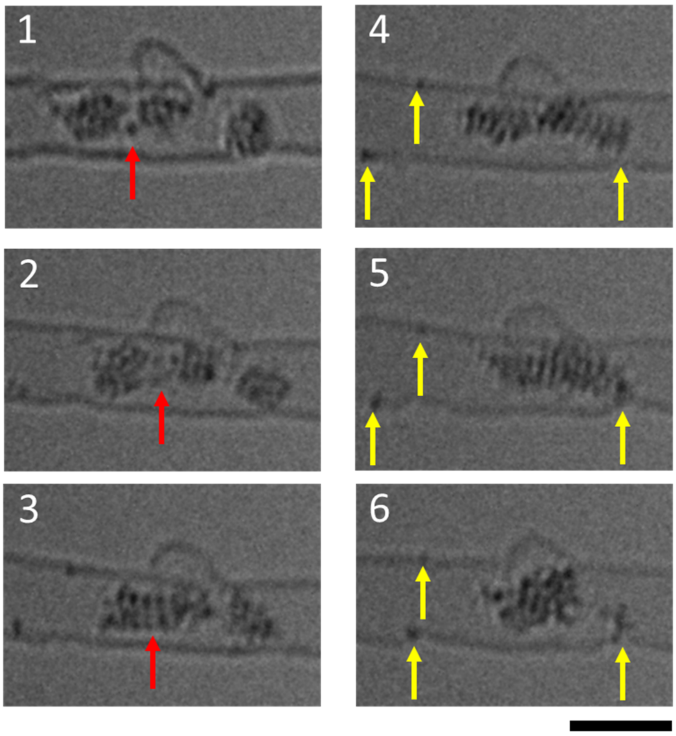

Figure 3.28. TEM image series of {$P_2W_{18}O_{62}$}@SWNT showing the condensation of multiple nanoclusters (red arrows) over the course of 170 seconds. The presence of multiple single atom species can also be seen. These small clusters could be seen interacting with the SWNT side wall (yellow arrows). Images acquired with an accelerating voltage of 80 kV. Scale bar 1 nm.

species was observed, which then appeared to strongly interact with the SWNT sidewall, forming defects.

These results suggested that although the M – M interatomic distance (approximately 0.25 nm) appeared to be close to that of metallic tungsten[57] the nanoclusters still contained a significant amount of oxygen, rendering them metal enriched metal oxide nanoclusters. When acquiring images with lower accelerating voltages (30 and 60 kV) there appeared to be no difference to the overall structure of the MO_x nanoclusters in the {POM}@SWNT materials, (**Fig. 3.29**) suggesting that the DKO reaction discussed above was promoted at unconventionally low accelerating voltages.

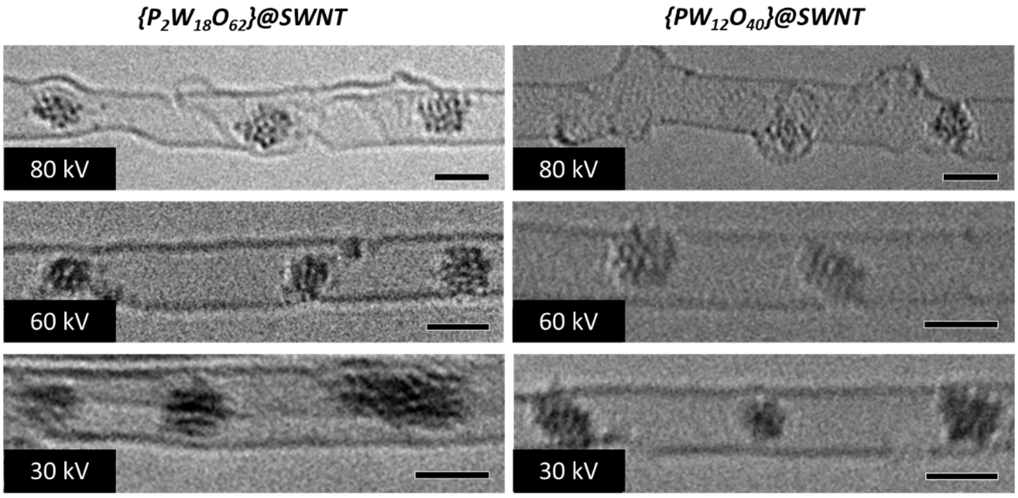

Figure 3.29. TEM images of {W-POM}@SWNT materials at varying accelerating voltages (labelled). Images acquired with an electron flux of 1 – 2 x 10^6 e^- nm^{-2} s^{-1}. Scale bars 1 nm.

3.3.6 Studying the Increased SWNT Defect Formation

Carbon is a light element (m_n = 12.01) and receives more energy from an 80 keV electron beam (E_{Tmax} = 15.77 eV) than oxygen (11.83 eV). However, the graphitic carbon lattice leads to a large stabilisation of the carbon atoms, raising the atomic displacement threshold energy, E_d, to approximately 17 eV,[60] above the E_{Tmax} value. However, in the {POM}@SWNT materials increased levels of SWNT defects were observed.

As discussed above, the electron beam induced POM condensation reaction likely proceeded with the loss of oxygen from the molecules, and SWNT defects were often observed, particularly at high electron flux. The increased level of SWNT defects along the SWNT sidewalls could be explained by considering the fate of the emitted oxygen atoms from the POM molecules and reactive WO_x nanoclusters, which likely reacted with the interior SWNT side wall.[61]

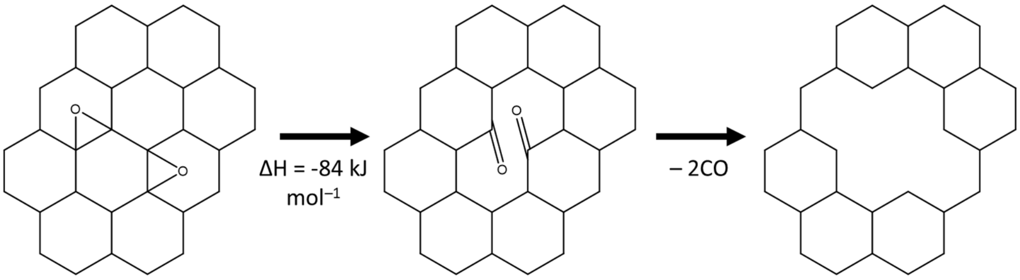

Figure 3.30. Scheme depicting the formation of SWNT sidewall defects following epoxide formation.

Vacancy defects formed from the oxidation of a graphitic lattice are induced by the formation of epoxide groups on the graphitic lattice. Once two or more epoxide groups are formed within close proximity, i.e. across a single C – C bond, they are known to undergo re-arrangement to carbonyl groups.[62] Considering the high energies that can be transferred to atoms from the electron beam, these dicarbonyl species could be emitted from the SWNT sidewall as carbon monoxide, forming vacancy defects (**Fig. 3.30**). Density functional theory (DFT) calculations were carried out (by Dr. Stephen

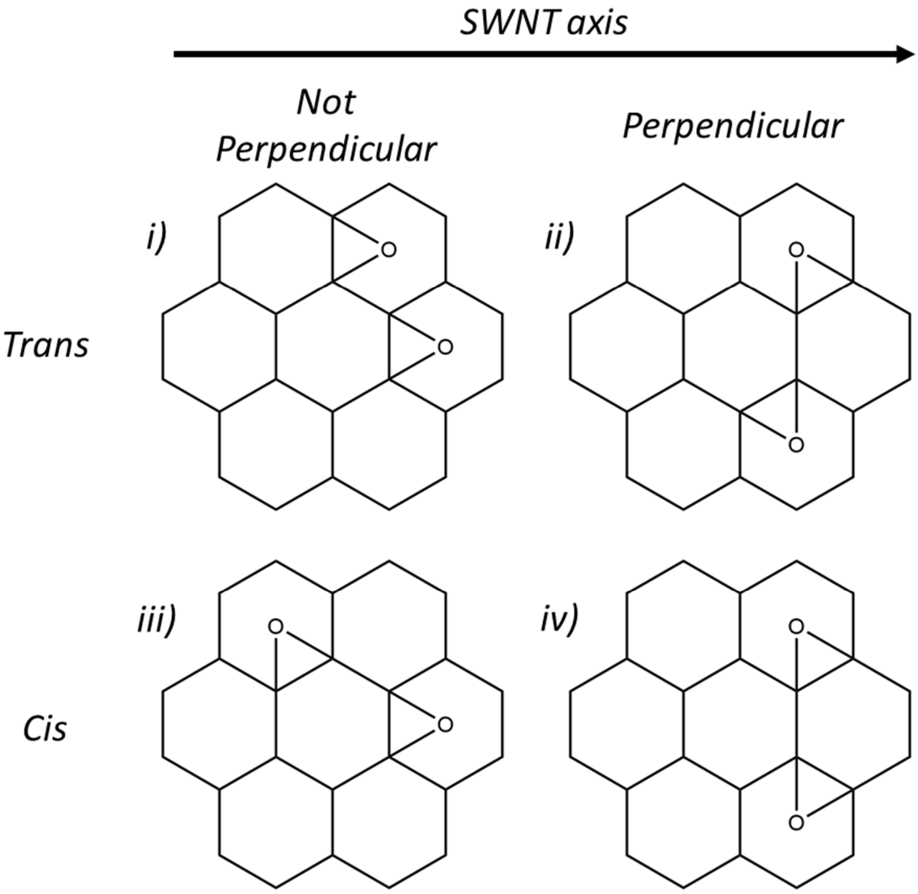

Figure 3.31. Structures of the four inequivalent di-epoxide configurations.

Table 3.1. Relative energies of the four different di-epoxide configurations shown in figure 3.31.

	Epoxide positions	Central C-C bond	Energy (eV)
i	Trans	Not Perpendicular	-2.90
ii	Trans	Perpendicular	-2.39
iii	**Cis**	**Not Perpendicular**	**-3.31**
iv	Cis	Perpendicular	-2.51

Skowron) on the stability of oxygen containing surface groups bound to the convex interior of a model (8, 8) SWNT, taking into account the two inequivalent C – C bonding environments, commonly referred to as type A and type B bonds.[63] These two different bonding environments can be described as perpendicular to the SWNT axis (Type A, bond length 1.424 Å) and not-perpendicular (at an angle of 13.1°) to the SWNT axis (Type B, bond length 1.406 Å). The formation of epoxide groups was found to be stable minima when located at either of these C – C bonds, with epoxide groups formed at not-perpendicular (type B) bonds approximately 0.36 eV more stable. The formation of a di-epoxide separated by a single C – C bond can be considered either cis or trans to one another which, when considering the position of the central C – C bond, leads to four bonding possibilities (**Fig. 3.31**).The formation of the di-epoxide species on the interior of the SWNT was found to be thermodynamically stable by 2.4 to 3.3 eV, (**table 3.1**) depending on the relative bonding configuration. Starting with the lowest energy di-epoxide configuration (not-perpendicular, cis) geometry

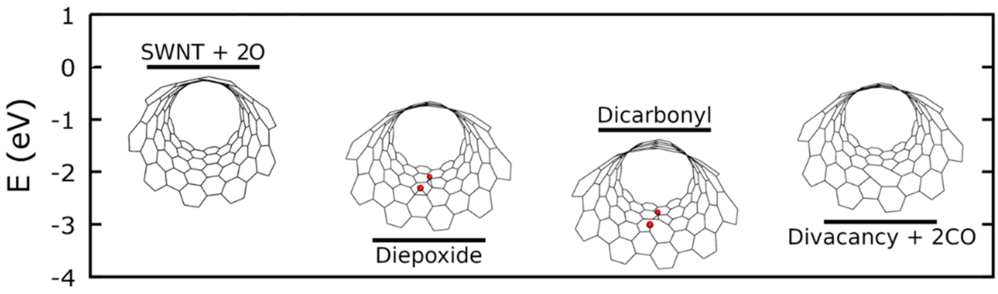

Figure 3.32. Energetic pathway of di-epoxide formation from atomic oxygen emitted from POM molecules and subsequent pathway to divacancy defect. Formation of the di-epoxide species can lead to the removal of carbon atoms from the SWNT lattice through the subsequent formation of di-carbonyl species. These defects can then propagate along the SWNT sidewall. Figure produced by Dr. Stephen Skowron.

optimisations for the corresponding di-carbonyl and resultant divacancy defect were performed giving the energetic pathway, (**Fig. 3.32**) demonstrating the ability of atomic oxygen to effectively bind to the interior SWNT sidewall and subsequently become emitted as CO, forming di-vacancy defects. Although the relative energies between each state are large, it is important to remember that the electron beam can provide a large amount of energy to the system, meaning that these states are easily accessed. A peroxide species (not shown) was also found to be relatively stable, although under electron beam irradiation would be expected to emit molecular oxygen rather than CO, leaving the graphitic wall intact.

Although the above calculations showed that divacancy defects could readily from under the imaging conditions, time resolved EDX analysis (**Fig. 3.33**) acquired under the high electron flux conditions indicated that the atomic % of oxygen did not measurably decrease with time. This indicated that either the concentration difference was too low to be detected *via* EDX measurements, the CO molecules were not as readily liberated to the TEM vacuum upon formation or oxygen was

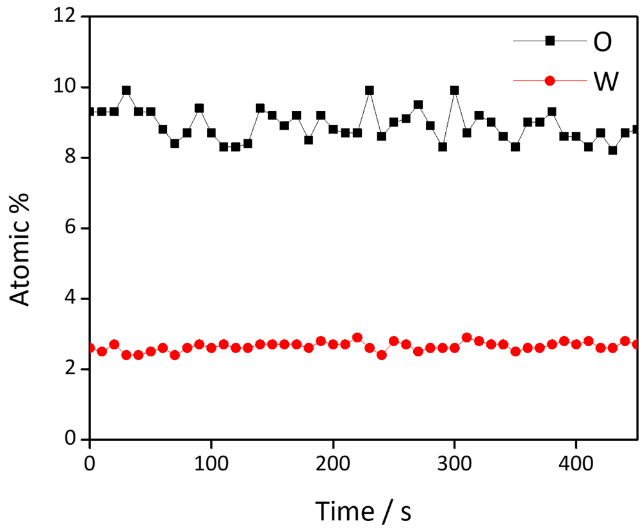

Figure 3.33. Time resolved EDX data demonstrating the change in W and O atomic % over approximately 450 s. Acquired with an electron flux of approximately 7 x 10^5 e^- nm^{-2} $s^{-1}$with an accelerating voltage of 80 kV.

permanently bound to the SWNT sidewall in epoxide and carbonyl functional groups, which could have also led to the SWNT defects observed in TEM.

Overall, whilst the POM can be thought of as becoming reduced to metallic tungsten through the emission of atomic oxygen throughout the overall reaction, the SWNT sidewall can be thought of as becoming oxidised by the emitted oxygen. These results are inconsistent with previous observations of inert tungsten nanoclusters confined within SWNTs imaged with an 80 keV electron beam, suggesting that the nanoclusters formed upon electron beam irradiation described above retained some oxygen.

3.4 Conclusion

In applying a range of different imaging conditions to the {POM}@SWNT materials, suitable conditions have been found that minimise the effect of the electron beam during imaging, allowing the true structure of the {POM}@SWNT materials to be elucidated. TEM at low electron flux showed the presence of closely packed, uniform molecules with high levels of encapsulation ubiquitous to the entire material. Over the course of exposure to the electron beam, the closely packed uniform molecules appeared to react to form condensed structures.

By applying AC-TEM methods utilising fast frame rates, the beginning of the electron beam induced reaction was observed, indicating that POM molecules begin to bridge to one another at the beginning of the reaction, before becoming amorphous nanoclusters. Under similar conditions pristine POM molecules were also observed at the beginning of the imaging series.

By imaging the materials at varying electron fluxes, it was observed that the electron beam induced reaction was dependent upon electron flux, suggesting that the initial electron beam induced process was in equilibrium which, due to the nature of the material was likely to be DKO leading to the removal of oxygen from the POM molecules, generating coordinatively unsaturated metal centres that reacted with molecular neighbours, leading to POM condensation. By applying the high frame rate AC-TEM, and the kinetic analysis of ~100 molecules under the same experimental conditions, both single molecule dynamics and kinetic behaviour of the material were studied.

The final products of the electron beam induced reaction appeared to be metal enriched metal oxide nanoparticles that were still reactive under high electron flux, partaking in further condensation reactions with one another, as well as reacting with the SWNT sidewall. The emitted oxygen from the condensation reaction appeared to readily react with the SWNT sidewall, forming oxygen containing functional groups and vacancy defects.

3.5 Experimental

Low magnification TEM images for kinetic analysis were acquired on a JEOL 2100F TEM field emission gun microscope at 80 kV. Atomically resolved AC-TEM at varying accelerating voltages was carried out at the University of Ulm on a C_s corrected FEI Titan 80-300 TEM operated at 80 kV (images were acquired using a Gatan Ultrascan 1000XP and exposure times of 0.25 to 1.0 s) and a C_s/C_C corrected SALVE microscope at 30 kV and 60 kV (images were acquired using a Gatan Ultrascan 1000XP and exposure times of 0.25 to 1.0 s). High frame rate AC-TEM imaging was carried out at ePSIC, Diamond Light Source on a C_s corrected JEOL ARM300F microscope at 80 kV (fast image acquisition with exposure times of 0.1 s and frame rates of 10 fps were required using a Gatan OneView camera). Samples were prepared by dispersion in isopropyl alcohol and were drop-cast onto a copper grid mounted with lacey carbon film.

All TEM images were processed using Gatan Digital Micrograph, and quoted distances were measured by drawing a line profile and measuring the electron density histogram.

TEM image simulations were produced using the QSTEM multislice code,[64] using 20 slices and a simulation pixel size of 0.0052 nm (re-binned 5x to the experimental pixel size of 0.026 nm). The following imaging parameters were used, in order to match the AC-TEM experiments acquired at a low doses per image (JEOL ARM300F): 80 kV accelerating voltage; -0.107 nm defocus (Scherzer); 5 nm defocal spread; 0.517 µm C_s; 1.7 mm C_c; 41.65 mrad α; 3.371 nm, 82.75° C_{12}; 0.0982 µm, 33.55° C_{21}; 0.0595 µm, -16.59° C_{23}. Poisson noise due to a finite electron dose was applied with the intensity of each pixel calculated as $I(x,y) = Poisson\ random[I_{sim}(x,y)D\Delta x\Delta y]$, where $I_{sim}(x,y)$ is the image intensity resulting from the multislice simulation, D is the electron dose per image ($4.6\text{x}10^4$ e^- nm^{-2}) and $\Delta x\Delta y$ is the pixel size.

Partial atomic charges of the $[P_2W_{18}O_{62}]^{6-}$ anion for QSTEM image simulations were calculated using a Mulliken population analysis of density functional theory (DFT) calculations. The Q-Chem 5.0 quantum chemistry software package[65] was used to optimise the geometry using the BP86VWN exchange-correlation functional,[66, 67] the def2-svpd basis set with the associated def2-ecp for tungsten,[68] and empirical Grimme dispersion, resulting in a structure with an RMSD of 0.0114 nm compared to the crystal structure.[46] These partial atomic charges were used in the multislice image simulations as described in the Supporting Information. Geometry optimisations of SWNT and oxygen species were performed at an initial B3LYP/6-31G* level of theory,[69, 70] followed by ωB97X-D/6-31G*.[71] A 1.1 nm diameter (8,8) SWNT with dangling bonds terminated by hydrogen atoms ($C_{160}H_{32}$) was the model SWNT, used to determine the stability of epoxides on the interior surface of the tube and the energetic landscape of a variety of 2O@SWNT species.

EDX data was acquired during TEM imaging, using an Oxford Instruments INCA X-ray microanalysis system over the course of 500 seconds with an electron flux of approximately 7 x 10^5 e^- nm^{-2} s^{-1}.

3.6 References

1. D. B. Williams and C. B. Carter, *Transmission Electron Microscopy* Springer, Second Edn., 2009.
2. Y. Jiang, Z. Chen, Y. Han, P. Deb, H. Gao, S. Xie, P. Purohit, M. W. Tate, J. Park, S. M. Gruner*, et al.*, *Nature*, 2018, **559**, 343-349.
3. T. Nakane, A. Kotecha, A. Sente, G. McMullan, S. Masiulis, P. M. G. E. Brown, I. T. Grigoras, L. Malinauskaite, T. Malinauskas, J. Miehling*, et al.*, *Nature*, 2020, DOI: 10.1038/s41586-020-2829-0.
4. D. Wrapp, N. Wang, K. S. Corbett, J. A. Goldsmith, C.-L. Hsieh, O. Abiona, B. S. Graham and J. S. McLellan, *Science*, 2020, **367**, 1260-1263.
5. A. W. Robertson and J. H. Warner, *Nanoscale*, 2013, **5**, 4079-4093.
6. R. R. Meyer, J. Sloan, R. E. Dunin-Borkowski, A. I. Kirkland, M. C. Novotny, S. R. Bailey, J. L. Hutchison and M. L. H. Green, *Science*, 2000, **289**, 1324-1326.
7. M. d. C. Gimenez-Lopez, A. Chuvilin, U. Kaiser and A. N. Khlobystov, *Chem. Commun.*, 2011, **47**, 2116-2118.
8. N. Agasti, M. A. Astle, G. A. Rance, J. Alves Fernandes, J. Dupont and A. N. Khlobystov, *Nano Lett.*, 2020, **20**, 1161-1171.
9. A. Botos, J. Biskupek, T. W. Chamberlain, G. A. Rance, C. T. Stoppiello, J. Sloan, Z. Liu, K. Suenaga, U. Kaiser and A. N. Khlobystov, *J. Am. Chem. Soc.*, 2016, **138**, 8175-8183.
10. C. T. Stoppiello, J. Biskupek, Z. Y. Li, G. A. Rance, A. Botos, R. M. Fogarty, R. A. Bourne, J. Yuan, K. R. J. Lovelock, P. Thompson*, et al.*, *Nanoscale*, 2017, **9**, 14385-14394.
11. B. W. Smith, M. Monthioux and D. E. Luzzi, *Nature*, 1998, **396**, 323-324.
12. K. Hirahara, K. Suenaga, S. Bandow, H. Kato, T. Okazaki, H. Shinohara and S. Iijima, *Phys. Rev. Lett.*, 2000, **85**, 5384-5387.

13. A. N. Khlobystov, R. Scipioni, D. Nguyen-Manh, D. A. Britz, D. G. Pettifor, G. A. D. Briggs, S. G. Lyapin, A. Ardavan and R. J. Nicholas, *Appl. Phys. Lett.*, 2004, **84**, 792-794.
14. A. N. Khlobystov, K. Porfyrakis, M. Kanai, D. A. Britz, A. Ardavan, H. Shinohara, T. J. S. Dennis and G. A. D. Briggs, *Angew. Chem., Int. Ed.*, 2004, **43**, 1386-1389.
15. J. Sloan, G. Matthewman, C. Dyer-Smith, A. Y. Sung, Z. Liu, K. Suenaga, A. I. Kirkland and E. Flahaut, *ACS Nano*, 2008, **2**, 966-976.
16. J. Sloan, Z. Liu, K. Suenaga, N. R. Wilson, P. A. Pandey, L. M. Perkins, J. P. Rourke and I. J. Shannon, *Nano Lett.*, 2010, **10**, 4600-4606.
17. C. Bosch-Navarro, L. M. Perkins, R. J. Kashtiban, J. P. Rourke, I. J. Shannon and J. Sloan, *ACS Nano*, 2016, **10**, 796-802.
18. N. Vats, S. Rauschenbach, W. Sigle, S. Sen, S. Abb, A. Portz, M. Durr, M. Burghard, P. A. van Aken and K. Kern, *Nanoscale*, 2018, **10**, 4952-4961.
19. T. Susi, D. Kepaptsoglou, Y.-C. Lin, Q. M. Ramasse, J. C. Meyer, K. Suenaga and J. Kotakoski, *2D Materials*, 2017, **4**, 042004.
20. M. Tripathi, A. Mittelberger, N. A. Pike, C. Mangler, J. C. Meyer, M. J. Verstraete, J. Kotakoski and T. Susi, *Nano Lett.*, 2018, **18**, 5319-5323.
21. K. Mustonen, A. Markevich, M. Tripathi, H. Inani, E.-X. Ding, A. Hussain, C. Mangler, E. I. Kauppinen, J. Kotakoski and T. Susi, *Adv. Funct. Mater.*, 2019, **29**, 1901327.
22. S. T. Skowron, T. W. Chamberlain, J. Biskupek, U. Kaiser, E. Besley and A. N. Khlobystov, *Accounts Chem. Res.*, 2017, **50**, 1797-1807.
23. S. Skowron, V. Koroteev, M. Baldoni, S. Lopatin, A. Zurutuza, A. Chuvilin and E. Besley, *Carbon*, 2016, **105**, 168-182.
24. A. P. LaGrow, D. C. Lloyd, P. L. Gai and E. D. Boyes, *Chem. Mater.*, 2018, **30**, 197-203.
25. X. Wei, D.-M. Tang, Q. Chen, Y. Bando and D. Golberg, *ACS Nano*, 2013, **7**, 3491-3497.
26. L. Luo, J. Wu, J. Luo, J. Huang and V. P. Dravid, *Sci. Rep.*, 2014, **4**, 3863.
27. E. D. Boyes, A. P. LaGrow, M. R. Ward, R. W. Mitchell and P. L. Gai, *Accounts Chem. Res.*, 2020, **53**, 390-399.

28. B. Hulsken, R. Van Hameren, J. W. Gerritsen, T. Khoury, P. Thordarson, M. J. Crossley, A. E. Rowan, R. J. M. Nolte, J. A. A. W. Elemans and S. Speller, *Nat. Nanotechnol.*, 2007, **2**, 285-289.
29. N. Pavliček, P. Gawel, D. R. Kohn, Z. Majzik, Y. Xiong, G. Meyer, H. L. Anderson and L. Gross, *Nat. Chem.*, 2018, **10**, 853-858.
30. K. Kaiser, L. Gross and F. Schulz, *ACS Nano*, 2019, **13**, 6947-6954.
31. A. Riss, A. P. Paz, S. Wickenburg, H.-Z. Tsai, D. G. De Oteyza, A. J. Bradley, M. M. Ugeda, P. Gorman, H. S. Jung, M. F. Crommie*, et al.*, *Nat. Chem.*, 2016, **8**, 678-683.
32. T. W. Chamberlain, J. Biskupek, S. T. Skowron, P. A. Bayliss, E. Bichoutskaia, U. Kaiser and A. N. Khlobystov, *Small*, 2017, **13**.
33. T. Zoberbier, T. W. Chamberlain, J. Biskupek, M. Suyetin, A. G. Majouga, E. Besley, U. Kaiser and A. N. Khlobystov, *Small (Weinheim an der Bergstrasse, Germany)*, 2016, **12**, 1649-1657.
34. S. T. Skowron, S. L. Roberts, A. N. Khlobystov and E. Besley, *Micron*, 2019, **120**, 96-103.
35. J. Biskupek, S. T. Skowron, C. T. Stoppiello, G. A. Rance, S. Alom, K. L. Y. Fung, R. J. Whitby, M. H. Levitt, Q. M. Ramasse, U. Kaiser*, et al.*, *ACS Nano*, 2020, **14**, 11178-11189.
36. B. M. Hudak, J. Song, H. Sims, M. C. Troparevsky, T. S. Humble, S. T. Pantelides, P. C. Snijders and A. R. Lupini, *ACS Nano*, 2018, **12**, 5873-5879.
37. A. H. Zewail, *Science*, 2010, **328**, 187-193.
38. K. Cao, T. Zoberbier, J. Biskupek, A. Botos, R. L. McSweeney, A. Kurtoglu, C. T. Stoppiello, A. V. Markevich, E. Besley, T. W. Chamberlain*, et al.*, *Nat. Commun.*, 2018, **9**, 3382.
39. T. W. Chamberlain, J. Biskupek, S. T. Skowron, A. V. Markevich, S. Kurasch, O. Reimer, K. E. Walker, G. A. Rance, X. Feng, K. Müllen*, et al.*, *ACS Nano*, 2017, **11**, 2509-2520.
40. A. Chuvilin, U. Kaiser, E. Bichoutskaia, N. A. Besley and A. N. Khlobystov, *Nat. Chem.*, 2010, **2**, 450-453.
41. E. Bichoutskaia, Z. Liu, N. Kuganathan, E. Faulques, K. Suenaga, I. J. Shannon and J. Sloan, *Nanoscale*, 2012, **4**, 1190-1199.
42. J. H. Warner, Y. Ito, M. Zaka, L. Ge, T. Akachi, H. Okimoto, K. Porfyrakis, A. A. R. Watt, H. Shinohara and G. A. D. Briggs, *Nano Lett.*, 2008, **8**, 2328-2335.

43. M. Koshino, Y. Niimi, E. Nakamura, H. Kataura, T. Okazaki, K. Suenaga and S. Iijima, *Nat. Chem.*, 2010, **2**, 117-124.

44. J. C. Meyer, A. Chuvilin, G. Algara-Siller, J. Biskupek and U. Kaiser, *Nano Lett.*, 2009, **9**, 2683-2689.

45. H. Lichte, P. Formanek, A. Lenk, M. Linck, C. Matzeck, M. Lehmann and P. Simon, *Annual Review of Materials Research*, 2007, **37**, 539-588.

46. B. Dawson, *Acta Crystallographica*, 1953, **6**, 113-126.

47. H. Wang, S. Hamanaka, Y. Nishimoto, S. Irle, T. Yokoyama, H. Yoshikawa and K. Awaga, *J. Am. Chem. Soc.*, 2012, **134**, 4918-4924.

48. Y. Nishimoto, D. Yokogawa, H. Yoshikawa, K. Awaga and S. Irle, *J. Am. Chem. Soc.*, 2014, **136**, 9042-9052.

49. J. M. Cameron, D. J. Wales and G. N. Newton, *Dalton Trans.*, 2018, **47**, 5120-5136.

50. T. W. Chamberlain, J. C. Meyer, J. Biskupek, J. Leschner, A. Santana, N. A. Besley, E. Bichoutskaia, U. Kaiser and A. N. Khlobystov, *Nat. Chem.*, 2011, **3**, 732-737.

51. N. Jiang, *Rep. Prog. Phys.*, 2015, **79**, 016501.

52. T. W. Chamberlain, J. Biskupek, S. T. Skowron, P. A. Bayliss, E. Bichoutskaia, U. Kaiser and A. N. Khlobystov, *Small*, 2015, **11**, 622-629.

53. P. M. F. J. Costa, J. Sloan, T. Rutherford and M. L. H. Green, *Chem. Mater.*, 2005, **17**, 6579-6582.

54. J. C. Meyer, F. Eder, S. Kurasch, V. Skakalova, J. Kotakoski, H. J. Park, S. Roth, A. Chuvilin, S. Eyhusen, G. Benner*, et al.*, *Phys. Rev. Lett.*, 2012, **108**, 196102.

55. A. W. Robertson, C. S. Allen, Y. A. Wu, K. He, J. Olivier, J. Neethling, A. I. Kirkland and J. H. Warner, *Nat. Commun.*, 2012, **3**, 1144.

56. N. Jiang and J. C. H. Spence, *Ultramicroscopy*, 2012, **113**, 77-82.

57. P. Atkins, T. Overton, J. Rourke, M. Weller and F. Armstrong, *Shriver and Atkins Inorganic Chemistry* OUP Oxford, Fifth Edn., 2009.

58. T. W. Chamberlain, T. Zoberbier, J. Biskupek, A. Botos, U. Kaiser and A. N. Khlobystov, *Chem. Sci.*, 2012, **3**, 1919-1924.

59. T. Zoberbier, T. W. Chamberlain, J. Biskupek, N. Kuganathan, S. Eyhusen, E. Bichoutskaia, U. Kaiser and A. N. Khlobystov, *J. Am. Chem. Soc.*, 2012, **134**, 3073-3079.

60. B. W. Smith and D. E. Luzzi, *J. Appl. Phys.*, 2001, **90**, 3509-3515.

61. K. Cao, S. T. Skowron, C. T. Stoppiello, J. Biskupek, A. N. Khlobystov and U. Kaiser, *Angew. Chem., Int. Ed.*, **n/a**.

62. A. Bagri, C. Mattevi, M. Acik, Y. J. Chabal, M. Chhowalla and V. B. Shenoy, *Nat. Chem.*, 2010, **2**, 581-587.

63. S. Niyogi, M. A. Hamon, H. Hu, B. Zhao, P. Bhowmik, R. Sen, M. E. Itkis and R. C. Haddon, *Accounts Chem. Res.*, 2002, **35**, 1105-1113.

64. C. T. Koch, *Determination of core structure periodicity and point defect density along dislocations,* Thesis, Arizona State Unviersity, 2002.

65. Y. Shao, Z. Gan, E. Epifanovsky, A. T. B. Gilbert, M. Wormit, J. Kussmann, A. W. Lange, A. Behn, J. Deng, X. Feng*, et al.*, *Mol. Phys.*, 2015, **113**, 184-215.

66. A. D. Becke, *Phys. Rev. A*, 1988, **38**, 3098-3100.

67. J. P. Perdew, *Phys. Rev. B: Condens. Matter Mater. Phys.*, 1986, **33**, 8822-8824.

68. F. Weigend and R. Ahlrichs, *Phys. Chem. Chem. Phys.*, 2005, **7**, 3297-3305.

69. A. D. Becke, *0*, 1993, **98**, 5648-5652.

70. P. J. Stephens, F. J. Devlin, C. F. Chabalowski and M. J. Frisch, *J. Phys. Chem.*, 1994, **98**, 11623-11627.

71. J.-D. Chai and M. Head-Gordon, *Phys. Chem. Chem. Phys.*, 2008, **10**, 6615-6620.

Chapter 4: Electrochemical Analysis of Polyoxometalates Confined within Single Walled Carbon Nanotubes

4.1 Background

The exceptional electrochemistry of polyoxometalates (POMs) has led to a significant interest into their use as redox active components in electrocatalysts and charge storage systems.[1] Generally, these molecular metal oxides can reversibly accept multiple electrons with minimal changes to their overall structure, meaning that cyclic voltammetry is often employed as an analytical technique to study the resultant properties of molecular,[2] macromolecular[3] and hybrid material[4] systems composed of POMs.

As discussed in Chapter 1, the high conductivity of carbon nanotubes (CNTs) and rich redox activity of POMs mean that they have been applied to electrocatalysis and charge storage.[5] Generally, the loading of POMs onto CNT exteriors allows electrical communication between the electrode and the insulating redox active POM, thereby allowing all molecules to collectively take part in redox processes. Additionally, if the POMs are well bound to the CNT structure, the cycling ability of the material may be enhanced.

POM-CNT materials have been applied to a range of electrocatalytic reactions, such as methanol oxidation,[6, 7] water oxidation[8, 9] and oxygen reduction.[10, 11] Pan *et al.* in 2006 reported an enhancement of the electrocatalytic activity of platinum and ruthenium nanoparticles in the methanol oxidation reaction, by depositing the nanoparticles onto multiwalled carbon nanotubes (MWNTs) modified with $[PMo_{12}O_{40}]^{3-}$.[6] The authors reported the enhancement was due to the interplay of CNT electronic properties and rich redox properties of the POMs, which increased the catalytic activity of the metallic nanoparticles and also removed products of the reaction that could poison the active surface. This study demonstrated that the intimate contact between the redox active POMs the conductive MWNTs allowed for catalytic activity to be increased. Toma *et al.* in 2010 reported a POM-CNT hybrid water oxidation catalyst composed of a ruthenium hybrid POM electrostatically loaded onto a "conducting-bed" of MWNTs.[8] This was achieved through the covalent modification of the MWNTs with positively charged functional groups[12] enabling the surface loading of the POMs through electrostatic interactions between the positively charged MWNTs and negatively charged sandwich POMs. Although this particular cluster was an already proven homogenous water oxidation catalyst,[13, 14] the ability to load this species onto a heterogenous conductive substrate allowed control of the overall morphology of the catalyst, increased the surface area of catalyst and reduced catalyst degradation through the rapid transfer of electrons to the counter electrode, preventing electron build up on the POM centre (**Fig. 4.1**).

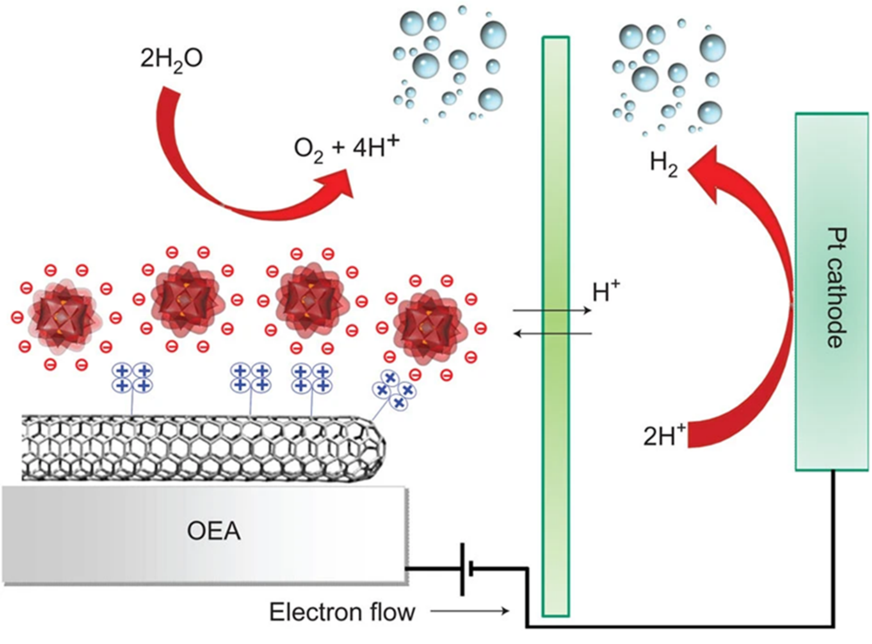

Figure 4.1. Scheme depicting a cell for water splitting utilising the POM-CNT hybrid reported by Toma et al. showing the loading of POMs onto the MWNTs via cationic surface groups. Reproduced from reference 8 with permission from Springer Nature.

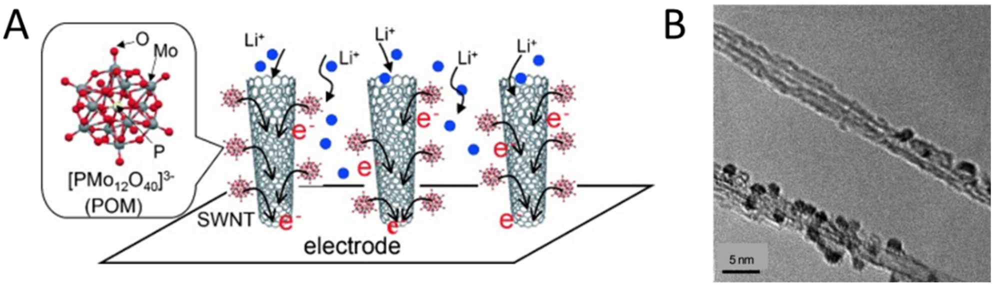

Figure 4.2. (A) Schematic showing the structure of the POM-CNT hybrid material. (B) Tranmission electron microscopy (TEM) image of the material. Adapted from reference 15 with permission from John Wiley and Sons.

POM-CNT hybrid materials have been applied to energy storage applications as electrode materials for lithium-ion batteries and supercapacitors. Kawasaki *et al.* loaded POMs onto the surface of SWNTs by mixing $[Bu_4N]_3[PMo_{12}O_{40}]$ with SWNTs in solution.[15] The large quaternary ammonium cations interacted strongly with the SWNT surface, creating a positive charge to facilitate loading of the POM anion. Upon reduction of the material, the authors stated that lithium cations could readily insert within the SWNTs, (**Fig. 4.2**) resulting in rapid and reversible charge-discharge cycles and giving an increased capacity of 320 mAh g^{-1} (*versus* 260 mAh g^{-1} for the cluster on its own).

Ma *et al.* also grafted POMs onto a SWNT surface *via* π-π stacking interactions, by synthesising an organo-functionalised $[SiW_{11}O_{39}]^{7-}$ POM with pyrene groups[16] (**Fig. 4.3, A**). Utilising this material as the anode material, the composite boasted high performance with an initial discharge capacity of 1570 mAh g^{-1}. Over repeated cycling,

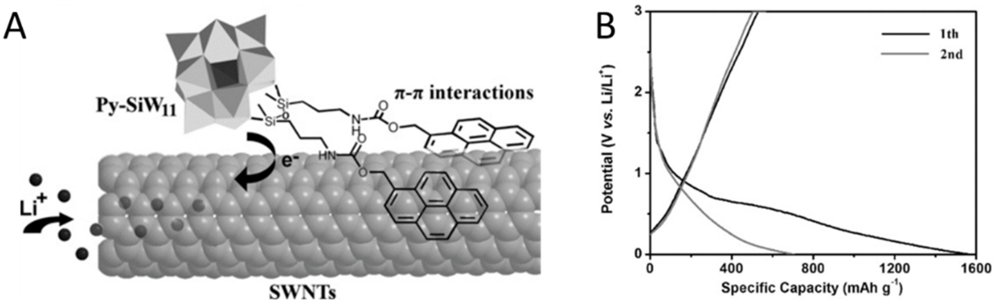

Figure 4.3. (A) schematic showing the structure of the POM-CNT hybrid (B) charge-discharge curves of the first and second cycle of the material at a current density of 0.5 mA cm^{-2}based on the weight of the hybrid POM only. Adapted from reference 16 with permission from John Wiley and Sons.

a reversible capacity of 580 mAh g^{-1} was observed for up to 100 cycles (**Fig. 4.3, B**). The authors also attributed the high capacity of the material to the insertion of Li^+ ions within the SWNT interior during charge-discharge.

More recently, the Lian group has reported several works on the grafting of POMs to the exterior of MWNTs through a layer-by-layer (LbL) approach, which were then analysed with cyclic voltammetry. Bajwa *et al.* first published a POM-CNT hybrid prepared by the LbL assembly of MWNTs, poly(diallyldimethylammonium chloride) (PDDA) and $H_3[PMo_{12}O_{40}]$ or $H_5[PMo_{12}V_2O_{40}]$ (added in this order from the respective solutions) onto their working electrode[17] (**Fig. 4.4**). Cyclic voltammograms (CVs) of the materials in 1M H_2SO_4 showed peaks due the loaded POM materials, with low peak-to-peak separation values (ΔE_p) that indicated the processes were surface confined and that the systems could charge rapidly (**Fig. 4.5, A**). The authors reported large increases in the capacities of these materials relative to MWNTs, which could be further increased by layering both POM moieties onto the MWNTs (**Fig. 4.5, B**). The group also applied this PDDA LbL method to $H_4[GeMo_{12}O_{40}]$ on MWNTs, which showed better capacitance retention than bare MWNTs.[18]

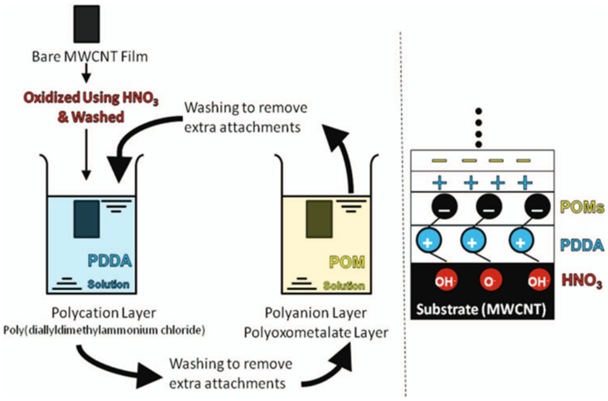

Figure 4.4. Schematic demonstrating the LbL assembly method, as well as the composition of the resultant electrode surface. Reproduced from reference 17 with permission from IOP Publishing.

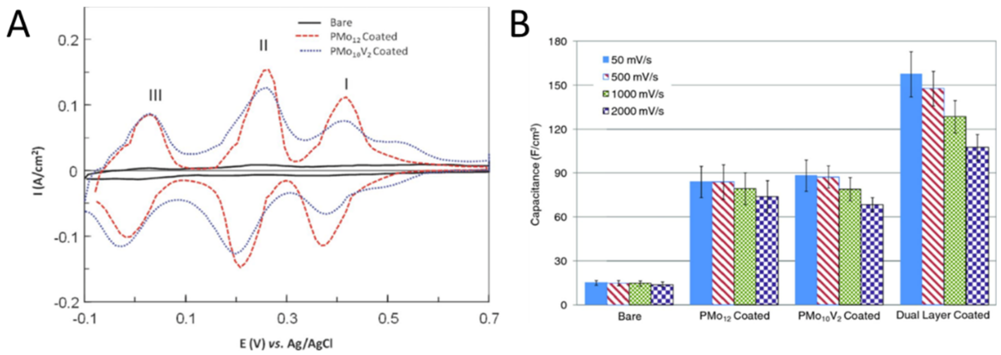

Figure 4.5. (A) CVs of bare MWNT, $H_3[PMo_{12}O_{40}]$-PDDA/MWNT and $H_5[PMo_{10}V_2O_{40}]$-PDDA/MWNT functionalised electrodes. (B) Volume specific capacitance of bare MWNT, single layer coated MWNTs and double layer coated MWNTs. Adapted from reference 17 with permission from IOP Publishing.

Later, Genovese *et al.* produced a POM-MWNT hybrid composed of mixed Mo and W Keggin anions.[19] Utilising the same LbL PDDA method as reported previously, the group instead opted for a POM layer composed of $H_3[PMo_{12}O_{40}]$ and $H_3[PW_{12}O_{40}]$/$H_4[SiW_{12}O_{40}]$, deposited onto the PDDA/MWNT material from the same solution. In all cases, the redox behaviour of the hybrid material, probed by cyclic voltammetry in 1M H_2SO_4, was dominated by the molybdate redox chemistry, which led to a potential window limited to approximately –0.15 V *vs* Ag/AgCl, due to the onset of the hydrogen evolution reaction (HER) at the active Mo(VI) centres. This meant that the redox chemistry of the W-Keggin anions, which normally occur at more negative potentials, could not be observed. When using the $H_3[PMo_{12}O_{40}]$/$H_4[SiW_{12}O_{40}]$ mixture, the authors reported that the electrode displayed

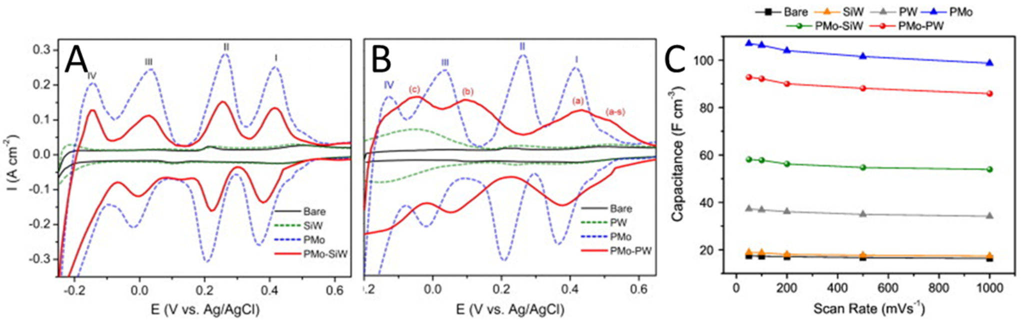

Figure 4.6. (A) CVs of bare MWNTs, pure $H_4[SiW_{12}O_{40}]$-MWNT, pure $H_3[PMo_{12}O_{40}]$-MWNT and $H_4[SiW_{12}O_{40}]$/$H_3[PMo_{12}O_{40}]$-MWNT electrodes. (B) CVs of bare MWNTs, pure $H_3[PW_{12}O_{40}]$-MWNTs, pure $H_3[PMo_{12}O_{40}]$-MWNT and $H_3[PW_{12}O_{40}]$/$H_3[PMo_{12}O_{40}]$-MWNT electrodes. A & B recorded in 1M H_2SO_4 electrolyte. (C) Capacitance of the POM@MWNT electrodes. Adapted from reference 19 with permission from Elsevier.

behaviour that was close to that of only $H_3[PMo_{12}O_{40}]$, however when the silicate W-POM was swapped for the phosphate W-POM, the material appeared to exhibit a synergistic effect, displaying redox behaviour different to that of the individual components (**Fig. 4.6, A & B**). The authors reported that all materials showed an increase in capacitance relative to that of unfunctionalised MWNTs (**Fig. 4.6, C**). The processes were noted to be highly reversible with low ΔE_p values of 29 mV at scan rates of 25 mV s^{-1}. The group later furthered this work by explaining the difference in the redox profiles of the materials by mixing the Mo and W POMs in different ratios and depositing them onto MWNTs.[20] When the different POMs were mixed in solution, they formed new species composed of mixed addenda atoms (**Fig. 4.7, A**). The authors found that the ratio would dictate the POM species deposited onto the MWNTs, and thus the redox profiles of the solid-state materials (**Fig. 4.7, B**).

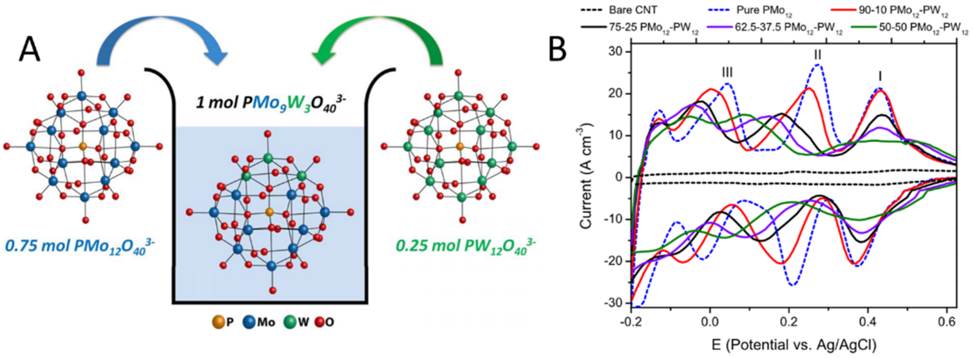

Figure 4.7. (A) Schematic of mixed addenda synthesis. (B) CVs of bare MWNTs and the mixed Mo-Keggin and W-Keggin -MWNT layered materials. Adapted from reference 20 with permission from IOP Publishing.

Genovese *et al.* later reported a new approach to the group's LbL method in the synthesis of POM-CNT hybrid materials for pseudocapacitive materials.[21] The group applied the PDDA similar to their previous studies as well as imidazolium cations as ionic liquids. The imidazolium cations acted as effective linkers to allow POMs to bind better to the MWNTs, and thus increase the electron transfer kinetics from the CNTs to the bound POMs. The ΔE_p values of the observed POM processes were around 45 mV at a scan rate of 100 mV s^{-1}, suggesting that the support material was conductive

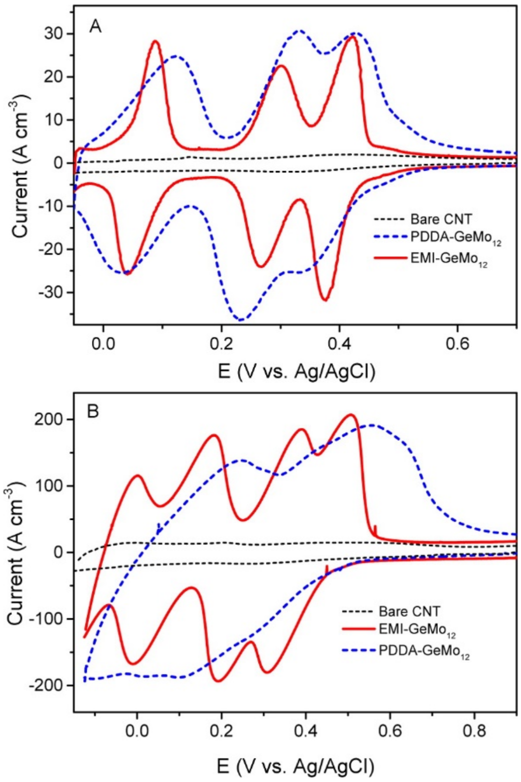

Figure 4.8. CVs of bare MWNTs, $H_4[GeMo_{12}O_{40}]$/imidazolium/PDDA-MWNTs and $H_4[GeMo_{12}O_{40}]$/PDDA-MWNTs at scan rates of 100 mV s^{-1} (A) and 1000 mV s^{-1}(B). Reproduced from reference 21 with permission from The American Chemical Society.

and that the electronic communication between electrode and POM was exceptional. Utilising branched imidazolium cations, the authors demonstrated that the results were largely the same, with some minor differences which they attributed to the varied geometries of the different imidazolium cations. When comparing the new ionic liquid functionalised POM-MWNTs to POM-MWNTs produced *via* their previous method (above) the CVs were clearly different, with the previously reported hybrid material showing wide redox processes and large ΔE_p values (97 mV at a scan rate of 100 mV s^{-1}) (**Fig. 4.8**). However, the capacitance of the materials synthesised without the imidazolium cations was larger, which the authors attributed to a higher POM loading. In order to overcome this, the authors polymerised the imidazolium ionic liquid, to retain both the rapid electron transfer rates of the cationic linkers and afford the higher loading ability of the PDDA. The resultant materials performed better than the PDDA samples, however they appeared to show slightly wider peaks and larger

ΔE_p values than when the imidazolium linkers were used monomerically. The authors further demonstrated that this new approach could increase electron transfer rates in their multilayer assemblies.

The work of the Lian group is the current gold standard in rapid electron transfer in POM-CNT hybrids. The examples discussed above show the ability of CNTs to readily transport electrons to/from the redox active POMs that are grafted onto their surfaces. However, these systems can encounter a myriad of issues, such as leaching and degradation over repeated cycles and poor electron transfer kinetics with increasing multilayer assemblies.

Encapsulation of redox active species confined within SWNTs and DWNTs (discussed in Chapter 1) have previously demonstrated the ability to reduce leaching and degradation. However, previous reports of POMs encapsulated within SWNTs[22-25] have not reported any electrochemical analysis. The successful encapsulation of POMs within SWNTs, driven by the charge transfer and resultant electrostatic attraction between the SWNTs and POMs in solution, (chapter 2) and extremely high levels of encapsulated POMs (chapter 3) mean that the POM@SWNT materials present an attractive target for charge storage. The intimate contact between the graphitic conducting SWNT walls and the redox active POMs would likely allow for rapid charge transfer between the electrode and POM. Additionally, it was observed that the POMs were stabilised in harsh conditions, such as exposure to high pH, demonstrating the potential of these hybrids as stable redox active solid-state materials.

However, as discussed in chapter 1, the effects of nanoconfinement within narrow SWNT channels may present challenges if the materials are to be used for the intercalation of cations (due to inhibited mass transport) over multiple cycles. The well-defined redox processes of the Keggin and Wells-Dawson anions makes the

{POM}@SWNT materials an ideal model system for studying the mass transport of electrolytes to nanoconfined species during electrochemical cycling. Cyclic voltammetry has previously been shown to be a powerful technique in the understanding of redox active POM-CNT hybrids and will therefore be widely utilised in this study.

4.2 Aims and Objectives

The aim of this study is to assess the electrochemical properties of the {POM}@SWNT materials. The high level of encapsulation and strong electrostatic interactions between the two species would likely allow for rapid electron transfer between the two species, however the mass transport of electrolyte ions to the redox active centres may lead to a poorer performance in the materials. The well-defined redox processes of the POMs may provide a suitable model system for studying the overall mass transport of ions within the nanoconfined environments of the SWNTs. This study will be achieved *via* the following aims:

1. Cyclic voltammetry of the materials in acidic electrolytes, which should provide the lowest barrier to mass transport.
2. Cyclability studies of the materials over 1000 cycles and harsh conditions to assess the stability of the materials.
3. Screening of a variety of electrolytes with varied cations and anions to study the effect of mass transport on the system during electrochemical cycling and assessing their applicability in real-world use.

4.3 Results and Discussion

4.3.1 POM Solution Cyclic Voltammetry

Cyclic voltammograms (CVs) in acidic solutions of the Mo Keggin, $[PMo_{12}O_{40}]^{3-}$, and Wells-Dawson, $[P_2Mo_{18}O_{62}]^{6-}$, anions (**Fig. 4.9**) showed reversible reductions in the range of -0.4 – 0.6 V. The $E_{1/2}$ values for these are summarised in **table 4.1**.

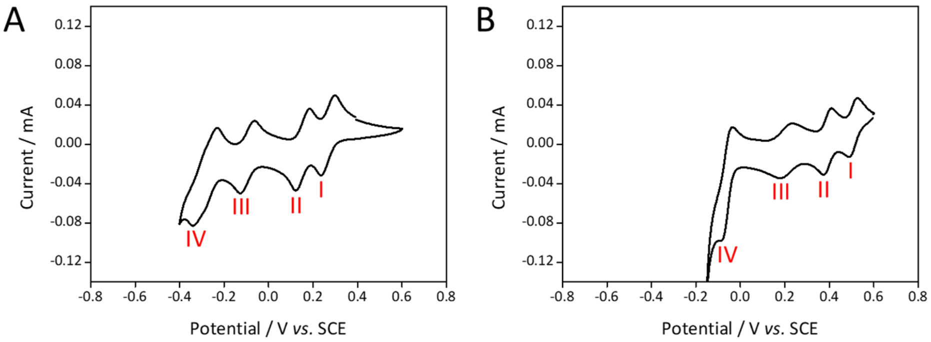

Figure 4.9. (A) CV of $H_3[PMo_{12}O_{40}]$ recorded in 0.1 M H_2SO_4 with 80% v/v MeCN. (B) CV of $K_6[P_2Mo_{18}O_{62}]$ recorded in 1 M H_2SO_4. Both CVs recorded with a glassy carbon working electrode (GCE), saturated calomel reference electrode (SCE) and platinum counter electrode at a scan rate of 0.1 V s^{-1} with an analyte concentration of 10 mM. All reductions labelled (red, inset).

Table 4.1. $E_{1/2}$ values for the Mo-POMs taken from figure 4.9. All potentials versus SCE.

$[PMo_{12}O_{40}]^{3-}$		$[P_2Mo_{18}O_{62}]^{6-}$	
Process	Potential / V	Process	Potential / V
I	0.271	I	0.430
II	0.151	II	0.330
III	-0.094	III	0.130
IV	-0.282	IV	-0.125

For $[PMo_{12}O_{40}]^{3-}$, these processes corresponded to four reversible reductions (I, II, III, IV) of two, two, two and four-electrons:[26, 27]

$$[PMo_{12}O_{40}]^{3-} + 2e^- + 2H^+ \rightleftharpoons [H_2PMo_{12}O_{40}]^{3-} \text{ (I)}$$

$$[H_2PMo_{12}O_{40}]^{3-} + 2e^- + 2H^+ \rightleftharpoons [H_4PMo_{12}O_{40}]^{3-} \text{ (II)}$$

$$[H_4PMo_{12}O_{40}]^{3-} + 2e^- + 2H^+ \rightleftharpoons [H_6PMo_{12}O_{40}]^{3-} \text{ (III)}$$

$$[H_6PMo_{12}O_{40}]^{3-} + 4e^- + 4H^+ \rightleftharpoons [H_{10}PMo_{12}O_{40}]^{3-} \text{ (IV)}$$

All processes occurred with proton coupled electron transfer (PCET).[26] For an ideal diffusion controlled reversible process at 25 °C the peak to peak separation, $\Delta E_{p,}$ of the redox waves can be described by:[28]

$$\Delta E_p = \frac{2.3RT}{nF} = \frac{59}{n}\ mV$$

Where n = number of electrons transferred in the redox reaction, R = the ideal gas constant, T = temperature and F = faraday's constant. Therefore, for a two-electron process this should be approximately 30 mV and for a four-electron process this should be approximately 15 mV. These values are rarely observed experimentally, but values close to these can be considered reversible. The three two-electron processes showed peak-to-peak separations close to that of 60 mV, the ideal ΔE_p value for a true reversible single electron electrochemical process, indicating that the processes were electrochemically quasi-reversible. The final and most negative process had a ΔE_p value of 90 mV (**table 4.2**).

As previously mentioned in chapter 2, for $[PMo_{12}O_{40}]^{3-}$ it is important to remember that a large amount of organic solvent must be added to stabilise the anion upon reduction in aqueous media.[27] In changing the ionic strength of the electrolyte media, and in turn the activity coefficient, the formal potential of the processes will have been altered.[26, 28] Additionally, the PCET exhibited by all four reductions of the POM is highly

Table 4.2. Peak-to-peak separation values for $H_3[PMo_{12}O_{40}]$ in acidic solution at a scan rate of 0.1 V s⁻.[1]

$[PMo_{12}O_{40}]^{3-}$	
Process	Δe_p / mV
I	59
II	59
III	61
IV	90

dependent on pH, causing changes to the electrochemical behaviour of the anion in the electrolyte chosen.

For $[P_2Mo_{18}O_{62}]^{6-}$, the four observed processes (I, II, III, IV) in the -0.2 – 0.6 V window also corresponded to two, two, two and four-electron processes:[26, 29]

$$[P_2Mo_{18}O_{62}]^{6-} + 2e^- + 2H^+ \rightleftharpoons [H_2P_2Mo_{18}O_{62}]^{6-} \text{ (I)}$$

$$[H_2P_2Mo_{18}O_{62}]^{6-} + 2e^- + 2H^+ \rightleftharpoons [H_4P_2Mo_{18}O_{62}]^{6-} \text{ (II)}$$

$$[H_4P_2Mo_{18}O_{62}]^{6-} + 2e^- + 2H^+ \rightleftharpoons [H_6P_2Mo_{18}O_{62}]^{6-} \text{ (III)}$$

$$[H_6P_2Mo_{18}O_{62}]^{6-} + 4e^- + 4H^+ \rightleftharpoons [H_{10}P_2Mo_{18}O_{62}]^{6-} \text{ (IV)}$$

The first two two-electron processes exhibited ΔE_p values of 29 mV, indicating that they were true reversible processes. The final two processes exhibited ΔE_p values of 46 mV (two-electron processes) and 29 mV (four-electron process) indicating that these processes were less reversible than the former two (**table 4.3**). The data reported above is in good agreement with previous literature describing Keggin and Wells-Dawson molybdate CV behaviour.[26]

Table 4.3. Peak-to-peak separation values for $K_6[P_2Mo_{18}O_{62}]$ in acidic solution at a scan rate of 0.1 V s^{-1}.

$[P_2Mo_{18}O_{62}]^{6-}$	
Process	Δe_p / mV
I	29
II	29
III	46
IV	29

CVs in acidic solutions of the W Keggin, $[PW_{12}O_{40}]^{3-}$, and W Wells-Dawson, $[P_2W_{18}O_{62}]^{6}$, anions (**Fig. 4.10**) showed multiple reversible reductions in the range of 0 - – 0.7 V. The $E_{1/2}$ values are summarised in **table 4.4**.

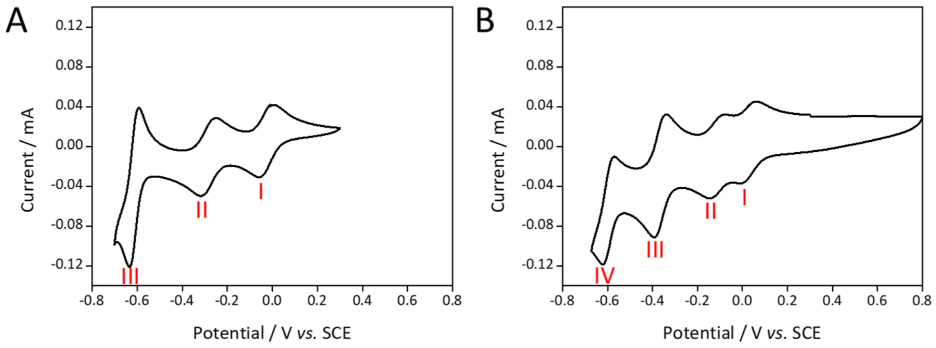

Figure 4.10. (A) CV of $H_3[PW_{12}O_{40}]$ recorded in 1 M H_2SO_4 (B) CV of $K_6[P_2W_{18}O_{62}]$recorded in 1 M H_2SO_4. Both CVs recorded with a GCE working electrode, SCE reference electrode and platinum counter electrode at a scan rate of 0.1 V s^{-1} with an analyte concentration of 10 mM. All reductions labelled (red, inset).

Table 4.4. $E_{1/2}$ values for the W-POMs taken from figure 4.10. All potentials versus SCE.

$[PW_{12}O_{40}]^{3-}$		$[P_2W_{18}O_{62}]^{6-}$	
Process	Potential / V	Process	Potential / V
I	-0.020	I	-0.005
II	-0.275	II	-0.135
III	-0.590	III	-0.380
- - - - - - - - - -		IV	-0.610

For $[PW_{12}O_{40}]^{3-}$ the observed processes corresponded to three reversible reductions (I, II, III) of one, one and two-electron processes:[26]

$$[PW_{12}O_{40}]^{3-} + e^- \rightleftharpoons [PW_{12}O_{40}]^{4-} \text{ (I)}$$

$$[PW_{12}O_{40}]^{4-} + e^- \rightleftharpoons [PW_{12}O_{40}]^{5-} \text{ (II)}$$

$$[PW_{12}O_{40}]^{5-} + 2e^- + 2H^+ \rightleftharpoons [H_2PW_{12}O_{40}]^{6-} \text{ (III)}$$

The one-electron processes both had ΔE_p values of 56 mV, indicating that the processes were fully reversible. The final two-electron process, which occurred with PCET,[26] had a ΔE_p value of 34, close to that of 29 mV (**table 4.5**). This indicated that all three processes were highly reversible.

Table 4.5. Peak-to-peak separation values for $H_3[PW_{12}O_{40}]$ in acidic solution at a scan rate of 0.1 V s⁻.[1]

$[PW_{12}O_{40}]^{3-}$	
Process	ΔE_p / mV
I	56
II	56
III	34

For $[P_2W_{18}O_{62}]^{6-}$ four processes were observed (I, II, III, IV) corresponding to two one-electron processes and two two-electron processes:[26]

$$[P_2W_{18}O_{62}]^{6-} + e^- \rightleftharpoons [P_2W_{18}O_{62}]^{7-} \text{ (I)}$$

$$[P_2W_{18}O_{62}]^{7-} + e^- \rightleftharpoons [P_2W_{18}O_{62}]^{8-} \text{ (II)}$$

$$[P_2W_{18}O_{62}]^{8-} + 2e^- + 2H^+ \rightleftharpoons [H_2P_2W_{18}O_{62}]^{8-} \text{ (III)}$$

$$[H_2P_2W_{18}O_{62}]^{8-} + 2e^- + 2H^+ \rightleftharpoons [H_4P_2W_{18}O_{62}]^{8-} \text{ (IV)}$$

The first two one-electron processes had peak-to-peak separation values around 50 mV, indicating the processes were highly reversible and that the POM may have adsorbed onto the electrode surface. The two two-electron processes, which occurred with PCET,[26] had ΔE_p values of 44 and 37 mV respectively, indicating the processes were highly reversible (**table 4.6**).

Table 4.6. Peak-to-peak separation values for $K_6[P_2W_{18}O_{62}]$ in acidic solution at a scan rate of 0.1 V s⁻.[1]

$[P_2W_{18}O_{62}]^{6-}$	
Process	ΔE_p / mV
I	51
II	49
III	44
IV	37

4.3.2 {Mo-POM}@SWNT Cyclic Voltammetry

In order to investigate the redox properties of the {POM}@SWNT materials they first had to be deposited onto a glassy carbon electrode (GCE) from an aqueous ink, composed of 1 wt% analyte ({POM}@SWNT) and 3 wt% polytetrafluoroethylene (PTFE) binder to prevent stripping of the active material from the working electrode during cyclic voltammetry measurements. Although PTFE is non-conductive, the SWNTs dispersed amongst the binder provided a conductive matrix to probe the redox activity of the material. This GCE working electrode was then added to an electrochemical cell with a saturated calomel reference electrode (SCE) and platinum counter electrode all submerged within a conductive electrolyte.

CVs of the {$PMo_{12}O_{40}$}@SWNT material acquired with a 1M H_2SO_4 supporting electrolyte showed a drastic change from the $[PMo_{12}O_{40}]^{3-}$ species dissolved in solution (**Fig. 4.11, B**). Within the window of 0 – 0.6 V two processes were observed

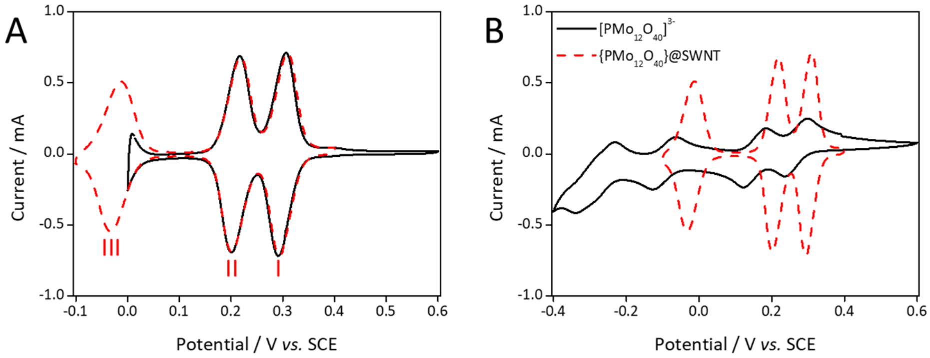

Figure 4.11. (A) CVs of {$PMo_{12}O_{40}$}@SWNT in 1 M H_2SO_4. (B) CV comparison between $[PMo_{12}O_{40}]^{3-}$ (current multiplied by 10 for clarity) and {$PMo_{12}O_{40}$}@SWNT. $[PMo_{12}O_{40}]^{3-}$ CV recorded in 0.1 M H_2SO_4 with 80% MeCN v/v. All CVs recorded with a GCE working electrode, SCE reference electrode and platinum counter electrode at a scan rate of 0.1 V s^{-1}. All reductions labelled (red, inset).

Table 4.7. $E_{1/2}$ values of $H_3[PMo_{12}O_{40}]$ and {$PMo_{12}O_{40}$}@SWNT. All potentials versus SCE.

$[PMo_{12}O_{40}]^{3-}$		**{$PMo_{12}O_{40}$}@SWNT**	
Process	Potential / V	Process	Potential / V
I	0.271	I	0.302
II	0.151	II	0.209
III	-0.094	III	-0.023
IV	-0.282	- - - - - - - - - -	

which appeared to be highly symmetrical, (**Fig. 4.11, A, black trace**) exhibiting surface confined behaviour. When the electrochemical window was extended to –0.1V (**Fig. 4.12, A, red dashed trace**) a further process was observed which appeared stable. The formal potentials, $E_{1/2}$, of these processes were 0.302 (I), 0.209 (II) and –0.023 (III) V *vs* SCE (**table 4.7**). This confirmed that the encapsulated POMs were still electrochemically active upon encapsulation within the SWNTs and indicated that the POMs were still discrete molecular species, in good agreement with XPS data (Chapter 2), although all four processes from the native POM did not appear accessible. The peak positions of the first two reductions relative to the free POM in solution did not appear to shift and the final peak appeared to shift positive, however due to the different electrolyte used to record the data, direct comparison of this system is problematic.[27]

For fully reversible surface confined processes, the peak-to-peak separation of a redox couple is expected to be 0 mV.[28, 30] For $\{PMo_{12}O_{40}\}$@SWNT the ΔE_p values were much lower than for the $[PMo_{12}O_{40}]^{3-}$ anion dissolved in solution. For the first two reductions, I and II, were found to be 15 and 17 mV respectively, approaching the value of 0 mV, confirming that the processes were surface confined, yet quasi-reversible. The final process had a ΔE_p value of 20 mV (**table 4.8**).

Table 4.8. Peak-to-peak separation values for $\{PMo_{12}O_{40}\}$@SWNT in acidic solution at a scan rate of 0.1 V s^{-1}.

$\{PMo_{12}O_{40}\}$@SWNT	
Process	ΔE_p / mV
I	15
II	17
III	20

The peak current of a diffusion controlled electrochemical reaction at a planar disk electrode can be described by the Randles-Ševćik equation:[28, 30]

$$i_p = 0.446AC\sqrt{\frac{n^3F^3\upsilon D}{RT}}$$

Where i_p = max current, A = electrode area, C = analyte concentration υ = scan rate and D = diffusion constant. Crucially, for a diffusion-controlled system, the peak current should increase linearly with respect to the square root of the scan rate used. For a process confined the electrode surface the peak current can be described by the equation:[28, 30]

$$i_p = \frac{n^2F^2\Gamma A\upsilon}{4RT}$$

Where Γ is the electrode surface coverage of the analyte. Therefore, for electrochemical processes confined to the electrode surface the peak current should increase linearly with scan rate. When cycling the $\{PMo_{12}O_{40}\}$@SWNT material at varying scan rates, the peak current for all three processes (both oxidation and reduction) was found to linearly increase with increasing scan rate (**Fig. 4.12**). Fitting

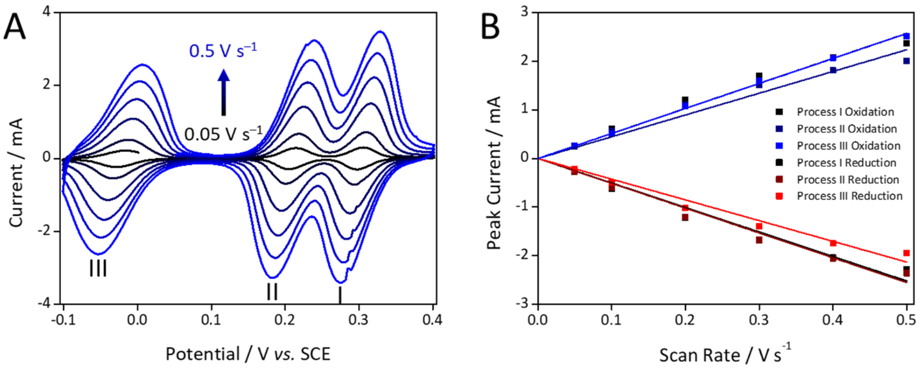

Figure 4.12. (A) CVs of $\{PMo_{12}O_{40}\}$*@SWNT at varying scan rates (inset) with labelled processes (inset). (B) Plot of peak current versus scan rate for the three processes, which shows a linear relationship again scan rate.* R^2 *values shown in table 4.9. CVs recorded with a GCE working electrode, SCE reference electrode and platinum counter electrode at a scan rate of 0.1 V* s^{-1}*. All reductions labelled inset.*

Table 4.9. R^2 values for the linear plots in figure 4.12, B.

$\{PMo_{12}O_{40}\}$@SWNT	
Process	R^2
I Reduction	0.987
II Reduction	0.991
III Reduction	0.989
I Oxidation	0.991
II Oxidation	0.985
III Oxidation	0.999

a linear trend to the data gave R^2 values all above 0.98 (**table 4.9**) demonstrating that the processes were all surface confined.

For a truly reversible process the peak to peak separation, ΔE_p, should be independent of the scan rate used, however for a quasi-reversible process, ΔE_p varies with scan rate. The ΔE_p values of the three processes of $\{PMo_{12}O_{40}\}$@SWMT appeared to scale with increasing scan rate, (**Fig. 4.13**) suggesting the processes were quasi-reversible.

For a reversible surface confined process, the full width at half max (FWHM) of a redox peak at 25 °C can be described by:[28, 30]

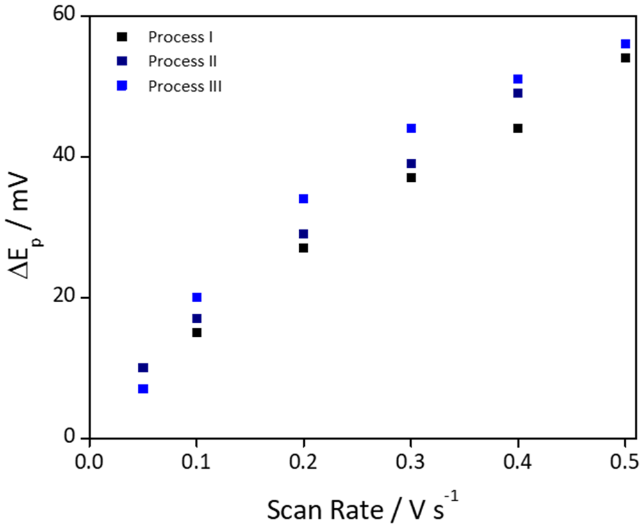

Figure 4.13. ΔE_p values for the three processes in $\{PMo_{12}O_{40}\}$@SWNT at varying scan rates. Data taken from CVs in figure 4.12, A.

$$FWHM = \frac{3.53RT}{nF} = \frac{90.6}{n}\ mV$$

The FWHM values of the three reductions of the material were used to identify the number of electrons transferred in each process. At a scan rate of 0.1 V s^{-1} in the 1 M H_2SO_4 electrolyte the three reduction processes had FWHM values of 42, 44 and 57 mV for I, II and III respectively. Solving these for n gave 2.15, 2.06 and 1.59 for I, II and III respectively, indicating that the first two processes were two-electron transfers whilst the final process was also likely a two-electron redox event, yet less reversible. The FWHM of the return oxidations were 42, 45 and 62 for I, II and III respectively, further supporting the poor reversibility of process III. These are summarised in **table 4.10**. FWHM values for a truly reversible surface process should not vary with scan rate, however these values did scale with increasing scan rate (**Fig. 4.14**) providing further evidence for the quasi-reversibility of the system. According to the FWHM, the three processes all appeared to be approximately two-electron processes, suggesting that upon encapsulation, the processes were akin to those observed in solution.

Table 4.10. FWHM values for reductions and oxidations of the {$PMo_{12}O_{40}$}@SWNT material, taken from figure 4.14.

{$PMo_{12}O_{40}$}@SWNT - Reduction			**{$PMo_{12}O_{40}$}@SWNT - Oxidation**		
Process	FWHM / mV	n (no. of electrons)	Process	FWHM / mV	n (no. of electrons)
I	42	2.15 (2)	I	42	2.15 (2)
II	44	2.06 (2)	II	45	2.01 (2)
III	57	1.59 (~2)	III	62	1.46 (~1)

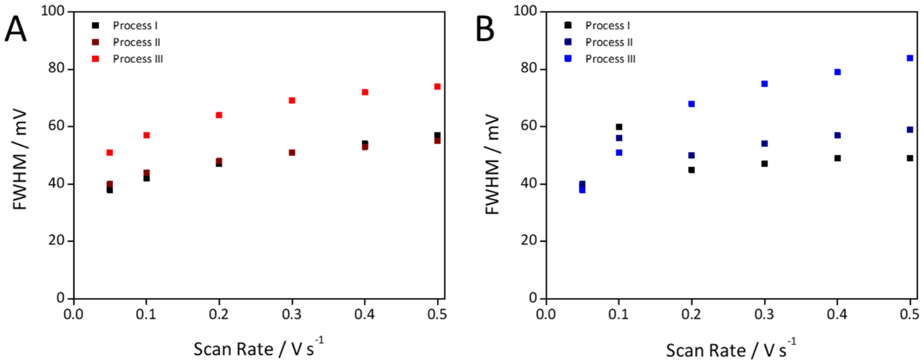

Figure 4.14. FWHM values of the (A) reduction waves and (B) oxidation waves of {$PMo_{12}O_{40}$}@SWNT taken from figure 4.12.

However, caution should be exercised when interpreting the FWHM values of surface confined processes, as beneficial interactions between the host-SWNT and guest-POM (as discussed in chapter 2) can lead to complicated electron transfer kinetics and a widening of the FWHM from the idealised shape; therefore FWHM values can give incorrect *n* assignments.[28, 31]

In an attempt to access the fourth process of confined $[PMo_{12}O_{40}]^{3-}$ molecules, the electrochemical window was increased during CV experiments and additional processes were observed (**Fig. 4.15, A**). These processes appeared to be completely irreversible, similar to POMs in solution at negative potentials,[26] and accessing them appeared to alter the nature of the stable processes observed at more positive potentials. A similar phenomenon was reported by Genovese *et al*. and discussed previously. The original stable processes could be recovered by narrowing the potential window after cycling; however, the peak current was drastically reduced, indicating that irreversible changes had occurred in the material, likely due to competing side reactions (such as hydrogen evolution) at these negative potentials (**Fig. 4.15, B**). Overall, the $\{PMo_{12}O_{40}\}$@SWNT material can be described as having three two-electron processes, with the first two processes exhibiting greater stability than the final process. Scanning outside of the stable window led to irreversible

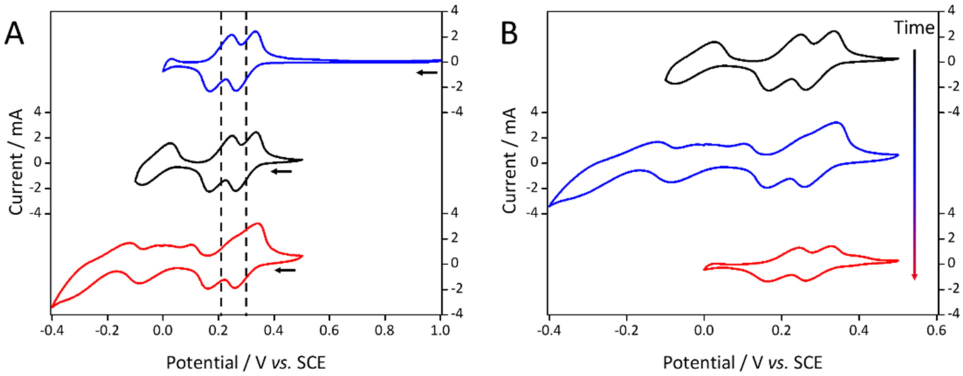

Figure 4.15. (A) CVs of $\{PMo_{12}O_{40}\}$@SWNT over different electrochemical windows. Arrows (inset) show the direction of the scan. (B) CVs over different electrochemical windows against time (indicated by arrow inset) demonstrating the effect of narrowing the electrochemical window on the CV trace. CVs recorded with a GCE working electrode, SCE reference electrode and platinum counter electrode at a scan rate of 0.1 V s^{-1}.

changes in the material, making access to the final process observed in the solution electrochemistry of the POM impossible.

Multiple processes were seen in the CV of $\{P_2Mo_{18}O_{62}\}$@SWNT over the potential range of –0.1 – +0.7 V with an acidic electrolyte (**Fig. 4.16**). The CV appeared to be highly symmetrical, similar to $\{PMo_{12}O_{40}\}$@SWNT, however the five processes that were present appeared qualitatively different in terms of peak height and width, with formal potentials of 0.490 (I), 0.398 (II), 0.310 (III), 0.205 (IV) and 0.024 (V) V *vs* SCE (**table 4.11**). Peak-to-peak separations of the processes were found to be 22 mV and lower, indicating that the processes were surface confined and quasi reversible (**table 4.12**). Peak II, IV and V all appeared to be of a similar magnitude, whereas peak III appeared to be larger in magnitude and I appeared to be much smaller in magnitude

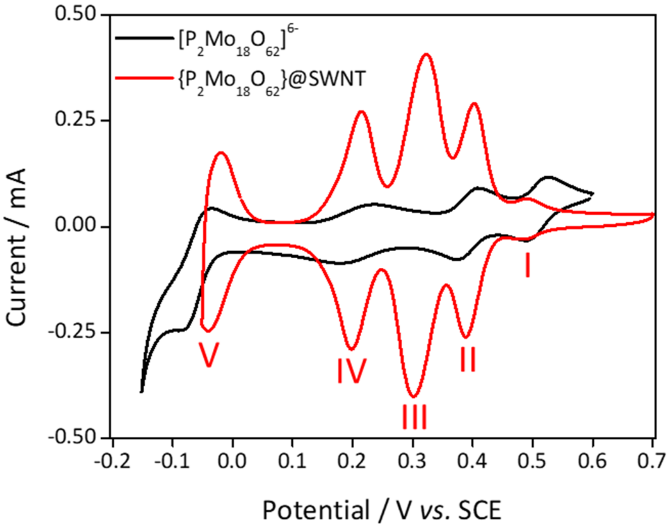

Figure 4.16. CV of $K_6[P_2Mo_{18}O_{62}]$ and $\{P_2Mo_{18}O_{62}\}$@SWNT recorded in 1 M H_2SO_4 with a GCE working electrode, SCE reference electrode and platinum counter electrode at a scan rate of 0.1 V s^{-1}. Processes labelled (red, inset).

Table 4.11. $E_{1/2}$ values of $K_6[P_2Mo_{18}O_{62}]$ and $\{P_2Mo_{18}O_{62}\}$@SWNT. All potentials versus SCE.

$[P_2Mo_{18}O_{62}]^{6-}$		$\{P_2Mo_{18}O_{62}\}$@SWNT	
Process	Potential / V	Process	Potential / V
I	0.430	I	0.490
II	0.330	II	0.398
III	0.130	III	0.310
IV	-0.125	IV	0.205
- - - - - - - - - -		V	-0.024

Table 4.12. ΔE_p values for $\{P_2Mo_{18}O_{62}\}$@SWNT taken from figure 4.16.

$\{P_2Mo_{18}O_{62}\}$@SWNT	
Process	ΔE_p / mV
I	7
II	15
III	22
IV	15
V	15

comparatively. Due to the lack of phase purity in the material, it was likely that some of the processes were due to encapsulated POM, and some were due to the large crystals observed on the SWNT surface. (Chapter 2) Due to the smaller magnitude of peak I, it could be expected that this process was from the large surface crystals, as the size of the crystals meant that the majority of the POM molecules within the crystal were not electrochemically addressable due to the insulating nature of POMs in the solid state. Cycling the material at varying scan rates (**Fig. 4.17, A**) showed that the central three processes, II, III and IV, exhibited surface confined behaviour (**Fig. 4.17, B**). Due to the instability of the material with increasing electrochemical window the window could not be increased whilst maintaining the integrity of the material, therefore the effect of varying the scan rate could not be assessed for the final process,

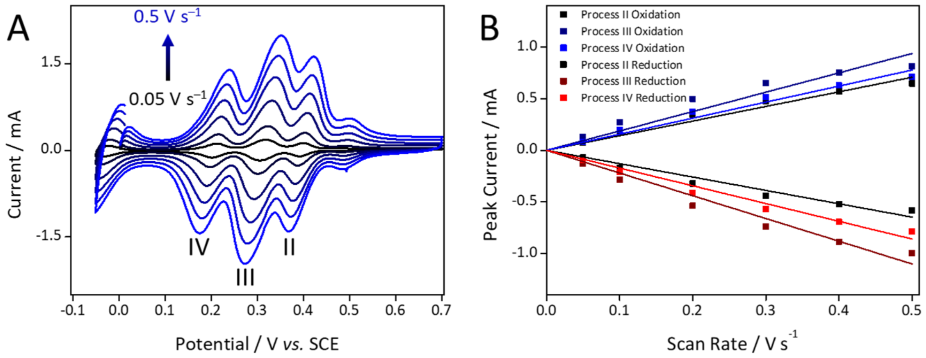

Figure 4.17. (A) CVs of $\{P_2Mo_{18}O_{62}\}$@SWNT at varying scan rates (inset) with labelled processes (inset). (B) Plot of peak current versus scan rate for the three processes, which shows a linear relationship again scan rate. R^2 values shown in table 4.13. CVs recorded with a GCE working electrode, SCE reference electrode and platinum counter electrode. All reductions labelled inset.

Table 4.13. R^2 values of the linear fits taken from figure 4.17, B.

$\{P_2Mo_{18}O_{62}\}$@SWNT	
Process	R^2
II Reduction	0.984
III Reduction	0.986
IV Reduction	0.990
II Oxidation	0.988
III Oxidation	0.972
IV Oxidation	0.989

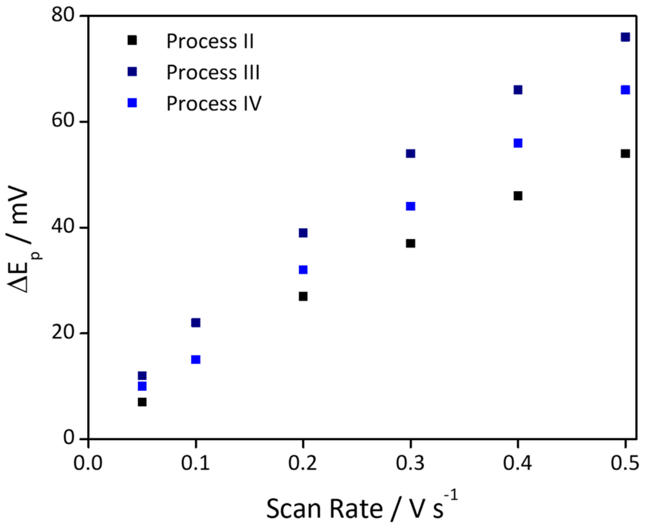

Figure 4.18. ΔE_p values for three of the $\{P_2Mo_{18}O_{62}\}$@SWNT processes at varying scan rates.

V. The three central processes had peak currents that increased linearly with increasing scan rate, with R^2 values all above 0.97 (**table 4.13**). ΔE_p values for the $\{P_2Mo_{18}O_{62}\}$@SWNT also increased with increasing scan rate for the central three processes, indicative of quasi-reversible processes (**Fig. 4.18**).

At a scan rate of 0.1 V s^{-1} the FWHM of the central three processes (reductions) were 39, 53 and 49 mV for II, III and IV respectively, indicating that the processes were all two-electron. The return oxidations were 45, 39 and 49 mV for II, III and IV respectively, in good agreement with the reductions (**table 4.14**). The FWHM values

Table 4.14. FWHM values for reductions and oxidations of the $\{P_2Mo_{18}O_{62}\}$@SWNT material, taken from fig 4.17.

$\{P_2Mo_{18}O_{62}\}$@SWNT - Reduction			$\{P_2Mo_{18}O_{62}\}$@SWNT - Oxidation		
Process	FWHM / mV	n (no. of electrons)	Process	FWHM / mV	n (no. of electrons)
I	39	2.32 (2)	I	45	2.01 (2)
II	53	1.71 (~2)	II	39	2.32 (2)
III	49	1.85 (2)	III	49	1.85 (2)

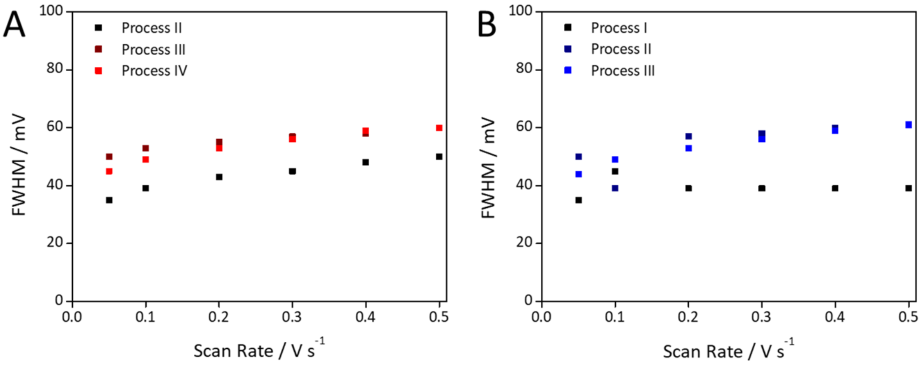

Figure 4.19. FWHM values of $\{P_2Mo_{18}O_{62}\}$@SWNT with increasing scan rates for the (A) reduction waves and (B) oxidation waves.

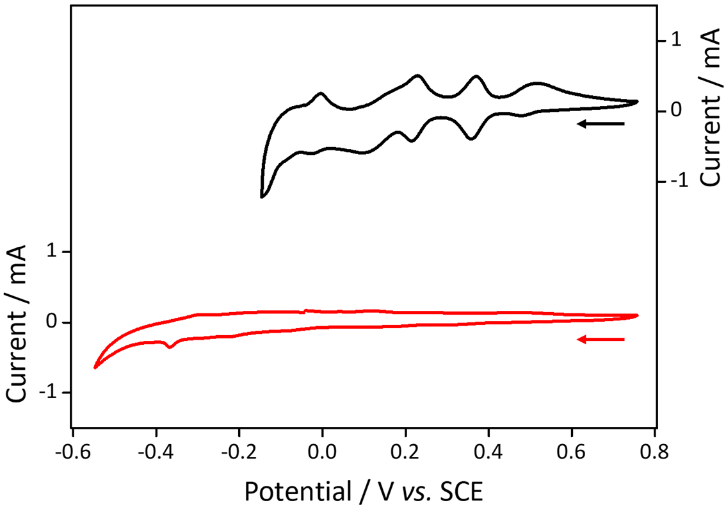

Figure 4.20. CVs of $\{P_2Mo_{18}O_{62}\}$@SWNT over extended potential windows recorded in 1 M H_2SO_4 with a GCE working electrode, SCE reference electrode and platinum counter electrode at a scan rate of 0.1 V s^{-1}.

scaled with increasing scan rate similar to $\{PMo_{12}O_{40}\}$@SWNT, however the magnitude of this increase appeared to be to a lesser extent (**Fig. 4.19**). Similar to the $\{PMo_{12}O_{40}\}$@SWNT material, expanding the potential window gave rise to further irreversible processes (**Fig. 4.20**). Further increasing this window led to the permanent loss of all redox peaks within a single cycle, suggesting that the material was particularly unstable outside of a narrow electrochemical window.

4.3.3 {W-POM}@SWNT Cyclic Voltammetry

As mentioned previously, the W-POM reductions were generally more electronegative in solution than the Mo analogues which was observed in the encapsulated POMs by cyclic voltammetry of the {$PW_{12}O_{40}$}@SWNT material (**Fig. 4.21**). Three processes were observed between 0 and –0.7 V with $E_{1/2}$ values of -0.302 (I), -0.454 (II) and -0.593 (III) V *vs* SCE (**table 4.15**). Qualitatively the processes appeared surface confined with two peaks of equal height, and one peak of a much greater height. The ΔE_p values of the

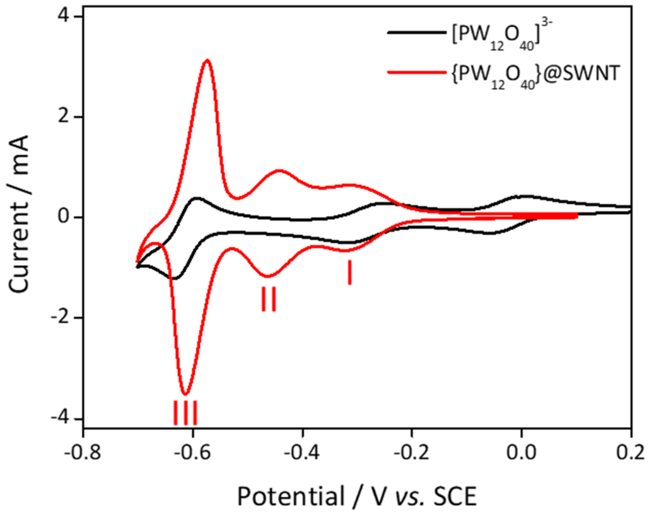

Figure 4.21. CVs of $H_3[PW_{12}O_{40}]$ (current multiplied by 10 for clarity) and {$PW_{12}O_{40}$}@SWNT recorded in 1 M H_2SO_4 with a GCE working electrode, SCE reference electrode and platinum counter electrode at a scan rate of 0.1 V s^{-1}. Processes labelled inset.

Table 4.15. $E_{1/2}$ values of $H_3[PW_{12}O_{40}]$ and {$PW_{12}O_{40}$}@SWNT. All potentials versus SCE.

$[PW_{12}O_{40}]^{3-}$		{$PW_{12}O_{40}$}@SWNT	
Process	Potential / V	Process	Potential / V
I	-0.020	I	-0.302
II	-0.275	II	-0.454
III	-0.590	III	-0.593

Table 4.16. ΔE_p values for {$PW_{12}O_{40}$}@SWNT taken from figure 4.21.

{$PW_{12}O_{40}$}@SWNT	
Process	ΔE_p / mV
I	12
II	20
III	39

processes were 12, 20 and 39 mV for I, II and III respectively, indicating that the processes were surface confined and quasi-reversible (**table 4.16**). The peak current for all redox processes increased linearly with scan rate (**Fig. 4.22**) also indicating all processes were surface confined. The R^2 values for all three processes were above 0.98 and are summarised in **table 4.17**.

ΔE_p values again increased with increasing scan rate, suggesting quasi-reversibility of the processes (**Fig. 4.23**). The FWHM values of the reduction waves at a scan rate of 0.1 V s^{-1} were 85, 72 and 52 mV for I, II and III respectively, indicating that I and II were one-electron processes and III was a two-electron process, the same as the parent POM. Unlike the Mo-POM species where it appeared only the first few processes could

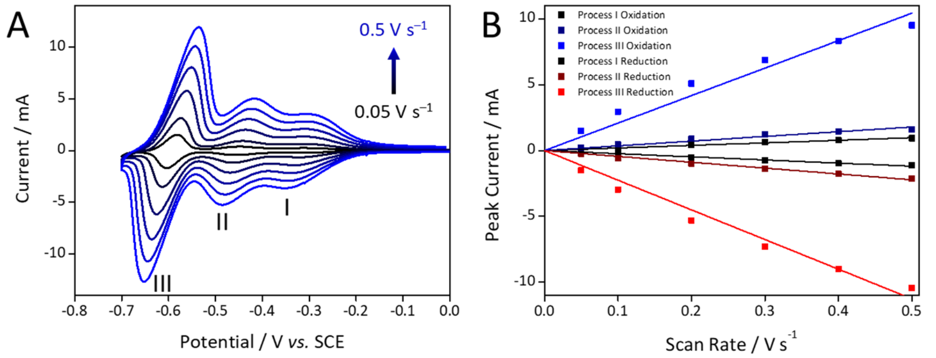

Figure 4.22. (A) CVs of {PW$_{12}$O$_{40}$}@SWNT at carrying scan rates (inset) with labelled processes (inset). (B) Plot of peak current versus scan rate for the three processes, which shows a linear relationship again scan rate. R^2 values shown in table 4.17. CVs recorded with a GCE working electrode, SCE reference electrode and platinum counter electrode at a scan rate of 0.1 V s^{-1}. All reductions labelled (inset).

Table 4.17. R^2 values of the linear fits taken from figure 4.22, B.

{PW$_{12}$O$_{40}$}@SWNT	
Process	R^2
I Reduction	0.996
II Reduction	0.995
III Reduction	0.990
I Oxidation	0.997
II Oxidation	0.983
III Oxidation	0.985

be accessed, for $\{PW_{12}O_{40}\}$@SWNT it appeared that all processes could be accessed upon POM confinement within the SWNT. The return oxidation waves were 92, 71 and 55 mV for I, II and III respectively (**table 4.18**). The FWHM increased with increasing scan rate as with the previous Mo-POMs (**Fig. 4.24**). Overall, the material can be described as having two one-electron processes and one two-electron process, the

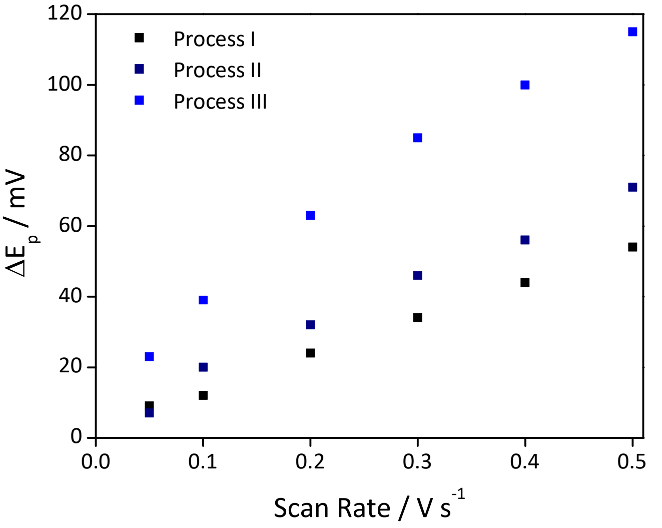

Figure 4.23. ΔE_p values for the $\{PW_{12}O_{40}\}$@SWNT processes at varying scan rates.

Table 4.18. FWHM values for $\{PW_{12}O_{40}\}$@SWNT at a scan rate of 0.1 V s^{-1}.

$\{PW_{12}O_{40}\}$@SWNT - Reduction			$\{PW_{12}O_{40}\}$@SWNT - Oxidation		
Process	FWHM / mV	n (no. of electrons)	Process	FWHM / mV	n (no. of electrons)
I	85	1.07 (1)	I	92	0.98 (1)
II	72	1.26 (1)	II	71	1.26 (1)
III	52	1.74 (2)	III	55	1.65 (~2)

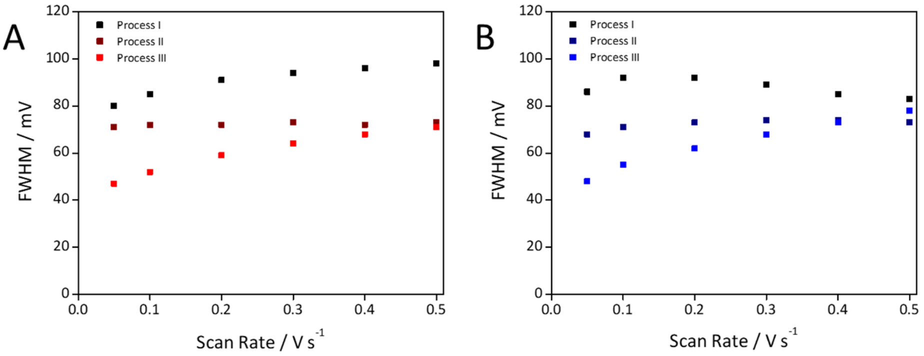

Figure 4.24. FWHM values of $\{PW_{12}O_{40}\}$@SWNT at increasing scan rates for (A) reduction waves and (B) oxidation waves.

same as the parent POM in solution, with the first two processes shifted slightly negative.

For {$P_2W_{18}O_{62}$}@SWNT three processes were observed between 0V and -0.7V (**Fig. 4.25**) with $E_{1/2}$ values of –0.201, –0.369 and –0.603 V *vs* SCE for I, II and III respectively (**table 4.18**). Qualitatively the CV appeared to be surface confined with all peaks of a relatively equal height, with the first process negative of the first two processes in

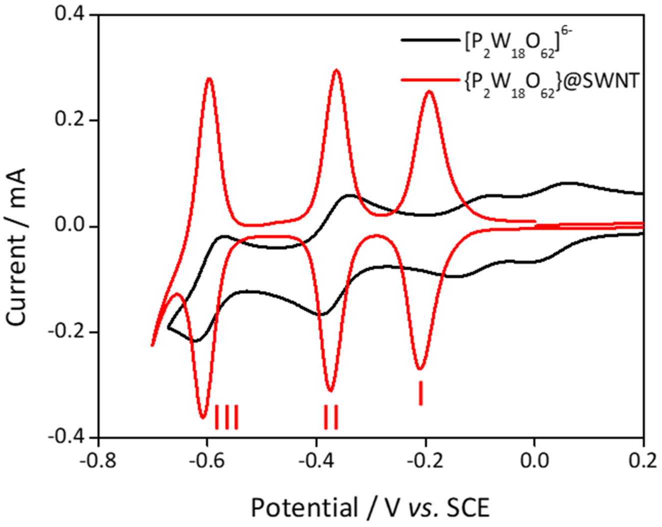

Figure 4.25. CVs of $K_6[P_2W_{18}O_{62}]$ (current multiplied by 5 for clarity) and {$P_2W_{18}O_{62}$}@SWNT recorded in 0.1M H_2SO_4 with a GCE working electrode, SCE reference electrode and platinum counter electrode at a scan rate of 0.1 V s^{-1}. Processes inset.

Table 4.19. $E_{1/2}$ values of $K_6[P_2W_{18}O_{62}]$ and {$P_2W_{18}O_{62}$}@SWNT. All potentials versus SCE.

$[P_2W_{18}O_{62}]^{6-}$		{$P_2W_{18}O_{62}$}@SWNT	
Process	Potential / V	Process	Potential / V
I	-0.005	I	-0.201
II	-0.135	II	-0.369
III	-0.380	III	-0.603
IV	-0.610	- - - - - - - - - -	

Table 4.20. ΔE_p values for the three redox processes in {$P_2W_{18}O_{62}$}@SWNT at a scan rate of 0.1 V s^{-1}.

{$P_2W_{18}O_{62}$}@SWNT	
Process	ΔE_p / mV
I	17
II	10
III	10

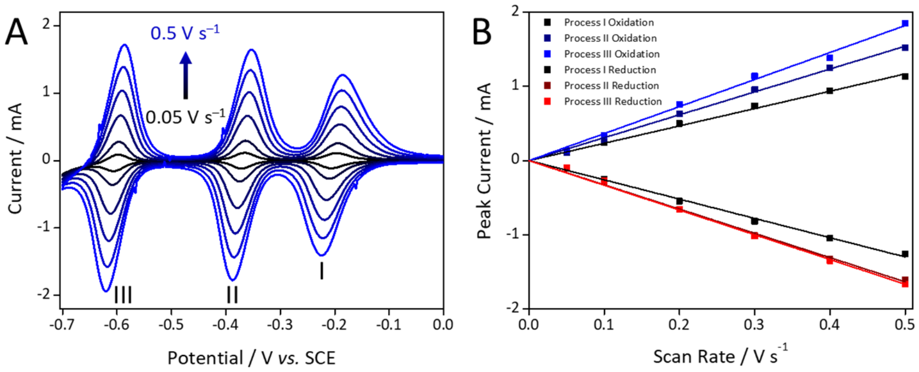

Figure 4.26. (A) CVs of {$P_2W_{18}O_{62}$}@SWNT at carrying scan rates (inset) with labelled processes (inset). (B) Plot of peak current versus scan rate for the three processes, which shows a linear relationship against scan rate. R^2 values shown in table 4.21. CVs recorded with a glassy carbon working electrode (GCE), saturated calomel reference electrode (SCE) and platinum counter electrode. All reductions labelled (inset).

Table 4.21. R^2 values of the linear fits taken from figure 4.26, B.

{$P_2W_{18}O_{62}$}@SWNT	
Process	R^2
I Reduction	0.998
II Reduction	0.999
III Reduction	0.998
I Oxidation	0.999
II Oxidation	0.999
III Oxidation	0.998

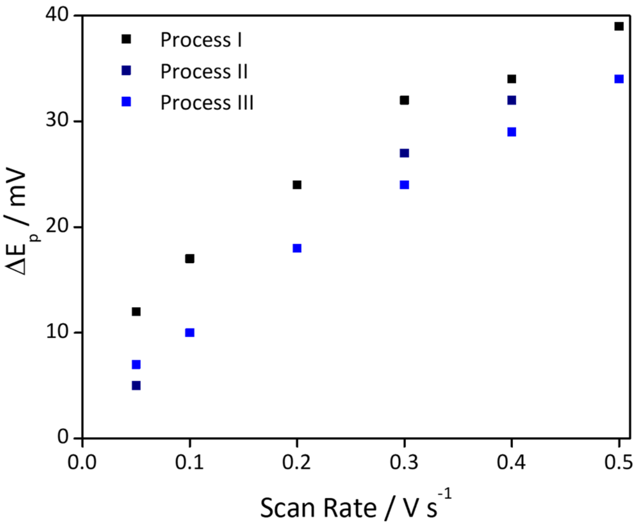

Figure 4.27. ΔE_p values for the {$P_2W_{18}O_{62}$}@SWNT processes at varying scan rates.

solution and the final two processes lying at similar potentials to those in solution. ΔE_p values were 17, 10 and 10 mV for I, II and III at a scan rate of 0.1 V s^{-1}, (**table 4.19**) indicating the processes were surface confined and highly reversible relative to the other {POM}@SWNT materials. Again, the peak current of all three processes appeared to increase with scan rate (**Fig. 4.26**) with R^2 values that were all above 0.99 (**table 4.20**). The peak-to-peak separation appeared to scale with scan rate (**Fig. 4.27**) indicating that the surface confined processes were quasi-reversible. The FWHM of the reduction waves at a scan rate of 0.1 V s^{-1} were 54, 45 and 41 mV for I, II and III suggesting that all three processes were two-electron. The return oxidations had FWHM values of 58, 47 and 47 mV (**table 4.21**). The FWHM values again appeared to increase with scan rate, suggesting that all three processes were quasi reversible (**Fig. 4.28**).

Unlike the Mo-POMs described above, the W-POMs appeared to reversibly accept the same number of electrons upon encapsulation as their parent anions in solution. For {$P_2W_{18}O_{62}$}@SWNT, the first two single electron processes in solution (**Fig. 4.10, B, I &**

Table 4.22. FWHM values for {$P_2W_{18}O_{62}$}@SWNT at a scan rate of 0.1 V s^{-1}.

{$P_2W_{18}O_{62}$}@SWNT - Reduction			{$P_2W_{18}O_{62}$}@SWNT - Oxidation		
Process	FWHM / mV	n (no. of electrons)	Process	FWHM / mV	n (no. of electrons)
I	54	1.67 (~2)	I	58	1.56 (~2)
II	45	2.01 (2)	II	47	1.93 (2)
III	41	2.21 (2)	III	47	1.93 (2)

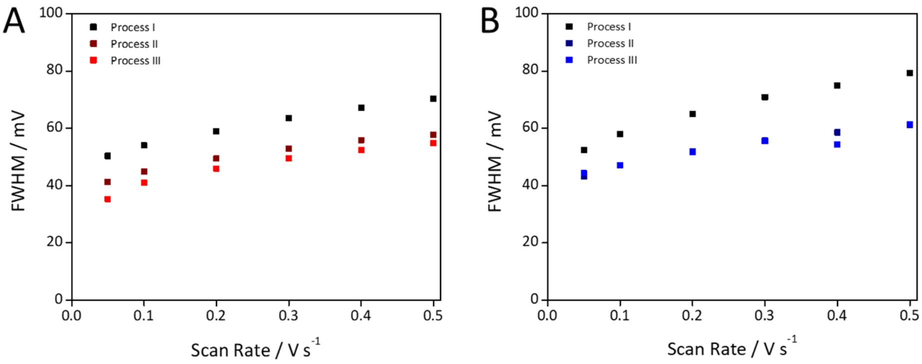

Figure 4.28. FWHM values of {$P_2W_{18}O_{62}$}@SWNT at increasing scan rates for (A) reduction waves and (B) oxidation waves.

II) appeared to merge to one single two-electron process (**Fig. 4.25, I**) similar to observations of the parent anion dissolved in solutions (12.4M HCl) with extremely low pH.[32] Extension of the electrochemical window to more negative potentials was not possible with the {W-POM}@SWNT materials as the potential window of acidic aqueous solutions is limited by the hydrogen evolution reaction (HER) that occurs at negative potentials.

The analysis of all {POM}@SWNT materials described above suggests that the electron transfer between the electrode and encapsulated POMs was extremely rapid and highly reversible, mediated by the highly conductive hosts, rendering host-guest SWNT materials ideal for fast charging and high-power energy storage devices, such as pseudo-capacitors.[33] The electron transfer rates appeared to be as good as, if not better, than the gold standards for hybrid POM-CNT materials set by the Lian group. {$P_2W_{18}O_{62}$}@SWNT and {$PMo_{12}O_{40}$}@SWNT appeared to be the most stable materials in acidic conditions based on the analysis described above.

4.3.4 Electrochemical Addressability of the Encapsulated POMs

Successful energy storage devices incorporating redox active molecules deposited onto an electrically conductive matrix should ideally possess a true molecular dispersion of the redox active nodes onto the redox inert matrix; that is, all the deposited molecules should partake in all redox events collectively. The surface coverage of an analyte, Γ, can be described by:[30]

$$\Gamma = \frac{Q}{nFA}$$

Where Q = total charge passed for the redox reaction, n = number of electrons transferred, F = Faraday's constant and A = the surface area of the electrode. Q can be calculated from the integration of the redox wave. Integration of the final two-electron reduction wave (due to this process not overlapping with the one-electron processes) at a scan rate of 0.1 V s^{-1} in the {$PW_{12}O_{40}$}@SWNT material gave a Γ value of 29.9 nmol cm^{-2}. This gave an absolute surface concentration, Γ_{eff}, of 8.4 nmol and mass loading of approximately 30.2 %. The mass loading of this particular sample was found to be ~31 wt% by thermal gravimetric analysis, indicating that almost all POMs within the material were partaking in electrochemical processes. When applying similar analysis and comparison to the {$P_2W_{18}O_{62}$}@SWNT material (using the second reduction wave) it was found that ~80 % of the encapsulated POMs could be accessed during cycling, based on the mass loading from TGA. The amount of charge passed for each molecular species did not appear to significantly scale with increasing scan rate, as would be expected for surface confined redox processes (**Fig. 4.29**).

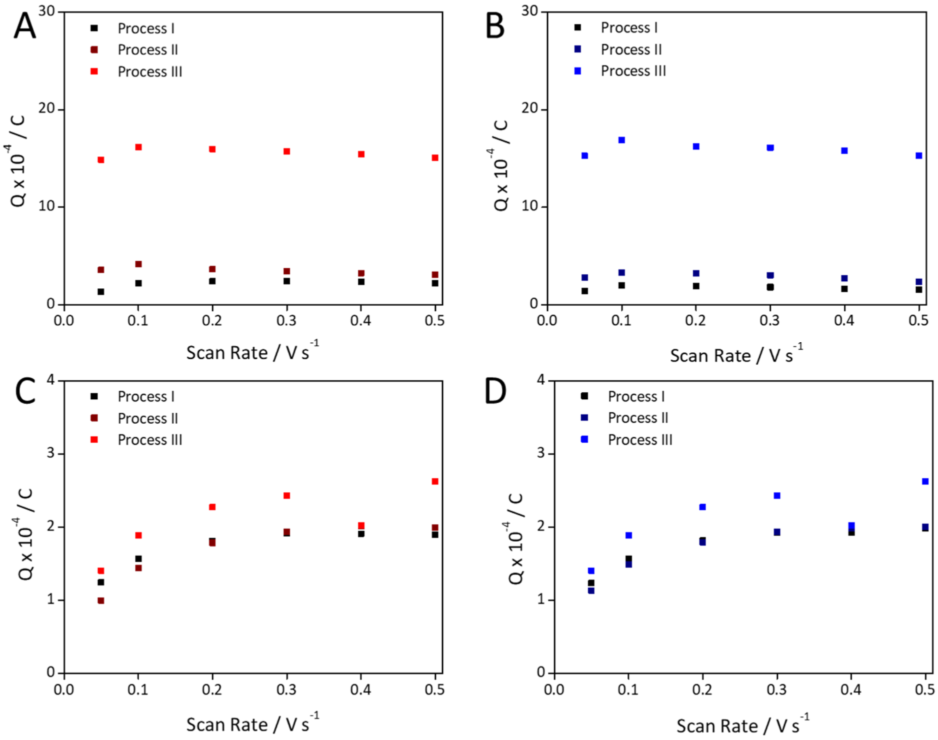

Figure 4.29. Charge passed for each redox wave, Q, against scan rate for (A) reduction waves and (B) oxidation waves of {$PW_{12}O_{40}$}@SWNT and (C) reduction waves and (D) oxidation waves for {$P_2W_{18}O_{62}$}@SWNT.

The same analysis was then applied to the {Mo-POM}@SWNT materials, for which thermal analysis proved inadequate for quantifying mass loading, (chapter 2) in an attempt to quantify the POM loading in the materials. For $\{PMo_{12}O_{40}\}$@SWNT (using the first reduction wave) a Γ value of 11 nmol cm^{-2} was obtained for the first reduction wave. This gave a mass loading of approximately 3.2 wt%. Similar analysis of the $\{P_2Mo_{18}O_{62}\}$@SWNT material (using the second reduction wave) gave a mass loading of 1.2 %, suggesting that a large amount of the surface adsorbed crystals were not partaking in redox reactions. Similarly, the charge passed for the redox events did not appear to scale significantly with scan rate (**Fig. 4.30**).

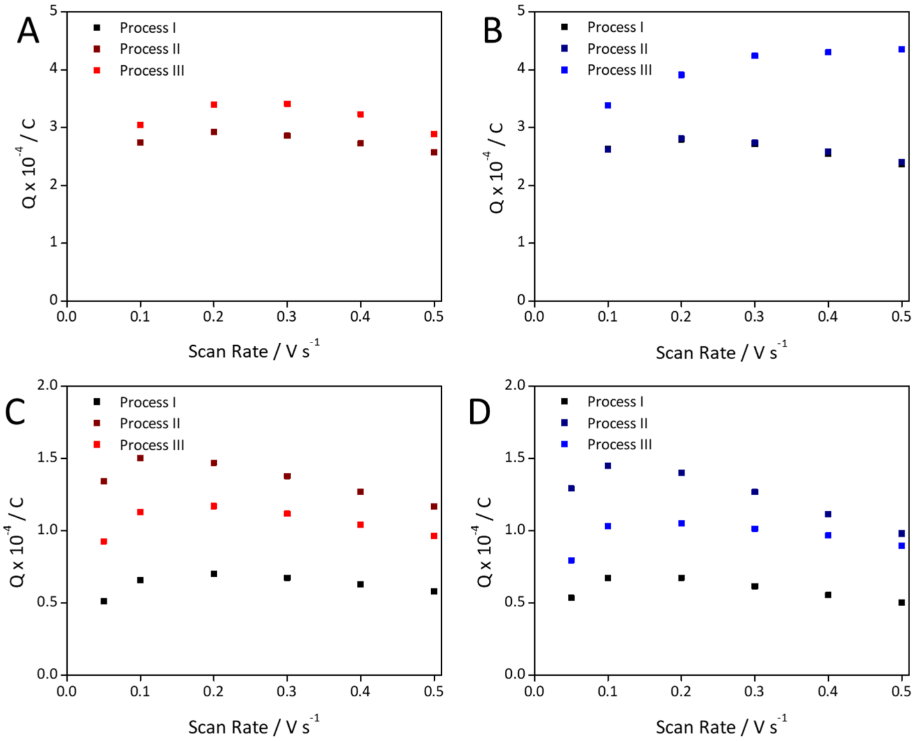

Figure 4.30. Charge passed for each redox wave, Q, against scan rate for (A) reduction waves and (B) oxidation waves of $\{PMo_{12}O_{40}\}$@SWNT and (C) reduction waves and (D) oxidation waves for $\{P_2Mo_{18}O_{62}\}$@SWNT.

4.3.5 {POM}@SWNT Stability

Next generation energy storage materials need to be stable over repeated charge-discharge cycles, without significant capacitance loss. The most stable of the {POM}@SWNT materials, {$PMo_{12}O_{40}$}@SWNT and {$P_2W_{18}O_{62}$}@SWNT, were cycled 1000 times in an acidic electrolyte to assess their charge retention (**Fig. 4.31**).

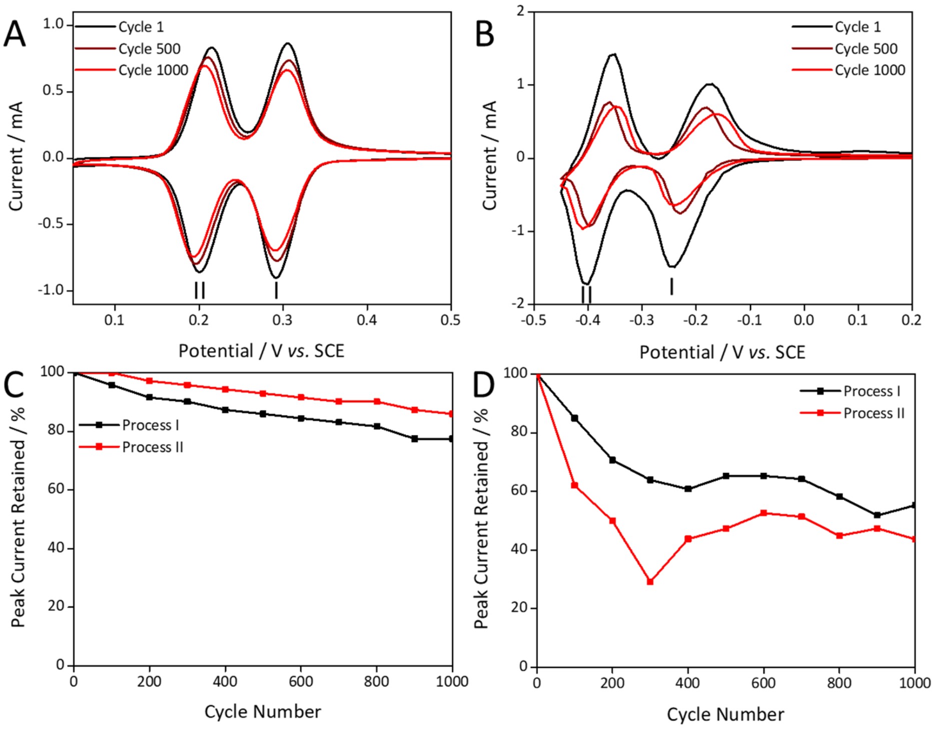

Figure 4.31. CVs over 1000 cycles of {$PMo_{12}O_{40}$}@SWNT (A) and {$P_2W_{18}O_{62}$}@SWNT (B). Changes in the peak current of the processes over 1000 cycles for {$PMo_{12}O_{40}$}@SWNT (C) and {$P_2W_{18}O_{62}$}@SWNT (D). All CVs recorded in 1M H_2SO_4 with a GCE working electrode, SCE reference electrode and platinum counter electrode at a scan rate of 0.1 V s^{-1}.

Overall, the two most stable processes in the {$PMo_{12}O_{40}$}@SWNT material appeared to retain capacitance over 1000 cycles better than the first two processes in {$P_2W_{18}O_{62}$}@SWNT, with 77 % and 86 % of the initial capacitance retained after 1000 cycles for processes I and II respectively. For {$P_2W_{18}O_{62}$}@SWNT 55 % and 44 % of the original capacitance was retained. This was likely due to the processes in {$PMo_{12}O_{40}$}@SWNT occurring at potentials where the 1M H_2SO_4 is a more stable electrolyte; at more negative potentials similar to where the {$P_2W_{18}O_{62}$}@SWNT processes occurred the HER and other competing side reactions also occur.

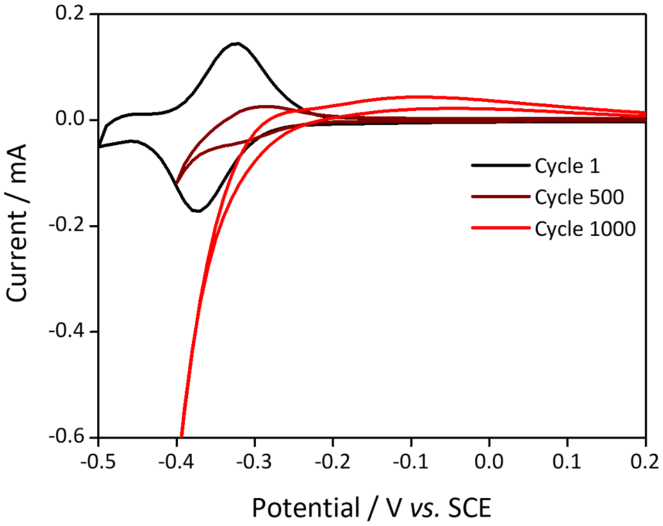

Figure 4.32. CVs over 1000 cycles of {$PW_{12}O_{40}$}@SWNT, demonstrating the evolution of the HER reaction with increasing cycle number. All CVs recorded in 1 M H_2SO_4 with a GCE working electrode, SCE reference electrode and platinum counter electrode at a scan rate of 0.1 V s^{-1}.

Additionally, there is increasing evidence of the dissolution of platinum counter electrodes in acidic electrolytes which is deposited onto the working electrode during electrochemical cycling, increasing its HER activity over time.[34] This was particularly prominent in the {$PW_{12}O_{40}$}@SWNT material, with HER significantly developing over the course of 1000 cycles even when only cycling the first one-electron process (**Fig. 4.32**). Generally, the 1M H_2SO_4 electrolyte was stable down to potentials as low as -0.7 V *vs* SCE, however after 1000 cycles the HER onset potential was approximately -0.3 V *vs* SCE, dominating the electrochemistry at these potentials. This result suggests that the stability of the {POM}@SWNT materials over repeated cycling was exceptionally high, with the {W-POM}@SWNT materials' stabilities largely effected by the choice of counter electrode in the described experiments.[34]

As mentioned previously (chapter 2) the SWNTs were able to effectively stabilise POMs in solutions of extremely high pH, where they would normally be hydrolysed. To further test this hypothesis the {POM}@SWNT materials were screened for electrochemical activity in 1M NaOH. For the {W-POM}@SWNT materials, redox

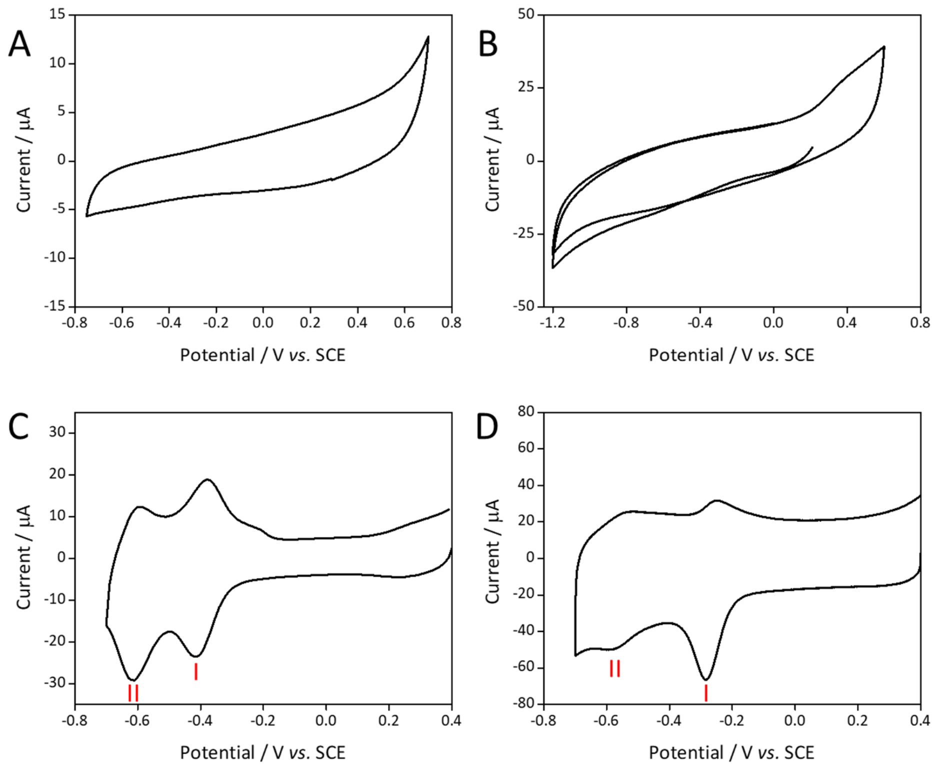

Figure 4.33. CVs of SWNTs (A) $H_3[PW_{12}O_{40}]$ (B) $\{PW_{12}O_{40}\}$@SWNT (C) and $\{P_2W_{18}O_{62}\}$@SWNT (D) recorded in 1M NaOH. All CVs recorded with a GCE working electrode, SCE reference electrode and platinum counter electrode at a scan rate of 0.1 V s^{-1}.

activity from the POM was observed, (**Fig. 4.33**) suggesting that upon encapsulation the POMs were protected from the harsh 1M NaOH and were still able to partake in redox reactions. For comparison, both unfunctionalised SWNTs and native POMs dissolved in solution exhibited no redox processes (**Fig. 4.33, A & B**). For the $\{PW_{12}O_{40}\}$@SWNT material, the first two redox processes were clearly observed (**Fig. 4.33, C**). For the $\{P_2W_{18}O_{62}\}$@SWNT material (**Fig. 4.33, D**) the first process was observed, however a large current was observed for the reduction wave and a low current was observed for the oxidation wave, indicative of a highly irreversible process. These results indicated that even in electrolytes with very high pH, the encapsulated POM molecules persisted in good agreement with the results discussed previously (chapter 2) and are the first examples of POM electrochemistry in extremely high pH. In $\{P_2W_{18}O_{62}\}$@SWNT the second process was also observed; however, the current was extremely low for this process. Over the course of

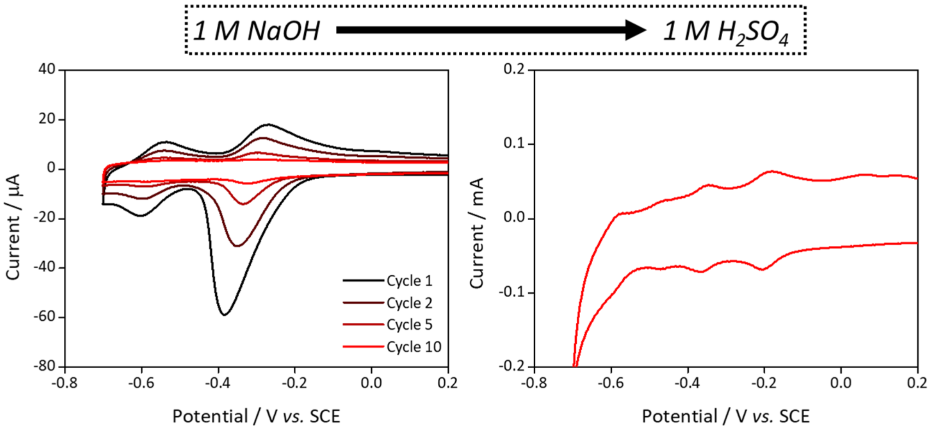

Figure 4.34. CVs of the same working electrode functionalised with {$P_2W_{18}O_{62}$}@SWNT cycled in 1M NaOH and then subsequently 1M H_2SO_4. CVs recorded on the same GCE working electrode, SCE reference electrode and platinum counter electrode at a scan rate of 0.1 V s^{-1}.

approximately 10 cycles the processes were lost, however redox activity could be partially recovered when cycling the same electrode in 1M H_2SO_4 (**Fig. 4.34**).

For the {Mo-POM}@SWNT materials, the processes observed in acid were absent (**Fig. 4.35**). This loss of redox behaviour can be explained by considering the processes of the parent anions in solution. For the Mo-POMs in solution, all of the reversible reductions observed in acidic solutions occurred with PCET. The absence of the processes in the {Mo-POM}@SWNT material indicated that these processes were still proton coupled upon encapsulation of the anions, and could not occur in a pH 12 solution due to the lack of protons. This hypothesis can also be used to explain the observation of a large first reduction wave in {$P_2W_{18}O_{62}$}@SWNT, as the first two reductions of the $[P_2W_{18}O_{62}]^{6-}$ in solution were not proton coupled. This indicated that the second reduction in {$P_2W_{18}O_{62}$}@SWNT was proton coupled. Both the first two reduction processes in the $[PW_{12}O_{40}]^{3-}$ anion were not proton coupled in solution, which also appeared to be a feature of the encapsulated anion in the {$PW_{12}O_{40}$}@SWNT material, as evidenced by the two processes observed in the {$PW_{12}O_{40}$}@SWNT material in basic conditions.

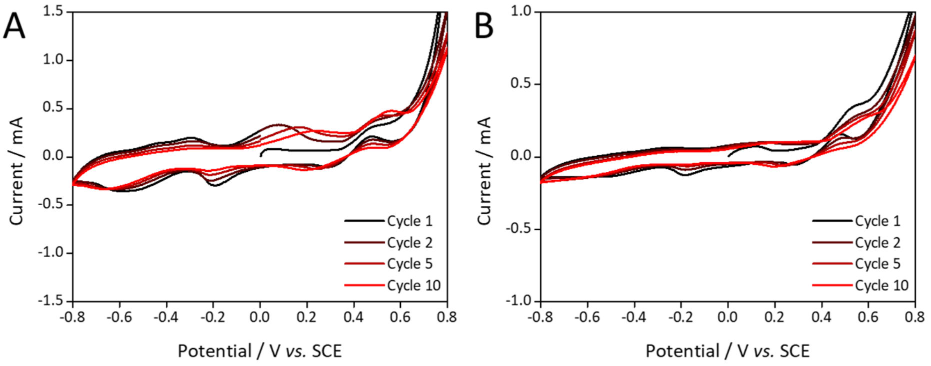

Figure 4.35. CVs of {$PMo_{12}O_{40}$}@SWNT (A) and {$P_2Mo_{18}O_{62}$}@SWNT (B) recorded in 1M NaOH with a GCE working electrode, SCE reference electrode and a platinum counter electrode at a scan rate of 0.1 V s^{-1}.

4.3.6 Electrolyte Dependence

Current state of the art batteries that are mass produced are based on lithium-ion chemistry. Due to their extremely narrow interiors, CNTs have previously been reported to cause mass transport issues for ion access in catalysis and charge storage mechanisms. As discussed in chapter 1, there is no consensus on the transport of cations to redox active encapsulants confined within SWNTs. Often, larger cations, such as quaternary ammonium cations, appear to readily extract faradaic current from encapsulated guests confined within SWNTs whilst smaller cations, such as lithium, cannot.

To probe the effect of the anion composition on the observed electrochemical response, the {POM}@SWNT materials were cycled in different acids (**Fig. 4.36**). Aside from small shifts in the redox potentials of the {Mo-POM}@SWNT materials and slight decreases in the faradaic currents in the {W-POM}@SWNT materials when cycling in $HClO_4$, overall there were minimal changes in the redox behaviour of the materials when altering the anion of the electrolyte used to record the CVs of the materials. Alternatively, altering the cation of the electrolyte led to large changes in the redox

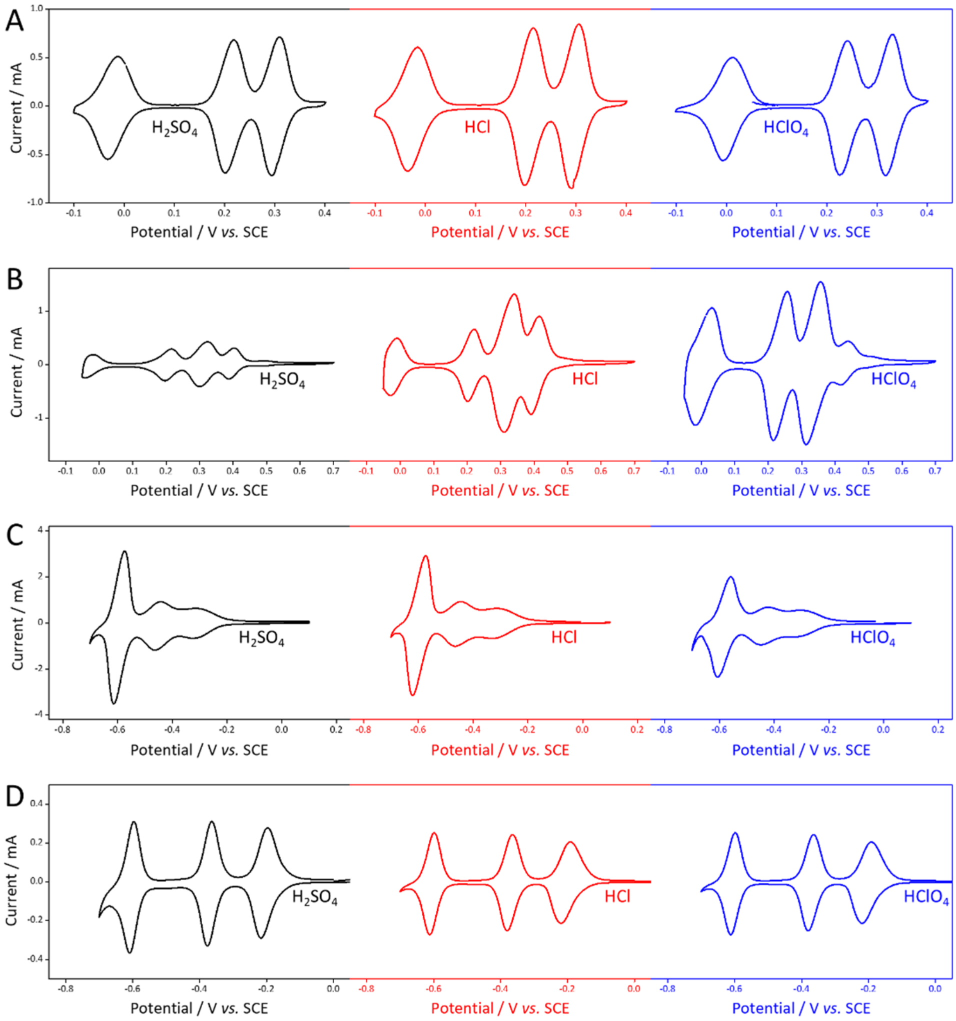

Figure 4.36. CVs of the {POM}@SWNT materials in 1M acid (labelled inset). (A) {PMo$_{12}$O$_{40}$}@SWNT (B) {P$_2$Mo$_{18}$O$_{62}$}@SWNT (C) {PW$_{12}$O$_{40}$}@SWNT and (D) {P$_2$W$_{18}$O$_{62}$}@SWNT. All CVs recorded with a GCE working electrode, SCE reference electrode and platinum counter electrode at a scan rate of 0.1 V s^{-1}.

response of all the {POM}@SWNT materials. Cycling the materials in 1M HCl, LiCl and NaCl (**Fig. 4.37**) led to CVs that contained new processes at varied potentials with significantly smaller currents. All processes observed in acidic electrolytes were lost for the {Mo-POM}@SWNT materials, similar to CVs of the {Mo-POM}@SWNT materials recorded in 1M NaOH. In contrast, new processes were observed in the {PW$_{12}$O$_{40}$}@SWNT material leading to four processes in total. This was ubiquitous to all analogous SO_4^{2-}, Cl^- and ClO_4^- salts (pH 7) (**Fig. 4.38**). Generally, the processes were far less reversible than those observed in acidic electrolytes, with relatively large currents observed for the reduction waves and low currents observed for the return

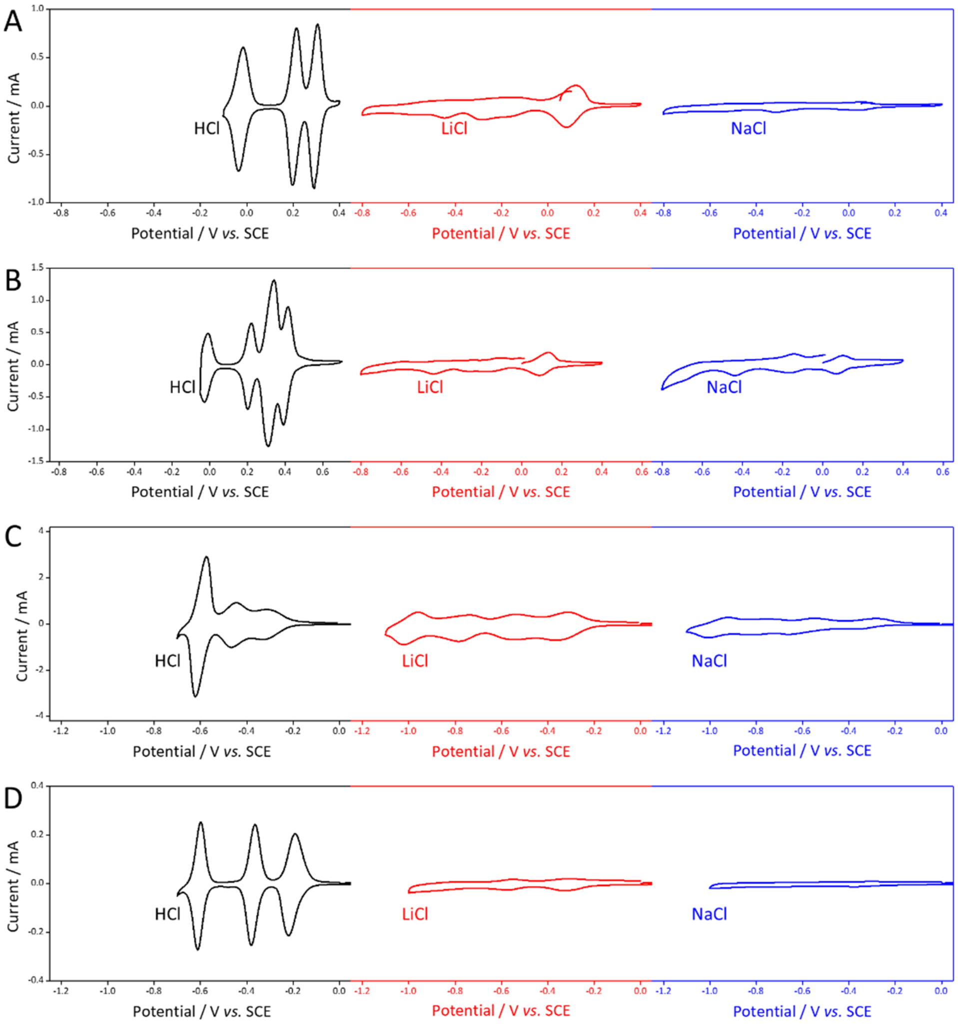

Figure 4.37. CVs of the {POM}@SWNT materials in 1M chloride salts (labelled inset). (A) {$PMo_{12}O_{40}$}@SWNT (B) {$P_2Mo_{18}O_{62}$}@SWNT (C) {$PW_{12}O_{40}$}@SWNT and (D) {$P_2W_{18}O_{62}$}@SWNT. All CVs recorded with a GCE working electrode, SCE reference electrode and platinum counter electrode at a scan rate of 0.1 V s^{-1}.

oxidations. The {Mo-POM}@SWNT materials had CVs that only contained new processes relative to CVs acquired in the corresponding acid, confirming that all the processes in acidic electrolytes were likely proton coupled. For both {Mo-POM}@SWNT materials there appeared to be a single reversible processes at approximately 0.1 V, however the definition, width and position of this process appeared to shift in different electrolytes. The {W-POM}@SWNT materials largely retained similar processes to that observed in acidic electrolytes at similar potentials, however for {$P_2W_{18}O_{62}$}@SWNT the processes became very broad with varied currents for the reduction waves and return oxidations, and not all of the processes observed

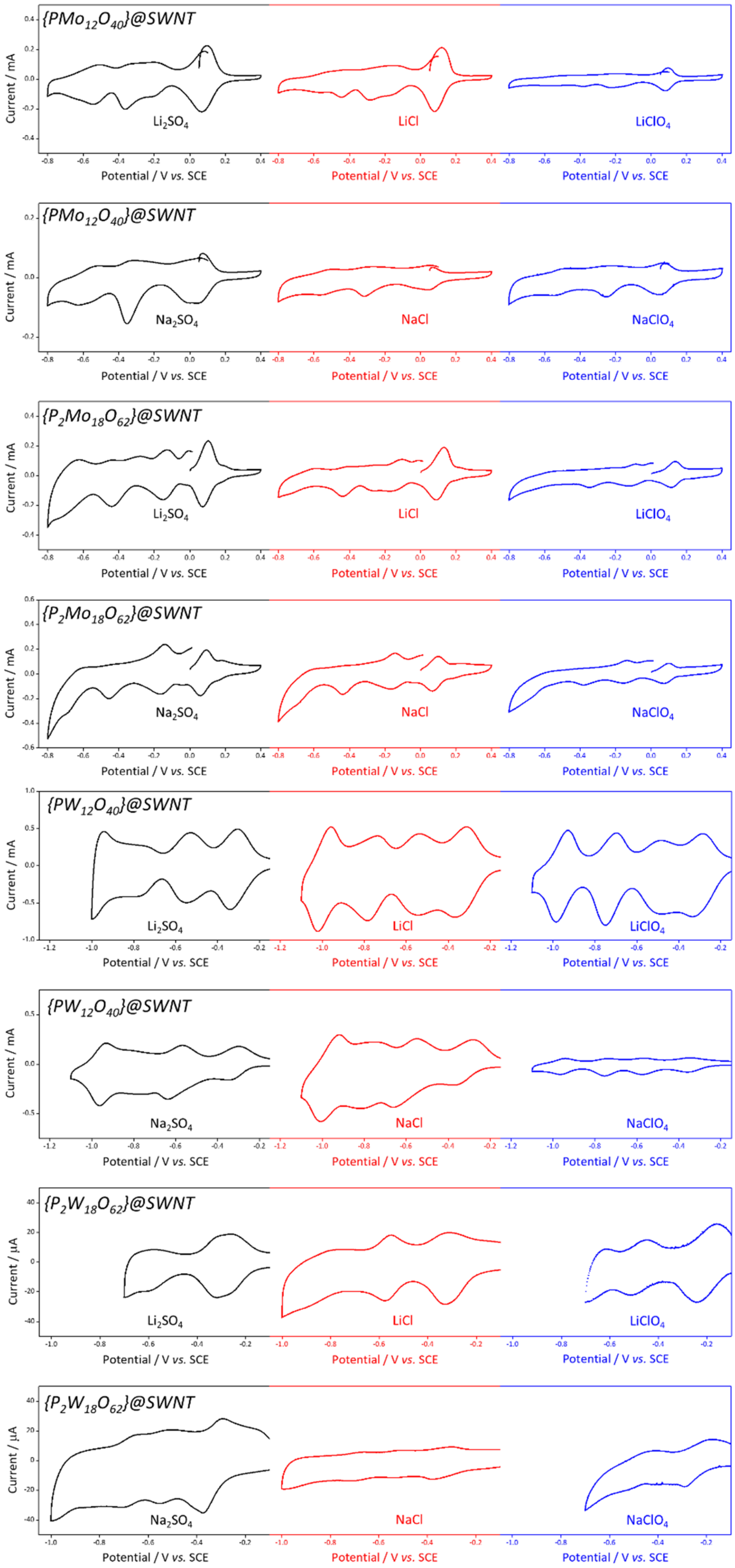

Figure 4.38. First cycles of the {POM}@SWNT materials (labelled) in varying 1M aqueous electrolytes (labelled inset). All CVs recorded with a GCE working electrode, SCE reference electrode and platinum counter electrode at a scan rate of 0.1 V s^{-1}.

in acid could be accessed. The $\{PW_{12}O_{40}\}$@SWNT material appeared particularly stable in non-acidic electrolytes relative to the other {POM}@SWNT materials, with four distinct processes observed in LiCl that appeared to have similar currents for their reductions and return oxidations. These processes all appeared qualitatively equal in terms of their magnitude, leading to the assumption that all four processes were one electron. This also indicated that at pH 7, the final two-electron process observed in acidic electrolytes separated to two one-electron processes. In acquiring CVs at pH 0, 7 and 14 the number of electrons and the nature of PCET for each process could be established for all four materials and is summarised in **table 4.22**.

Table 4.23. Redox processes of the {POM}@SWNT materials.

<table>
<tr><th colspan="3">$\{PMo_{12}O_{40}\}$@SWNT</th></tr>
<tr><td>Process</td><td>Equation at pH ≤1</td><td>Equation at pH ≥7</td></tr>
<tr><td>I</td><td>$\{PMo_{12}O_{40}\} + 2e^- + 2H^+ \rightleftharpoons \{H_2PMo_{12}O_{40}\}$</td><td>----------</td></tr>
<tr><td>II</td><td>$\{H_2PMo_{12}O_{40}\} + 2e^- + 2H^+ \rightleftharpoons \{H_4PMo_{12}O_{40}\}$</td><td>----------</td></tr>
<tr><td>III</td><td>$\{H_4PMo_{12}O_{40}\} + 2e^- + 2H^+ \rightleftharpoons \{H_6PMo_{12}O_{40}\}$</td><td>----------</td></tr>
<tr><th colspan="3">$\{P_2Mo_{18}O_{62}\}$@SWNT</th></tr>
<tr><td>Process</td><td>Equation at pH ≤1</td><td>Equation at pH ≥7</td></tr>
<tr><td>I</td><td>$\{P_2Mo_{18}O_{62}\} + 2e^- + 2H^+ \rightleftharpoons \{H_2P_2Mo_{18}O_{62}\}$</td><td>----------</td></tr>
<tr><td>II</td><td>$\{H_2P_2Mo_{18}O_{62}\} + 2e^- + 2H^+ \rightleftharpoons \{H_4P_2Mo_{18}O_{62}\}$</td><td>----------</td></tr>
<tr><td>III</td><td>$\{H_4P_2Mo_{18}O_{62}\} + 2e^- + 2H^+ \rightleftharpoons \{H_6P_2Mo_{18}O_{62}\}$</td><td>----------</td></tr>
<tr><th colspan="3">$\{PW_{12}O_{40}\}$@SWNT</th></tr>
<tr><td>Process</td><td>Equation at pH ≤1</td><td>Equation at pH ≥7</td></tr>
<tr><td>I</td><td>$\{PW_{12}O_{40}\} + e^- \rightleftharpoons \{PW_{12}O_{40}\}^-$</td><td>$\{PW_{12}O_{40}\} + e^- \rightleftharpoons \{PW_{12}O_{40}\}^-$</td></tr>
<tr><td>II</td><td>$\{PW_{12}O_{40}\}^- + e^- \rightleftharpoons \{PW_{12}O_{40}\}^{2-}$</td><td>$\{PW_{12}O_{40}\}^- + e^- \rightleftharpoons \{PW_{12}O_{40}\}^{2-}$</td></tr>
<tr><td>III</td><td>$\{PW_{12}O_{40}\}^{2-} + 2e^- + 2H^+ \rightleftharpoons \{H_2PW_{12}O_{40}\}^{2-}$</td><td>$\{PW_{12}O_{40}\}^{2-} + e^- \rightleftharpoons \{PW_{12}O_{40}\}^{3-}$</td></tr>
<tr><td>IV</td><td>----------</td><td>$\{PW_{12}O_{40}\}^{3-} + e^- \rightleftharpoons \{PW_{12}O_{40}\}^{4-}$</td></tr>
<tr><th colspan="3">$\{P_2W_{18}O_{62}\}$@SWNT</th></tr>
<tr><td>Process</td><td>Equation at pH ≤1</td><td>Equation at pH ≥7</td></tr>
<tr><td>I</td><td>$\{P_2W_{18}O_{62}\} + 2e^- \rightleftharpoons \{P_2W_{18}O_{62}\}^{2-}$</td><td>$\{P_2W_{18}O_{62}\} + 2e^- \rightleftharpoons \{P_2W_{18}O_{62}\}^{2-}$</td></tr>
<tr><td>II</td><td>$\{P_2W_{18}O_{62}\}^{2-} + 2e^- + 2H^+ \rightleftharpoons \{H_2P_2W_{18}O_{62}\}^{2-}$</td><td>----------</td></tr>
<tr><td>III</td><td>$\{H_2P_2W_{18}O_{62}\}^{2-} + 2e^- + 2H^+ \rightleftharpoons \{H_4P_2W_{18}O_{62}\}^{2-}$</td><td>----------</td></tr>
</table>

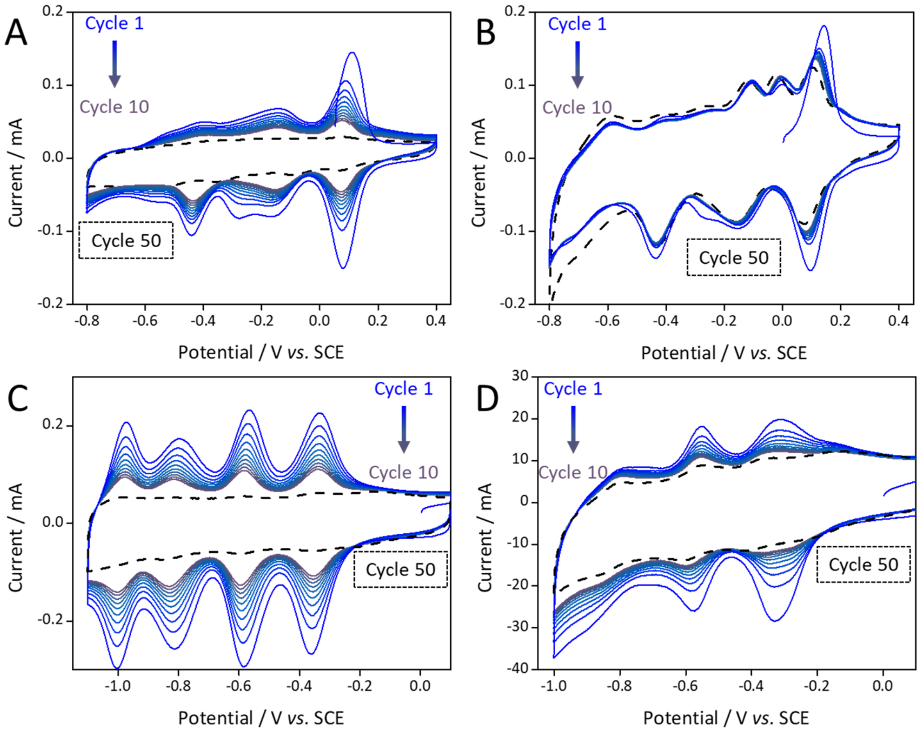

Figure 4.39. CVs recorded in 1M LiCl, demonstrating the effect of repeated cycling on {$PMo_{12}O_{40}$}@SWNT (A) {$P_2Mo_{18}O_{62}$}@SWNT (B) {$PW_{12}O_{40}$}@SWNT (C) and {$P_2W_{18}O_{62}$}@SWNT (D) materials in pH 7 electrolytes. All CVs recorded with a GCE working electrode, SCE reference electrode and platinum counter electrode at a scan rate of 0.1 V s^{-1}.

As well as lower currents and changes to the observed processes in non-acidic electrolytes, any redox activity observed was rapidly lost over the course of 50 cycles, (**Fig. 4.39**) much quicker than the 1000 cycle stability observed in acidic electrolytes reported above, indicating that overall, the reduction of the encapsulated POMs was significantly less reversible in non-acidic electrolytes. This was mostly ubiquitous to all {POM}@SWNT materials for all lithium and sodium SO_4^{2-}, Cl^- and ClO_4^- salts (data shown in appendix), however the {$P_2Mo_{18}O_{62}$}@SWNT material appeared to be more stable compared to the other materials (**Fig. 4.39, B**). This suggests that the presence of the large surface crystals in the material were still being accessed during repeated cycling with LiCl. Changing the cation of a Cl^- electrolyte to Li^+ and Na^+ led to reductions in the currents of the processes observed in all {POM}@SWNT materials. They all also displayed a rapid decrease of the peak currents over 50 cycles, (**Fig. 4.40**) however this effect appeared to be less pronounced in the {$P_2Mo_{18}O_{62}$}@SWNT material; likely due

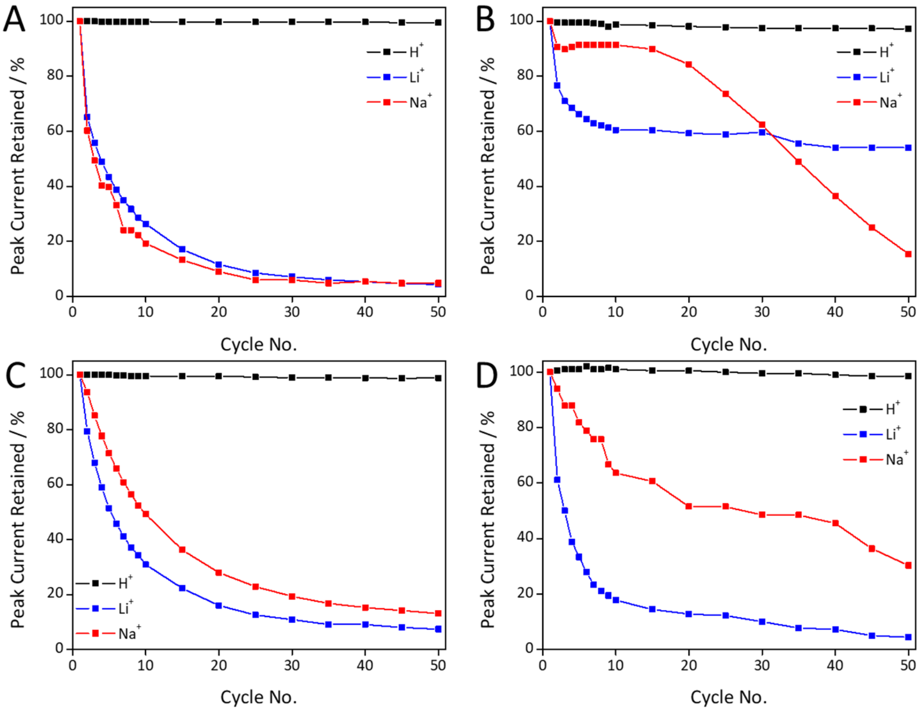

Figure 4.40. Peak currents of the first reduction waves over 50 cycles in various 1M chloride electrolytes (labelled inset) for {$PMo_{12}O_{40}$}@SWNT (A) {$P_2Mo_{18}O_{62}$}@SWNT (B) {$PW_{12}O_{40}$}@SWNT (C) and {$P_2W_{18}O_{62}$}@SWNT (D). All CVs recorded with a GCE working electrode, SCE reference electrode and platinum counter electrode at a scan rate of 0.1 V s^{-1}.

to the fact that the processes observed in this material also included the surface adsorbed crystals. This effect was ubiquitous to all SO_4^{2-}, Cl^- and ClO_4^- salts. There appeared to be very little difference between Li^+ and Na^+ in terms of how quickly the capacity of the materials decreased, apart from in the encapsulated Wells-Dawson anions, where it appeared to remain relatively high for Na^+.

The electrochemical activity of the {POM}@SWNT materials could be partially recovered after the capacity had appeared to reach close to zero after cycling the {POM}@SWNT materials in electrolytes of pH 7 by taking the working electrode, rinsing the material on the electrode with a small amount of deionised water and adding it to a cell with fresh acidic electrolyte (similar to the experiments in 1M NaOH described previously) (**Fig. 4.41**). The activity could be recovered to the point where the CV resembled that of an acidic CV, but overall changes in the material were apparent due to the lower currents observed.

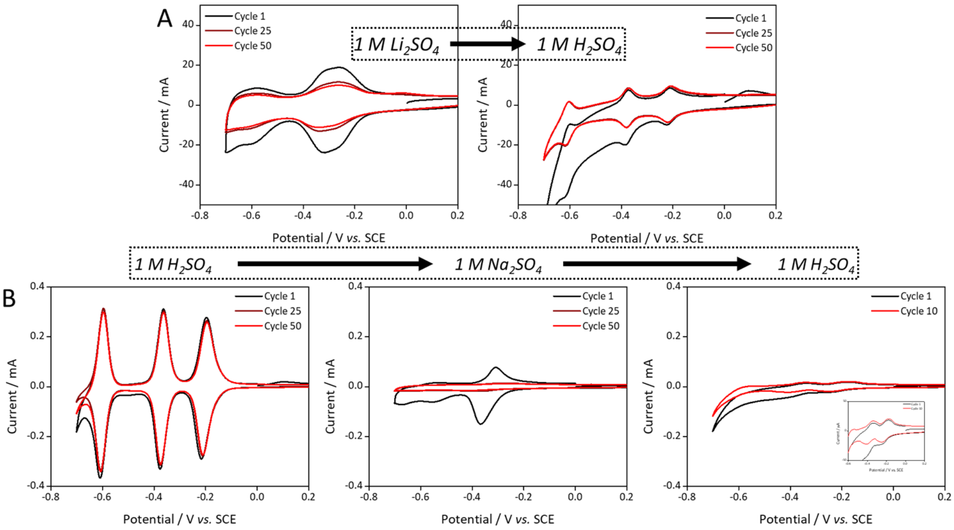

Figure 4.41. CVs of the same working electrodes (A & B separate electrodes) functionalised with $\{P_2W_{18}O_{62}\}$*@SWNT cycling in* Li_2SO_4 *and then* H_2SO_4 *(A) and cycled in* H_2SO_4 *then* Na_2SO_4 *and finally* H_2SO_4 *once again (lower current range inset) (B). CVs recorded on the same GCE working electrode (for A & B respectively), SCE reference electrode and platinum counter electrode at a scan rate of 0.1 V* s^{-1}*.*

The drastic reduction in current and loss of certain processes in the {POM}@SWNT materials can partly be explained by the different pH of the electrolytes, due to the PCET exhibited by many of the POMs. However, the POMs were still electrochemically active when dissolved in LiCl (**Fig. 4.42**), albeit with different redox profiles to the analogous acids, which was ubiquitous to all the SO_4^{2-}, Cl^- and ClO_4^- electrolytes described above (data shown in appendix). Additionally, the rapid decline in the peak current of the reductions observed over 50 cycles indicated that the pH of the supporting electrolyte was not the only contributing factor leading to the change in the redox behaviour of the {POM}@SWNT materials. The relatively high stability of the $\{P_2Mo_{18}O_{62}\}$@SWNT material, which contained large surface crystals of POM, in pH 7 electrolytes also indicated that when electrolyte cations had access to surface bound POM there were smaller changes in the peak currents when repeatedly cycling the materials.

The main role of an electrolyte in cyclic voltammetry is to ensure sufficient conductivity within the cell, by balancing the charge transfer that occurs during

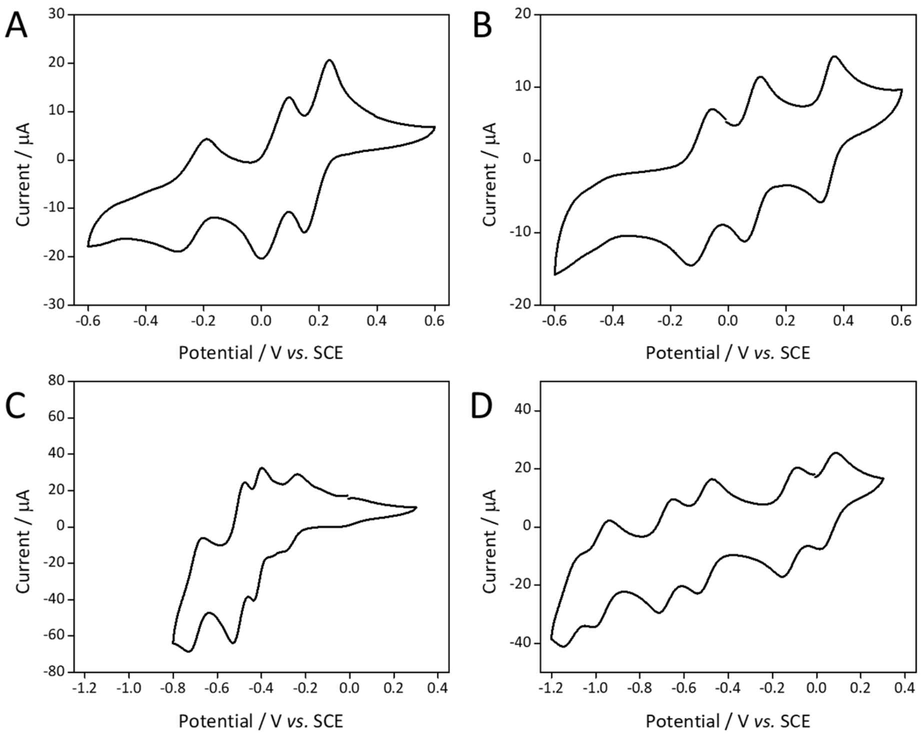

Figure 4.42. CVs recorded in 0.1M LiCl with 80% MeCN (v/v) of $H_3[PMo_{12}O_{40}]$ *(A) and CVs recorded in 1M LiCl of* $K_6[P_2Mo_{18}O_{62}]$ *(B)* $H_3[PW_{12}O_{40}]$ *(C) and* $K_6[P_2W_{18}O_{62}]$ *(D).CVs recorded with a GCE working electrode, SCE reference electrode and platinum counter electrode at a scan rate of 0.1 V* s^{-1} *with an analyte concentration of 10 mM.*

electrochemical reactions, such that positive ions flow towards negatively charged electrodes (or negatively charged analytes dissolved in solution or at the electrode surface) and *vice versa* (**Fig. 4.43**). If charge is to flow for an electrochemical process, ions from the electrolyte must freely move towards the opposite electrode. Normally for solution cyclic voltammetry experiments, the electrolyte concentration is at least an order of magnitude higher than that of the analyte, ensuring that spontaneous electron transfer can occur uninhibited by the balanced flow of ions in the electrolyte, thus minimising resistance. In the {POM}@SWNT materials, cations of the electrolyte (in this case H^+, Li^+ and Na^+) must be able to interact with the encapsulated POM as it becomes reduced, in order to balance the negative charge deposited during reduction. If this flow of positively charged ions is inhibited, charge cannot flow from the electrode to the POM.

4.44).

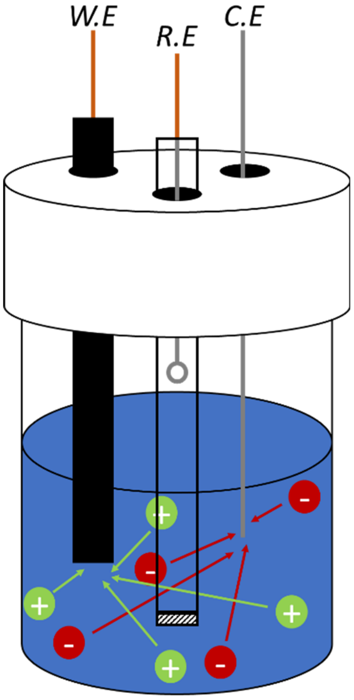

Figure 4.43. Schematic showing the flow of ions in an electrolyte solution during the reduction of an analyte species adsorbed onto the working electrode surface during a cyclic voltammetry experiment (not to scale). W.E. = working electrode, R.E. = reference electrode and C.E. = counter electrode.

The data above describing the low currents and rapid loss of electrochemical activity over 50 cycles when substituting H^+ for Li^+ and Na^+ therefore suggests that the transport of the larger cations to the encapsulated POMs was severely inhibited. Locally, the interaction between a reduced POM encapsulated within a SWNT and a cation from the electrolyte solution may occur through four different mechanisms: firstly, the cation may diffuse along the SWNT axis to the reduced POM, which can be accessed *via* the open ends of the nanotubes. Secondly, the ion may diffuse through the pristine graphitic lattice of the SWNT sidewall to the reduced POM. Thirdly, the cation may diffuse through any defects present within the SWNT sidewall large enough to accommodate the hydrated ion. Finally, the ion may interact with the reduced POM through the SWNT sidewall without directly diffusing through the graphitic lattice (**Fig. 4.44**).

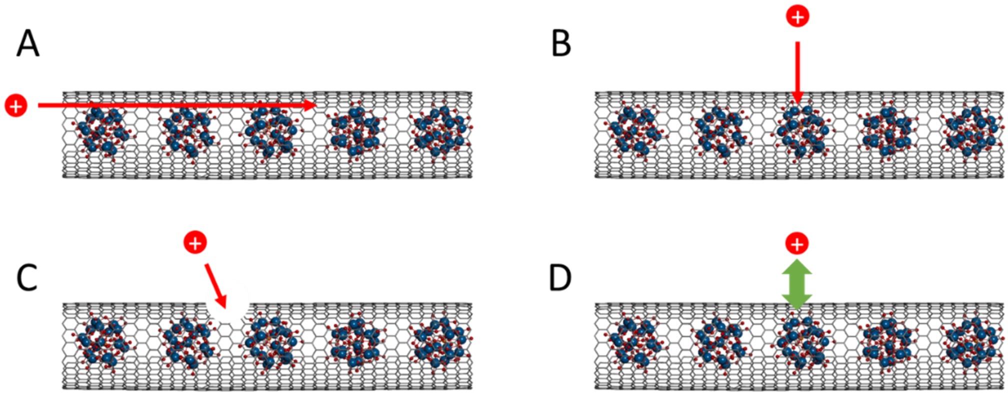

Figure 4.44. Schemes depicting the possible routes for cation access to encapsulated POMs upon reduction. (A) Through the SWNT open ends (B) diffusion through the pristine graphitic lattice of the SWNT side wall (C) through defects present in the SWNT side wall and (D) interacting with the reduced POM through the SWNT sidewall without diffusion through the graphitic lattice.

Energetically, the most likely route for diffusion to an encapsulated POM is through the opened SWNT ends,[35] due to the lack of steric barriers for hydrated cations. Although the initial steric barrier would be low, the presence of the encapsulated POMs would lead to large barriers further into the nanotube due to the presence of guest species,[36] therefore only allowing access to a small number of encapsulated POMs located close to the open ends of the SWNTs. As discussed previously (chapter 3), the rate of POM encapsulation was extremely high. For a cation to reach POMs close to centre of the SWNT many other POM molecules would have to be bypassed which, due to the close geometric match between the size of the POMs and the SWNT interior diameter, (chapter 2) would present significant energetic barriers.

For a H^+ ion however, transport rates would be expected to be higher *via* a hydrophobic SWNT channel.[37] There is also evidence of high proton mobility between POM[38] molecules, as well as a previous study on POMs encapsulated within DWNTs in which the authors reported high rates of proton transport.[39] The energy barrier for the transport of the larger Li^+ and Na^+ cations is likely to be much higher for this diffusion route due to their much larger radii.

Although single atom defects in the SWNT sidewall are large enough to mediate the diffusion of larger atoms,[40] for the main diffusion mechanism to be transport of the cations through defects in the SWNT sidewall the number of inherent defects within the SWNT sidewall would have to be extremely high, only achievable by purposely introducing a high level of defects by refluxing the SWNTs in acid.[41, 42] Assuming that the concentration of defects large enough to mediate the transport of Li^+ and Na^+ through the SWNT sidewalls was sufficiently high enough, the capacity retention for Li^+ and Na^+ CVs described above would also be much higher, indicating that this was not the primary diffusion mechanism.

Interactions between externally bound cations and the encapsulated POMs through the SWNT sidewall is also dubious. Previous work by Schmickler *et al.* has shown that ions of equal and opposite charge are mostly coulombically screened by the SWNT sidewall.[43] The authors reported that whilst there was an overall attractive force, this was mostly due to local modifications of the SWNT Density of States (DoS), leading to a large covalent-like component to the overall ion attraction.[44] Ions of equal charge, a pair of Li^+ ions[43] and a pair of Cl^- ions,[44] were similarly attracted to one another through the SWNT sidewall, further suggesting that any coulombic interactions are screened. The cationic SWNTs (chapter 2) would also likely lead to a less attractive force between the electrolyte cation and encapsulated POM. Additionally, whilst the reasons above cast doubt to this being the main ion-POM interaction, the loss or partial loss of certain peaks with increasing electrolyte pH mean that H^+ ions must have direct access to encapsulated POMs for PCET to take place in acidic electrolytes, which cannot be achieved *via* an interaction through the SWNT sidewall. The reduction in the current of the redox peaks in Li^+ and Na^+ electrolytes over repeated cycling also indicated that this interaction would not be sufficient to stabilise the encapsulated reduced POMs.

Whilst it is widely understood that atoms cannot diffuse through defect-free graphene under ambient conditions,[45] recent work has shown that protons can penetrate the hexagonal graphene lattice with applied potentials or at high temperatures.[45-47] The publication of experimental and theoretical data supporting this hypothesis has led to significant interest around the permeation of protons and deuterons through single atom crystals for use in fuel cells and isotope separation.[48] The work is still in its infancy and the hypothesis is currently debated. This is largely due to concerns over purity of the single graphene crystals used in the experimental studies, compounded by the publication of such theoretical results describing enhanced ion flow through seven-membered rings large enough that undetectable concentrations of such defects would lead to the experimentally observed levels of proton conductivity.[49] Despite the non-planar nature of the SWNT sidewall, the graphitic hexagonal lattice is comparable to that of graphene, with similar bond lengths. Overall, this leaves ion diffusion through

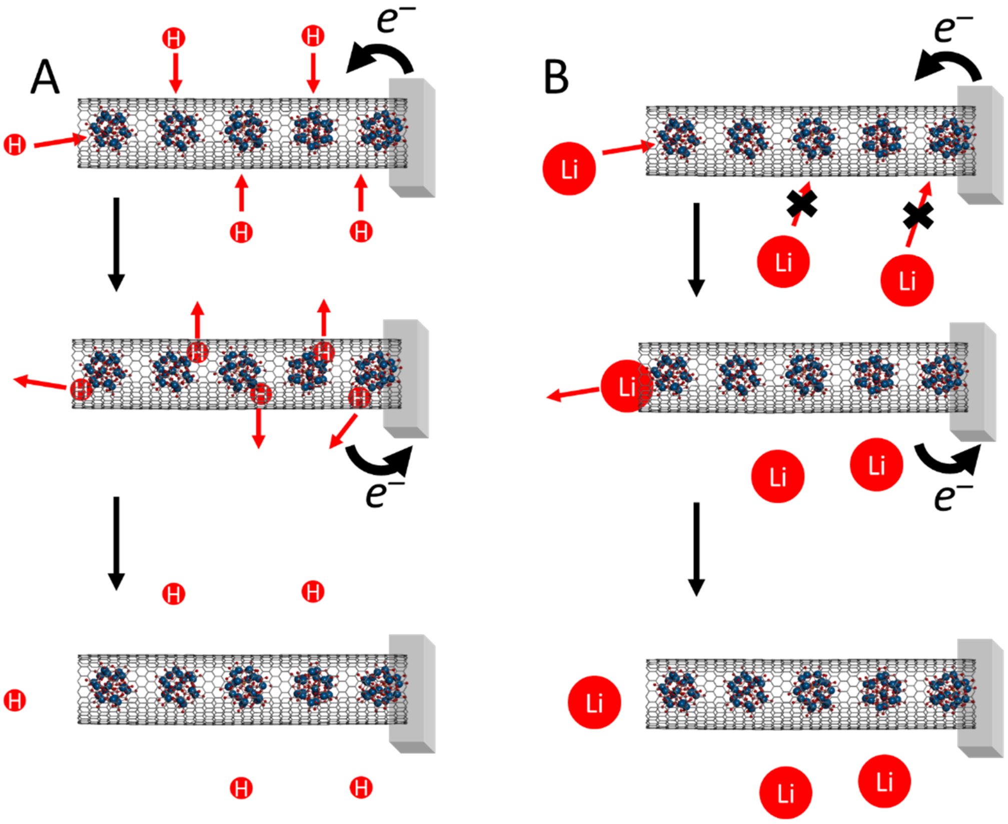

Figure 4.45. Schemes showing possible diffusion routes for H^+ ions (A) and Li^+ ions (B) (shown in red). Some Li^+ ions removed and model not to scale for clarity.

the SWNT sidewall as a possible contributing mechanism for ion access (specifically protons) to the encapsulated POMs during reduction, along with diffusion along the SWNT axis accessed through the open ends (**Fig. 4.45**).

To test the hypothesis of H^+ diffusion through the SWNT sidewall, the open ends of the {POM}@SWNT materials were capped with molecules of C_{60} after their deposition onto the electrode using a modified "nano-condensation" method,[50] to sterically hinder any ions that accessed the SWNT interior during POM reduction through the SWNT open ends. When applying this methodology to unfunctionalised SWNTs deposited on a GCE, the rate of encapsulation of the C_{60} molecules appeared high, (**Fig. 4.46, A**) and carbon debris was also visible when applying this methodology to the {$P_2W_{18}O_{62}$}@SWNT material. (**Fig. 4.46, B**) To test the effect on the electrochemical response of the {$P_2W_{18}O_{62}$}@SWNT material, {$P_2W_{18}O_{62}$}@SWNT was first deposited onto a GCE which was cycled once uncapped, then removed from the cell and capped using the described method. The electrodes were then added back to the same cell and cycled once again. When cycling the material in 1M H_2SO_4, there appeared to be very little difference in the current passed when the {POM}@SWNT sample was

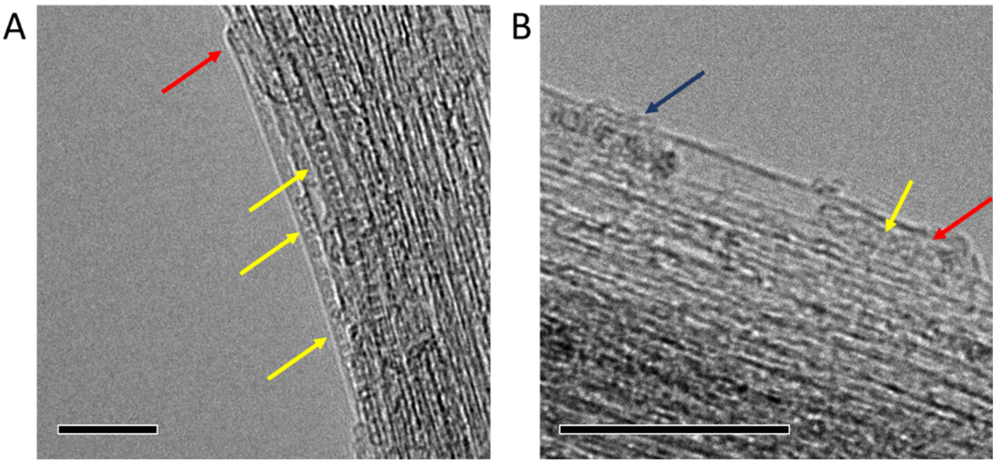

Figure 4.46. TEM images of (A) C_{60}@SWNT synthesised using the nanocondensation methodology on the GCE and (B) {$P_2W_{18}O_{62}$}@SWNT treated with the same method. Yellow arrows indicate the presence of C_{60}/carbon debris, red arrows indicate SWNT tips and blue arrows indicate POM molecules that have already begun to react under the electron beam. Images acquired with an accelerating voltage of 80 kV. Scale bars 10 nm.

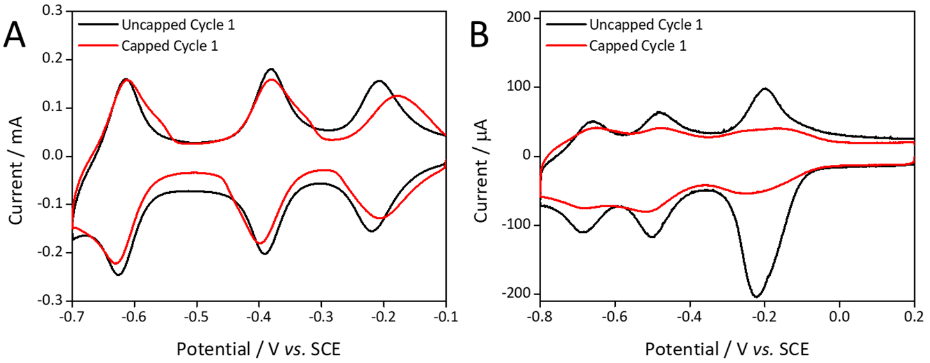

Figure 4.47. CVs of {$P_2W_{18}O_{62}$}@SWNT recorded in 1M H_2SO_4 (A) and 1M $LiClO_4$ (B) before capping with C_{60} (black) and after capping with C_{60} (red). CVs recorded with a GCE working electrode, SCE reference electrode and a platinum counter electrode at a scan rate of 0.1 V^{-1}.

uncapped and after the sample had been capped (**Fig. 4.47, A**). When cycling the {$P_2W_{18}O_{62}$}@SWNT material in 1M $LiClO_4$ however, there was a large reduction in the current observed upon the capping of the material (**Fig. 4.47, B**). These changes in the current for acidic and non-acidic electrolytes suggest that diffusion of H^+ ions through the graphitic lattice was a largely contributing diffusion route during the POM reduction, for which the barrier to H^+ penetration was sufficiently low enough for this to occur.

The barrier for Li^+ transport through the graphitic lattice was likely too high to occur, leading to the loss of the redox processes. This is in stark contrast to the proposed mechanism of Li^+-S interaction through the SWNT wall proposed by Fu and co-workers[51] and the intercalation of Li^+ ions in peapod materials proposed by the Kawasaki group[52, 53] and is also in good agreement with the arguments put forth by Kavan and co-authors.[54, 55] Such poor transport of Li^+ ions to the encapsulated POMs during repeated cycling led to extremely poor capacity retention, unlike what was observed in acidic electrolytes. This is problematic when considering the use of the {POM}@SWNT materials, or indeed any redox active species encapsulated with SWNTs, in current generation lithium-ion electrochemical energy storage devices. However, it does offer an interesting model system for studying ion transport in confined electrochemical environments, as well as ion penetration through one-dimensional crystals.

Although the overall influence of the cation on the observed electrochemistry was much greater, the anion could also affect the redox response of the {POM}@SWNT materials. When changing the anion of the electrolyte between SO_4^{2-} and Cl^- there appeared to be very few differences between the electrochemical response in all the materials. When carrying out cyclic voltammetry experiments with a ClO_4^- anion however, there appeared to be changes in the peak positions and peak currents of the redox processes in the {Mo-POM}@SWNT materials, (**Fig. 4.48**) as well as the apparent loss of some processes altogether in the {$P_2Mo_{18}O_{62}$}@SWNT material. The use of a $HClO_4$ electrolyte did not appear to shift the redox processes in the {W-POM}@SWNT materials in the same way, however the use of this electrolyte led to extremely noisy CVs in the {$P_2W_{18}O_{62}$}@SWNT material, and rapid drop off of the peak currents over repeated cycles even when cycling with a H^+ cation for both {W-POM}@SWNT

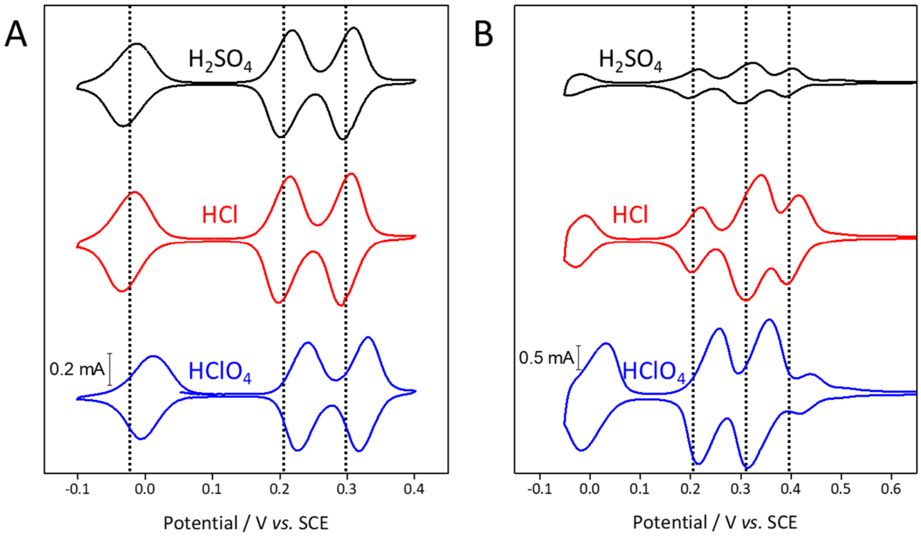

Figure 4.48. CVs of {$PMo_{12}O_{40}$}@SWNT (A) and {$P_2Mo_{18}O_{62}$}@SWNT (B) recorded in different 1 M acids (labelled, inset). All CVs recorded with a GCE working electrode, SCE reference electrode and platinum counter electrode at a scan rate of 0.1 V s^{-1}.

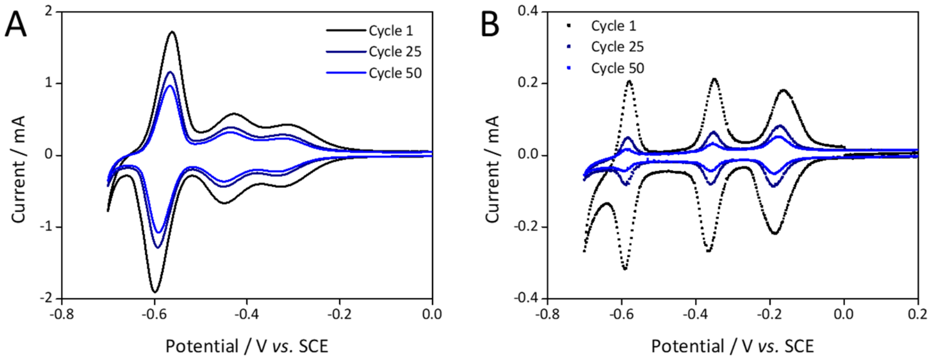

Figure 4.49. CVs of {$PW_{12}O_{40}$}@SWNT (A) and {$P_2W_{18}O_{62}$}@SWNT (B) recorded in 1M $HClO_4$. The current of the processes appears to decrease rapidly relative to HCl and H_2SO_4. (B) plotted as discrete data point due to the large amount of noise in the voltammograms. CVs recorded with a GCE working electrode, SCE reference electrode and platinum counter electrode at scan rate of 0.1 V s^{-1}.

materials (**Fig. 4.49**). Cycling the native POM dissolved in the electrolyte did not appear to have the same effect on the redox chemistry of the POMs. The reason surrounding this change in the redox chemistry is not entirely clear, however it has been previously reported that chlorine oxoanions can affect the band structure of CNTs when they are adsorbed onto their surfaces.[56] This in turn may alter the electronic properties of the SWNTs in the {POM}@SWNT materials, leading to the shifts in the redox processes and rapid reduction in currents described above.

4.4.7 $\{V_6\}$@SWNT Cyclic Voltammetry

In contrast to the Mo/W-POMs, the $V_6O_7(OMe)_{12}$ molecule could partake in both reductions and oxidations (**Fig. 4.50**) of which all processes were one-electron and are summarised in **table 4.24**. The processes were all independent of any PCET processes, and the poor solubility and stability of the compound in aqueous solutions meant that

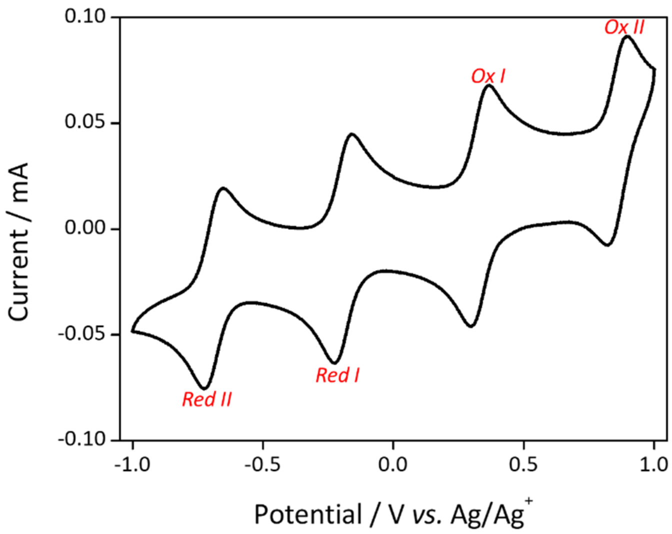

Figure 4.50. CV of $V_6O_7(OMe)_{12}$ recorded in MeCN with a 0.1M $TBAPF_6$ supporting electrolyte with a GCE working electrode, SCE reference electrode and platinum counter electrode at a scan rate of 0.1 V s^{-1}.

Table 4.24. Summary of the $V_6O_7(OMe)_{12}$ redox processes taken from figure 4.50. All potentials vs. Ag/Ag^+.

$V_6O_7(OMe)_{12}$ Processes		
Process	Equation	Potential / V
Ox II	$[V^{IV}{}_3V^{V}{}_3O_7(OMe)_{12}]^{+} \rightleftharpoons [V^{IV}{}_2V^{V}{}_4O_7(OMe)_{12}]^{2+} + e^-$	0.864
Ox I	$[V^{IV}{}_4V^{V}{}_2O_7(OMe)_{12}]^{0} \rightleftharpoons [V^{IV}{}_3V^{V}{}_3O_7(OMe)_{12}]^{+} + e^-$	0.328
Red I	$[V^{IV}{}_4V^{V}{}_2O_7(OMe)_{12}]^{0} + e^- \rightleftharpoons [V^{IV}{}_5V^{V}O_7(OMe)_{12}]^{-}$	-0.193
Red II	$[V^{IV}{}_5V^{V}O_7(OMe)_{12}]^{-} + e^- \rightleftharpoons [V^{IV}{}_6O_7(OMe)_{12}]^{2-}$	-0.690

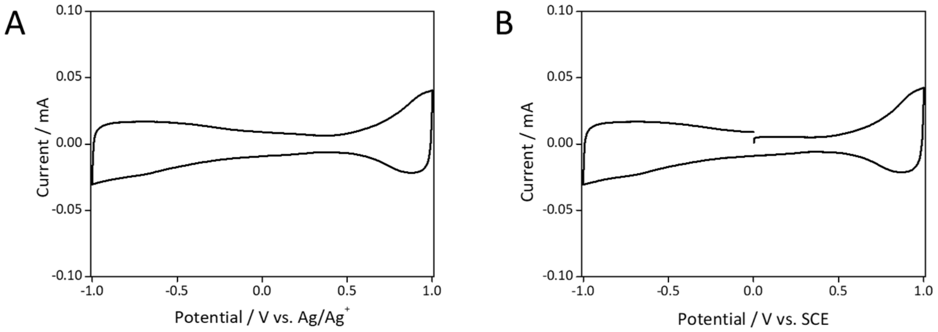

Figure 4.51. (A) CV of {V_6}@SWNT recorded in MeCN with a 0.1M $TBAPF_6$ supporting electrolyte against a Ag/Ag^+ non-aqueous reference electrode. (B) CV of {V_6}@SWNT recorded in 1M H_2SO_4 against a SCE reference electrode. Both CVs recorded with a GCE working electrode and platinum counter electrode at a scan rate of 0.1 V s^{-1}.

the electrochemical studies had to be carried out in MeCN with a 0.1M tetrabutylammonium hexafluorophosphate ($TBAPF_6$) supporting electrolyte.

In contrast to the {Mo/W-POM}@SWNT materials reported above, the {V_6}@SWNT material (chapter 2) appeared to have no electrochemical activity, (**Fig. 4.51**) indicating that either upon encapsulation the [V_6] molecule could no longer partake in electrochemical processes, or the TBA^+ cation was too large to interact with the encapsulated [V_6] molecules upon reduction. Due to the electrolyte cation effect

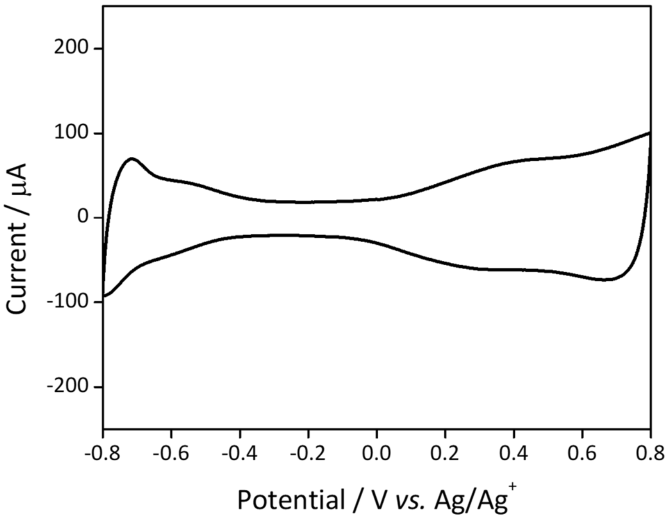

Figure 4.52. CV of {$P_2W_{18}O_{62}$}@SWNT recorded in MeCN with a 0.1M $TBAPF_6$ supporting electrolyte with a GCE working electrode, non-aqueous Ag/Ag^+ reference electrode and a platinum counter electrode at a scan rate of 0.1 V s^{-1}.

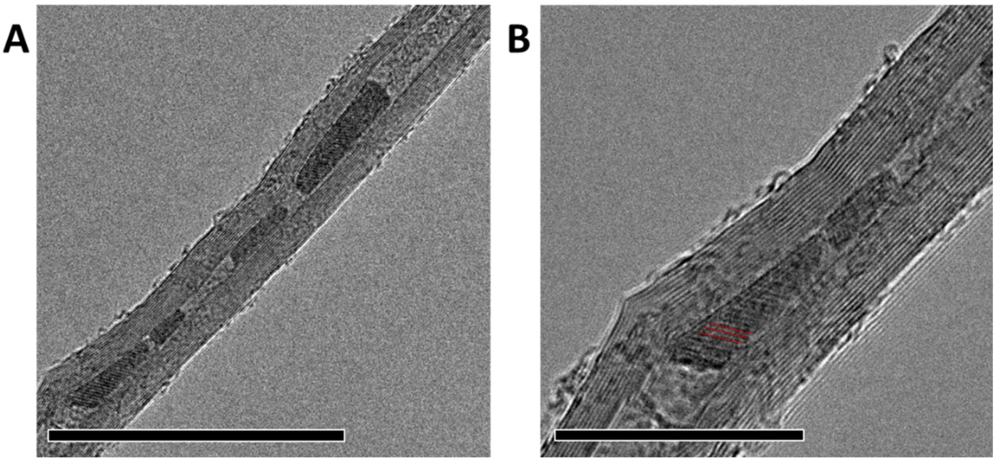

Figure 4.53. (A) TEM image of {V_6}@MWNT scale bar 50 nm. (B) Magnified TEM image of {V_6}@MWNT showing the d-spacing of the crystalline nanoparticle (red lines, inset) scale bar 20 nm. Both images acquired with an accelerating voltage of 80 kV.

described above (a TBA^+ electrolyte also led to the absence of any redox activity from the encapsulated POM in the {$P_2W_{18}O_{62}$}@SWNT material (**Fig. 5.52**)) cyclic voltammetry of the {V_6}@SWNT material was also carried out in 1M H_2SO_4. This again incited no electrochemical response from the material (**Fig. 4.51**).

To ensure that the acidic electrolyte was not destabilising the encapsulated [V_6] molecules, the [V_6] was instead encapsulated within multiwalled carbon nanotubes (MWNTs) with a larger average internal diameter of 15 nm. The use of CNTs with such a large internal cavity would not inhibit the mass transport of the large TBA^+ and PF_6^- ions during reduction/oxidation. Encapsulating the [V_6] material within the MWNTs was carried out using a similar solution methodology as reported previously for the {V_6}@SWNT material (chapter 2). TEM analysis of the {V_6}@MWNT material showed the presence of large, continuous nanoparticles encapsulated within the MWNT (**Fig. 4.53**). Qualitatively, the loading of metal oxide appeared extremely low *via* TEM analysis, with mostly unfunctionalised MWNTs present within the sample, suggesting a poor affinity between the [V_6] and MWNT. The nanoparticles were crystalline with a d-spacing of approximately 0.50 nm. This suggested that upon encapsulation of the [V_6], the molecule's structure was lost upon the formation of bulk vanadium oxide.

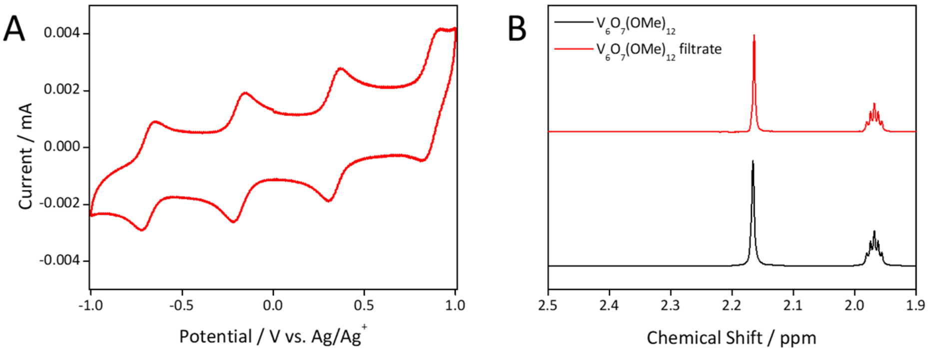

Figure 4.54. (A) CV of the compound removed from solution of the {V_6}@MWNT synthesis recorded in MeCN with a 0.1M $TBAPF_6$ supporting electrolyte with a GCE working electrode, Ag/Ag^+ non-aqueous reference electrode and platinum counter electrode at a scan rate of 0.1 V s^{-1}. (B) ^1H NMR of the native [V_6] molecule and the compound removed from the solution of the {V_6}@MWNT synthesis in CD_3CN.

A CV of the compound that persisted in the solution after the encapsulation experiment showed that [V_6] molecules remaining in solution were not chemically modified during the encapsulation experiment (**Fig. 4.54, A**). This was again further evidenced by comparing the ^1H NMR spectra of the native [V_6] compound and the compound removed from the solution after the encapsulation experiment (**Fig. 4.54, B**). This suggested that the conditions used during the experiment were not destroying the [V_6] in solution. Furthermore, the TGA of the material showed a [V_6] loading largely consistent with that of the {V_6}@SWNT material (**Fig. 4.55**).

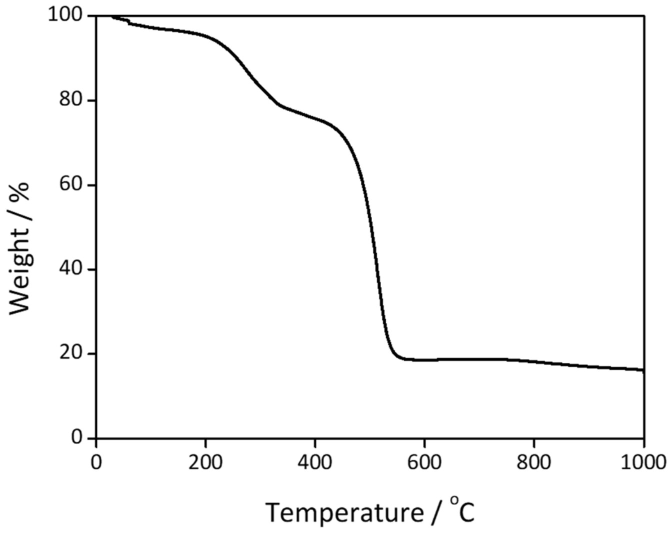

Figure 4.55. TGA of {V_6}@MWNT. Sample heated in air to 1000 °C at a ramp rate of 10 °C per minute.

The electrochemical activity of the [V_6] molecule was once again lost in the {V_6}@MWNT material, (**Fig. 4.56**) in good agreement with the TEM analysis, suggesting that upon encapsulation within the MWNTs there was loss of structure, leading to loss of electrochemical activity. The overall loss of [V_6] electrochemical activity after both encapsulation within SWNTs and MWNTs suggests that the confined environment was too destabilising on the $V_6O_7(OMe)_{12}$ molecule, likely leading to the loss of the molecular structure in both cases.

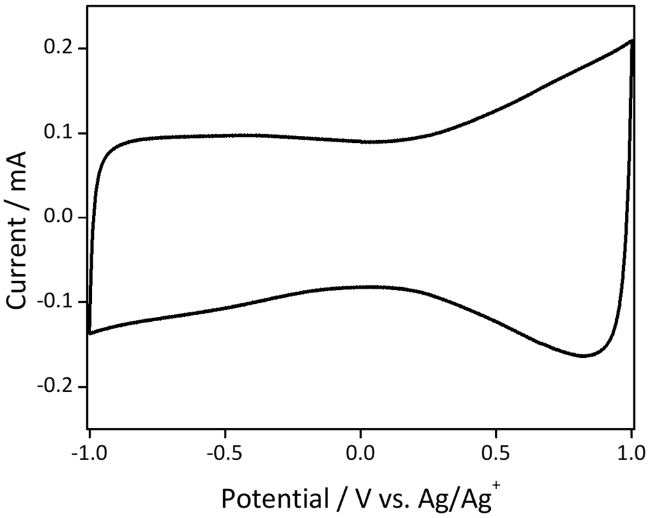

Figure 4.56. CV of {V_6}@MWNT recorded in MeCN with a 0.1M $TBAPF_6$ supporting electrolyte with a GCE working electrode, Ag/Ag^+ non-aqueous reference electrode and a platinum counter electrode at a scan rate of 0.1 V s^{-1}.

4.4 Conclusion

The cyclic voltammetry of the POM@SWNT materials revealed that the POMs were still electrochemically addressable upon their encapsulation within the SWNTs. In acidic electrolytes, the CVs of the materials were characterised by large peak currents, low ΔE_p values and narrow FWHM values. These all demonstrated rapid charge transfer between the redox active POMs and the electrode, mediated by the highly conductive SWNTs. For the {Mo-POM}@SWNT materials, the total number of redox processes associated with the clusters could not be accessed during electrochemical cycling, and the potential windows of the materials were limited by HER at lower potentials. For the {W-POM}@SWNT materials, it appeared that the POMs could still readily accept the same number of electrons as in solutions, with changes to one of the processes in the $\{P_2W_{18}O_{62}\}$@SWNT material, associated with the confined environment.

Comparisons between the TGA of the materials and the charge passed during cycling revealed that a large amount of the encapsulated POM could be electrochemically addressed during charge-discharge, indicating that the material was approaching a true molecular dispersion. CVs of the materials over 1000 cycles in acidic electrolytes and in electrolytes with a high pH demonstrated the stabilising ability of the SWNTs, which could be electrochemically addressed in harsh conditions for approximately 15 cycles.

This low cyclability of the POM@SWNT materials in basic conditions also applied to CVs acquired in non-acidic electrolytes with a pH of 7. Altering the cation from proton to Li^+ and Na^+ appeared to lead to the loss of current over a short number of cycles relative to that in acid, as well as changes in the number of observed process and their peak intensities. Analysing the data in different electrolytes and the FWHM values in acidic electrolytes, the nature of the reductions of the encapsulated POMs, such as number of electrons and amount of PCET, could be determined.

The low cyclability of the non-acidic electrolytes suggested that the transport of protons to the encapsulated POMs upon reduction was rapid, which was likely made up of access along the SWNT open ends, as well as significant contributions from diffusion through the graphitic side wall. The larger Li^+ and Na^+ cations were too large for these pathways, leading to their low cyclability. This was further probed by capping the SWNT ends with fullerene molecules, restricting the transport of these species further. Upon capping, there appeared to be no differences in the recorded CV of the {POM}@SWNT materials in acidic conditions, however there were large reductions in the current when utilising Li^+ in the electrolyte.

The {V_6}@SWNT material exhibited no confined redox chemistry when utilising a range of different electrolytes. Loading of this material within MWNTs suggested that this was due to decomposition of the vanadium cluster upon contact with the carbon supports.

Overall, this study has shown that encapsulated species within SWNTs can benefit from rapid charge-discharge and high stability providing an opportunity to develop stable, high power solid-state redox materials. However, the inhibited diffusion of cations to the redox active species within these nano domains is a significant drawback if the species are to be utilised in current generation technologies, requiring further work to overcome this.

4.5 Experimental

4.5.1 General

All common reagents and solvents were used as received from Sigma-Aldrich, Acros Organics or Thermo Fisher. Single walled carbon nanotubes (P2) were purchased from Carbon Solutions Inc. Multiwalled carbon nanotubes (PD30L520) were purchased from NanoLab Inc. $V_6O_7(OMe)_{12}$ was acquired from Dr. Ellen Matson's group (University of Rochester, NY).

Electrochemistry experiments were performed on an Autolab PGSTAT302N. Aqueous electrochemistry was performed using a three-electrode set up with a reference saturated calomel electrode, a glassy carbon working electrode and platinum counter electrode. MeCN electrochemistry used a three-electrode set up with a Ag/Ag^+ non-aqueous reference electrode, glassy carbon working electrode and platinum counter electrode. The analytes were dissolved in the supporting electrolyte to a concentration of 10 mM. {POM}@SWNT and SWNT materials were first sonicated for 15 minutes in a 10 mg/mL aqueous suspension containing 3 wt % PTFE binder. After they had been sonicated 8 µL of the suspension was deposited onto the GCE working electrode and left until completely dry. Electrodes were purchased from IJ Cambria.

HRTEM images were acquired on a JEOL 2100F field emission gun microscope with an accelerating voltage of 200 kV. Samples were prepared by first dispersing them in isopropyl alcohol which were then dropped onto a copper grid mounted with a "lacey" carbon film.

Micro-Raman spectroscopy was performed using a Horiba-Jobin-Yvon LabRAM HR spectrometer. Single-point spectra were recorded using a 100× objective, a 300-µm confocal pinhole, and a 660 nm (1.88 eV) laser at < 0.3 mW. The spectral resolution was better than 1.2 cm^{-1}. Instrument calibration was performed using the zero-order line and a standard Si(100) reference band at 520.7 cm^{-1}. Samples were prepared by depositing a small quantity of sample from a methanolic suspension onto Si(100) wafers. A typical spectrum was recorded by averaging 4-8 acquisitions, each of 5-30 s duration.

All TEM images were processed using Gatan Digital Micrograph, and quoted distances were measured by drawing a line profile and measuring the electron density histogram.

Thermogravimetric analysis was obtained using a TA Q500 analyser, on platinum pans. In all cases ramp rate were 10 °C per minute to 1000 °C followed by an isothermal hold for 10 minutes, all in an air flow of 90 mL/min.

NMR data was acquired using a Bruker AVIII400 400 MHz spectrometer using the University of Nottingham's open access analytical services.

4.5.2 C_{60} capping of $\{P_2W_{18}O_{62}\}$@SWNT[50]

To first test the capping process, SWNTs (15 mg) were heated at 600 °C for 30 minutes giving a black solid (8 mg), which was made to 10 mg/mL aqueous dispersion with 3 wt% PTFE binder. 10 µL of this dispersion was drop cast onto a GCE electrode and allowed to fully dry. 10 µL of a solution of C_{60} (2 mg/mL) in toluene was then dropcast onto the dry electrode.

When applying this to the $\{P_2W_{18}O_{62}\}$@SWNT material, the same procedure was followed as stated above, followed by the addition of 10 µL of toluene to facilitate the encapsulation of any fullerene crystals on the surface.

4.5.3 Synthesis of $\{V_6\}$@MWNT

$V_6O_7(OMe)_{12}$ (30 mg) was dissolved in MeCN (3 mL) under an atmosphere of argon. MWNTs (15 mg) were heated to 500 °C for 15 minutes yielding a black solid (8 mg).

This was subsequently added to the green solution, sonicated for 5 minutes and stirred at room temperature under an atmosphere of argon for 48 hours. The solution was then filtered to give a black solid (8 mg).

4.6 References

1. N. I. Gumerova and A. Rompel, *Nat. Rev. Chem*, 2018, **2**, 0112.
2. J. M. Cameron, S. Fujimoto, K. Kastner, R.-J. Wei, D. Robinson, V. Sans, G. N. Newton and H. H. Oshio, *Chem. - Eur. J.*, 2017, **23**, 47-50.
3. D.-L. Long, R. Tsunashima and L. Cronin, *Angew. Chem., Int. Ed.*, 2010, **49**, 1736-1758.
4. M. Genovese and K. Lian, *Curr. Opin. Solid State Mater. Sci.*, 2015, **19**, 126-137.
5. Y. Ji, L. Huang, J. Hu, C. Streb and Y.-F. Song, *Energy Environ. Sci.*, 2015, **8**, 776-789.
6. D. Pan, J. Chen, W. Tao, L. Nie and S. Yao, *Langmuir*, 2006, **22**, 5872-5876.
7. S. Li, X. Yu, G. Zhang, Y. Ma, J. Yao and P. de Oliveira, *Carbon*, 2011, **49**, 1906-1911.
8. F. M. Toma, A. Sartorel, M. Iurlo, M. Carraro, P. Parisse, C. Maccato, S. Rapino, B. R. Gonzalez, H. Amenitsch, T. Da Ros*, et al.*, *Nat. Chem.*, 2010, **2**, 826-831.
9. F. M. Toma, A. Sartorel, M. Iurlo, M. Carraro, S. Rapino, L. Hoober-Burkhardt, T. Da Ros, M. Marcaccio, G. Scorrano, F. Paolucci*, et al.*, *ChemSusChem*, 2011, **4**, 1447-1451.
10. D. Wang, S. Lu and S. P. Jiang, *Chem. Commun.*, 2010, **46**, 2058-2060.
11. R. Liu, S. Li, X. Yu, G. Zhang, Y. Ma and J. Yao, *J. Mater. Chem.*, 2011, **21**, 14917-14924.
12. M. A. Herrero, F. M. Toma, K. T. Al-Jamal, K. Kostarelos, A. Bianco, T. Da Ros, F. Bano, L. Casalis, G. Scoles and M. Prato, *J. Am. Chem. Soc.*, 2009, **131**, 9843-9848.
13. A. Sartorel, M. Carraro, G. Scorrano, R. D. Zorzi, S. Geremia, N. D. McDaniel, S. Bernhard and M. Bonchio, *J. Am. Chem. Soc.*, 2008, **130**, 5006-5007.
14. A. Sartorel, P. Miró, E. Salvadori, S. Romain, M. Carraro, G. Scorrano, M. D. Valentin, A. Llobet, C. Bo and M. Bonchio, *J. Am. Chem. Soc.*, 2009, **131**, 16051-16053.

15. N. Kawasaki, H. Wang, R. Nakanishi, S. Hamanaka, R. Kitaura, H. Shinohara, T. Yokoyama, H. Yoshikawa and K. Awaga, *Angew. Chem., Int. Ed.*, 2011, **50**, 3471-3474.
16. D. Ma, L. Liang, W. Chen, H. Liu and Y.-F. Song, *Adv. Funct. Mater.*, 2013, **23**, 6100-6105.
17. G. Bajwa, M. Genovese and K. Lian, *ECS J. Solid State SC.*, 2013, **2**, M3046-M3050.
18. M. Genovese, Y. W. Foong and K. Lian, *Electrochimica Acta*, 2014, **117**, 153-158.
19. M. Genovese and K. Lian, *Electrochem. Commun.*, 2014, **43**, 60-62.
20. M. Genovese, Y. W. Foong and K. Lian, *J. Electrochem. Soc.*, 2015, **162**, A5041-A5046.
21. M. Genovese and K. Lian, *ACS Appl. Mater. Interfaces*, 2016, **8**, 19100-19109.
22. Z. Wang, H. Li, Z. Liu, Z. Shi, J. Lu, K. Suenaga, S.-K. Joung, T. Okazaki, Z. Gu, J. Zhou*, et al.*, *J. Am. Chem. Soc.*, 2010, **132**, 13840-13847.
23. Z. Wang, K. Zhao, H. Li, Z. Liu, Z. Shi, J. Lu, K. Suenaga, S.-K. Joung, T. Okazaki, Z. Jin*, et al.*, *J. Mater. Chem.*, 2011, **21**, 171-180.
24. J. Sloan, G. Matthewman, C. Dyer-Smith, A. Y. Sung, Z. Liu, K. Suenaga, A. I. Kirkland and E. Flahaut, *ACS Nano*, 2008, **2**, 966-976.
25. B. Fei, H. Lu, W. Chen and J. H. Xin, *Carbon*, 2006, **44**, 2261-2264.
26. M. Sadakane and E. Steckhan, *Chem. Rev.*, 1998, **98**, 219-238.
27. H. Sadayuki, O. Toshiyuki and S. Atsuyoshi, *Bull. Chem. Soc. Jpn.*, 1989, **62**, 1335-1337.
28. A. J. Bard and L. R. Faulkner, *Electrochemical Methods Fundamentals and Applications* John Wiley & Sons, Second Edn., 2001.
29. W. Baoxing and D. Shaojun, *J. Electroanal. Chem.*, 1992, **328**, 245-257.
30. D. A. C. Brownson and C. E. Banks, *The Handbook of Graphene Electrochemistry*, Springer, 2014.
31. N. Sun, L. Guan, Z. Shi, Z. Zhu, N. Li, M. Li and Z. Gu, *Electrochem. Commun.*, 2005, **7**, 1148-1152.
32. B. Keita and L. Nadjo, *J. Electroanal. Chem. Inter. Electrochem.*, 1987, **227**, 77-98.
33. S. Fleischmann, J. B. Mitchell, R. Wang, C. Zhan, D.-e. Jiang, V. Presser and V. Augustyn, *Chem. Rev.*, 2020, **120**, 6738-6782.

34. M. A. Bird, S. E. Goodwin and D. A. Walsh, *ACS Appl. Mater. Interfaces*, 2020, **12**, 20500-20506.
35. W. Choi, Z. W. Ulissi, S. F. E. Shimizu, D. O. Bellisario, M. D. Ellison and M. S. Strano, *Nat. Commun.*, 2013, **4**, 2397.
36. K. Gopinadhan, S. Hu, A. Esfandiar, M. Lozada-Hidalgo, F. C. Wang, Q. Yang, A. V. Tyurnina, A. Keerthi, B. Radha and A. K. Geim, *Science*, 2019, **363**, 145-148.
37. R. H. Tunuguntla, F. I. Allen, K. Kim, A. Belliveau and A. Noy, *Nat. Nanotechnol.*, 2016, **11**, 639-644.
38. M. J. Janik, R. J. Davis and M. Neurock, *J. Am. Chem. Soc.*, 2005, **127**, 5238-5245.
39. M. M. Hasani-Sadrabadi, E. Dashtimoghadam, F. S. Majedi, J. J. VanDersarl, A. Bertsch, P. Renaud and K. I. Jacob, *Nano Energy*, 2016, **23**, 114-121.
40. K. Cao, S. T. Skowron, C. T. Stoppiello, J. Biskupek, A. N. Khlobystov and U. Kaiser, *Angew. Chem., Int. Ed.*, **n/a**.
41. H. Hu, B. Zhao, M. E. Itkis and R. C. Haddon, *J. Phys. Chem. B*, 2003, **107**, 13838-13842.
42. P.-X. Hou, C. Liu and H.-M. Cheng, *Carbon*, 2008, **46**, 2003-2025.
43. F. Juarez, F. Dominguez-Flores, P. Quaino, E. Santos and W. Schmickler, *Phys. Chem. Chem. Phys.*, 2020, **22**, 10603-10608.
44. F. Dominguez-Flores, E. Santos, W. Schmickler and F. Juarez, *J. Solid State Electrochem.*, 2020, **24**, 3207-3214.
45. L. Mogg, S. Zhang, G. P. Hao, K. Gopinadhan, D. Barry, B. L. Liu, H. M. Cheng, A. K. Geim and M. Lozada-Hidalgo, *Nat. Commun.*, 2019, **10**, 4243.
46. S. Hu, M. Lozada-Hidalgo, F. C. Wang, A. Mishchenko, F. Schedin, R. R. Nair, E. W. Hill, D. W. Boukhvalov, M. I. Katsnelson, R. A. W. Dryfe*, et al.*, *Nature*, 2014, **516**, 227-230.
47. J. L. Achtyl, R. R. Unocic, L. Xu, Y. Cai, M. Raju, W. Zhang, R. L. Sacci, I. V. Vlassiouk, P. F. Fulvio, P. Ganesh*, et al.*, *Nat. Commun.*, 2015, **6**, 6539.
48. M. Lozada-Hidalgo, S. Hu, O. Marshall, A. Mishchenko, A. N. Grigorenko, R. A. W. Dryfe, B. Radha, I. V. Grigorieva and A. K. Geim, *Science*, 2016, **351**, 68-70.
49. Y. An, A. F. Oliveira, T. Brumme, A. Kuc and T. Heine, *Adv. Mater.*, 2020, **32**, 2002442.

50. M. Yudasaka, K. Ajima, K. Suenaga, T. Ichihashi, A. Hashimoto and S. Iijima, *Chem. Phys. Lett.*, 2003, **380**, 42-46.

51. C. Fu, M. B. Oviedo, Y. Zhu, A. von Wald Cresce, K. Xu, G. Li, M. E. Itkis, R. C. Haddon, M. Chi, Y. Han*, et al.*, *ACS Nano*, 2018, **12**, 9775-9784.

52. S. Kawasaki, Y. Iwai and M. Hirose, *Mater. Res. Bull.*, 2009, **44**, 415-417.

53. T. Matsushita, Y. Ishii and S. Kawasaki, *Mater. Express*, 2013, **3**, 30-36.

54. L. Kavan, L. Dunsch, H. Kataura, A. Oshiyama, M. Otani and S. Okada, *J. Phys. Chem. B*, 2003, **107**, 7666-7675.

55. L. Kavan, L. Dunsch and H. Kataura, *Carbon*, 2004, **42**, 1011-1019.

56. S.-M. Yoon, S. J. Kim, H.-J. Shin, A. Benayad, S. J. Choi, K. K. Kim, S. M. Kim, Y. J. Park, G. Kim, J.-Y. Choi*, et al.*, *J. Am. Chem. Soc.*, 2008, **130**, 2610-2616.

Chapter 5: Encapsulating Polyoxometalates within Boron Nitride Nanotubes

5.1 Background

Akin to the many allotropes of carbon, boron nitride may exhibit multiple phases. Boron nitride nanotubes (BNNTs) are structural analogues of carbon nanotubes (CNTs), made up of rolled-up sheets of hexagonal boron nitride (h-BN)[1] (**Fig. 5.1**). The h-BN lattice is composed of boron and nitrogen in a 1:1 ratio and is isostructural to graphene,[2] albeit with a slightly longer bond length (1.44 *vs* 1.42 Å).[3]

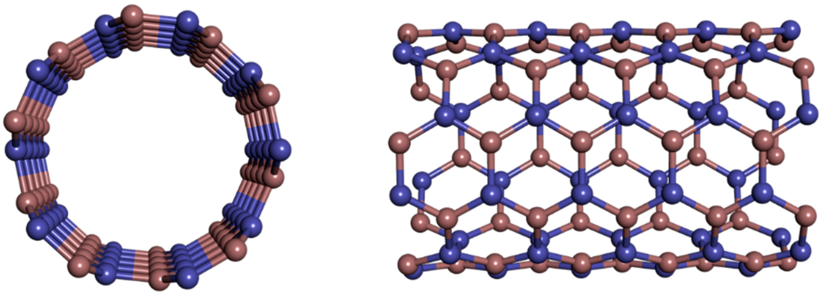

Figure 5.1. End on and side on view of a short single walled (5,5) BNNT. Nitrogen atoms are shown in blue and boron atoms shown in pink.

Both h-BN and BNNTs are white and transparent to visible light. The strong B-N bonds[4] (386 kJ mol^{-1}) (slightly stronger than that of the C–C bonds in graphene, 357 kJ mol^{-1}) mean that the BN structures are more chemically and thermally stable than CNTs[5] and possess high tensile strength.[6] The structure is isoelectronic to graphene; however, the bonding network is made up of localised π-bonding, rather than delocalised in the case of graphene, through electron donation from the electron rich nitrogen p_z orbitals to the electron deficient boron p_z orbitals (**Fig. 5.2**). Boron nitride sheets and BNNTs possess wide band gaps, estimated to be approximately 5.5 – 6.5 eV (depending on the number of h-BN layers) in h-BN sheets,[7-9] which is also manifested in BNNTs.[10]

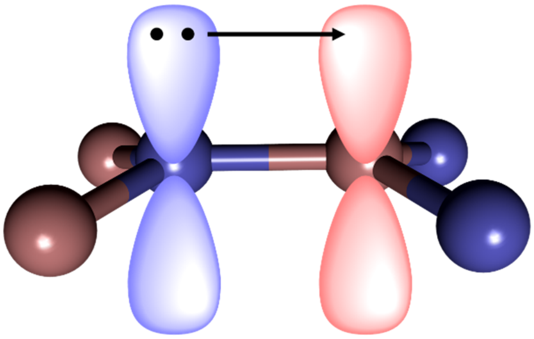

Figure 5.2. Local bonding in a BN lattice showing charge donation from the p_z orbital of the nitrogen atom the p_z orbital of the boron atom. Nitrogen shown in blue, boron shown in pink.

Unlike SWNTs, the electronic band structure of BNNTs is independent of their chirality and diameter,[11] meaning that all BNNTs are considered wide bang-gap semiconductors. Photoexcitation of h-BN and BNNTs with UV light (due to the wide band gaps) leads to the production of excitons, however these are very short lived and rapidly recombine, leading to photoluminescence (PL) emissions.[12]

Only recently have BNNTs been produced on a large enough scale for experimental studies.[13] Often, commercially available BNNTs have high levels of impurities and contain wide ranges in the diameters and number of sidewalls. Like graphene and CNTs, guest-species can be loaded onto/encapsulated within h-BN/BNNTs. Whilst examples of encapsulated guests within BNNTs is far scarcer than that of CNTs, there are examples where C_{60},[14, 15] metals[16-19] and metal halides[20] have been encapsulated within BNNTs. Examples on the loading of active materials onto h-BN sheets are more common[4, 21] however, the insulating nature of h-BN/BNNTs and lack of low-lying energy states means that charge transfer between host and guest is not as energetically favourable. Normally, electronic transitions between the two species require an external stimulus, such as light, leading to the promotion of electrons to higher energies.

Ma *et al.* described electronic transitions between h-BN sheets and adsorbed CdS nanoparticles.[22] The authors loaded the CdS nanoparticles onto the h-BN surface using an *in situ* approach during nanoparticle synthesis, leading to strong interactions between the CdS nanoparticles and BN support. Structural characterisation of the material suggested that the CdS preferentially grew on defect sites and edge sites of the BN lattice, leading to strong interactions between the two species. The composite showed an increase in the turnover number (TON) of the photocatalytic hydrogen evolution reaction (HER) by 2.3 when comparing neat CdS nanoparticles to those supported on the h-BN sheets. Based on the above structural characterisation, increases in generated photocurrents of the hybrid material and the broader absorption profile, the authors attributed the increase in catalytic rate to electronic transitions between the BN support and the CdS nanoparticles, which was possible due to lower energy band gap transitions (as low as 0.90 eV) in the BN sheets at defect and vacancy sites.[23] This led to increased charge separation, as well as charge transfer from the BN sheets to the active CdS nanoparticles (**Fig. 5.3**).

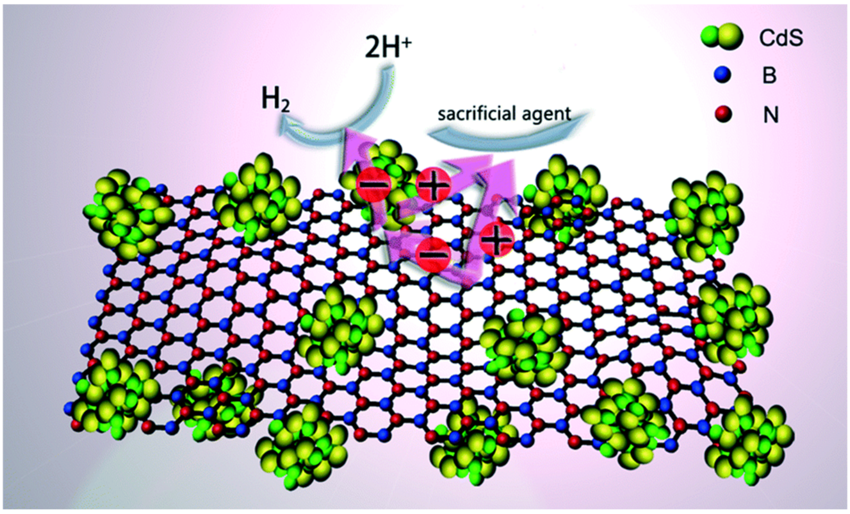

Figure 5.3. Schematic of charge separation and transfer in the CdS/h-BN hybrid material. Reproduced from reference 22 with permission from The Royal Society of Chemistry (RSC).

Alternatively, Choi *et al.* formed AgI nanoparticles on h-BN sheets.[24] A decrease in the intensity of the PL emission in the AgI nanoparticles after being loaded onto the h-BN sheets suggested increased exciton separation upon photoexcitation of the system. This increased charge separation led to an increase in the photocatalytic activity of the system towards the reduction of 4-nitrophenol to 4-aminophenol, which was reduced by the AgI nanoparticles (**Fig. 5.4**). The loading of biphasic AgI/AgBr nanoparticles onto h-BN sheets was also reported by Wu *et al.,* which also demonstrated photoexcited charge transfer from the adsorbed nanoparticles to the h-BN support, increasing the catalytic rate on the degradation of rhodamine B.[25] Similar results were also shown with Ag_2CrO_4 nanoparticles, where photoexcited charge injection from the nanoparticles to h-BN also occurred.[26] These studies demonstrate the ability of h-BN to increase charge separation and reduce exciton recombination in photoactive systems by accepting both holes and electrons.

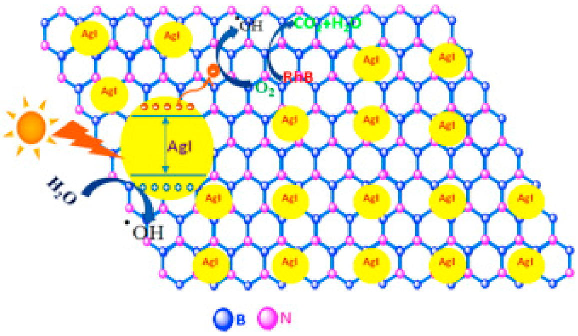

Figure 5.4. Schematic demonstrating the flow of excitons in the AgI/h-BN system. Reproduced from reference 24 with permission from Elsevier.

POMs have also previously been loaded onto h-BN surfaces. Wang *et al.* described the loading of decavanadate ionic liquids onto h-BN *via* solution deposition, utilising the material as a heterogenous catalyst in the oxidative desulfurisation (ODS) reaction.[27] Using optimised ODS reaction conditions (120 °C, air flow of 100 mL/min) 100% of the sulfur contaminants were oxidised in a model fuel within 4 hours, *versus* ~10% for the POM and BN on their own. The authors indicated that the O_2 could not be successfully activated without the presence of both species, suggesting a synergistic effect in which the BN could act as a surface adsorption site for O_2, upon which the vanadate could then activate it. Additionally, the POM/BN catalyst was active towards several different sulfur contaminants and was recyclable. Karimi-Maleh *et al.* loaded POM capped Pt nanoparticles, using an *in situ* formation process, onto a h-BN surface as a material for the electrochemical sensing of N-hydroxysuccinimide.[28] By mixing the material with large amounts of 1-hexyl-3-methlimidazolium (an ionic liquid) and graphite powder, the authors reported that the "tri-component" material could determine the N-hydroxysuccinimide concentration in a variety of water samples, based on the anodic current passed during electrochemical cycling.

Recently, Pomilla *et al.* developed an alcohol dehydration catalyst by depositing $H_3[P_2W_{12}O_{40}]$ onto h-BN and C_3N_4 sheets.[29] The POM/h-BN material showed better catalytic activity than the pristine POM, as well as better activity than the POM loaded onto the carbon nitride support. The catalytic activity of the material was slightly increased with UV irradiation; however, this was observed for all the materials (apart from the POM on its own) suggesting that photoexcitation of the POM on supports increased the reactivity. Whilst the activity appeared the highest when the POMs were loaded onto the h-BN support, the increase with UV irradiation did not particularly stand out for this material, suggesting that electronic transitions between the two was not a key factor in the increase of catalytic activity that was observed.

The previously mentioned rich redox chemistry of POMs can also be accessed photochemically. Normally POMs exhibit intense absorptions in the UV regions due to ligand to metal charge transfer (LMCT) transitions from terminal oxo-ligands to the d^0 metal centres.[30] As a result of this, an electron is promoted from the fully occupied highest occupied molecular orbital (HOMO) to the lowest unoccupied molecular orbital (LUMO). This photo excited state leads to an oxo-centred radical, a triplet state species, which is highly reactive (**Fig. 5.5**). If the POM is in the presence of a solvent that can act as a sacrificial electron donor, this state can lead to the oxidation of the solvent. This leads to a reduction of the POM and gives rise to the intervalence charge transfer (IVCT) band in the absorption spectrum and an intense blue colour (discussed in Chapter 1). As such they have been investigated as photocatalysts.[30, 31] Their rich and reversible redox chemistry and high oxidation state mean that they may act as both an oxidant and reductant in photocatalytic reactions (**Fig. 5.6**).

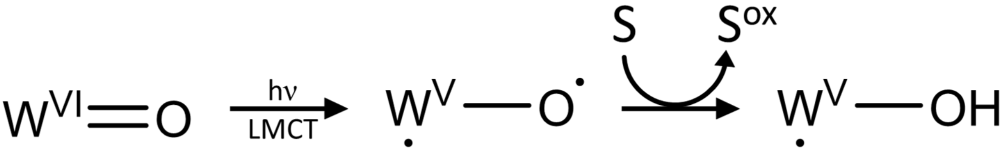

Figure 5.5. Scheme demonstrating W-POM LMCT and subsequent reduction by solvent molecule.

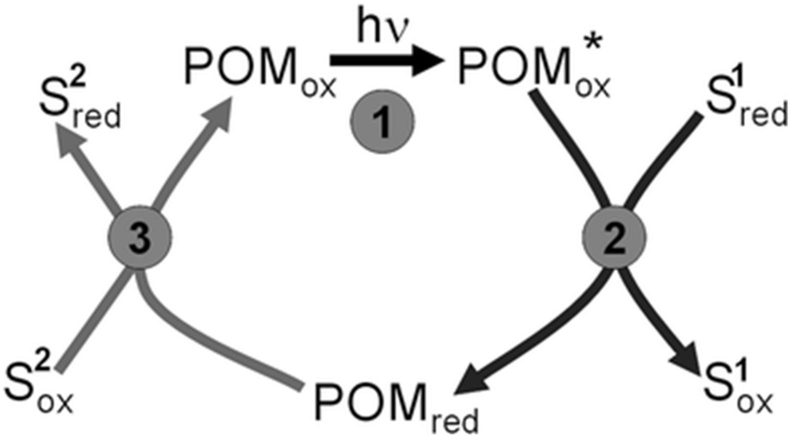

Figure 5.6. Scheme depicting a POM photo-redox cycle. (1) Photoexcitation (2) Reduction via electron donor/catalytic oxidation of the donor (3) Re-oxidation of the POM/catalytic reduction of the substrate. Reproduced from reference 30 with permission from The Royal Society of Chemistry (RSC).

Functionalisation of POMs with optically active antenna groups (as mentioned in chapter 1) leads to a range of materials with absorptions within the visible range. The ability of POMs to accept multiple electrons means these may they readily accept charge from photoexcited antenna groups leading to enhanced charge separation, an important requirement for any photocatalytic reaction.

A series of works published by the Proust group demonstrated the ability of hybrid POMs to effectively trap charged states and apply these to photocatalytic reactions.[32-34] In this series of works, the group developed a chemical method to anchor optically active Ir(III)-chromophores to the lacunary POM structures *via* a highly conjugated and aromatic carbon chain. Photo-measurements of the hybridised POMs showed the presence of a long-lived charge separated states, where the POM was reduced and the Ir chromophore was oxidised, with the rate of charge transfer highly dependent on the nature of the POM.

Matt *et al*. took the Wells-Dawson lacunary structure $[P_2W_{17}O_{61}]^{10-}$ with the anchored Ir chromophore and applied the system to the HER.[33] This particular POM-hybrid offered the best balance between efficient charge separation and lifetime of the charge separated state. The authors demonstrated that the POM could be reduced by two electrons, achieved under irradiation with visible light in the presence of a sacrificial electron donor, trimethylamine (TEA), which was able to irreversibly quench the first charge separated state of the complex (**Fig. 5.7**). This allowed a second photo-

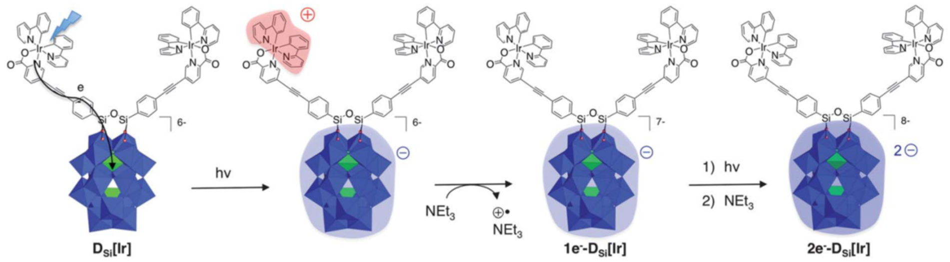

Figure 5.7. Scheme depicting the charge accumulation on the POM from photoexcitation of the Ir(III) chromophore. Reproduced from reference 33 with permission from The Royal Society of Chemistry (RSC).

induced process to take place. This was probed with UV-vis spectroscopy, which showed the growth of two IVCT bands (first at 840 nm, second at 710 nm) upon prolonged visible light irradiation. When applying the cluster to the HER, the cluster showed turnover frequencies (TOF) of 0.25 h^{-1} and catalytic activity was stable over seven days of constant irradiation. This group of studies showed the ability of the POMs to readily accept charge from proximal optically active components and increase the lifetimes of reactive states.

The grafting of a POM-hybrid to the surface of single walled carbon nanotubes (SWNTs) reported by Bosch-Navarro *et al.* similarly demonstrated the ability of POMs to accept electrons during photoexcitation, leading to charge separated states.[35] In this study the authors first functionalised a lacunary Wells-Dawson species with a conjugated carbon chain attached to a pyrene ligand. Similar to works discussed previously[36] (chapter 4), the POM-hybrid was then loaded onto the SWNT surface *via* π-π stacking interactions (**Fig. 5.8**). The hybrid material was then probed with a series of absorption and PL measurements, which demonstrated that charge transfer from the SWNT to the surface bound POM-hybrid took place upon photoexcitation of the system, with lifetimes of approximately 2 ns.

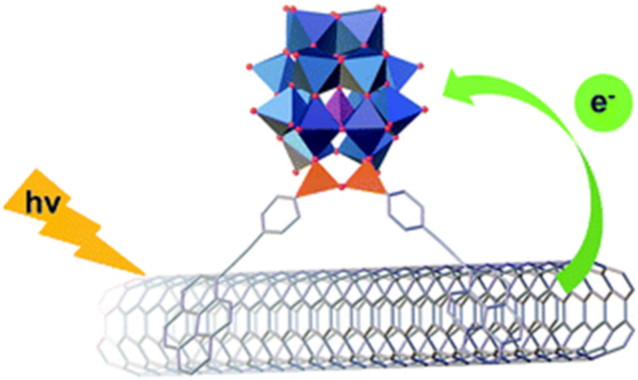

Figure 5.8. Schematic showing the charge transfer from photoexcited SWNTs to the POM-hybrid, bound by π-π stacking interactions between the SWNT surface and pyrene ligands. Reproduced from reference 35 with permission from The Royal Society of Chemistry (RSC).

These works demonstrate that h-BN may act as charge accepters or donors in photoexcited systems, enhancing charge separation and increasing catalytic rates. However, the scarcity of literature on the encapsulation of materials within BNNTs, mostly due to their limited availability, means that photo- and redox active materials have yet to be encapsulated within BNNTs. Similarly, the works described above serve to demonstrate the ability of the molecular metal oxides to act as a photoactive component themselves, or as electron reservoirs in molecular and hybrid material systems, enhancing charge separation and increasing catalytic rates.

The photoactivity of POMs and their ability to enhance charge separation in photoactive systems mean that encapsulation of POMs within BNNTs presents an opportunity to study host-guest interactions in BNNTs and guest species encapsulated within them. Unlike CNTs, the insulating nature of BNNTs likely means that the POMs would not be electrochemically addressable upon encapsulation. However, the optical transparency of the BNNTs mean that UV-vis and vibrational spectroscopies would be well placed to study the interactions between the host and guest.

5.2 Aims and Objectives

The aim of this study is to investigate host-guest interactions between a redox and photoactive guest (POM) and an optically transparent and insulating host (BNNT). This will be achieved *via* the following steps:

1. Encapsulate a POM within BNNTs and probe the structure to confirm encapsulation using local probe techniques.
2. Investigate the nature of the intermolecular interactions using Raman spectroscopy to probe both the POM-guest and BNNT-host.
3. Investigate charge transfer effects in photoexcited states using PL spectroscopy.

5.3 Results and Discussion

5.3.1 Encapsulation of $[P_2W_{18}O_{62}]^{6-}$ within BNNTs

BNNTs received from the manufacturer contained a large amount of impurities, such as residual elemental boron, BN sheets and amorphous nanoparticles. These impurities can hinder the encapsulation of guest species, as well as alter the physical properties of the BNNTs. Additionally, they were closed tipped. Therefore, in order to encapsulate guest species within the interior of the BNNTs, the closed tips and impurities had to be removed. The higher thermal stability of BNNTs (relative to CNTs) and difference in elemental composition (oxidation of the boron at higher temperatures leading to a solid contaminant at the BNNT tips), meant that heating in air was not a possible route to remove the BNNT ends.

Purification and tip removal was achieved by a previously developed wet-chemical method,[15, 37] where the grey and impure BNNTs were dispersed in a concentrated ammonia solution (NH_3(aq)). The Lewis base attacks the empty p_z orbitals of the electron poor boron centres in the BN lattice making up the BNNT sidewall, (**Fig. 5.9**) activating the B–N bonds to further hydrolysis in solution. This method is well suited

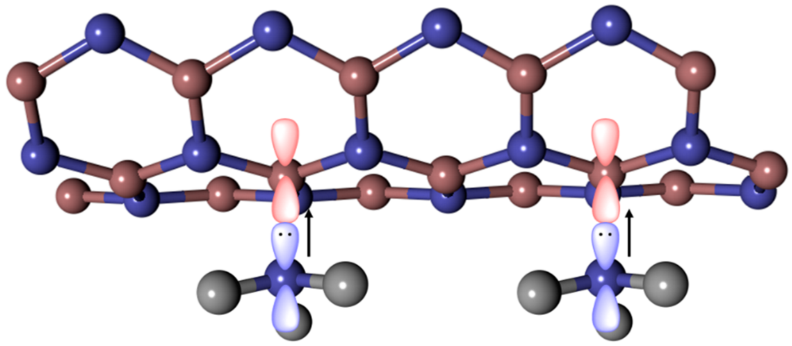

Figure 5.9. Model showing ammonia molecules attacking boron atoms of the BN lattice. Electrons from the lone pair (sp^3 orbital) of the ammonia are donated to the empty p_z orbital of the boron. Nitrogen shown in blue, boron shown in pink and hydrogen shown in grey.

to the removal of BNNT tips, as well as shortening and reducing the overall number of BN layers making up the BNNTs.

Again, this reaction occurs preferentially at the BNNT tips, although this reaction will also occur along the entirety of the BNNT sidewalls, due to the strain on the bonds and presence of 4 and 8 membered rings at these sites. Following the NH_3(aq) treatment of the as-received BNNTs, the sample was heated to 800 ^{o}C in order to oxidise remaining elemental boron. The elemental boron was oxidised to boron oxide[38] (B_2O_3) which was then washed away with boiling water, leaving purified BNNT as a solid white powder.

Encapsulation of the Wells-Dawson anion was achieved *via* a similar method used for POM encapsulation within SWNTs. $K_6[P_2W_{18}O_{62}]$ was dissolved in water, and BNNTs (heated to 200 ^{o}C to remove any residual water) were added to the solution. Following stirring at room temperature for 48 hours (under ambient light conditions), the solid was filtered from the dispersion. After stirring for 48 hours, the solution appeared blue, and when the dispersion was filtered, the solid of the material also appeared to be a faint blue colour, indicating the presence of reduced POM anions. This suggested that the aqueous solution of POM was readily reduced in the presence of the BNNTs. However, after 48 hours the material had become colourless again, indicative of POM re-oxidation.

Unlike the SWNT materials discussed in previous chapters, the BNNT sample contained a large range of BNNT diameters, both internal and external, meaning that the overall sample was more heterogenous than the SWNT materials (**Fig. 5.10**). Transmission electron microscopy (TEM) analysis of the material showed the presence of POMs within the BNNT walls, clearly visible as higher contrasting species (**Fig. 5.11**). The material encapsulated within the BNNTs appeared more continuous (with a lack of discrete molecules) than what was observed within SWNTs, however this was likely due to the wider diameters of the BNNTs and the known reactivity of the POMs under the electron beam (chapter 2).

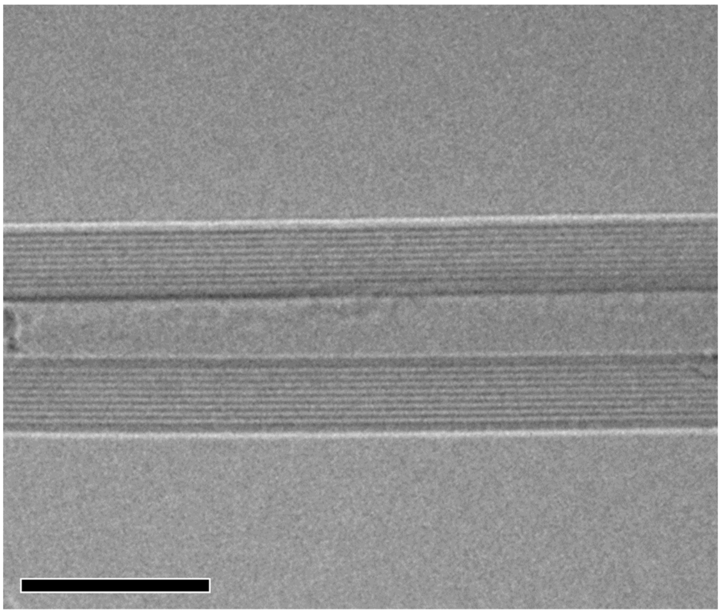

Figure 5.10. An unfunctionalised multiwalled BNNT. Image acquired with an accelerating voltage of 200 kV. Scale bar 10 nm.

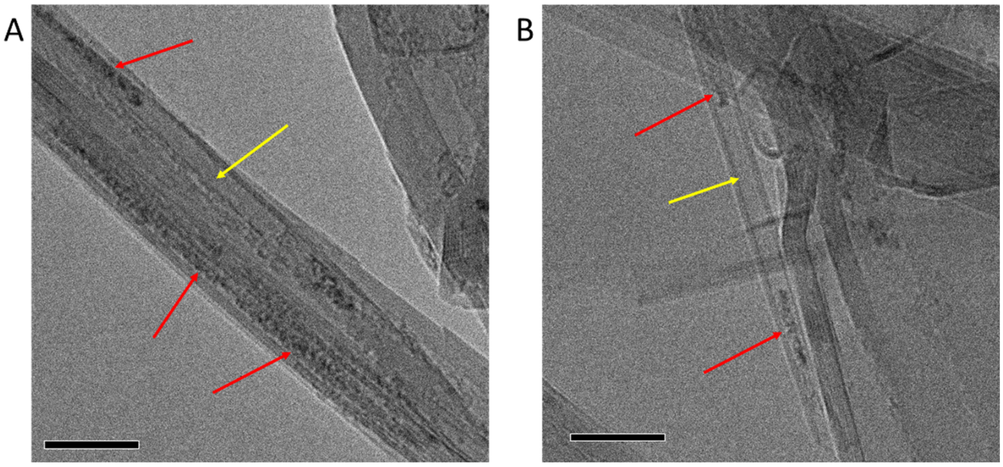

Figure 5.11. TEM images of {$P_2W_{18}O_{62}$}@BNNT. (A) shows a bundle of BNNTs with encapsulated POM and (B) shows a single BNNT with encapsulated POM. Red arrows show POM and yellow arrows show unfunctionalised BNNT. Images acquired with an accelerating voltage of 80 kV. Scale bars 10 nm.

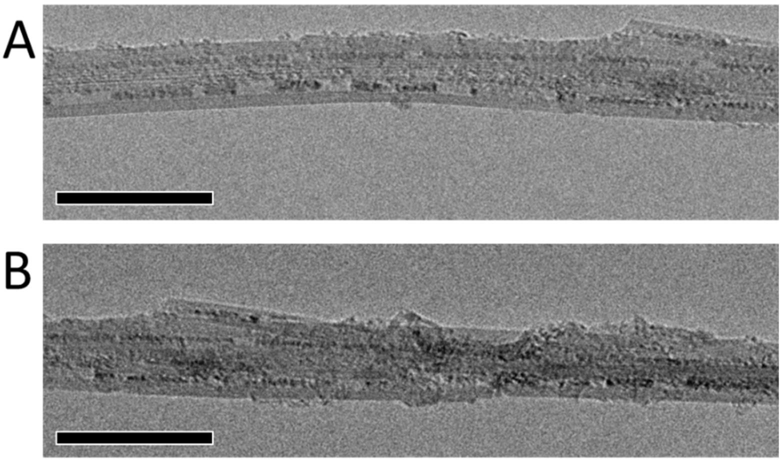

Figure 5.12. TEM images of {$P_2W_{18}O_{62}$}@BNNT showing (A) after brief electron beam irradiation and (B) after 30s of electron beam irradiation. Images acquired at 80 kV. Scale bars 20 nm.

When narrower BNNTs were observed however, molecular species could be observed which ranged in size between 0.8 – 1 nm, suggesting that these were still close to pristine POM molecules. These molecular species appeared to condense under the electron beam similar to the {POM}@SWNT materials discussed in chapter 3 (**Fig. 5.12**).

Energy dispersive X-ray spectroscopy (EDX) analysis of the materials, (**Fig. 5.13**) acquired over a small area of the material, showed the presence of the POM constituent elements potassium, tungsten and oxygen in the ratio (K : W : O) of 0.028 : 0.67 : 0.30. The lack of phosphorous is not surprising given the low atomic % of the atom in the parent anion and the low number of POMs captured in the dataset. Expected ratios would be (K : P : W : O) 0.07 : 0.02 : 0.20 : 0.70. The increase in the atomic percentage of tungsten suggests that oxygen was readily emitted during imaging as discussed in chapter 3. Whilst the loss of oxygen was not observable *via* EDX during the TEM induced reactions within the SWNTs (chapter 3), the larger diameter BNNTs likely allowed oxygen to leave more easily due to less hindered mass transport. The presence of potassium within the EDX suggests that despite the POM solution becoming blue during encapsulation and the {POM}@BNNT material initially being blue upon filtration, the BNNTs were not fulfilling the role of cation as was the

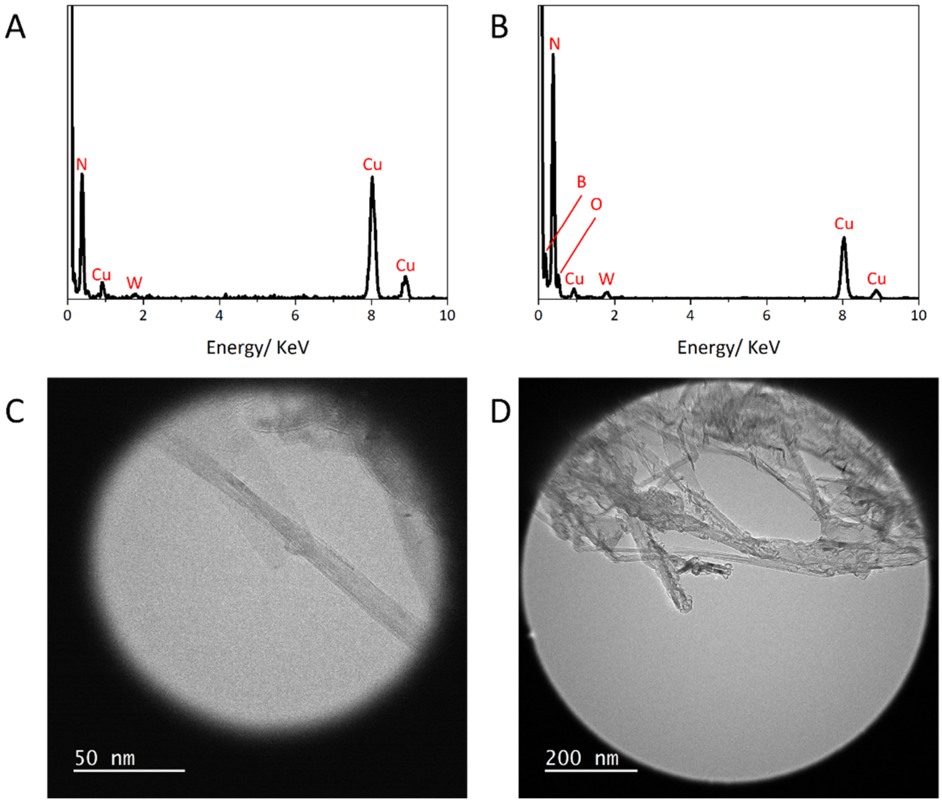

Figure 5.13. EDX spectra of the {$P_2W_{18}O_{62}$}@BNNT material acquired with a narrow field of view (A) and wide field of view (B). (C) shows field of view for spectrum (A). (D) shows field of view for spectrum (B). Images acquired with an accelerating voltage of 80 kV. Scale bars shown.

case with the SWNTs (chapter 2). Due to the larger sizes of the BNNTs, both solvated potassium and $[P_2W_{18}O_{62}]^{6-}$ ions could likely encapsulate within the nanotube interior. Additionally, BNNTs consist of wide band gap, as discussed above, meaning that electronic modification of the species would be less likely. When acquiring EDX data from a larger field of view, (**Fig. 5.13, B & D**) when the flux of electron beam was significantly reduced, all of the POM constituent elements were observed in a ratio of (K : P : W : O) 0.005 : 0.005 : 0.26 : 0.73 in better agreement with the expected ratios, suggesting that anion remained intact upon encapsulation. The lower counts from the EDX spectra of the {$P_2W_{18}O_{62}$}@BNNT material suggested that the overall loading of the anion was lower relative to that of the SWNTs discussed in chapter 2.

The initial coloration of the {POM}@BNNT material, TEM of individual molecular species and the elemental composition from EDX suggested that the $[P_2W_{18}O_{62}]^{6-}$

remained intact upon encapsulation within the BNNTs. Although the sample was significantly more heterogenous than the {POM}@SWNT materials, the $[P_2W_{18}O_{62}]^{6-}$ appeared to readily encapsulate within the range of BNNTs in the material. Rather than driven by electrostatic interactions upon charge transfer, as was the case with the {POM}@SWNT materials, the encapsulation of the $[P_2W_{18}O_{62}]^{6-}$ was likely driven by van der Waals interactions between the guest and host.

5.3.2 Vibrational Analysis

The Raman spectra of the BNNTs showed the presence of a single mode, an in-plane B–N stretching mode, located at approximately 1370 cm^{-1} (**Fig. 5.14, B**). The baseline of the Raman spectrum was inherently raised, due to the intrinsic photoluminescence (PL) of the BNNTs, leading to wide emissions across the entire spectrum. Raman analysis of the native $K_6[P_2W_{18}O_{62}]$ species showed the presence of many bands associated with the many types W–O vibrational modes[39] (**Fig. 5.14, A**).

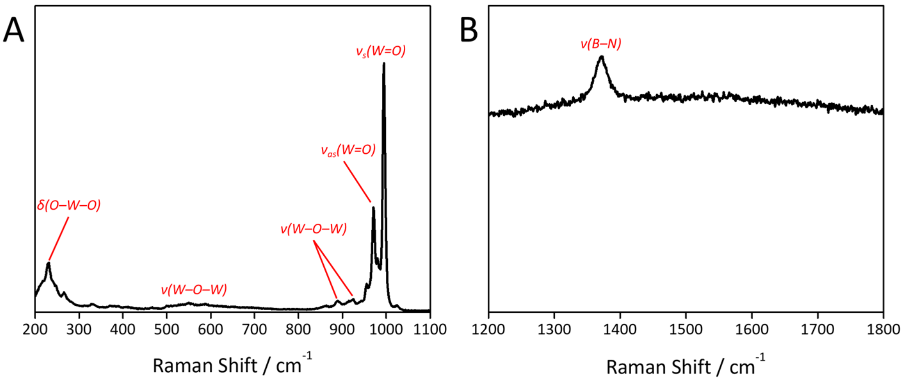

Figure 5.14. Raman spectra of $K_6[P_2W_{18}O_{62}]$ (A) and BNNTs (B). Note the raised baseline in the spectrum of BNNT due to PL. Spectra acquired with an excitation wavelength of 633 nm. ν denotes stretch (s - symmetric, as - asymmetric) and δ denotes a bend.

The optical properties of the BNNTs and the lack of resonance vibrational modes, as seen in SWNTs, meant that the vibrational bands of the confined POM species within BNNTs could be observed, providing insight into the nature of the host-guest interactions by directly probing the vibrational energies of the guest. Raman analysis of the $\{P_2W_{18}O_{62}\}$@BNNT material showed the presence of multiple bands from the

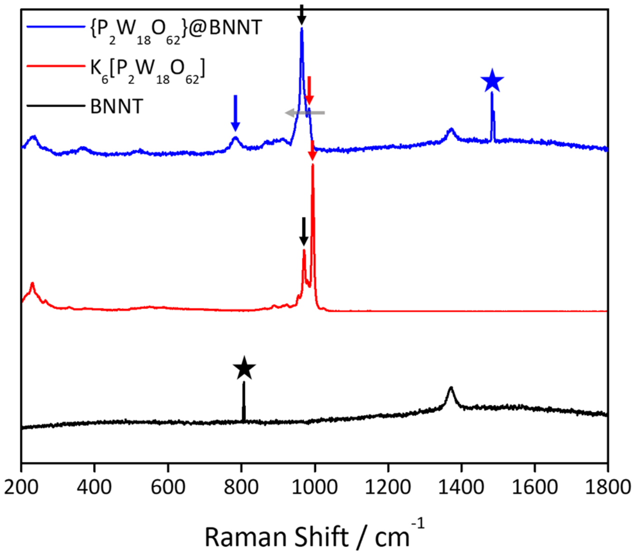

Figure 5.15. Raman spectra of BNNTs, $K_6[P_2W_{18}O_{62}]$ and $\{P_2W_{18}O_{62}\}$@BNNT. Stars denote cosmic ray interference. Black and red arrows show the switching in the W=O stretches upon POM encapsulation, blue arrows show the appearance of a new band at 777 cm^{-1}upon POM encapsulation and the grey arrow shows the redshift in the bands at 980 cm^{-1}. Data acquired with an excitation wavelength of 633 nm.

$[P_2W_{18}O_{62}]^{6-}$ anion, (**Fig. 5.15**) as well as the single mode associated with BNNT. When comparing the Raman spectrum of the native POM to that of POM@BNNT, shifts in some of the POM modes were observed, as well as the appearance of new bands.

Bands at ~980 cm^{-1}, associated with the terminal W=O bond stretch, were redshifted in the encapsulated POM relative to that of the native species, indicating a weakening of the bond. This was likely due to interactions between the $[P_2W_{18}O_{62}]^{6-}$ anion and the BN lattice upon encapsulation through the terminal oxygen atoms of the $[P_2W_{18}O_{62}]^{6-}$ interacting with the electron poor boron centres in the BN lattice. Additionally, the intensity of these W=O stretches, both asymmetric and symmetric, were switched upon encapsulation, such that the asymmetric stretch was more intense upon encapsulation. The selection rules of vibrational Raman spectroscopy require a change in the polarisability of the molecule during vibration, whereas IR requires an overall change in the dipole moment, making Raman spectroscopy sensitive to changes in molecular symmetry.[40] This indicated a change in the polarisation of the of the molecule upon encapsulation, changing the conditions that satisfied Raman selection rules. This was further evidenced by the appearance of a new band at 777 cm^{-1} in the Raman spectrum of {$P_2W_{18}O_{62}$}@BNNT, indicating that a Raman silent vibration had been activated. The infra-red (IR) spectrum of the POM showed a broad band at ~732 cm^{-1} from a W–O–W asymmetric stretch[41, 42] (**Fig. 5.16**). This stretch was IR active yet Raman silent in the native POM,[39] indicating that the activation of the vibrational mode upon encapsulation was due to the changes in the polarisability of the molecule, similar to the terminal W=O bond mentioned above. This band was shifted 45 cm^{-1} relative to the band in the IR spectrum, however due to the differences in data acquisition methods (attenuated total reflectance for IR) direct comparison between these bands is problematic. Additionally, the mode appeared to be much sharper in the Raman spectrum of the {$P_2W_{18}O_{62}$}@BNNT material, rather than broad in the IR spectrum of pristine $K_6[P_2W_{18}O_{62}]$.

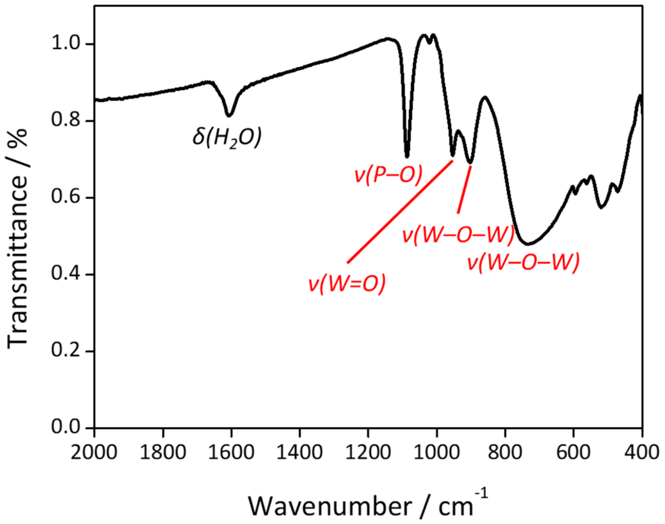

Figure 5.16. FT-IR spectrum of $K_6[P_2W_{18}O_{62}]$, acquired in ATR mode. ν denotes a stretch and δ denotes a bend.

When considering the geometry of the $[P_2W_{18}O_{62}]^{6-}$ molecule (**Fig. 5.17**), the W=O and W–O–W bonds are located at the POM "surface" and not the core of the molecule, and thus could be influenced by an external surface (such as the BN lattice) in close proximity. This is similar to work on Keggin ions deposited onto noble-metal electrodes, which also exhibited changes in the vibrational spectrum upon surface deposition and charging with a potential bias.[39] The switching in the intensities of the terminal W=O stretches and the activation of the Raman silent W–O–W asymmetric stretch were indicative of overall changes in the polarizability of the POM molecule, likely due to intermolecular interactions between the POM molecules and the external BN surface. When considering the red shift of the W=O stretches, it can be considered that there is a slight charge transfer from the oxo-ligands of the POM molecules to the BN surface, likely to electron poor boron centres (**Fig. 5.17**).

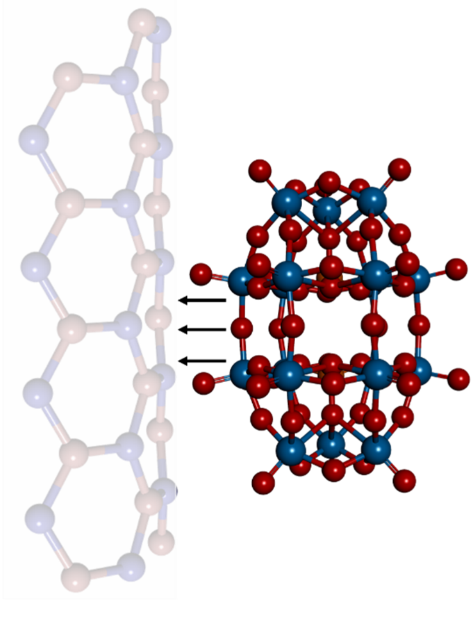

Figure 5.17. Schematic demonstrating the interaction of a $[P_2W_{18}O_{62}]^{6-}$ molecule with the BN surface.

When using an excitation wavelength of 633 nm (1.96 eV), low-temperature Raman spectra (4 Kelvin) of the POM@BNNT materials led to increased intensities of the peaks associated with the POM, due to a greater population of ground state energy levels at these low temperatures. (**Fig. 5.18, A & C**) Additionally, new bands appeared

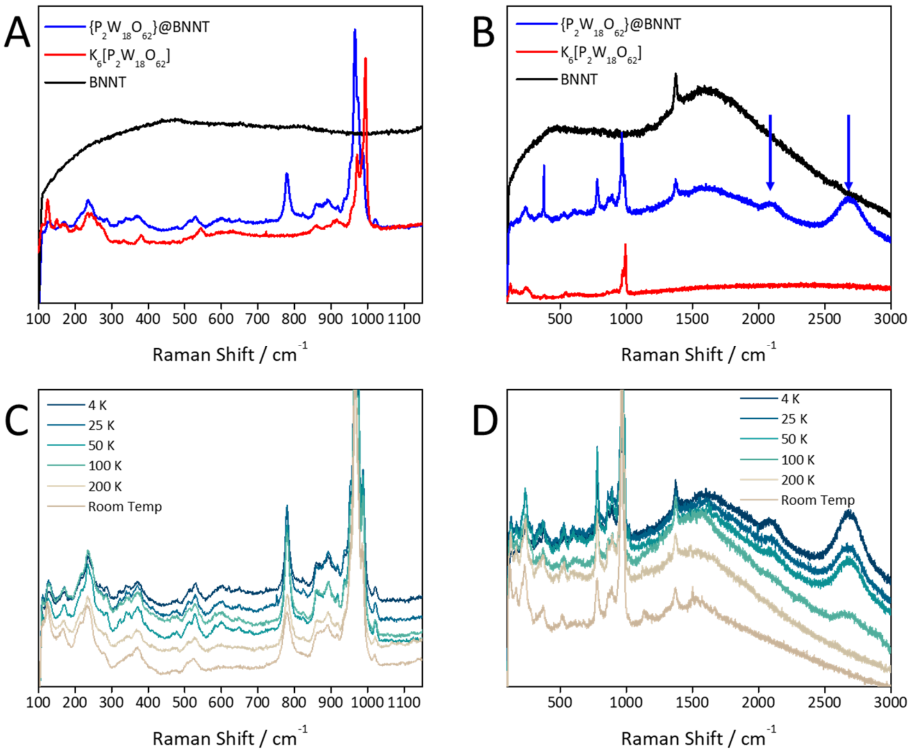

Figure 5.18. Raman spectra of BNNTs, $K_6[P_2W_{18}O_{62}]$ and $\{P_2W_{18}O_{62}\}$@BNNT at 4 K (A & B). Variable temperature Raman spectra of $\{P_2W_{18}O_{62}\}$@BNNT (C & D). Acquired with an excitation wavelength of 633 nm. Intensities across the spectra are not comparable.

at 2090 cm^{-1} and 2680 cm^{-1} which were intense and very broad (**Fig. 5.18, B, blue arrows**). The feature at 2090 cm^{-1} appeared lower in intensity compared to the feature at 2680 cm^{-1}. These features were not observed at room temperature or in the native BNNT or POM materials, suggesting that they were due to an interplay between the two constituent parts of the hybrid material that became apparent at cryogenic temperature. The broadness of these peaks indicated that these were not vibrational modes, which are generally much sharper. Raman spectra of the material at varying temperatures (**Fig. 5.18, D**) showed the growth of the PL emissions with decreasing temperatures. The band at 2680 cm^{-1} emerged at 100 K and subsequently increased in intensity with decreasing temperature. The lower intensity emission at 2090 cm^{-1} became measurable below 50 K and increased in intensity with decreasing temperature after that.

Whilst PL processes are generally very broad with emissions that span over hundreds of wavelengths (see below), low temperatures lead to narrow emission features.[43] This is due to the lower number of non-radiative decay pathways at these temperatures, leading to more narrow emissions. The appearance of these features at extremely low temperatures suggests that non-radiative decay of the excited states was greatly inhibited at low temperature, leading to the observed PL emission.[43] Raman shift can be described by:

$$\Delta\nu = \left(\frac{1}{\lambda_0} - \frac{1}{\lambda_1}\right)$$

Where $\Delta\nu$ = Raman shift, λ_0 = excitation wavelength and λ_1 = emitted wavelength of light. Converting the Raman shifts observed at 4 K with a 633 nm laser gave wavelengths of approximately 730 and 762 nm for the 2090 and 2680 cm^{-1} emissions respectively, corresponding to 1.70 and 1.63 eV respectively.

When utilising an excitation wavelength of 532 nm (2.33 eV) the POM@BNNT material generally showed more broad PL emissions, similar to that observed in pristine BNNT (**Fig. 5.19**). The activated Raman mode at 777 cm^{-1} appeared less intense and slightly broader. Decreasing the temperature again led to an increase in the intensity of the 777 cm^{-1} peak. However, cooling the material to 4 K did not lead to the appearance PL emissions. This suggested that the excitation energy of 2.33 eV was not in resonance with the required energy levels to induce the PL transitions observed with an excitation of 633 nm. The emergence of new PL bands unique to the POM@BNNT material at low temperatures suggested that there was electronic communication between the host and the guest.

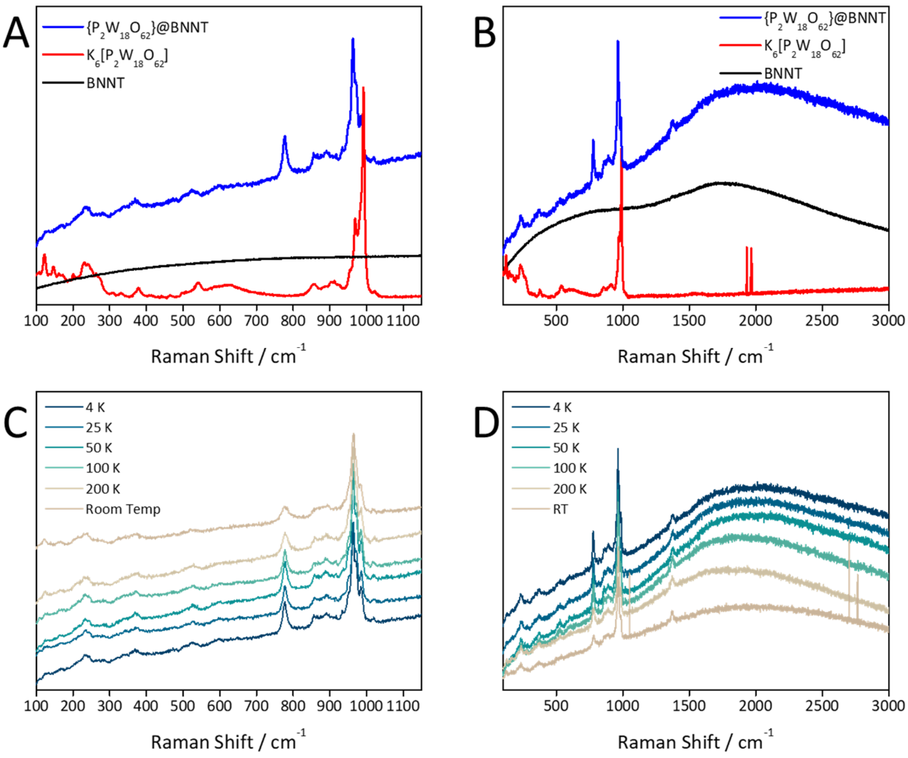

Figure 5.19. Raman spectra of BNNTs, K$_6$[P$_2$W$_{18}$O$_{62}$] and {P$_2$W$_{18}$O$_{62}$}@BNNT at 4 K (A & B). Variable temperature Raman spectra of {P$_2$W$_{18}$O$_{62}$}@BNNT (C & D). Acquired with an excitation wavelength of 532 nm. Spikes in the spectra are cosmic rays. Intensities across the spectra are not comparable.

5.3.3 Photoluminescence Measurements

The UV-vis absorption profile of the {$P_2W_{18}O_{62}$}@BNNT material appeared to show a broader range of absorptions than the native BNNTs (**Fig. 5.20**) which appeared to correspond to the broader absorption profile of POMs dissolved in water. This suggested that the both the BNNT and POM could both absorb incident photons.

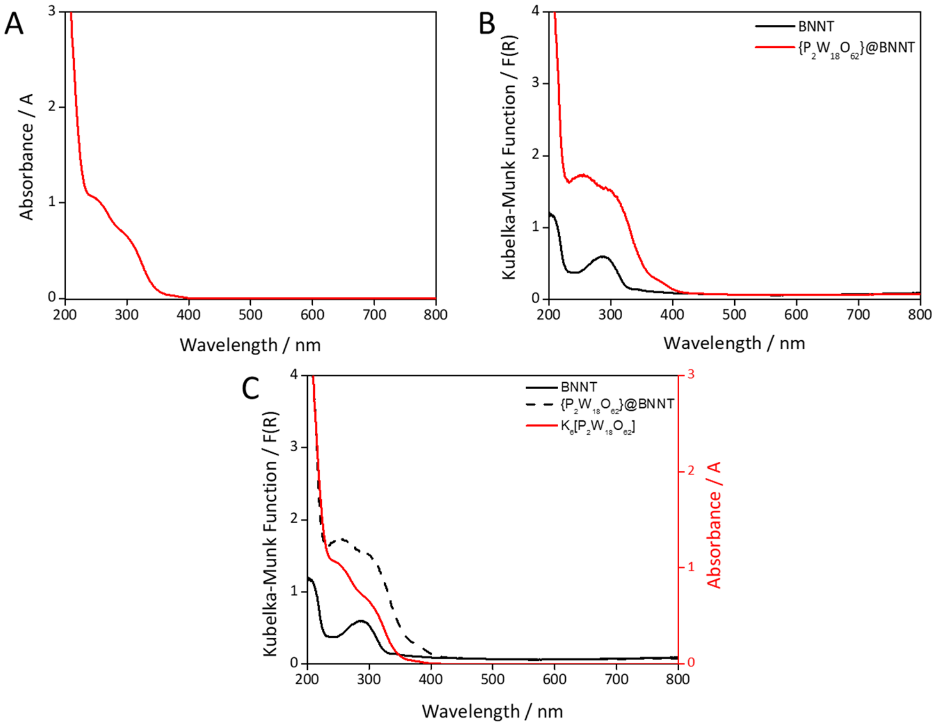

Figure 5.20. UV-vis absorption spectra of $K_6[P_2W_{18}O_{62}]$ dissolved in water (A) BNNT and {$P_2W_{18}O_{62}$}@BNNT in the solid-state (B) and each spectrum overlaid (C).

Based on the emergence of PL emissions at low temperature during Raman measurements, indicating that the electronic communication between species occurred, room temperature PL measurements of the POM, BNNT and POM@BNNT materials were acquired. In general, POMs do not exhibit PL, due to the large number of discrete energy levels that they possess. Additionally, POMs are known to quench PL emission,[44] due to the large number of available energy levels that can readily accept excited electrons, leading to charge separation. BNNTs show broad emissions when excited with UV wavelengths, with high energy emissions (~5.4 eV) due to band gap transitions and broad lower energy emissions (2.5–4.5 eV) due to vacancies, defects and adatoms within the BN lattice.[10, 23] The BNNT material showed an emission centred around 380 nm (3.26 eV), which was likely due to atomic defects, which has previously been reported to centre around 340 nm.[10]

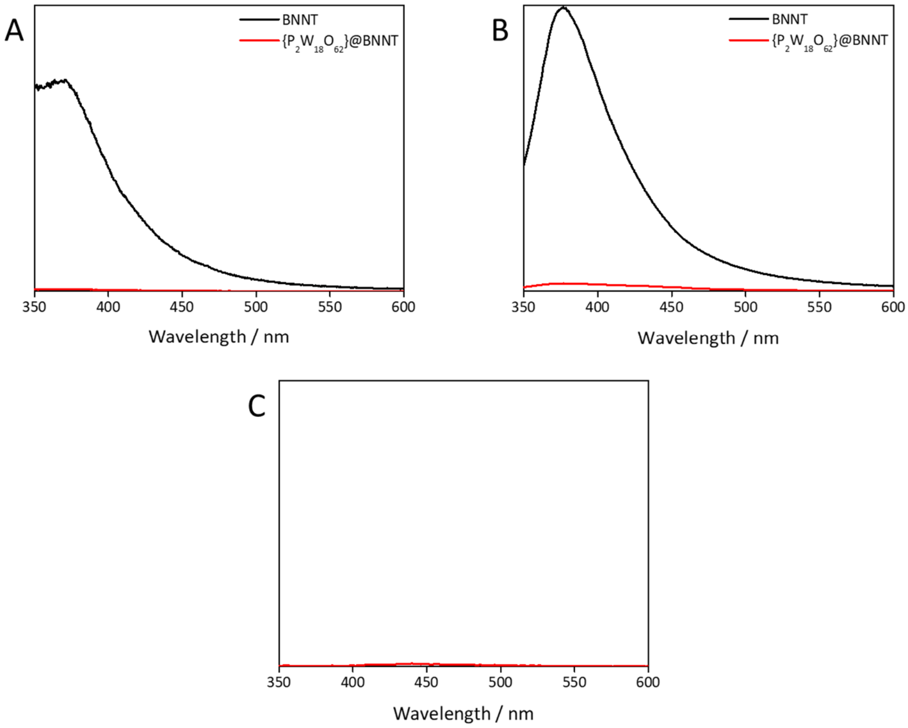

Figure 5.21. PL spectra of BNNTs and {$P_2W_{18}O_{62}$}@BNNT using excitation wavelengths of 250 nm (A) and 275 nm (B). (C) shows POM PL spectra using an excitation wavelength of 275 nm.

The PL spectra of the POM@BNNT showed a large reduction in the intensity of the PL from the BNNT (**Fig. 5.21**), suggesting that the encapsulation of the POM within the BNNTs was sufficient to quench the BNNT emission and that the electronic communication between the host and guest was efficient, in good agreement with low temperature Raman spectroscopy. The PL quench was likely due to charge transfer from the photoexcited BNNT to the encapsulated POM, which would either lead to reduced POM species or exciton recombination through non-radiative pathways. This was observed across a range of excitation wavelengths (250 – 300 nm). Interestingly, after the sample was removed from the fluorometer, the now white powder had become blue, indicative of the reduced POM under UV irradiation (**Fig. 5.22, A**).

Exposing the native POM to similar conditions did not result in a colour change of the material (**Fig. 5.22**). This indicated that the POMs had become reduced upon irradiation, however the native POM in its crystal could not undergo the same photoreduction without BNNT.

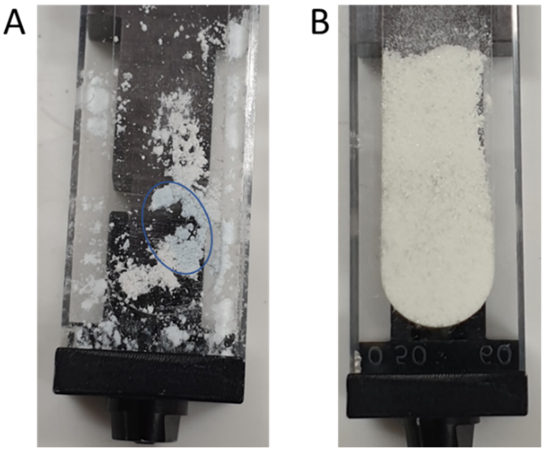

Figure 5.22. $\{P_2W_{18}O_{62}\}$@BNNT (A) and $K_6[P_2W_{18}O_{62}]$ (B) materials after PL spectroscopy measurements. Blue colouration (corresponding to the illumination spot) is visible in the $\{P_2W_{18}O_{62}\}$@BNNT material (blue circle).

One possible explanation for the emergence of this blue colour in the $\{P_2W_{18}O_{62}\}$@BNNT material is promoted electrons from the BNNT valence band to interstitial energy levels and the conduction band (promoted from UV light irradiation) reduced the POM *via* intermolecular charge transfer from the excited BNNTs and encapsulated POMs. This could explain both the quenching of the BNNT photoemission in the $\{P_2W_{18}O_{62}\}$@BNNT material and the emergence of the blue colour during irradiation. This additionally supports the observation of the formation of the blue solution and blue solid upon initial isolation during the encapsulation experiment, discussed above, suggesting that the POMs readily reduced in the presence of BNNTs and light. Whilst POMs may also undergo photoreduction in solution, when an aqueous solution of $K_6[P_2W_{18}O_{62}]$ was left for 48 hours under the same conditions (stirring in ambient light) no reduction took place.

This leaves three possibilities for the role of BNNT. Firstly, if electrons were transferred to the POM from the photoexcited BNNT, positive charge carriers could have remained localised to the BNNT, which could have slowly recombined with the photo-excited electrons residing on the encapsulated POMs, leading to the eventual loss of the blue colour (**Fig. 5.23**). This is unlikely, due to length of time that the reduced POMs persisted for following irradiation.

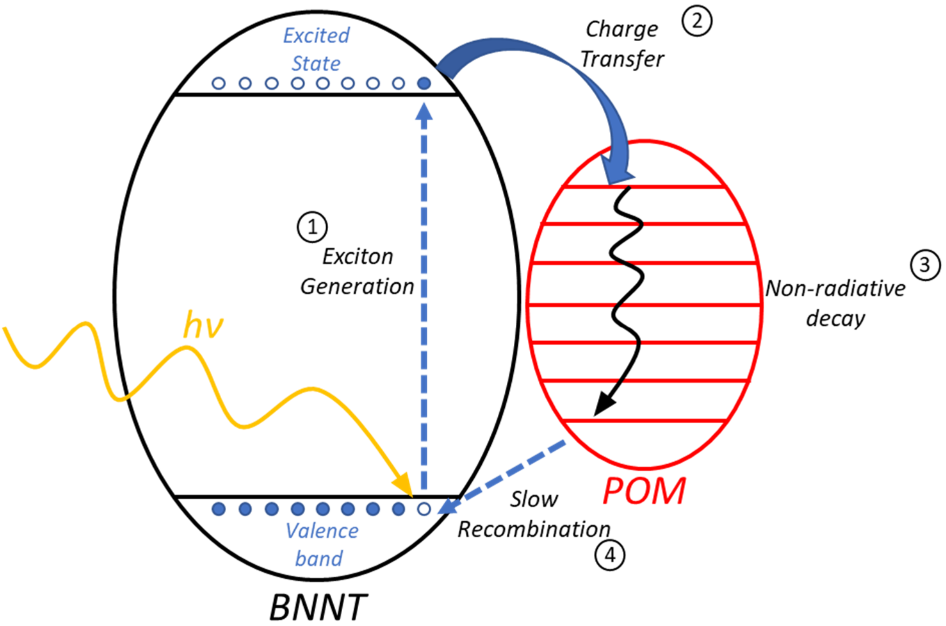

Figure 5.23. Possible mechanism of charge transfer between the photoexcited BNNT-host and encapsulated POM-guest, leading to slow charge recombination from the encapsulated reduced POM and BNNT.

Secondly, water from the solution during the encapsulation experiment could have been sacrificially oxidised by the BNNT positive charge carriers following POM reduction, leaving the BNNT in its native state (**Fig. 5.24**). The much larger internal diameters of the BNNTs and the varied distribution of the BNNT sample mean that water molecules could have been concomitantly encapsulated with the POM molecules too, meaning that this could have also occurred from irradiation during PL measurements.

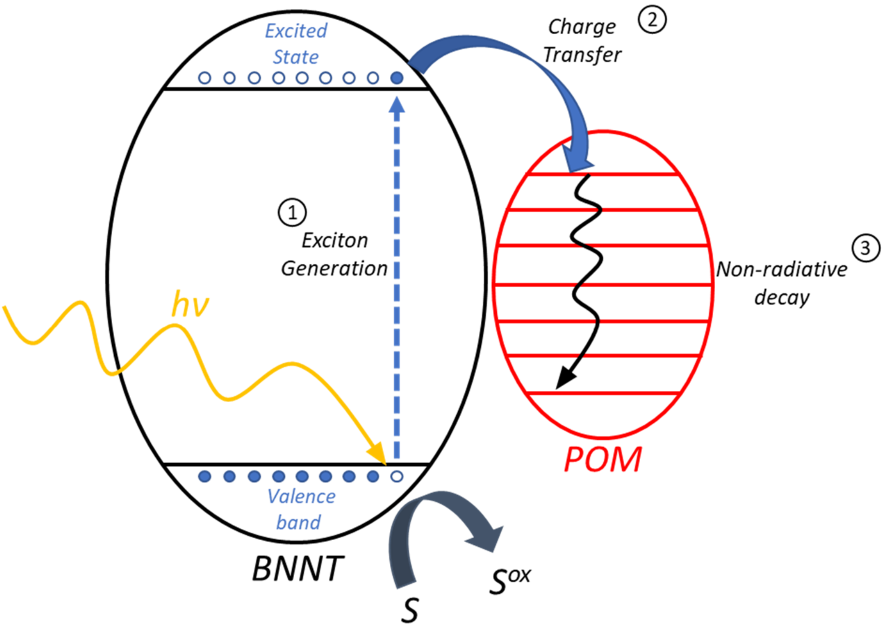

Figure 5.24. Second possible mechanism of charge transfer from the photoexcited BNNT-host to POM-guest, leading to the oxidation of water (shown as S for solvent) by the hole in the BNNT valence band.

Finally, the photo-reduction of the POMs could have been due to the presence of solvent molecules encapsulated within the BNNTs, with no interaction from the BNNT at all. (Akin to the mechanism shown in **Fig. 5.5**) This final option fails to explain the large quenching of the BNNT PL emissions, however. BNNTs are known to readily charge under electron beam irradiation,[45] as well as being difficult to handle during laboratory manipulations due to static build up, suggesting that charging of the BNNTs is a likely option. Alternatively, all of the processes described above could have been occurring simultaneously in a material with such heterogeneity.

When exciting the sample with a wavelength of 405 nm (3.06 eV), the BNNT material showed two emissions centred around ~500 (2.48 eV) and ~620 nm (2 eV) (**Fig. 5.25**). These emissions were not quenched to the same degree as the higher energy emission discussed above, however there was still a considerable quenching of the emissions. The emissions are both close to the excitation wavelengths used for the low temperature Raman spectroscopy described above, suggesting that these were energy levels of defect or vacancy sites within the BNNT structure that could be accessed *via*

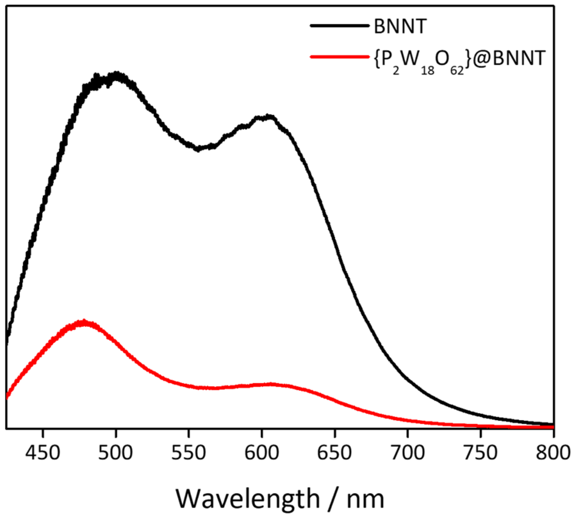

Figure 5.25. PL spectra of BNNT and {$P_2W_{18}O_{62}$}@BNNT acquired with an excitation wavelength of 405 nm.

photoexcitation with the corresponding wavelengths used in the low temperature Raman experiments.

Based on the various PL measurements of the BNNTs, it could be concluded that there were three energy levels of the BNNT between the valance and conduction band of the BNNTs, at ~2, 2.48 and 3.36 eV. The quenching of the 3.36 eV emission at room temperature suggests that energy levels of the POM could readily accept photoexcited electrons *via* intermolecular charge transfer, quenching the emission through further non-radiative decay and a potential reduction of the encapsulated POMs as evidenced by the emergence of the blue coloration following irradiation. The partial quenching of the 2 and 2.48 eV emissions suggests that similarly there were energy levels of the POMs that could readily accept photoexcited electrons, albeit to a lesser degree.

Raman measurements of the {$P_2W_{18}O_{62}$}@BNNT material at 4 K however showed the presence of narrow PL bands at lower energies than emissions observed for the BNNTs or POM@BNNT materials at room temperature. This suggests that at lower temperatures, where non-radiative decay would have been inhibited, there was an intermolecular charge transfer from the BNNT excited state to molecular orbitals of the encapsulated POMs, followed by a radiative decay to the BNNT valence band. There was no visible POM reduction after the low temperature Raman measurements (however this is hard to tell, due to the confocal laser utilised for the Raman experiments), indicating that the final state of the POM was fully oxidised. This suggests that the 1.63 and 1.7 eV (762 and 730 nm) emissions observed in the low temperature Raman were from POM*→BNNT (**Fig. 5.26**). This hypothesis is in good agreement with the quenching of the BNNT PL emissions which also suggested that charge separation was occurring in the system during photoexcitation of the $\{P_2W_{18}O_{62}\}$@BNNT material.

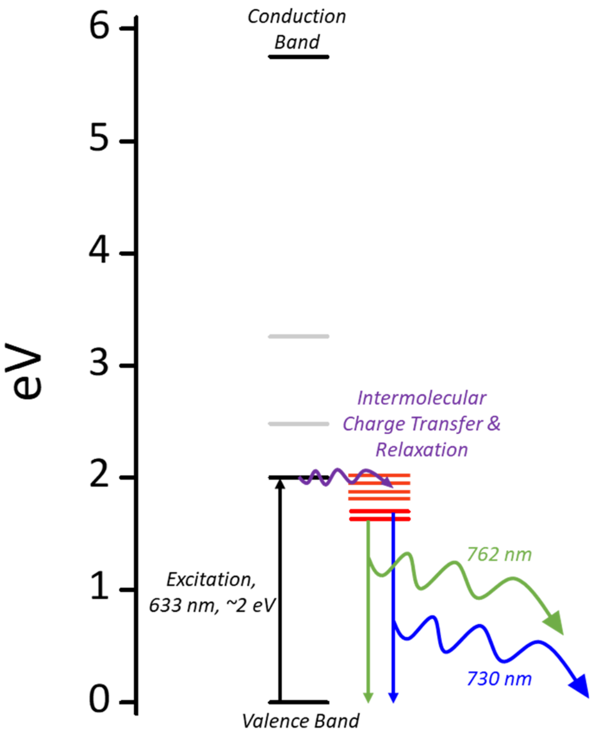

Figure 5.26. Possible photoexcitation and emission mechanism of the $\{P_2W_{18}O_{62}\}$@BNNT material excited at 633 nm at 4 K. Black energy levels are the BNNT, with greyed depicting the energy levels observed from PL emission. Red energy levels are empty MO levels of the encapsulated POM. Energy is not referenced, with the BNNT valence band set as zero eV.

5.4 Conclusion

Tungsten Wells-Dawson POMs appeared to readily encapsulate within BNNTs at room temperature in water under ambient light. This was likely driven by van der Waals forces rather than coulombic attraction. POMs appeared to readily encapsulate within a range of BNNTs with varied diameters. EDX analysis confirmed the presence of the potassium counter ion, suggesting that the BNNTs were not readily oxidised, as was observed in the {POM}@SWNT materials, and under ambient conditions remained a redox inactive host.

Raman spectroscopy of the {POM}@BNNT material was utilised to probe the vibrational bands of the encapsulated POM and in turn the nature of the interactions between the encapsulated POMs and the BNNTs. Changes in the intensity and shifting of POM Raman bands suggested that the polarisability of the encapsulated POM molecules had been altered. This was also evidenced by the appearance of a new vibrational mode, which was likely a POM IR mode that had become Raman active upon encapsulation.

Low temperature Raman measurements showed the emergence of narrow PL emissions at low energies, which was only observed in the {POM}@BNNT hybrid material, which suggested that electronic communication between the host and guest was effective. Correlation of the Raman results with PL measurements with variable excitation energies at room temperature showed the quenching of BNNT PL emissions, also suggesting the effective transfer of photo-excited electrons from the BNNT to encapsulated POMs. The quenching of the BNNT emissions was also accompanied with the colour change of the {POM}@BNNT material, consistent with reduced states of the encapsulated POM, further supporting the hypothesis of photoexcited molecular charge transfer.

Overall, characterisation of the properties of POM@BNNT by a correlative approach involving Raman, IR, PL and UV-vis spectroscopies, revealed interactions between the POM guest and boron nitride host, as well as electronic coupling after photoexcitation. This is the first study that comprehensively addresses the nature of metal oxide and boron nitride interactions, opening a door for applications of this new type of hybrid material in applications such as photocatalysis and solar energy harnessing.

5.5 Experimental

5.5.1 General

All common reagents and solvents were used as received from Sigma-Aldrich, Acros Organics or Thermo Fisher. Boron Nitride Nanotubes (BNNT P1-Beta) were purchased from BNNT LLC.

HRTEM images were acquired on a JEOL 2100+ LaB_6 emission microscope with an accelerating voltage of 80 kV. Samples were prepared by first dispersing them in isopropyl alcohol which were then dropped onto a copper grid mounted with a “lacey” carbon film.

All TEM images were processed using Gatan Digital Micrograph, and quoted distances were measured by drawing a line profile and measuring the electron density histogram.

EDX spectra were acquired during TEM imaging, using an Oxford Instruments INCA X-Ray microanalysis system.

Micro-Raman spectroscopy was performed using a Horiba-Jobin-Yvon LabRAM HR spectrometer. Single-point spectra were recorded using a 100× objective, a 300-µm confocal pinhole, and a 660 nm (1.88 eV) laser at < 0.3 mW. The spectral resolution was better than 1.2 cm^{-1}. Instrument calibration was performed using the zero-order line and a standard Si(100) reference band at 520.7 cm^{-1}. Samples were prepared by depositing a small quantity of sample from a methanolic suspension onto Si(100) wafers. A typical spectrum was recorded by averaging 4-8 acquisitions, each of 5-30 s duration.

FTIR spectroscopy was performed on a Bruker IFS66v spectrometer using an attenuated total reflectance (ATR).

Low temperature Raman measurements were performed with a cryostat Microstat liquid helium system mounted on a 3-axis coordinate stage, aligned with a InVia Renishaw Raman spectrometer. A 50x objective and a focal distance of 20.5 mm was used at a power of 1 mW. Instrument calibration was performed using the zero-order line and a standard Si(100) reference band at 520.7 cm^{-1}. Samples were prepared by depositing a small quantity of sample from a methanolic suspension onto Si(100) wafers.

Solid state UV-vis spectroscopy was performed on an Agilent Cary 5000 UV-vis NIR Spectometer on neat sample powders. The data was acquired in reflectance mode, which was subsequently converted to Kubelka-Munk function. Solution UV-vis spectroscopy was performed on a Perkin-Elmer Lambda 25 UV/Vis spectrometer in quartz cuvettes. The sample was dissolved in water.

PL measurements were acquired with an Edinburgh Instruments FLS980 Photoluminescence spectrometer at wavelengths of 250 and 275 nm. Measurements at 405 nm were acquired with Horiba-Jobin-Yvon iHR550 spectrometer.

5.5.2 Purification and Opening of BNNTs

A BNNT puffball (112 mg) was torn into small chunks with tweezers, which was subsequently dispersed in NH_3(aq) (10% v/v, 200 mL). The mixture was sonicated for

4 hours with a sonic probe, with the flask submerged in ice water to limit heating. The dark grey dispersion was filtered, with care taken to only decant dispersed BNNTs, through a PTFE membrane (pore size 0.2 µm). The grey solid was dried on the filter membrane and was then heated to 800 °C for 1 hour, producing a white solid. The white solid was washed with boiling water (1000 mL) to give a white solid (50 mg, 25%).

5.5.3 Synthesis of $\{P_2W_{18}O_{62}\}$@BNNT

Purified BNNTs (9.5 mg) were heated to 200 °C for 1 hour. $K_6[P_2W_{18}O_{62}]$ (200 mg, 0.04 mM) was dissolved in water (3 mL) to which the dried BNNTs were added. The dispersion was sonicated for 5 minutes before being stirred for 48 hours. The dispersion was filtered through a PTFE membrane (pore size 0.2 µm) giving a pale blue solid (12.2 mg).

5.6 References

1. N. G. Chopra, R. J. Luyken, K. Cherrey, V. H. Crespi, M. L. Cohen, S. G. Louie and A. Zettl, *Science*, 1995, **269**, 966-967.
2. K. J. Erickson, A. L. Gibb, A. Sinitskii, M. Rousseas, N. Alem, J. M. Tour and A. K. Zettl, *Nano Lett.*, 2011, **11**, 3221-3226.
3. L. H. Li and Y. Chen, *Adv. Funct. Mater.*, 2016, **26**, 2594-2608.
4. Q. W. Xiang-Fen Jiang, Xue-Bin Wang, Xia Li, Jun Zhang, Dmitri Golberg, Yoshio Bando, *J. Mater. Sci. Technol.*, 2015, **31**, 589-598.
5. Y. Chen, J. Zou, S. J. Campbell and G. L. Caer, *Appl. Phys. Lett.*, 2004, **84**, 2430-2432.
6. H. M. Ghassemi and R. S. Yassar, *Appl. Mech. Rev.*, 2010, **63**.
7. D. Wickramaratne, L. Weston and C. G. Van de Walle, *J. Phys. Chem. C*, 2018, **122**, 25524-25529.
8. G. Cassabois, P. Valvin and B. Gil, *Nat. Photonics*, 2016, **10**, 262-266.
9. C. Elias, P. Valvin, T. Pelini, A. Summerfield, C. J. Mellor, T. S. Cheng, L. Eaves, C. T. Foxon, P. H. Beton, S. V. Novikov*, et al.*, *Nat. Commun.*, 2019, **10**, 2639.
10. L. Museur and A. Kanaev, *J. Appl. Phys.*, 2015, **118**, 084305.

11. X. Blase, A. Rubio, S. G. Louie and M. L. Cohen, *EPL*, 1994, **28**, 335.
12. H. Chen, Y. Chen, Y. Liu, C.-N. Xu and J. S. Williams, *Opt. Mater.*, 2007, **29**, 1295-1298.
13. C. Zhi, Y. Bando, C. Tang and D. Golberg, *Mater. Sci. Eng. R Rep.*, 2010, **70**, 92-111.
14. W. Mickelson, S. Aloni, W.-Q. Han, J. Cumings and A. Zettl, *Science*, 2003, **300**, 467-469.
15. K. E. Walker, G. A. Rance, Á. Pekker, H. M. Tóháti, M. W. Fay, R. W. Lodge, C. T. Stoppiello, K. Kamarás and A. N. Khlobystov, *Small Methods*, 2017, **1**, 1700184.
16. T. Pham, A. Fathalizadeh, B. Shevitski, S. Turner, S. Aloni and A. Zettl, *Nano Lett.*, 2016, **16**, 320-325.
17. Y. Bando, K. Ogawa and D. Golberg, *Chem. Phys. Lett.*, 2001, **347**, 349-354.
18. F.-F. Xu, Y. Bando, D. Golberg, M. Hasegawa and M. Mitome, *Acta Materialia*, 2004, **52**, 601-606.
19. D. Golberg, F. F. Xu and Y. Bando, *Appl. Phys. A*, 2003, **76**, 479-485.
20. W.-Q. Han, C. W. Chang and A. Zettl, *Nano Lett.*, 2004, **4**, 1355-1357.
21. Q. Weng, X. Wang, X. Wang, Y. Bando and D. Golberg, *Chem. Soc. Rev.*, 2016, **45**, 3989-4012.
22. F. Ma, G. Zhao, C. Li, T. Wang, Y. Wu, J. Lv, Y. Zhong and X. Hao, *CrystEngComm*, 2016, **18**, 631-637.
23. S. Azevedo, J. R. Kaschny, C. M. C. de Castilho and F. de Brito Mota, *Eur. Phys. J. B*, 2009, **67**, 507-512.
24. J. Choi, D. A. Reddy and T. K. Kim, *Ceram. Int.*, 2015, **41**, 13793-13803.
25. W. Wu, X. Lv, J. Wang and J. Xie, *J. Colloid Interface Sci.*, 2017, **496**, 434-445.
26. X.-f. Wu, Z.-h. Zhao, Y. Sun, H. Li, C.-x. Zhang, Y.-j. Wang, Y. Liu, Y.-d. Wang, X.-y. Yang and X.-d. Gong, *J. Nanopart. Res.*, 2017, **19**, 193.
27. C. Wang, Z. Chen, X. Yao, Y. Chao, S. Xun, J. Xiong, L. Fan, W. Zhu and H. Li, *Fuel*, 2018, **230**, 104-112.
28. H. Karimi-Maleh, F. Karimi, S. Malekmohammadi, N. Zakariae, R. Esmaeili, S. Rostamnia, M. L. Yola, N. Atar, S. Movaghgharnezhad, S. Rajendran*, et al.*, *Journal of Molecular Liquids*, 2020, **310**, 113185.

29. F. R. Pomilla, F. Fazlali, E. I. García-López, G. Marcì, A. R. Mahjoub, I. Krivtsov, L. F. Liotta and L. Palmisano, *Mater. Sci. Semicond. Process.*, 2020, **112**, 104987.

30. J. M. Cameron, D. J. Wales and G. N. Newton, *Dalton Trans.*, 2018, **47**, 5120-5136.

31. C. Streb, *Dalton Trans.*, 2012, **41**, 1651-1659.

32. B. Matt, J. Moussa, L.-M. Chamoreau, C. Afonso, A. Proust, H. Amouri and G. Izzet, *Organometallics*, 2012, **31**, 35-38.

33. B. Matt, J. Fize, J. Moussa, H. Amouri, A. Pereira, V. Artero, G. Izzet and A. Proust, *Energy Environ. Sci.*, 2013, **6**, 1504-1508.

34. B. Matt, X. Xiang, A. L. Kaledin, N. Han, J. Moussa, H. Amouri, S. Alves, C. L. Hill, T. Lian, D. G. Musaev*, et al.*, *Chem. Sci.*, 2013, **4**, 1737-1745.

35. C. Bosch-Navarro, B. Matt, G. Izzet, C. Romero-Nieto, K. Dirian, A. Raya, S. I. Molina, A. Proust, D. M. Guldi, C. Marti-Gastaldo*, et al.*, *Chem. Sci.*, 2014, **5**, 4346-4354.

36. D. Ma, L. Liang, W. Chen, H. Liu and Y.-F. Song, *Adv. Funct. Mater.*, 2013, **23**, 6100-6105.

37. Y. L. Liao, Z. F. Chen, J. W. Connell, C. C. Fay, C. Park, J. W. Kim and Y. Lin, *Adv. Funct. Mater.*, 2014, **24**, 4497-4506.

38. H. Chen, Y. Chen, J. Yu and J. S. Williams, *Chem. Phys. Lett.*, 2006, **425**, 315-319.

39. C. M. Teague, X. Li, M. E. Biggin, L. Lee, J. Kim and A. A. Gewirth, *J. Phys. Chem. B*, 2004, **108**, 1974-1985.

40. J. Haines, J. Rouquette, V. Bornand, M. Pintard, P. Papet and F. A. Gorelli, *J. Raman Spectrosc.*, 2003, **34**, 519-523.

41. R. Tayebee, M. M. Amini, H. Rostamian and A. Aliakbari, *Dalton Trans.*, 2014, **43**, 1550-1563.

42. C. R. Graham and R. G. Finke, *Inorg. Chem.*, 2008, **47**, 3679-3686.

43. H. D. Cho, I. T. Yoon, K. B. Chung, D. Y. Kim, T. W. Kang and S. U. Yuldashev, *J. Lumin.*, 2018, **195**, 344-347.

44. S. Zhao, X. Zhao, H. Zhang, J. Li and Y. Zhu, *Nano Energy*, 2017, **35**, 405-414.

45. X. Wei, D.-M. Tang, Q. Chen, Y. Bando and D. Golberg, *ACS Nano*, 2013, **7**, 3491-3497.

Concluding Remarks and Outlook

The work set out and described in this thesis has demonstrated the properties of confined polyoxometalates (POMs) within nanotubes, harnessing the high electrical conductivity of single walled carbon nanotubes (SWNTs) and intimate electronic contact between the encapsulated POM and nanotubes. Additionally, the encapsulation of POMs within the SWNTs allowed the nature of host-guest interactions between highly charged redox active species and SWNTs to be studied. The high rate of encapsulation and reactivity under the influence of the electron beam allowed for studies on the stability of POMs during electron microscopy imaging conditions and their encapsulation within boron nitride nanotubes (BNNTs) also allowed studies into the host-guest interactions of these systems.

The redox driven nanoconfinement of these species occurred at room temperature with minimal energetic input, due to the spontaneous electron transfer that occurred between the POMs in solution upon contact with the singe walled carbon nanotubes (SWNTs), leading to strong coulombic interactions between the anionic POMs and cationic SWNTs, driving the encapsulation. The materials showed a high rate of encapsulation within the seemingly hydrophobic channel as a result. When probing the hybrid materials with Raman spectroscopy, it was found that the level of oxidation of the SWNTs was dependent on the POM utilised during encapsulation, where a lower LUMO energy resulted in a more oxidised SWNT. X-ray photoelectron spectroscopy (XPS) of the hybrid materials confirmed that the POMs were in their native state upon encapsulation. When tuning the LUMO level of the POMs or utilising a species in which the oxidation of the SWNTs was not energetically favourable, the encapsulation rate appeared much lower. Additionally, the encapsulation of the vanadate species appeared to lead to a loss of its molecular structure.

Transmission electron microscopy (TEM) of the {POM}@SWNT materials was highly dependent on the electron flux used for imaging, indicating that the POMs were highly reactive upon irradiation with an electron beam, manifested as rapid POM condensation to metallic nanoparticles due to the sputtering of oxygen atoms. This reaction was found to be dependent on the flux of the electron beam. The extremely high rate of encapsulation meant that the material was an ideal model for studying both atomic scale dynamics of the condensation reaction as well as beginning to study ~100 molecules simultaneously. Aberration corrected-TEM (AC-TEM) studies of the products revealed highly reactive oxygen rich nanoclusters which continued to take part in reactions with confined neighbours and the SWNT itself.

Electrochemical evaluation of the {POM}@SWNT materials revealed that the POMs were still electrochemically addressable upon encapsulation and possessed rapid solid-state electron transfer properties which were observed as low peak-to-peak separation values. Most of the POM processes were retained upon encapsulation when carrying out the cyclic voltammograms (CVs) of the materials in acidic electrolytes. The materials were highly stable when repeatedly cycling and a large amount (80 % or more) of the POMs were electrochemically addressable when encapsulated within the SWNTs. This inherent stability also allowed a CV of the {POM}@SWNT materials to be obtained in electrolytes with a pH of 14. When altering the electrolytes to those with a pH of 7 and above, the acidic processes were largely lost in the {POM}@SWNT materials, leading to new processes, confirming that the processes in acidic electrolytes were proton coupled. In addition, the processes that were observed in the pH 7 electrolytes were rapidly lost over approximately 50 cycles, indicating that the steric barriers of the larger cations (Li^+ and Na^+) diffusing to the encapsulated POMs during cycling were too high. Blocking the uncapped open ends of the SWNTs with fullerene molecules led to minimal changes in the responses of the materials in acidic electrolytes, and drastic reductions in redox currents when utilising Li^+ cations in the supporting electrolyte.

POMs also readily encapsulated within BNNTs at room temperature in water. The host-guest interactions could be probed with Raman spectroscopy by analysing the POM vibrational modes upon encapsulation, which showed changes in the vibrational bands upon encapsulation, such as the "switching on" of a Raman silent mode and the switching of symmetric and asymmetric vibrational modes. These were indicative of changes in the polarizability of the molecule upon encapsulation, likely through the surface interactions with the BNNT sidewalls, thus satisfying Raman selection rules. Low temperature Raman spectroscopy of the material showed the emergence of new photoluminescent emissions in the hybrid material, suggesting that the encapsulated POMs and BNNTs were in good electronic communication with one another. Photoluminescence (PL) spectroscopy further confirmed this, which showed that PL emissions from the BNNTs were largely quenched upon the encapsulation of the POM molecules, suggesting that charge transfer between the host and guest could occur upon photoexcitation.

This work has presented an opportunity for new methods of encapsulation within SWNTs, studying electron beam induced reactions, studying electrochemical processes within nanoconfined environments and studying electron transitions between BNNT-hosts and their guests. Further exploiting these materials and methods for a myriad of different applications will likely lead to new material opportunities.

The natural progression for this work would be to further explore the redox driven nanoconfinement of other redox active species, or utilising POMs as oxidants in the encapsulation reaction to incorporate other charged species within the hydrophobic channel. Such methodologies could lead to the incorporation of much lighter elements that could be used in energy storage. Additionally, the *in situ* encapsulation of Mo and W based POMs could also be explored, possibly leading to novel POM structures, as well as making the process more applicable to industrial scale up.

Whilst the {POM}@SWNT materials served as fascinating systems to probe cation mass transport in the channels of SWNTs, more work should be carried out, particularly on the transport of deuterium through the graphitic lattice. This reduced mass transport appears to hamper the ability to use these materials in current generation lithium ion batteries and as such work should be carried out on lowering the steric barriers of ion intercalation within the {POM}@SWNT materials, through strategies such as the introduction of sidewall defects, or increasing the diameter of the carbon nanotube. Such solutions may pave the way for the incorporation guest@CNT materials in energy storage materials.

Other POM species should be encapsulated within BNNTs, such as the one encapsulated within the SWNTs. The varied energy levels of the different POMs would likely lead to tuneable photoactive systems that could find use in photocatalysis or other photoactive devices.

The tuneability of POMs through atomic substitutions and the formation of hybrids mean that the potential applications of {POM}@CNT and {POM}@BNNT materials is very broad, and as such this work has only begun to scratch the surface of what could be possible with polyoxometalates confined within nanotubes.

Appendix

{POM}@SWNT Raman Spectra

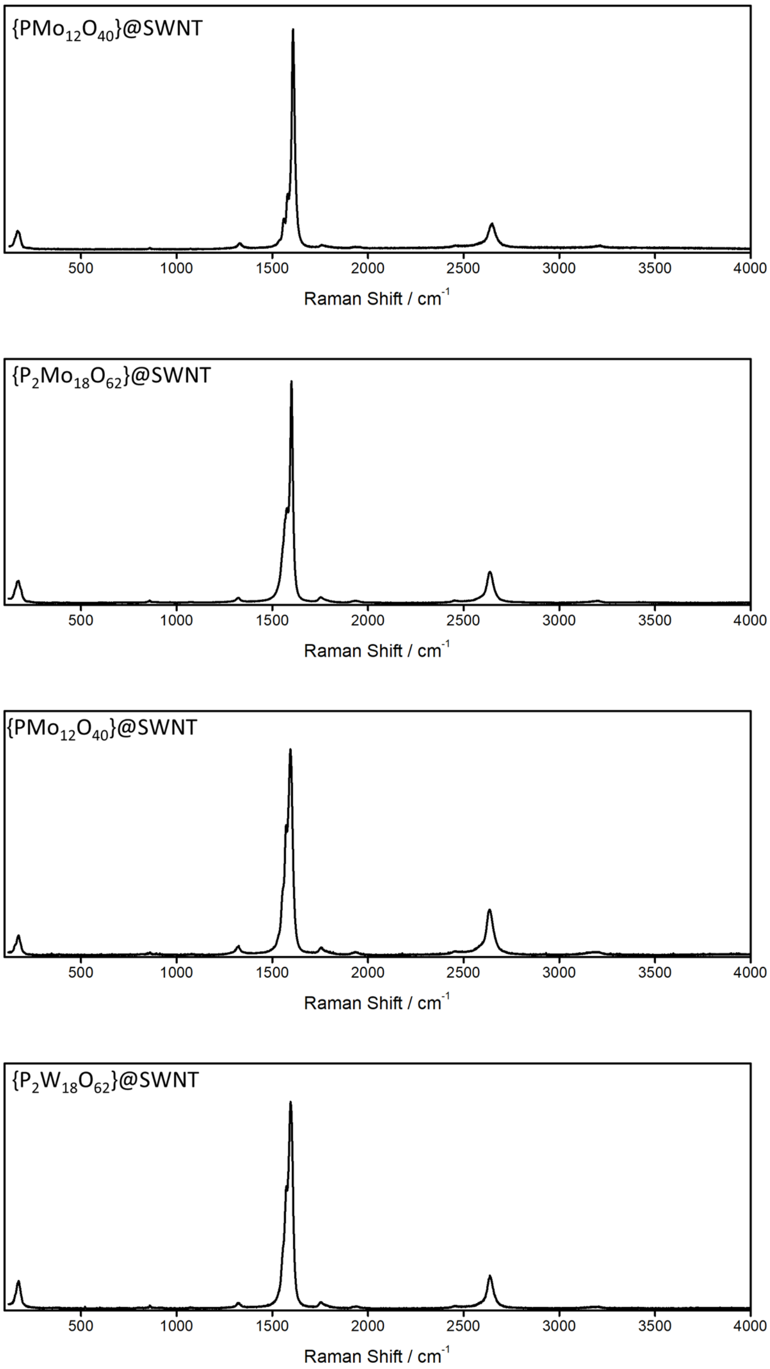

Figure A1. Full Raman spectra of the {POM}@SWNT materials (labelled). Spectra acquired with an excitation wavelength of 660 nm (1.88 eV).

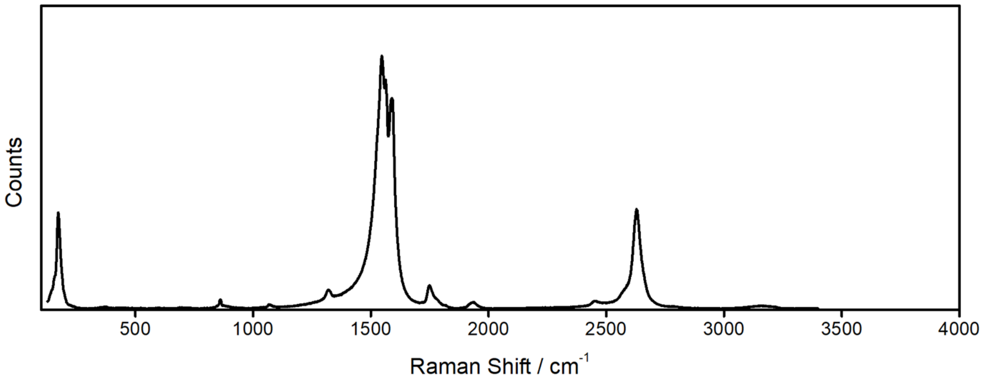

Figure A2. Full Raman spectrum of {TBA-$P_2W_{18}O_{62}$*}@SWNT. Spectrum acquired with an excitation wavelength of 660 nm (1.88eV).*

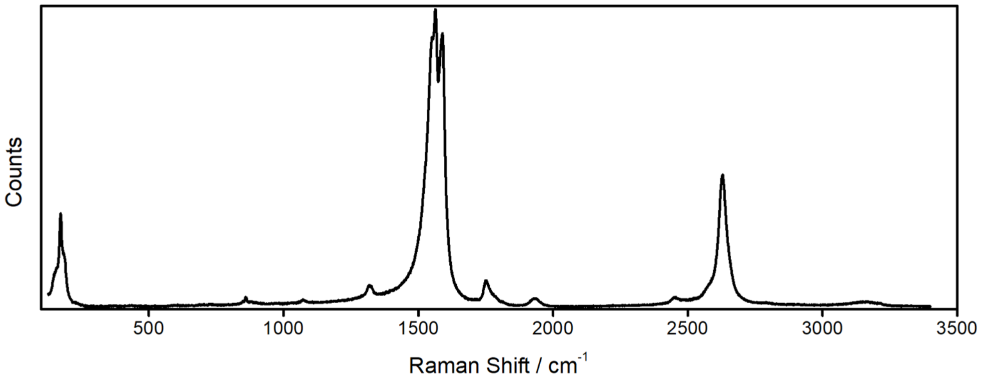

Figure A3. Full Raman spectrum of {V_6*}@SWNT. Spectrum acquired with an excitation wavelength of 660 nm (1.88 eV).*

{POM}@SWNT XPS Spectra

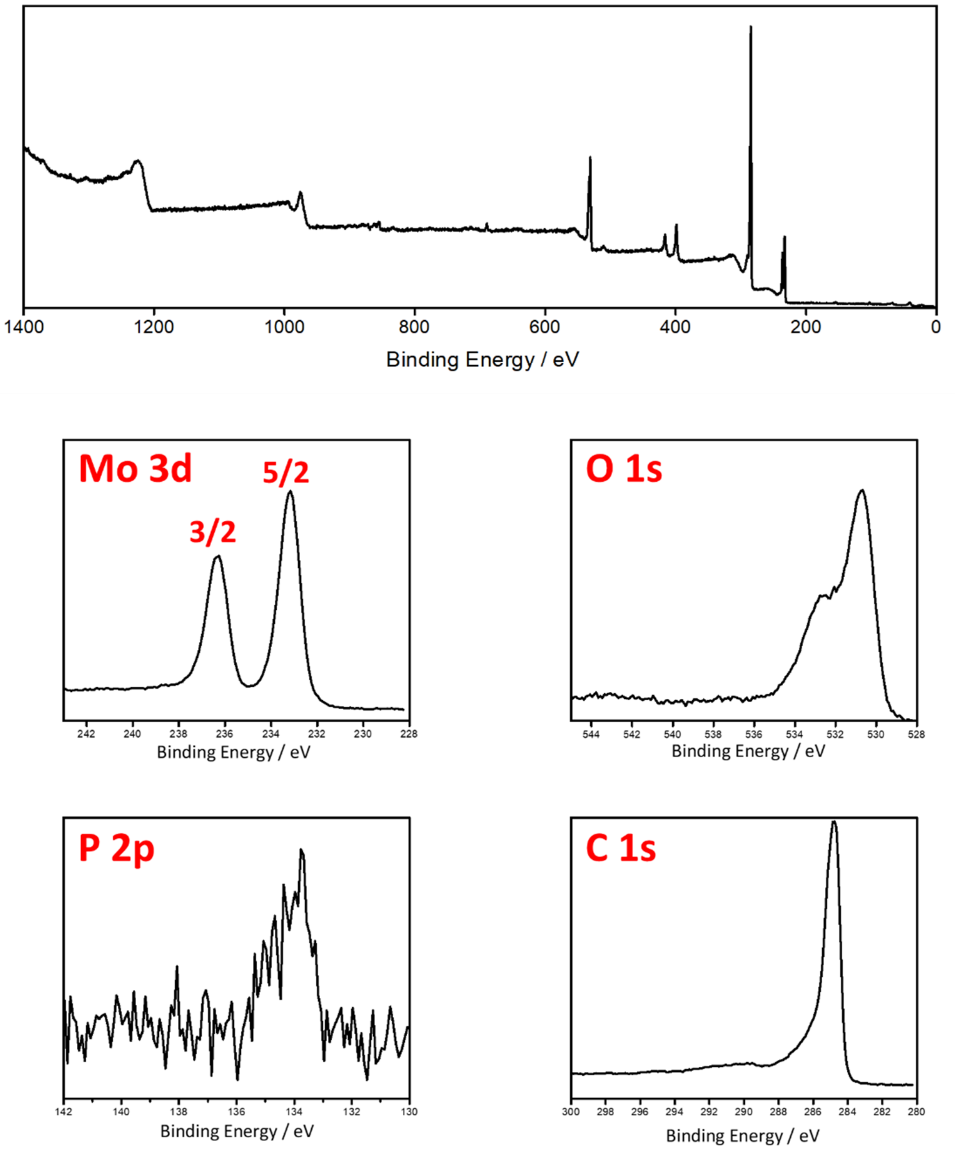

Figure A4. XPS spectra of {$PMo_{12}O_{40}$}@SWNT. Spectra charge corrected to C 1s at 284.5 eV.

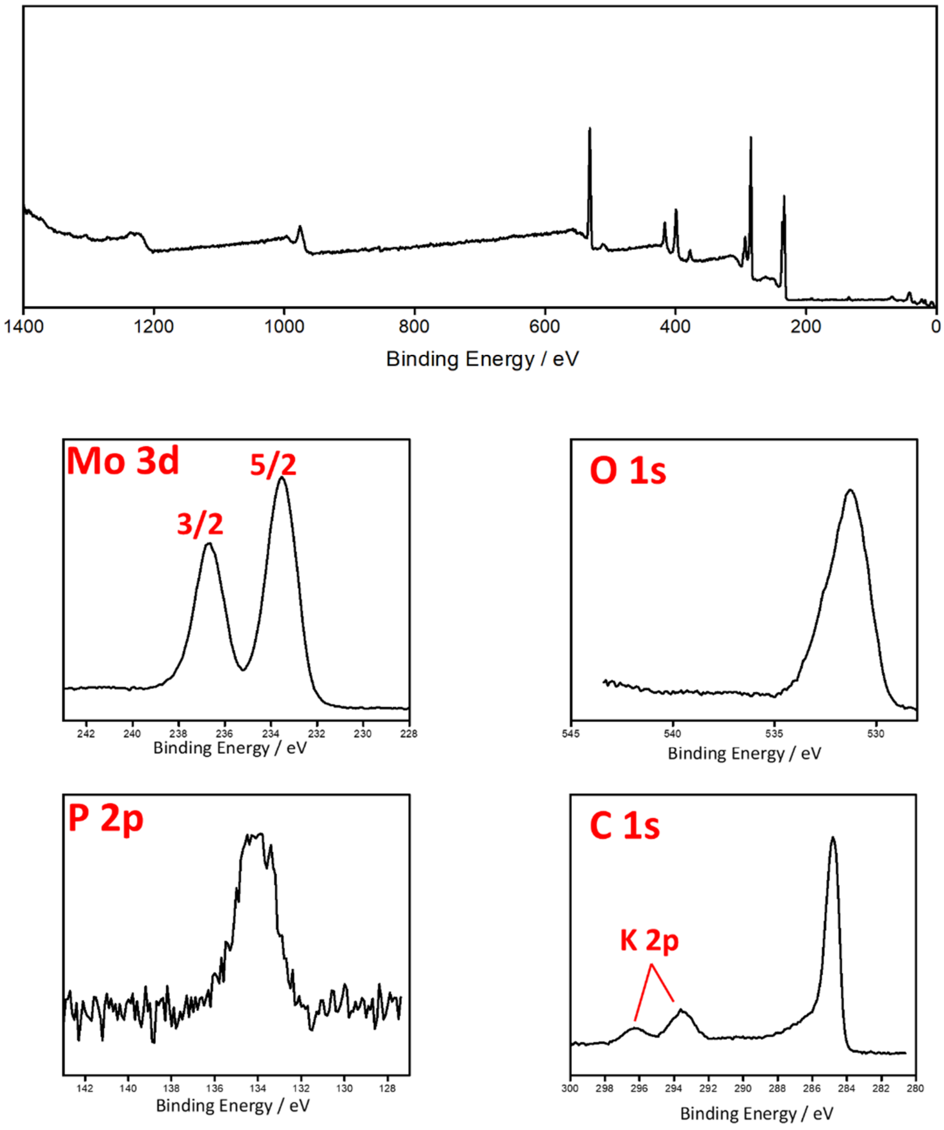

Figure A5. XPS spectra of $\{P_2Mo_{18}O_{62}\}$@SWNT. Spectra charge corrected to C 1s at 284.5 eV.

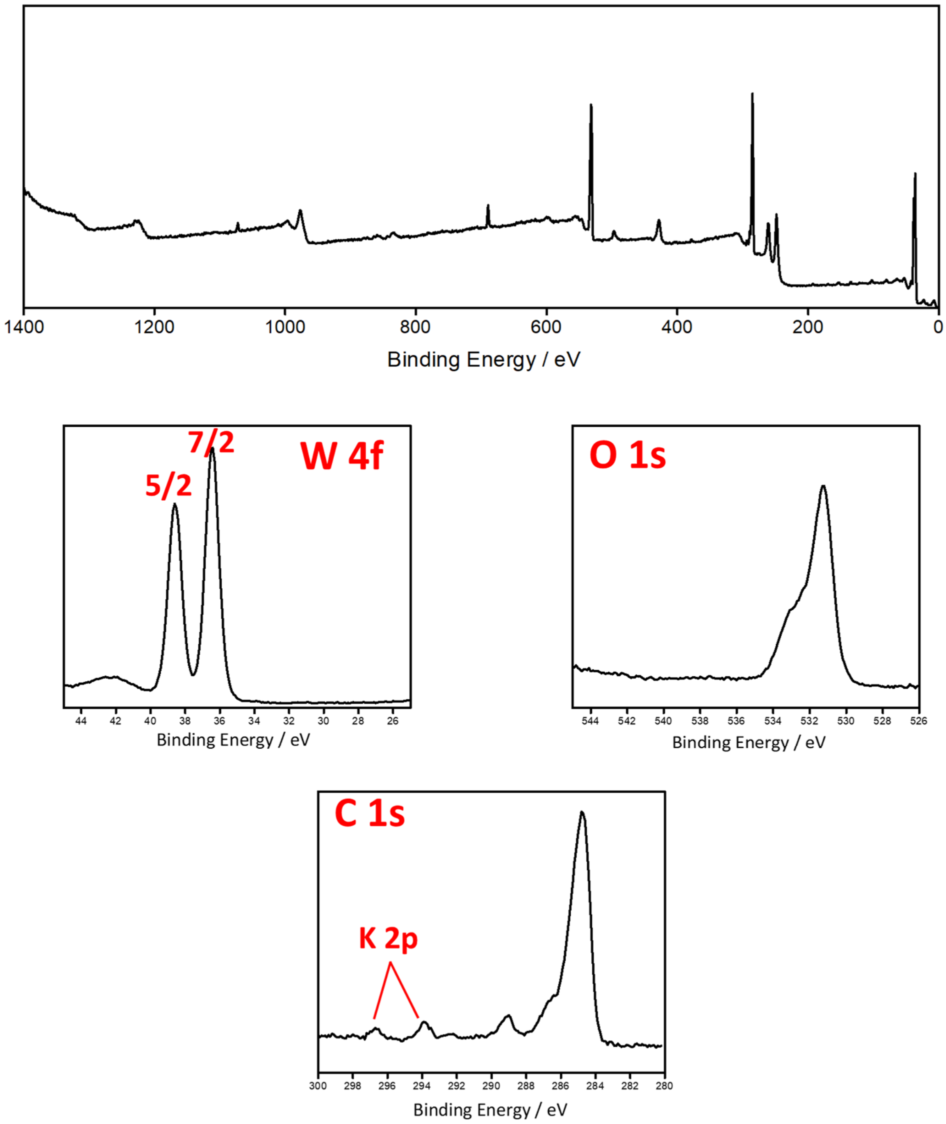

Figure A6. XPS spectra of {$PW_{12}O_{40}$}@SWNT. Spectra charge corrected to C 1s at 284.5 eV.

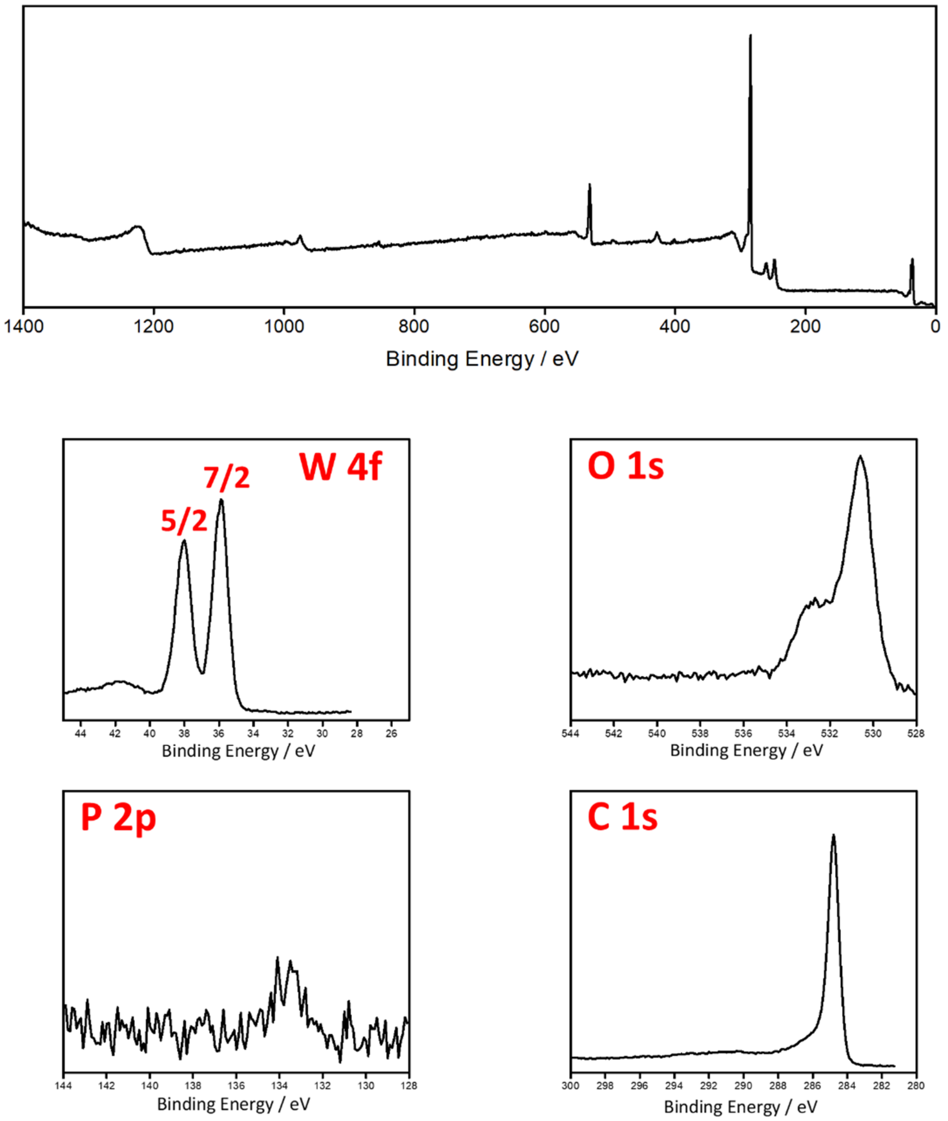

Figure A7. XPS spectra of {$P_2W_{18}O_{62}$}@SWNT. Spectra charge corrected to C 1s at 284.5 eV.

{POM}@SWNT Varied Electrolytes

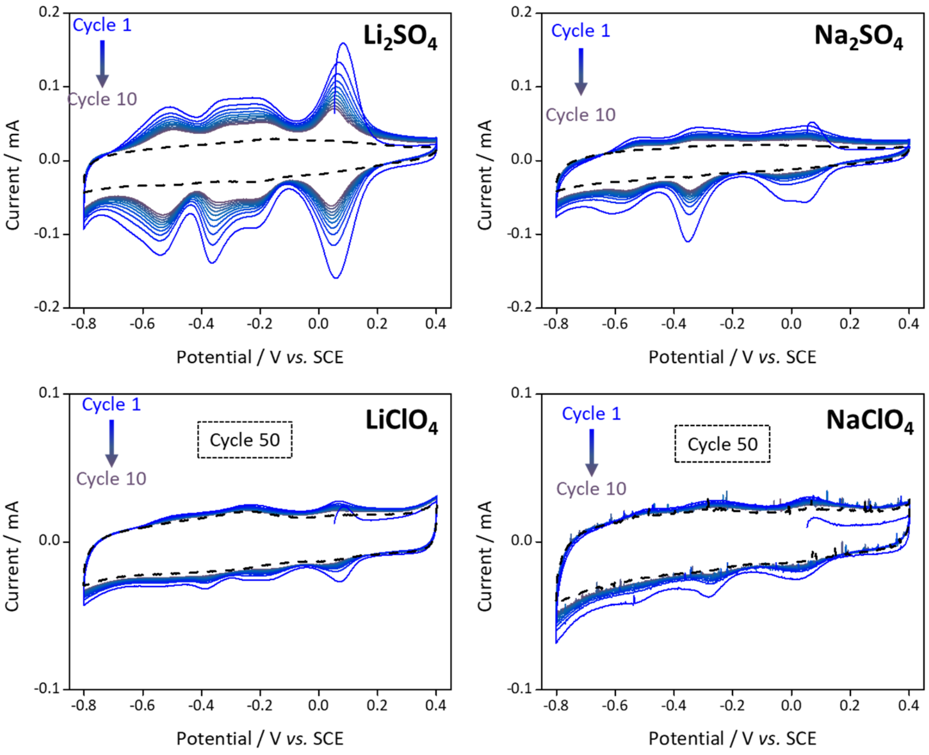

Figure A8. CVs of {$PMo_{12}O_{40}$}@SWNT recorded in 1 M electrolytes (labelled). All CVs recorded with a GCE working electrode, SCE reference electrode and platinum counter electrode at a scan rate of 0.1 V s^{-1}.

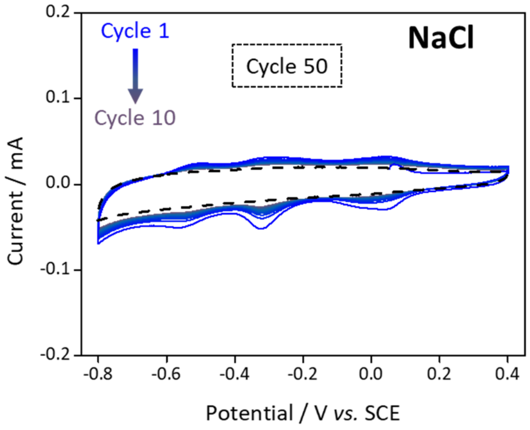

Figure A9. CV of {$PMo_{12}O_{40}$}@SWNT recorded in 1 M NaCl. CV recorded with a GCE working electrode, SCE reference electrode and platinum counter electrode at a scan rate of 0.1 V s^{-1}.

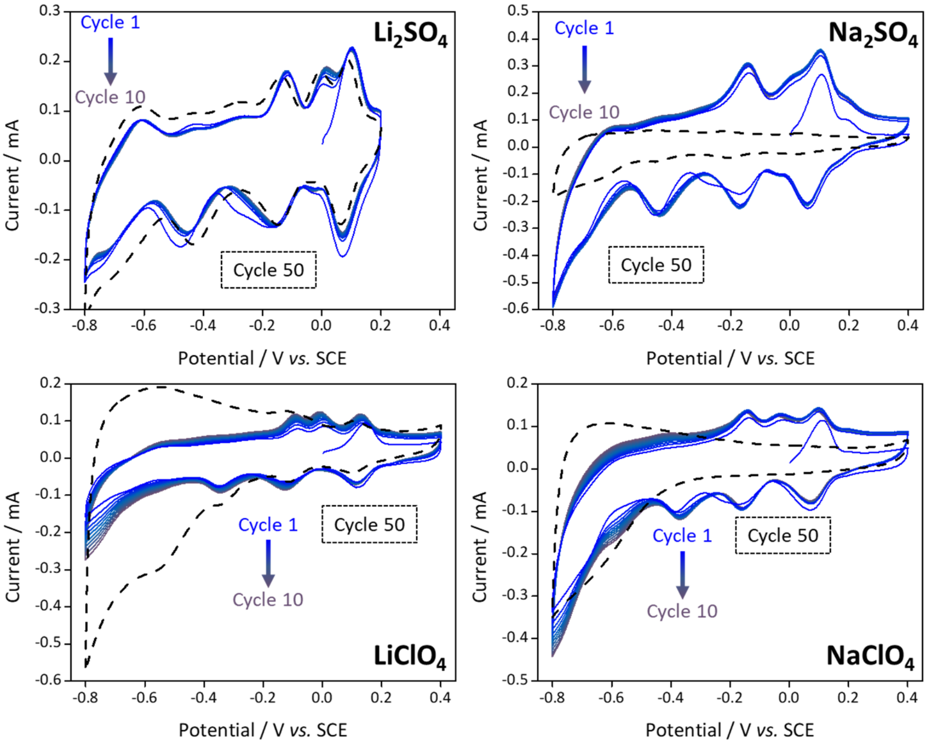

Figure A10. CVs of {$P_2Mo_{18}O_{62}$}@SWNT recorded in 1 M electrolytes (labelled). All CVs recorded with a GCE working electrode, SCE reference electrode and platinum counter electrode at a scan rate of 0.1 V s^{-1}.

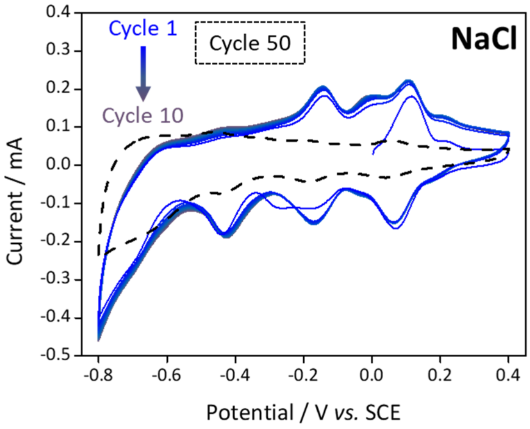

Figure A11. CV of {$P_2Mo_{18}O_{62}$}@SWNT recorded in 1 M NaCl. CV recorded with a GCE working electrode, SCE reference electrode and platinum counter electrode at a scan rate of 0.1 V s^{-1}.

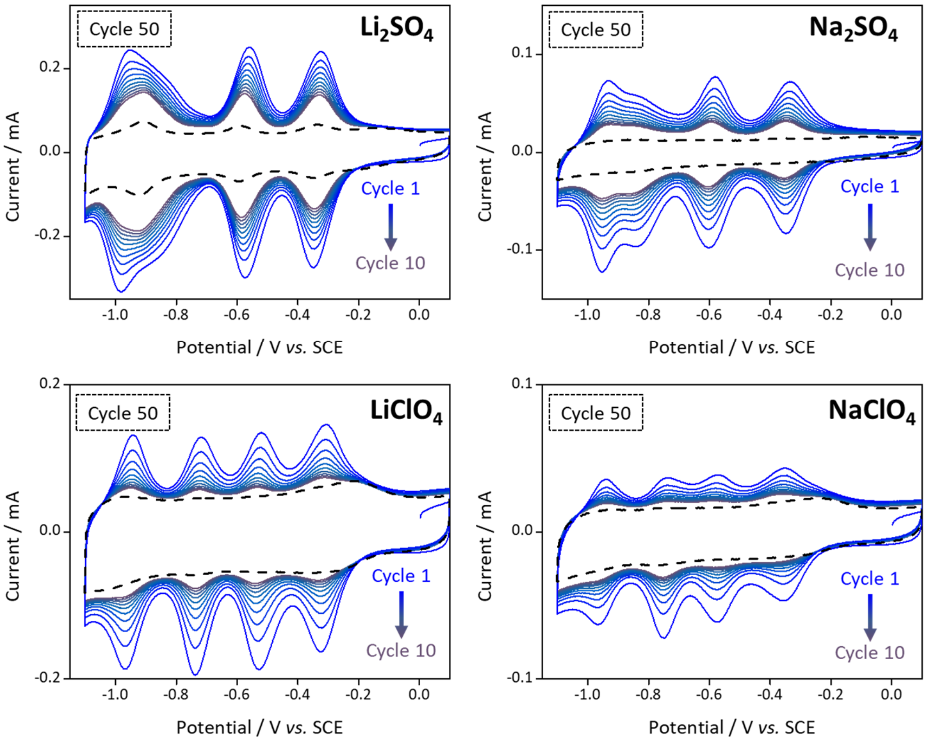

Figure A12. CVs of {$PW_{12}O_{40}$}@SWNT recorded in 1 M electrolytes (labelled). All CVs recorded with a GCE working electrode, SCE reference electrode and platinum counter electrode at a scan rate of 0.1 V s^{-1}.

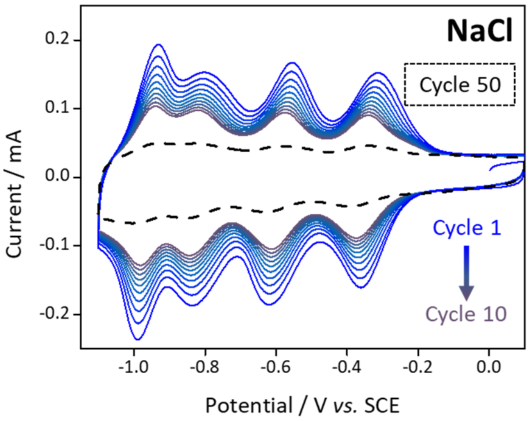

Figure A13. CV of {$PW_{12}O_{40}$}@SWNT recorded in 1 M NaCl. CV recorded with a GCE working electrode, SCE reference electrode and platinum counter electrode at a scan rate of 0.1 V s^{-1}.

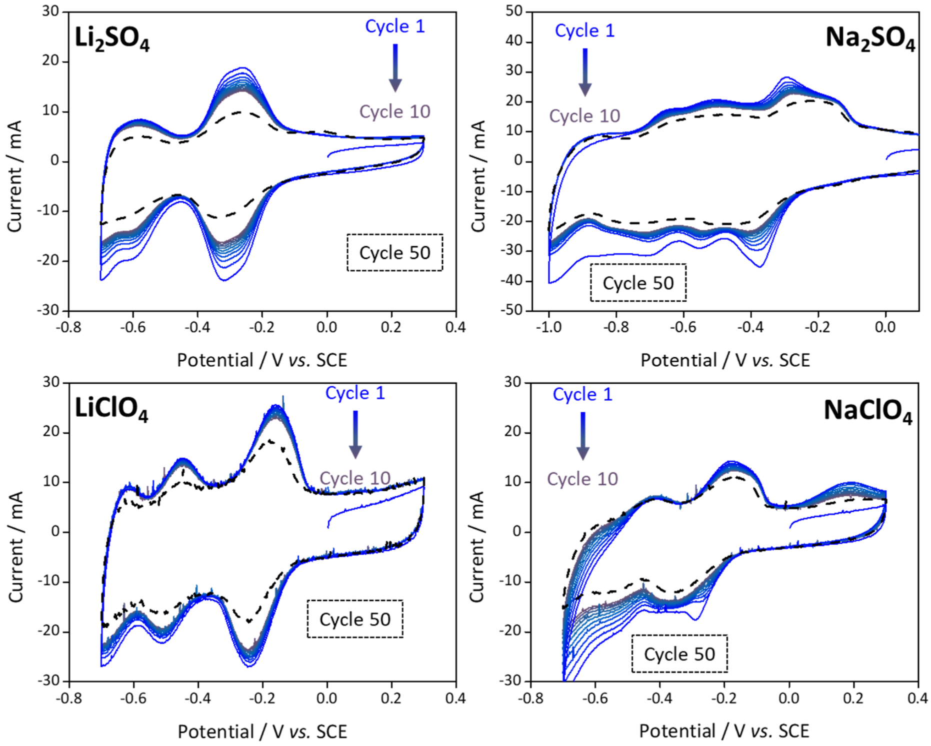

Figure A14. CVs of {$P_2W_{18}O_{62}$}@SWNT recorded in 1 M electrolytes (labelled). All CVs recorded with a GCE working electrode, SCE reference electrode and platinum counter electrode at a scan rate of 0.1 V s^{-1}.

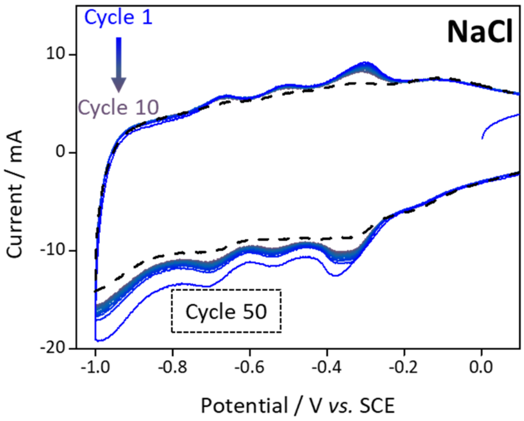

Figure A15. CV of {$P_2W_{18}O_{62}$}@SWNT recorded in 1 M NaCl. CV recorded with a GCE working electrode, SCE reference electrode and platinum counter electrode at a scan rate of 0.1 V s^{-1}.

Solution Cyclic Voltammetry

$H_3[PMo_{12}O_{40}]$

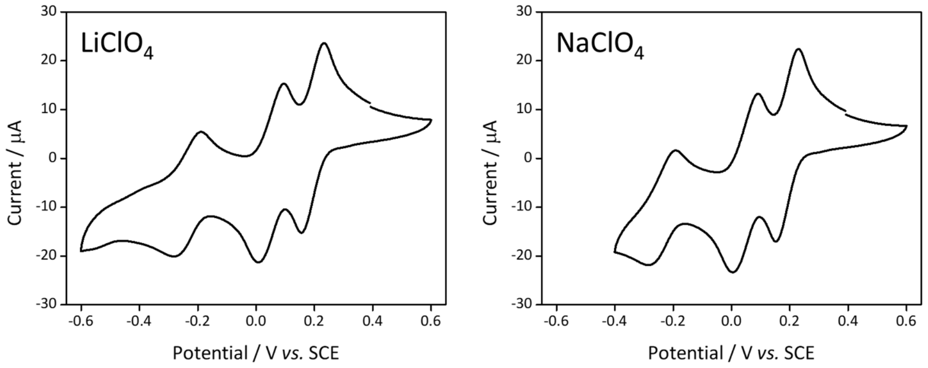

Figure A16. Cyclic voltammograms of $H_3[PMo_{12}O_{40}]$ recorded in 0.1 M $LiClO_4$ & $NaClO_4$ (labelled) with 80% v/v MeCN. Both CVs recorded with a glassy carbon working electrode (GCE), saturated calomel reference electrode (SCE) and platinum counter electrode at a scan rate of 0.1 V s^{-1} with an analyte concentration of 10 mM.

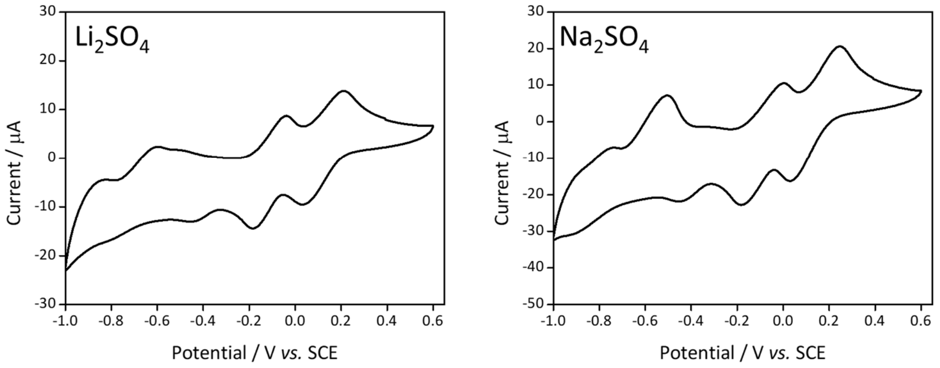

Figure A17. Cyclic voltammograms of $H_3[PMo_{12}O_{40}]$ recorded in 0.1 M Li_2SO_4 & Na_2SO_4 (labelled) with 80% v/v MeCN. Both CVs recorded with a glassy carbon working electrode (GCE), saturated calomel reference electrode (SCE) and platinum counter electrode at a scan rate of 0.1 V s^{-1} with an analyte concentration of 10 mM.

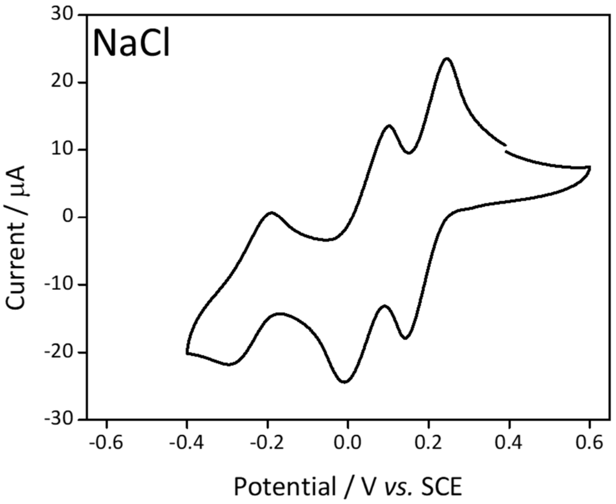

Figure A18. Cyclic voltammogram of $H_3[PMo_{12}O_{40}]$ recorded in 0.1 NaCl with 80% v/v MeCN. CV recorded with a glassy carbon working electrode (GCE), saturated calomel reference electrode (SCE) and platinum counter electrode at a scan rate of 0.1 V s^{-1} with an analyte concentration of 10 mM.

$K_6[P_2Mo_{18}O_{62}]$

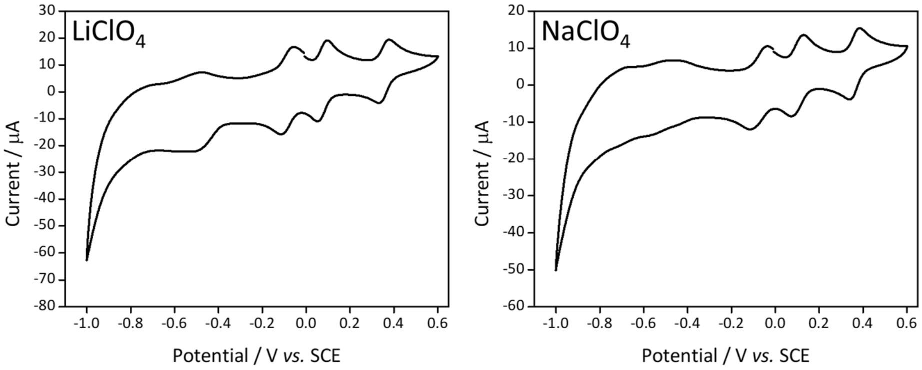

Figure A19. Cyclic voltammograms of $K_6[P_2Mo_{18}O_{62}]$ recorded in 1 M $LiClO_4$ & $NaClO_4$ (labelled). Both CVs recorded with a glassy carbon working electrode (GCE), saturated calomel reference electrode (SCE) and platinum counter electrode at a scan rate of 0.1 V s^{-1} with an analyte concentration of 10 mM.

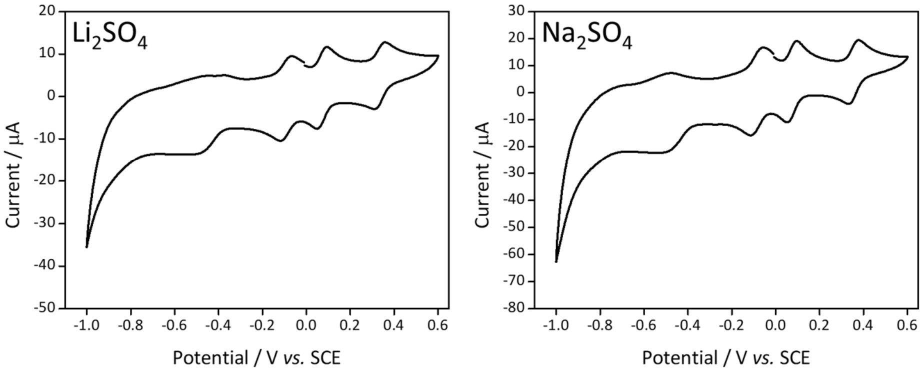

Figure A20. Cyclic voltammograms of $K_6[P_2Mo_{18}O_{62}]$ recorded in 1 M Li_2SO_4 & Na_2SO_4 (labelled). Both CVs recorded with a glassy carbon working electrode (GCE), saturated calomel reference electrode (SCE) and platinum counter electrode at a scan rate of 0.1 V s^{-1} with an analyte concentration of 10 mM.

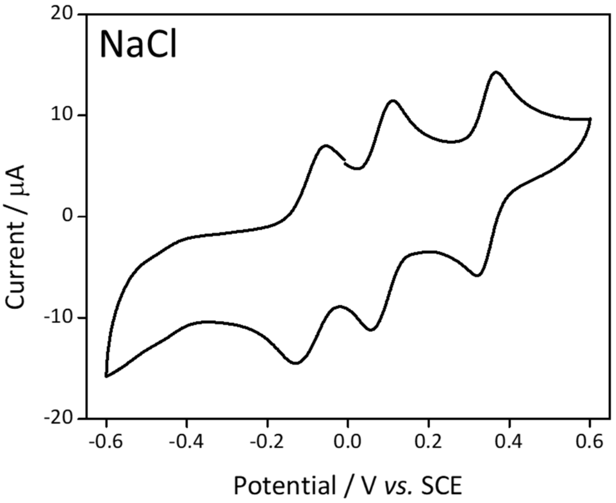

Figure A21. Cyclic voltammogram of $K_6[P_2Mo_{18}O_{62}]$ recorded in 1 M NaCl. CV recorded with a glassy carbon working electrode (GCE), saturated calomel reference electrode (SCE) and platinum counter electrode at a scan rate of 0.1 V s^{-1} with an analyte concentration of 10 mM.

$H_3[PW_{12}O_{40}]$

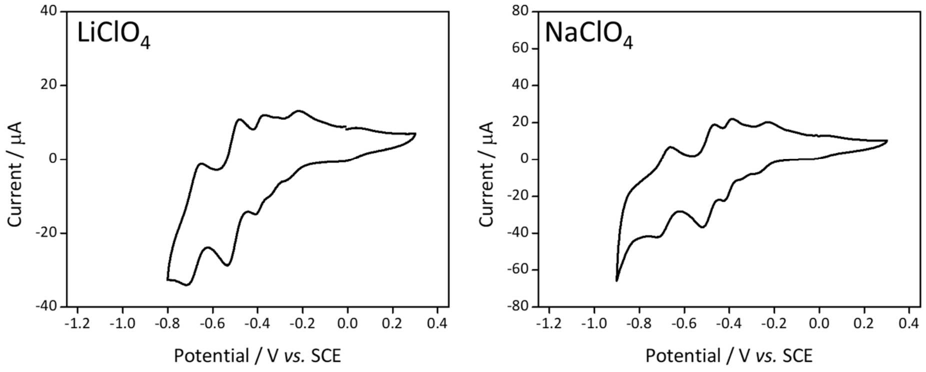

Figure A22. Cyclic voltammograms of $H_3[PW_{12}O_{40}]$ recorded in 1 M $LiClO_4$ & $NaClO_4$ (labelled). Both CVs recorded with a glassy carbon working electrode (GCE), saturated calomel reference electrode (SCE) and platinum counter electrode at a scan rate of 0.1 V s^{-1} with an analyte concentration of 10 mM.

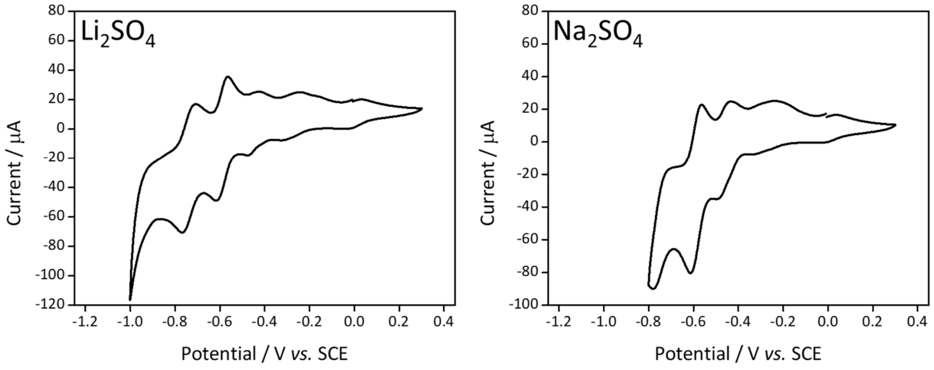

Figure A23. Cyclic voltammograms of $H_3[PW_{12}O_{40}]$ recorded in 1 M Li_2SO_4 & Na_2SO_4 (labelled). Both CVs recorded with a glassy carbon working electrode (GCE), saturated calomel reference electrode (SCE) and platinum counter electrode at a scan rate of 0.1 V s^{-1} with an analyte concentration of 10 mM.

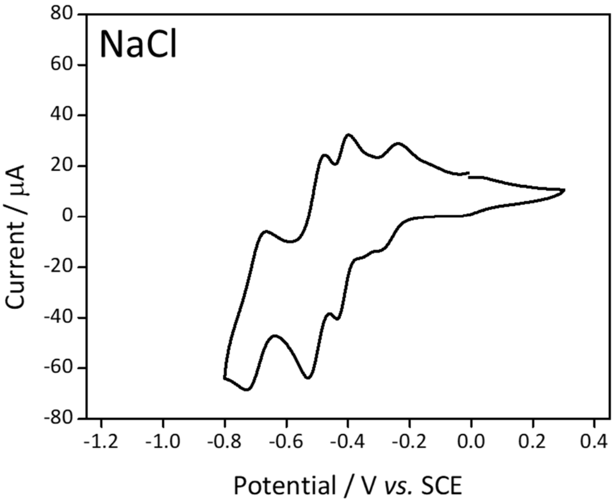

Figure A24. Cyclic voltammogram of $H_3[PW_{12}O_{40}]$ recorded in 1 M NaCl. CV recorded with a glassy carbon working electrode (GCE), saturated calomel reference electrode (SCE) and platinum counter electrode at a scan rate of 0.1 V s^{-1} with an analyte concentration of 10 mM.

$K_6[P_2W_{18}O_{62}]$

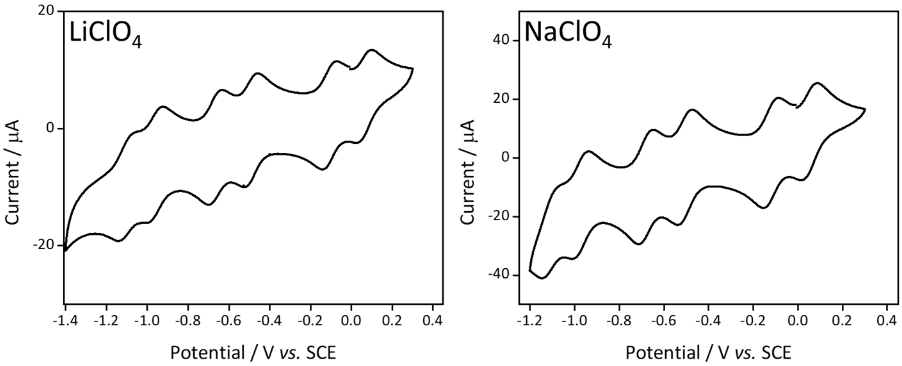

Figure A25. Cyclic voltammograms of $K_6[P_2W_{18}O_{62}]$ recorded in 1 M $LiClO_4$ & $NaClO_4$ (labelled). Both CVs recorded with a glassy carbon working electrode (GCE), saturated calomel reference electrode (SCE) and platinum counter electrode at a scan rate of 0.1 V s^{-1} with an analyte concentration of 10 mM.

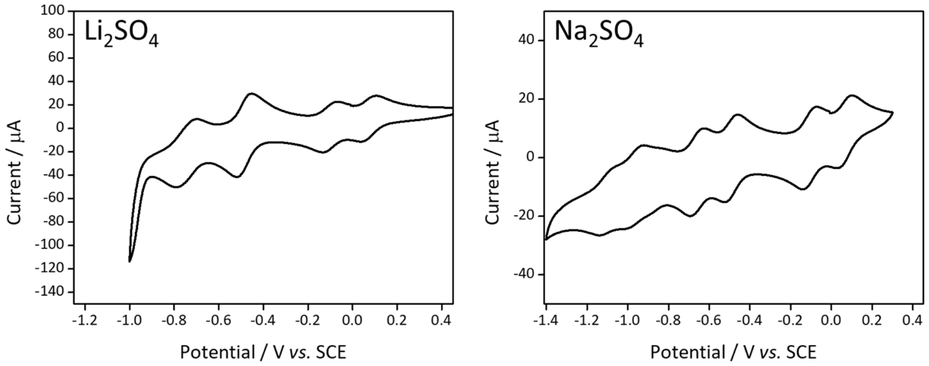

Figure A26. Cyclic voltammograms of $K_6[P_2W_{18}O_{62}]$ recorded in 1 M Li_2SO_4 & Na_2SO_4 (labelled). Both CVs recorded with a glassy carbon working electrode (GCE), saturated calomel reference electrode (SCE) and platinum counter electrode at a scan rate of 0.1 V s^{-1} with an analyte concentration of 10 mM.

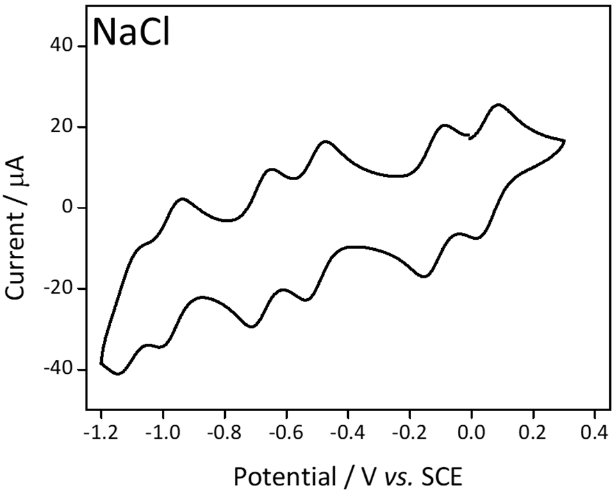

Figure A27. Cyclic voltammogram of $K_6[P_2W_{18}O_{62}]$ recorded in 1 M NaCl. CV recorded with a glassy carbon working electrode (GCE), saturated calomel reference electrode (SCE) and platinum counter electrode at a scan rate of 0.1 V s^{-1} with an analyte concentration of 10 mM.